

HYDRO-CLIMATIC INFLUENCES OF EL-NINO/SOUTHERN OSCILLATION ON  
NUTRIENT LOADS IN THE SOUTHEAST UNITED STATES

By

VICTORIA WHITWORTH KEENER

A DISSERTATION PRESENTED TO THE GRADUATE SCHOOL  
OF THE UNIVERSITY OF FLORIDA IN PARTIAL FULFILLMENT  
OF THE REQUIREMENTS FOR THE DEGREE OF  
DOCTOR OF PHILOSOPHY

UNIVERSITY OF FLORIDA

2010

© 2010 Victoria Whitworth Keener

To my wonderful grandmother, Yue Mei-Fong,  
who continues to be a woman ahead of her time

獻給我非凡的祖母,余美芳,  
一個永遠走在時代前面的人

## ACKNOWLEDGMENTS

Completing a Doctoral dissertation is as much an exercise in perseverance as one of learning and research. Of the multitude of times I was discouraged, depressed, or despairing of ever finishing, there have been people that empathized with me, then promptly reminded me that not only *could* I do it, in fact, I *had* to do it, and should probably get back to work and stop complaining.

I would like to thank my advisor, Dr. James Jones, for his encouragement, intelligence, generosity, and kindness. I can not imagine a more positive mentoring experience with better opportunities than the ones he has provided for me. I also thank my Committee members, Drs Wendy Graham, Greg Kiker, Ken Campbell, and Mike Annable for their thoughtful input and help in completing this research. For their graciousness in both collecting and sharing massive amounts of data with me, I thank the members of the USDA-ARS Southeast Watershed Research Laboratory in Tifton, Georgia, without whom most of this research would not have been possible.

The friends I made in graduate school are for-a-lifetime, and I would have not been able to make it through without their understanding and commiseration. Special thanks go out to my Tanks In Series band-mates David Kaplan and Dan Tankersley, with whom I made “beautiful” music, and released a lot of stress by learning how to play the drums. Other creatures and molecules that made graduate school endurable include my cats, Odette (R.I.P), Bun-Bun, and Frey, and caffeine.

A significant part of maintaining my happiness and sanity is attributable to my husband, Keith. Although not a day passed near the very end that I did not envy his already being done with his Ph.D., his love, confidence, and laid-back attitude was a large part of what allowed me to get through Graduate School in (mostly) one piece.

Most importantly, I thank my parents, Tom and Nanda Keener, for their unwavering love, support, inspiration, happiness, and belief in me. This dissertation would not have been possible without the traits I inherited and learned from each of them. From my father: logic, scientific curiosity, a love of nature and the outdoors, the desire to question the dominant paradigm, and impatience. From my mother: patience (to balance the impatience inherited from my father), perseverance, assertiveness, the ability and inclination to understand that with which you disagree, and the power to stay awake and alert late into the night. I have a bad habit of forgetting to thank them, which is because they are such wonderful parents that it is all too easy to take them for granted. Much like breathing or having a heartbeat, they are always there, keeping me going, and for that I love and thank them with all my heart.

# TABLE OF CONTENTS

	<u>page</u>
ACKNOWLEDGMENTS.....	4
LIST OF TABLES.....	9
LIST OF FIGURES.....	10
ABSTRACT .....	13
CHAPTER	
1 INTRODUCTION AND LITERATURE REVIEW .....	15
Motivating Issues .....	15
Global Climate Change and Water Supply.....	15
Climate Indices and the El-Niño/Southern Oscillation .....	17
Global ENSO effects .....	20
Paleo-climate and future of ENSO.....	22
Climate and Agriculture in the Southeast United States.....	25
Objectives .....	27
Literature Review .....	28
Agricultural Pollution: Nutrients .....	28
Water Management Policies in the Southeast.....	31
The Watershed Restoration Act (WRA) and TMDL standards .....	31
Best Management Practices (BMP).....	33
Simulation of Natural Systems .....	36
Global circulation models and ENSO .....	39
Agro-hydrological models .....	40
Time series models .....	42
Spectral analysis and models .....	44
2 EFFECTS OF CATEGORICAL EL NIÑO/SOUTHERN OSCILLATION ON SIMULATED PHOSPHORUS LOADING IN SOUTH FLORIDA .....	49
Introduction .....	49
Data and Methods .....	53
The Lake Okeechobee Watershed.....	53
History and hydrology .....	54
Geology and soils .....	56
Ecology and wildlife .....	57
Management and restoration.....	58
Data .....	59
Watershed Assessment Model (WAM).....	61
Analysis and Statistics.....	64
Precipitation and stream flow.....	64

	Phosphorus concentration and loading: JMA ENSO classification .....	64
	Phosphorus concentration and loading: M-ENSO classification .....	69
Results .....		70
	Monthly Precipitation and ENSO Phase .....	70
	Monthly Simulated Stream Flow and ENSO Phase .....	72
	Simulated Monthly P Concentration and ENSO Phase .....	73
	Simulated Monthly P Load and ENSO Phase .....	74
	Simulated Seasonal P Load, Concentration, Stream flow, and JMA ENSO Phase .....	76
	February-March-April .....	78
	May-June-July .....	79
	August-September-October .....	80
	November-December-January .....	81
	M-ENSO Statistics (ANOVA) of Monthly Precipitation, Flow, P Concentration and Load .....	82
Summary and Discussion .....		83
<b>3</b>	<b>EL-NIÑO/SOUTHERN OSCILLATION (ENSO) INFLUENCES ON MONTHLY NO<sub>3</sub> LOAD AND CONCENTRATION, STREAM FLOW AND PRECIPITATION IN THE LITTLE RIVER WATERSHED, TIFTON, GEORGIA. ....</b>	<b>102</b>
	Introduction .....	102
	Data and Methods .....	106
	Field Site: Little River Watershed .....	106
	History and monitoring .....	107
	Soils and geology .....	109
	Climate and hydrology .....	110
	Land use, management and policies .....	111
	Little River Watershed Data .....	113
	Wavelet Analysis .....	115
	Cross Wavelet and Coherence Transforms .....	118
	Cross-Correlation Time Series Analysis .....	119
Results .....		120
	Wavelet Analysis .....	120
	Cross-Wavelet Analysis .....	124
	Wavelet Coherence Analysis .....	125
	Cross Correlation Analysis .....	127
Summary and Discussion .....		128
<b>4</b>	<b>INTEGRATION OF ENSO SIGNAL POWER THROUGH HYDROLOGICAL PROCESSES IN THE LITTLE RIVER WATERSHED .....</b>	<b>146</b>
	Introduction .....	146
	Data and Methods .....	150
	Field Site and Data: The Little River Watershed .....	150
	SWAT Model Hydrologic Calibration and Validation .....	151
	Water Budget and Exceedance Curves .....	156

Wavelet Analysis .....	157
Results .....	158
Observed Precipitation and Stream Flow .....	158
SWAT Water Budget and Exceedance Curves by ENSO Phase .....	159
Univariate Wavelet Analysis .....	162
Cross Wavelet and Wavelet Coherence Analysis .....	165
Summary and Discussion .....	167
5 AN ENSO BASED MULTIVARIATE TIME-SERIES MODEL FOR FLOWS AND NITROGEN LOADS IN THE LITTLE RIVER WATERSHED .....	182
Introduction .....	182
Data and Methods .....	187
Field Site and Hydro-Climate Data .....	187
SWAT Nutrient Calibration and CP Implementation .....	187
Wavelet Reconstruction .....	190
Wavelet Time Series Model: VARX(p,s).....	191
Forecasting and Uncertainty .....	194
Tercile Analysis .....	195
Results .....	195
VAR, VARX, and W-VAR Time Series Models.....	196
Bi-monthly updated W-VAR forecasts and SWAT simulations.....	201
Summary and Discussion .....	203
6 CONCLUSIONS .....	224
APPENDIX	
A WAVELET ANALYSIS OF LAKE OKEECHOBEE BASIN S-191 MONTHLY OBSERVED PRECIPITATION AND WAM SIMULATED STREAM FLOW, TOTAL P LOAD AND CONCENTRATION .....	236
Introduction .....	236
Data and Methods .....	238
Data: WAM, Basin S-191 and the NINO 3.4 Index.....	238
Wavelet Analysis .....	238
Cross-Correlation Analysis .....	239
Results .....	239
Univariate Wavelet Analysis .....	239
Cross-Wavelet and Wavelet-Coherence Analysis .....	241
Cross Correlation Analysis .....	243
Summary and Discussion .....	244
LIST OF REFERENCES .....	251
BIOGRAPHICAL SKETCH .....	266

## LIST OF TABLES

<u>Table</u>	<u>page</u>
2-1 Example of a 3 × 2 contingency table.....	87
2-2 Total P load (kg) anomaly summary statistics separated by month.....	87
2-3 Total P load (kg) anomaly summary statistics separated by JMA and M- ENSO phase.....	87
2-4 Seasonal contingency table for P loads.....	88
2-5 Seasonal contingency table for P concentrations.....	88
2-6 Single factor ANOVA results between M-ENSO phases.....	88
3-1 LRW time series data and sources used.....	133
4-1 Reference probabilities from all M-ENSO separated exceedance curves.....	172
5-1 Summary of SWAT performance measures for calibration period.....	208
5-2 Time series descriptions and attributes for W-VAR and VARX models.....	208
5-3 Tercile predictions for 2003 W-VAR, VARX forecasts and SWAT simulation...	209
5-4 Summary of time series model forecast performance.....	210

## LIST OF FIGURES

<u>Figure</u>	<u>page</u>
1-1 Global air circulation patterns .....	47
1-2 ENSO anomaly mechanisms.....	47
1-3 Physical locations of different ENSO indices.....	48
2-1 Location of Lake Okeechobee and basin S-191 .....	89
2-2 Monthly precipitation and simulated P load anomaliesin each ENSO phase.....	90
2-3 Box and whisker plots of observed JMA precipitation anomalies .....	91
2-4 Box and whisker plots of observed M-ENSO precipitation anomalies .....	92
2-5 Box and whisker plots of simulated JMA stream flow anomalies.....	93
2-6 Box and whisker plots of simulated M-ENSO stream flow anomalies.....	94
2-7 Box and whisker plots of simulated JMA TP concentration anomalies .....	95
2-8 Box and whisker plots of simulated M-ENSO TP concentration anomalies.....	96
2-9 Box and whisker plots of monthly JMA P load anomalies.....	97
2-10 Box and whisker plots of monthly M-ENSO P load anomalies.....	98
2-11 Seasonal JMA P load anomaly box plots .....	99
2-12 Seasonal JMA stream flow anomaly box plots .....	100
2-13 Seasonal JMA TP concentration anomaly box plots.....	101
3-1 The Little River Watershed (LRW) and sub-basins, Tifton, Georgia .....	134
3-2 LRW univariate wavelet power spectra .....	135
3-3 LRW cross wavelet spectra .....	137
3-4 LRW wavelet coherence analysis.....	138
3-5 Cross-correlation analyses .....	139
3-6 Box and whisker plots of observed M-ENSO NINO 3.4 SST anomalies.....	140
3-7 Box and whisker plots of observed M-ENSO precipitation anomalies .....	141

3-8	Box and whisker plots of observed M-ENSO stream flow anomalies .....	142
3-9	Box and whisker plots of observed M-ENSO NO <sub>3</sub> concentration anomalies ....	143
3-10	Box and whisker plots of observed M-ENSO NO <sub>3</sub> load anomalies .....	144
3-11	Raw monthly LRW time series.....	145
4-1	Observed land-use from 1975-2003 in the LRW basin K. ....	173
4-2	Cartoon of relevant SWAT simulated hydrological processes .....	173
4-3	Univariate observed LRW wavelet power spectra .....	174
4-4	Average M-ENSO annual water yield of selected SWAT variables .....	175
4-5	Average M-ENSO annual water yield as percentage of observed annual average precipitation of selected SWAT variables .....	175
4-6	Probability of exceedance curves in different M-ENSO phases.....	176
4-7	Univariate SWAT wavelet power spectra .....	178
4-8	SWAT cross wavelet spectra.....	180
4-9	SWAT wavelet coherence analysis .....	181
5-1	SWAT simulated total monthly stream flow in LRW basin K.....	211
5-2	SWAT simulated total monthly total nitrogen load in LRW basin K.....	212
5-3	Original observed time series and significant reconstructed components .....	213
5-4	VAR(1) time series model for streamflow and nitrate load.....	214
5-5	VARX(1) + Observed NINO 3.4 time series model for streamflow and nitrate load.....	215
5-6	VARX(1) + Predicted NINO 3.4 time series model for streamflow and nitrate load.....	216
5-7	W-VAR(5) time series model for streamflow and nitrate load .....	217
5-8	VAR(1) time series model for streamflow and total nitrogen load .....	218
5-9	VARX(1) + Observed NINO 3.4 SST time series model for streamflow and total nitrogen load .....	219

5-10	VARX(1) + Predicted NINO 3.4 SST time series model for streamflow and total nitrogen load .....	220
5-11	W-VAR(7) time series model for streamflow and total nitrogen load .....	221
5-12	Bi-monthly updated W-VAR(5) time series model for streamflow and nitrate load.....	222
5-13	Bi-monthly updated W-VAR(7) time series model for streamflow and total nitrogen load.....	223
A-1	WAM simulated S-191 univariate wavelet power spectra .....	246
A-2	WAM simulated S-191 cross wavelet spectra.....	248
A-3	WAM simulated S-191 wavelet coherence spectra .....	249
A-4	WAM simulated S-191 cross-correlation analysis.....	250

Abstract of Dissertation Presented to the Graduate School  
of the University of Florida in Partial Fulfillment of the  
Requirements for the Degree of Doctor of Philosophy

HYDRO-CLIMATIC INFLUENCES OF EL-NINO/SOUTHERN OSCILLATION ON  
NUTRIENT LOADS IN THE SOUTHEAST UNITED STATES

By

Victoria Whitworth Keener

May 2010

Chair: James W. Jones

Major: Agricultural and Biological Engineering

As global climate change becomes more of a problem, it is crucial to understand regional variability. In the southeast U.S.A., natural resource managers wish to reduce climate associated risks. This research explores the relationship between the El-Niño/Southern Oscillation (ENSO), a major driver of global climate variability, with hydrology and water quality in two watersheds.

In basin S-191 of Lake Okeechobee, we quantified relationships between 36 years of WAM simulated phosphorus (P) loading and categorical measures of ENSO. Results showed ENSO strongly affects seasonal and monthly P runoff, with significant loading in spring of El Niño and summer of La Niña years. Greater P load in certain months was consistent with greater precipitation, with large flow and nutrient flushes following drought. Observed data from the Little River Watershed (LRW) was used with wavelet analysis to quantify the significance of a teleconnection between the NINO 3.4 index and precipitation, stream flow, nitrate concentration and load. Areas of high power and inter-annual variability manifested in the 3-7 year ENSO periodic signal.

To explain the powerful relationship between ENSO and stream flow, a calibrated SWAT model of the LRW mechanistically identified how the power of a climate signal

can be increased through natural processes. Using SWAT and wavelet analysis, we found that the presence of a confining layer in the LRW increased the groundwater/baseflow signal such that the ENSO signal in flow was more significant than the chaotic precipitation signal. Finally, significant 3-7 year reconstructed components from the wavelet analyses were extracted and used to create a monthly vector time series model that more accurately forecasts 1-3 month  $\text{NO}_3$  loads than time-domain signals only.

IPCC reports have concluded that climate variability and extreme events will be more common in the future. Research that focuses on understanding and predicting the effects will be increasingly helpful for making robust management decisions in an uncertain world. Models of water quality and ENSO can help stakeholders effectively manage their risk in the near future, and are a step towards faster integration of climate information into daily decision making.

## CHAPTER 1 INTRODUCTION AND LITERATURE REVIEW

### **Motivating Issues**

#### **Global Climate Change and Water Supply**

Global climate change has been called the socio-economic, environmental, and energy challenge of our lifetime. The possible consequences of a changing climate are both far-reaching and severe, making research that can help us better understand, adapt to, mitigate, or stop and reverse its consequences a crucial part of modern environmental science. Warming of the average global climate over the past century has been proven unequivocally [*IPCC et al.*, 2007], and because the hydrological cycle is linked closely to variations in climate, citizens and water resource managers both will have to deal with new challenges associated with both water quantity and quality. Over the past several decades, research into global warming has revealed significant changes in precipitation patterns, weather extremes such as floods, droughts and storms, snow-pack duration and amount, increased evaporation, increased wildfire risk, and changes in soil moisture and runoff [*Mote et al.*, 2005; *Stewart et al.*, 2005; *Westerling et al.*, 2006]. These relatively sudden changes make it increasingly difficult to efficiently adapt current anthropological practices such as large-scale agriculture and maintaining a municipal water supply, while continuing to provide clean, safe drinking water and adequate food to an ever increasing population.

These systemic changes in the hydrological cycle alter global agricultural practices and economies, affecting the health and welfare of the environment and the people. With the exception of a few industrialized nations, global municipal water use over the last few decades has increased due to population growth and a higher standard of living

[Bates *et al.*, 2008]. Global irrigation water withdrawals have seen the largest increase, accounting for approximately 70% of total withdrawals, and more than 90% of consumptive use [Cai and Rosegrant, 2002]. This drastic increase in agricultural water usage has contributed to the general decline of surface water quality in recent decades [UN, 2006], and it is very likely that due to increasing availability and price of fertilizers and pesticides in developing countries and increasing population and demand for meat, declining water quality will continue to be a problem into the future [IPCC *et al.*, 2007].

The mass use of fertilizers and pesticides in modern agricultural practices is commonly used to harvest maximum yields from the available land and possibly less than desirable environmental growing conditions. Nitrogen (N) and phosphorus (P) are two nutrients of limited resource found in fertilizers and from animal production, which have a large impact on ecosystem function due to their leaching into surface and groundwaters. During the last 50 years of agricultural improvements, fertilization has reached a point where humans annually release as much N and P to terrestrial ecosystems as all natural sources combined [Tilman *et al.*, 2001]. The abundance of N and P can eutrophy surface waters, causing blooms of algae in lakes and streams, estuaries, and even has created a large “dead zone” in the Gulf of Mexico [Tilman *et al.*, 2001; Carpenter *et al.*, 1998; Rabalais *et al.*, 2002]. Combined with future climate uncertainties, it is likely that non-point source agricultural nutrient pollution will continue to have a major negative impact on global ecosystems unless it is addressed through research and management.

Specifically, it is difficult to say exactly what climate change effects will be, as climate signals are fairly chaotic and noisy, encompassing annual, inter-annual,

decadal, or much longer periods of variability. This climate variability combined with the effect of exogenous variables and the lack of extensive monitoring systems, both spatially and temporally, can make extracting short or long term climatic patterns an uncertain process. For both short and middle term risk management planning, inter-annual modes of climate variability and their seasonal expression are of interest. There is a need to identify climate non-stationarities and their links to watershed water quality outcomes. In this dissertation, the focus is on isolating, modeling and forecasting the effects of climate variability on hydrology, specifically water quality, in the southeast United States, rather than making statements about global warming or any possible anthropogenic causes thereof. Variability for our purposes is defined as fluctuations in climate from the monthly to seasonal and multi-annual scale, and will be quantified via standard climate indices, while climate change refers to recorded multivariate trends over decades to centuries.

### **Climate Indices and the El-Niño/Southern Oscillation**

Climate indices are researcher-created diagnostic monitoring tools that describe an important or significant pattern or state of a climate system. Generally, climate indices are represented as time series, with one index value representing a particular point in time. There are dozens of indices, which can describe any atmospheric event including monsoon precipitation, air pressure differences, sea surface temperatures (SST's), hurricane activity, or solar radiation. Spatially averaged areas of sea surface temperatures in various parts of the world are particularly relevant to describing climate phenomena in specific locations, and the El-Niño/Southern Oscillation (ENSO) has proven to be one of the most consistent in describing low-frequency climate variability on both a regional and local scale [*Ropelewski and Halpert, 1986*]. The ENSO

maintains an irregular 2-7 year periodicity that gives it a level of predictability, yet retains some variability in its occurrence, magnitude and climate consequences around the world [*Cane*, 2005].

While the definition of ENSO has changed slightly since it was coined, it has always remained centered on SST's in a narrow band of the equatorial Pacific Ocean. The original term, "El Niño" was from South American fisherman and sailors who noticed an unusually warm band of water off the coast of Peru and Ecuador in the Pacific during the end of the year, near Christmastime, that disrupted normal fish and bird populations. The term "El Niño" therefore refers to "The Christ Child". It was not until 1969 that Dr. Jacob Bjerknes of UCLA described the full extent of the physical mechanism of El Niño, including the atmospheric pressure component referred to as the "Southern Oscillation" [*Bjerknes*, 1969].

The entire ENSO phenomenon is coupled through the ocean and the atmosphere, centered over the tropical Pacific Ocean. The mechanism of ENSO can be divided into the cold (La Niña) and warm (El Niño) phases, each representing a deviation from the average or neutral condition. The main ocean-drivers of ENSO are the unusual "normal" conditions of the equatorial Pacific Ocean, where the east may be 4-10° C colder than the west, due to the raising of the thermocline from equatorial upwelling in the east and the transport of cold water from the South Pacific [*Cane*, 1986]. These ocean dynamics are driven by easterly trade winds (Figure1-1), which in turn are partly driven by SST differences causing higher pressures in the east, forcing surface air to flow along this gradient [*Bjerknes*, 1969]. The 3-7 year oscillation associated with ENSO was not more fully explained until two decades after Bjerknes' groundbreaking research, and has to

do with the depth of the warm water above the thermocline. The changes involving the trade winds and SST are tightly correlated, yet the thermocline depth lags behind. Although physically very complex, it is the lagged change in the mean depth of the tropical thermocline which creates an oscillating system, as every oscillation must by definition contain an out-of-phase variable-- technically, the "delayed oscillator" [C. Wang, 2001]. Taken all together, this forms the coupled ocean-atmosphere positive feedback system that results in what we call the El-Niño/Southern Oscillation.

During El Niño events, low air pressure in the eastern Pacific weakens the atmospheric pressure gradient heading westward. This causes unusually high SST's and increased convection in the central and eastern equatorial Pacific. In a La Niña, trade winds strengthen, amplifying the SST gradient so that lower than average SST's are recorded instead (Figure 1-2). The relative strength and precise oscillation of these warm or cool phase events depends on the strength of the mean winds, how much heat is generated by SST gradients from specific temperatures and humidity, how deep the thermocline is, and chaotic system dynamics. The details of these mechanics were fairly recently published by Federov and Philander, although there is not yet a comprehensive theory as to why the average oscillations tend to remain between 2-7 years [*Fedorov and Philander, 2001*].

Even as a climate index, the definition of ENSO is not standard, however. There are several accepted indices in use, including the NINO1 & 2, NINO3, NINO3.4, NINO4, Multivariate ENSO Index (MEI), and Japan Meteorological Agency (JMA) index. Each uses slightly different definitions of ENSO coordinates and phases (Figure1-3), and is the most relevant to slightly different regions around the world. The MEI is a composite

index using not only SST, but also surface air temperature, sea-level pressure, zonal and meridional surface wind, and cloudiness [Wolter and Timlin, 1993]. For having the most relevance to the southeast United States, the JMA index and the NINO 3.4 index were used in this research.

### **Global ENSO effects**

Due to global ocean and atmospheric flow patterns, ENSO effects can have a significant effect or little effect at all in different locations throughout the world, which are presented in detail by Molnar and Cane [Molnar and Cane, 2007]. One of the clearest ENSO signals is seen where the phenomenon was first named-- off the coast of Peru, Venezuela, eastern Colombia, and northeastern Brazil and the Amazon Basin. In El Niño years, these areas commonly receive lower than normal precipitation especially in boreal (November to April) winter and the preceding late summer and autumn [Aceituno, 1988; Kiladis and Diaz, 1989; Mason and Goddard, 2001; Ropelewski and Halpert, 1987]. La Niña events in the same locations are associated with greater than normal precipitation, and lower temperatures [Aceituno, 1988; Ropelewski and Halpert, 1987].

Another well known and clear signal that has been recorded for over a century is the negative relationship between precipitation from the Indian Monsoon and El Niño events [Ropelewski and Halpert, 1987; Charles et al., 1997]. As a critical component of Indian sub-continent water supply and agriculture, historic monsoon failures have often coincided with strong El Niño events [Kiladis and Diaz, 1989; Ropelewski and Halpert, 1987; Charles et al., 1997]. Australia also experiences a strong ENSO signal, with drought commonly occurring over much of the continent during El Niño phases [Kiladis and Diaz, 1989; Ropelewski and Halpert, 1987]. During an El Niño event, central

Australia will remain dry for most of that year, while the north and northeastern areas will experience drought localized in the winter, and the southern areas during the summer [*Ropelewski and Halpert, 1987*]. During La Niña events in Australia, the same areas and seasons are associated with flooding.

Much of Asia is affected by the Pacific Decadal Oscillation (PDO), but China also correlates with ENSO. During El Niño summers and autumns, China north of the Yangtze River and east towards Beijing tends to have less precipitation than normal [*Mason and Goddard, 2001; Ropelewski and Halpert, 1987; Lau and Sheu, 1991*]. China south of the Yangtze River, however, has the opposite correlation with ENSO, with flooding and heavy rainfall during strong El Niño winter seasons, but with little to no connection to La Niña years [*Mason and Goddard, 2001; Lau and Sheu, 1991*].

Many different climate indices affect regions of Europe, including ENSO. During strong El Niño winters, west and central Europe may experience increased temperatures and precipitation, while north Europe receives less. During La Niña events, higher pressures are observed over central Europe, and increased temperatures and precipitation are seen in northern Europe [*Fraedrich and Muller, 1992*]. During El Niño years, the southeastern area of Africa and the eastern equatorial regions have also been shown to have greater temperatures and precipitation than normal [*Ropelewski and Halpert, 1987; Halpert and Ropelewski, 1992*].

Finally, in the North and Central American continent, there are a variety of significant ENSO correlations. West and south Canada and the northern United States experience warmer winters and less precipitation during El Niño events [*Ropelewski and Halpert, 1986; Rasmusson and Wallace, 1983; Kiladis and Diaz, 1989; Halpert and*

*Ropelewski*, 1992]. The southwestern United States has greater than average precipitation during El Niño summers, while the north central and northwestern receives less. Again, this pattern is reversed during strong La Niña years [*Ropelewski and Halpert*, 1986; *Mason and Goddard*, 2001; *Rasmusson and Wallace*, 1983].

While most of the world tends to warm up during El Niño, the Gulf of Mexico area encompassing both Mexico and the southeastern United States cools and receives more precipitation than normal in the winter season, while La Niña winters are drier than average [*Hoskins and Karoly*, 1981; *Ropelewski and Halpert*, 1986; *Kiladis and Diaz*, 1989; *Mason and Goddard*, 2001; *Schmidt et al.*, 2001]. This distinctive winter El Niño pattern in the southeast United States is now understood as a deflection of the subtropical jet due to stronger Hadley Circulation over the eastern Pacific Ocean [*Cane*, 2005]. It is here, in Florida and Georgia, that we are analyzing data from two different watersheds for their ENSO responses.

### **Paleo-climate and future of ENSO**

A subject of interest for climatologists is comparing ancient Earth's climate, or, paleo-climate, to modern conditions. In the mid-Pliocene (pre-Ice Age) epoch, approximately 3-5 million years ago, Earth's climate was much warmer than current conditions, with extremely high carbon dioxide (CO<sub>2</sub>) concentrations and a coupled ocean-atmosphere system resembling that of modern El Niño conditions [*Molnar and Cane*, 2007]. By learning about the climate feedbacks and causes of warming or cooling in Earth's past when anthropogenic change was not a variable, researchers hope to understand Earth's natural periodic variability.

The mid-Pliocene climate closely resembles that associated with modern El Niño teleconnections and conditions [*Molnar and Cane*, 2007], suggesting that a permanent

El Niño-like state most similar in precipitation and warming patterns to the 1997-98 “Niño of the Century” was the normal condition. These recent climate reconstructions are based on data collected from oxygen isotope analysis from Foraminifera specimens from marine cores [*Koutavas et al.*, 2006], coral bands that show the current incarnation of ENSO existing for the last 130,000 years [*Tudhope et al.*, 2001], glacial varve spectral analysis [*Huber and Caballero*, 2003], and proxy records such as mollusk fossils, pollen taxa, lake sediment, and general animal and plant fossil types and locations. This permanent El Niño condition, or “El Padre” as it has been coined [*Bonham et al.*, 2009], was characterized by less of an east-west temperature gradient in the Pacific Ocean, with no oscillations in ENSO phase that we recognize today. As CO<sub>2</sub> levels in the mid-Pliocene were 30% higher than pre-industrial conditions and global average temperature was 3° higher than the current [*Haywood and Valdes*, 2004], the geographic and greenhouse gas conditions make it the best analogue to those occurring currently. The drastic changes in the past four million years of SST and thermocline temperature and depth in the equatorial Pacific are unusually active, relative to the age of the Earth [*Molnar and Cane*, 2007].

It is still under question why despite having equal or arguably higher current atmospheric CO<sub>2</sub> levels, Earth’s current average surface temperature is still significantly cooler than average temperatures in the mid-Pliocene. Although there are many possible variables under study, it is apparent that greenhouse gases are not the entire story behind either global warming, and global phenomena such as the ENSO could be an important part of being able to more accurately model both past and future climates. Interestingly, although most of the world was warmer and drier in the early to mid-

Pliocene than today, many studies have shown that the Gulf of Mexico region, including the southeast seaboard of the United States, was actually cooler and wetter [*Graham*, 1989]. As is discussed in the section in Chapter 1, Southeast United States Climate, current conditions in the southeast are also on average cooler, despite global temperatures rising—another analog to the present.

Also of interest is how ENSO may change in the future, so current models are not rendered obsolete immediately if they are predicting conditions predicated on an ENSO that no longer exists. As it is difficult to accurately model current global ENSO dynamics and the other low frequency climate patterns it is affected by, it is even more difficult to predict future ENSO patterns. Much of the work in the past two decades involves working out the details of ENSO specific teleconnections, or patterns between regional precipitation or temperatures and larger modes of climate variability, which helps modelers create a more accurate model of ENSO. Accurate prediction of ENSO phase up to 12 months in advance has been claimed [*Cane*, 1986; *Latif et al.*, 1998], however, unbiased skill estimates suggest that many ENSO events can only be predicted several months in advance, and sometimes only after the start of an event [*Goddard et al.*, 2001]. In a review of 20 Global Circulation Models (GCM) that modeled future ENSO conditions with a 1% increase in greenhouse gas concentrations per year of simulation, there was no significant trend in seeing either a more Niña or more Niño like state [*Collins*, 2005]. Although some studies have found modest trends in both directions, there is little conclusive evidence to say exactly how ENSO dynamics will change in either the near or distant future.

## Climate and Agriculture in the Southeast United States

The humid sub-tropical southeast sunbelt region is important for many reasons, including its agricultural importance both locally and for the entire country. Although the number of farms has decreased by 80% in the last 50 years in the southeast [USDA, 1999], 25% of all national crops, including softwood forests such as Loblolly pines, and 50% of all fresh winter vegetables are still grown there [Hansen *et al.*, 1999]. Both weather and climate are very important determinants of the population growth, and hence the economic development of the region, agricultural production, and how well the unique ecosystems in the area will fare in the near and far future. Because of the sunbelt's rapidly increasing population—especially in the coastal regions, which are projected to increase by another 40% between 2000 and 2025—It is especially crucial to understand how the changing climate will affect flora, fauna, and the human population.

Prior to European settlement, the Southeast was mainly upland forests, grasslands, and up to 33% wetlands [Dahl, 1990]. By 1990, wetland area had been reduced to about 16% of the Southeastern landscape, and is still decreasing in area, although Florida retains the most wetland area of all US states, with 9.3 million acres [Dahl, 1990; Hefner *et al.*, 1994]. Research has also shown that C3 and C4 plant abundance in central Florida has changed drastically on a thousands-of-year scale. In an analysis of the past 62,000 years in Florida, it was found that during times of precipitation increase and low atmospheric CO<sub>2</sub>, C4 plant abundance decreased dramatically, while C3 plants and pine forests blossomed [Huang *et al.*, 2006]. In a future with higher CO<sub>2</sub> concentrations, these relationships may be very telling in what flora and fauna populations will flourish.

The southeast in general receives generous amounts of summer rainfall, with annual amounts in Florida alone totaling 53 inches [*Purdum*, 2002]. Even with this relative abundance of water, however, there are still both heated water quantity and quality debates in the southeast, as the timing and amount can be quite variable. During the last century, temperature trends have varied inter-decadally, with a warm period during 1920-40, and a cooling trend through the 1960s. The 1970s were the beginning of another warming trend, and 1990s temperatures reached peaks as high as those of the 1920s [*Burkett et al.*, 2001]. These cooling and warming trends have made the Southeast the only region in the US to show an overall cooling of 1-2 °C, although north Louisiana and peninsular Florida have shown a slight (1 °C) warming [*Burkett et al.*, 2001]. In terms of temperature extremes over the last century, the Southeast has shown an average annual decrease of 5 days exceeding 90 °F, and an increase of six days in the annual number of days below freezing [*Burkett et al.*, 2001]. These extreme temperature trends can again be explained by the mid 20<sup>th</sup> century cooling trend balancing out the early and late warming trends in the regional average.

Rainfall trends in the last century, on the other hand, show overall strong increases of 20-30% or more in Mississippi, Alabama, and Louisiana, with mixed results in Georgia and Florida. Although increased precipitation is generally thought of as beneficial for agricultural production, especially in the southeast, where rain-fed crops are more common than irrigated ones, the precipitation increase can mainly be attributed to intense events, which are generally damaging to agriculture and do not provide even moisture, speed erosion, and cause floods [*Rosensweig and Hillel*, 1995]. Stream flow analysis is usually correlated to precipitation trends, however, stream flow

trends in the latter half of the 20<sup>th</sup> century show little change in maximum daily discharge, but increases in both annual median and minimum flows in Mississippi and Georgia [*Lins and Slack, 1999*].

In the southeast United States, farmers and ranchers use weather forecasts on a daily basis to manage their crops. Despite this, a case study in Florida found that only a few farmers had integrated climate forecasts into their decision making [*Jagtap et al., 2002*]. It was also found that there were varying degrees of flexibility to adjust management using climate forecasts, depending on the size and type of farm and the specific situation. Using modeling studies and available data on crop production in Florida, results suggest that there is a large potential benefit to farmers who use ENSO based climate forecasts in planning their growing season [*Hansen et al., 1999, 1997; Jagtap et al., 2002; Messina et al., 2001*]. Several of the same studies have also found that there are associated risks with using ENSO climate forecasts, such as overproduction. These reasons prevent ENSO forecasts in agriculture from being quickly and widely adopted in the southeast. However, the voluntary incorporation of ENSO forecasts into managing agricultural water quality outputs may be a less risky proposition, while also potentially saving farmers money on fertilizer and improving ecosystem function in the southeast United States.

## **Objectives**

Water management agencies in the southeast United States wish to reduce climate associated risks in managing water resources and agricultural systems. The main goal of this research is targeted at exploring the relationship between and modeling the climate variability at the seasonal and inter-annual level via the El Niño/Southern Oscillation and hydrology and water quality at the watershed scale in two

basins in the southeast United States. If nitrogen and phosphorus loads in the southeast U.S. can be correlated with climate variability via ENSO phase or climate indices, then we can make seasonal or monthly predictions of loads based on sea surface temperatures. This model could aid decision makers in making seasonal choices in water and agricultural management that would reduce the chance of exceeding stated TMDL goals for problematic nutrient loads. In greater detail, this dissertation will:

1. Investigate and quantify the significance of the relationship between discrete annual ENSO phase based water quality via nutrient loading in surface waters of basin S-191 of the Lake Okechobee watershed, Florida, using hydrological simulation with Watershed Assessment Model (WAM) so as to remove confounding land-use change and management variables.
2. Show a climatic teleconnection by extracting significant ENSO spectra from observed hydrology data in the Little River Watershed (LRW) in Georgia, and compare it to the continuous classification of ENSO through monthly NINO 3.4 SST.
3. Show, through simulation using the Soil and Water Assessment Tool (SWAT), the mechanism of hydrological increase of ENSO signal power in the stream flow and nutrient loads in the Little River Watershed.
4. Extract dominant modes of variability in each LRW and NINO 3.4 time series to rebuild and create a multivariate wavelet based time series model, able to make seasonal predictions of nutrient loads in the LRW based on NINO 3.4 SST forecasts.

## **Literature Review**

### **Agricultural Pollution: Nutrients**

Clean and abundant water is necessary for human and animal life, providing drinking water, recreation, fishing habitat, irrigation, hunting, transportation, industry, and support of biodiversity. Pollution of ground and surface waters negatively impacts all these necessities, making it a major concern in the southeast. Water pollution inputs into the environment can be divided into two main types: point and non-point source. A point source discharge tends to be continuous and relatively localized, with little

temporal variation, such as effluent from an industrial plant or a municipal sewage treatment center. As a result, point source pollution can be easier to locate, regulate and fix by treating it at the source. Non-point sources of pollution are often intermittent or irregularly discharged, and are many times linked to activity from extensive areas of agricultural land. These sources may travel underground, in the atmosphere, or over land to a receiving water body, making them very difficult to monitor, regulate and fix. In the well known examples of the impacted Chesapeake Bay watershed and the hypoxic zone in the Gulf of Mexico, 35 states are known to contribute nutrient loadings, making regional regulation very difficult [U.S. EPA , 1996]. As a result, control of non-point sources is usually centered on continued good land management practices, which makes a climate forecast system that could reduce variability in best management an attractive prospect.

The main non-sediment non-point water pollutants from agriculture stem from use and overuse of chemical fertilizer, specifically those containing nitrogen (N) and phosphorus (P). Although beneficial and necessary for plant growth, N and P in overabundance can result in negative ecosystem impacts such as eutrophication and toxic fish kills. Nitrogen is a limiting nutrient in the productivity of many aquatic and terrestrial ecosystems, for it is a necessary component of all amino acids and proteins yet can only be utilized by many plants and animals in its non-gaseous form. The Nitrogen Cycle is how life on earth fixes atmospheric  $N_2$  (gas) into widely useable forms of N such as nitrate ( $NO_3$ ), nitrogen dioxide ( $NO_2$ ), or ammonia ( $NH_3$ ) [Postgate, 1998]. Nitrogen is fixed naturally through a number of bacteria, prokaryotes, fungi and microorganisms via nitrogenase enzymes. Some plants and the majority of legumes can

fix N through a symbiotic relationship with Rhizobia bacteria in their root systems. However, nitrate is water soluble, and can enter ground and surface waters easily, contributing to eutrophication and declines in water quality.

Phosphorus, another limiting nutrient, is essential for life in DNA and RNA molecules, ATP, and cell membranes. The majority of natural P is locked up in inorganic mineral deposits such as phosphates ( $\text{PO}_4$ ), which slowly weather and dissolve into soil water to be taken up by plants and converted to organic orthophosphate ( $\text{PO}_4^{3-}$ ), and in turn consumed by animals. A limiting factor in plant growth, P is a major component of fertilizers and is partly responsible for the major increases in crop yields seen throughout the last century. The overuse of P fertilizer has affected water quality and is a main pollutant in eutrophic lakes today [*Carpenter et al.*, 1998; *Gakstatter et al.*, 1978].

Non-point sources are a major part of water pollution in the United States. Even if point source inputs were eliminated entirely, 72-85% of eutrophic lakes would still require non-point P control to meet water quality standards [*Gakstatter et al.*, 1978]. Eutrophication occurs when large N and P inputs cause excessive blooms of aquatic weeds or algae, and is a problem in fresh, brackish and salt water. The overgrowth and decomposition of the plants and algae can create hypoxic zones, destroy fish and aquatic insect habitat, kill entire fish populations, destroy coral reefs and aquaculture, and create toxic byproducts that make the water undrinkable [*Carpenter et al.*, 1998; *Gakstatter et al.*, 1978].

Virtually every state is adversely affected by nutrient water quality degradation, and 49 states have listed Clean Water Act Section 303(d) nutrient-related water

impairments as defined by the U.S. Environmental Protection Agency (U.S. EPA) [*U.S. EPA*, 1998]. The EPA's national strategy for nutrient criteria in 1998 was followed in 2001 by an action plan for the establishment of specific regional numeric nutrient criteria for streams, river, lakes, and reservoirs, of which there has been progress. Dictating quantitative nutrient loads is very tricky, as natural regional levels vary widely both spatially and temporally; however the establishment of these limits is very important to create measurable and objective water quality baselines to measure progress against and create appropriate laws and regulations. In 2008, the EPA released a report detailing the progress of all states in defining regional nutrient loads [*U.S. EPA*, 2008]. The southeast United States is doing well overall, with Alabama, Georgia, and Florida already using some specific nutrient standards for chlorophyll-a, total N and P, and Louisiana and Mississippi planning to start implementation of their standards in the next few years [*U.S. EPA*, 2008]. The next section will detail relevant regional nutrient related policies and Best Management Practices (BMP's).

### **Water Management Policies in the Southeast**

Although there are state regulations and policies too numerous to describe in detail, this section will focus on the implementation of federal nutrient related water quality standards and management from the US EPA in Florida and Georgia, where the two watersheds under study in this dissertation are located.

### **The Watershed Restoration Act (WRA) and TMDL standards**

In 1999, the Florida legislature enacted the Florida Watershed Restoration Act (FWRA) with the intent of preserving and improving water quality. This was accomplished through the development of EPA encouraged Total Maximum Daily Loads (TMDL) for ground and surface waters. In turn, TMDL's are required by the

federal Clean Water Act (CWA) as an extension of the nutrient control program. The FWRA created a process to collect data on and identify impaired water through Florida, and is enforced by the Florida Department of Environmental Protection (DEP) and the Department of Agriculture and Consumer Services (DACS). One of the main innovations in the FWRA program was the regulation of water bodies via watershed delineation instead of political boundaries, which has been too frequently used in the past.

The federal TMDL program was created to systematically establish the maximum pollution specific bodies of water could handle while still meeting water quality standards and controlling both point and non-point source pollution. By providing measurable nutrient water quality baselines, the TMDL program makes measuring progress easier and facilitates the writing of National Pollution Discharge Elimination System (NPDES) permits, which allow polluters a certain amount of loading. Given that Florida has 52,000 miles of rivers and streams, 800 lakes, 4,500 square miles of estuaries and more than 700 springs, gathering enough data to make informed TMDL decisions for each is a monumental undertaking [*Florida DEP, 2005*]. The DEP addressed this by splitting up the state into five groups of basins, each of which would be researched one at a time over a five year cycle and put into practice.

The Lake Okeechobee basin was in the first group of watersheds, meaning that TMDL's have been established for basin S-191, a basin used as a field site in this dissertation. TMDL's are decided upon by a process of data collection and monitoring, historical data, public meetings, and the environmental goals decided upon. These limits can later be altered by public hearings, new information, or updated Basin Management

Action Plans (BMAP). By addressing all water users and stakeholders in the process, there is environmental education of both the public and agricultural partnerships to employ appropriate BMP's to achieve the mandated TMDL. The specifics of these loadings for S-191 are discussed in greater detail in Chapter 2.

The state of Georgia has a grant system under the federal Clean Water Act section 319(h) to specifically address cleaning up non-point pollution sources. The Environmental Protection Division of the Georgia Department of Natural Resources oversees the grants and implementation, and the basin of interest in this dissertation, the Little River Watershed, has a four year TMDL development project grant under this section, that will be discussed in Chapter 3. The Soil and Water Commission works with landowners and agricultural users to develop nutrient management plans and install appropriate BMP's under one year contracts. After a BMP is installed and inspected, landowners are reimbursed for 60% or more of the cost, depending on its size.

BMP implementation in both Florida and Georgia programs are voluntary, although stakeholders must meet NPDES guidelines or TMDL's. If landowners successfully implement a BMP and are certified by the state, actions cannot be brought against them if they are still not meeting the TMDL limits. The voluntary nature of BMP's makes them a contentious issue for those concerned with ecological restoration projects, as their validity and effectiveness is still under discussion.

### **Best Management Practices (BMP)**

The history of the environmental BMP stems from the more managerial aspect of "Best Practices". In a corporate environment, "Best Practice" is a buzzword used to describe the process of developing and following a standard way of doing something. It is not necessarily the "best" way of doing anything, but is instead a "standard operating

procedure” that can be followed uniformly between companies and industries. Often, the benefit of Best Practice implementation in this context is that organizations that have poorly designed (or evolved) processes are given a choice between a typically expensive modification to their system, or choosing to follow a Best Practice. The rate of enormous technological change over the past century forces rapid adaptation and versatile Best Practices. Ideally, Best Practice in these cases is meant to “get things done”, with the added benefits of quality results and consistency.

In the United States, BMP’s are practical control measures that have been shown to minimize environmental damage via nonpoint pollution in water bodies. The evolution of BMP’s, however, is not easily traceable, and the implementation and enforcers of BMP’s are not obvious. BMP’s originated during the Dust Bowl era in the United States [Ice, 2004]. As drought and soil erosion continued to negatively affect a largely farm-based citizenship, the Soil Conservation Act of 1935 started advising farmers on methods to manage their lands to protect essential watershed functions. These land management practices were the predecessors of modern day BMP’s.

In 1972, the Federal Water Pollution Control Act Amendments separated point from nonpoint pollution control measures, and defined BMP’s to control nonpoint sources. In these amendments, BMP’s were defined as voluntary, incentive, or regulatory control programs, giving states a large measure of control as to how they would be enforced and defined. Point source pollution, on the other hand, is subject to federal laws and permits. BMP’s are inherently a compromise between the environmental ideal “zero pollutant” state, and practical management options, and as such are continually adjusting to adapt to new ideas in the scope of both science and

society. Best Management Practices can be thought of as a narrow and specific subset of Adaptive Management, in which an optimal decision is reached in the face of uncertainty through an iterative process, with an aim of reducing uncertainty over time via system monitoring. BMP's become a specific subset of Adaptive Management because of their narrow aim, and because the "optimal decision" that is sought is also in flux.

Different states use different BMP incentives and implementation, such as performance bonds, permits, required written management plans, on-site project reviews, random inspections, cost share programs, and education. In some studies, BMP effectiveness has been demonstrated to reduce water quality impacts from pre-BMP era forestry practices by 90% or better [Ice, 2004], showing that these practices do have noticeable and significant effects, as continually evolving and innovating measures that meet demands for tighter control of water quality impacts while remaining economically viable for stakeholders [Veith *et al.*, 2003; Malik *et al.*, 1994].

Compared to other environmental water quality policies such as wetland mitigation, BMP's also have been successful. Part of their success is certainly dependent on the fact that many stakeholders are individuals with a connection to the land and environment, or small businesses, rather than sprawling corporations with a financial bottom line. However, it seems that BMP's also represent a compromise between top down and bottom up management. The lack of inflexible regulations enforced by a federal bureaucratic institution are instead carried out by researchers and the Water Management Districts (WMD) in Florida, which gives stakeholders a feeling of being more personally involved in the adoption and success of the process.

In a study of 400 private forest owners in Belgium, it was found that management suggestions were most accepted when the owners were well educated and informed, and when implementation did not decrease their profits. Additionally, those who were purely motivated by profit had no interest in the ecological aspects of forest management, implying that owners of mid-size farms in the Everglades region may indeed have a deeper connection to their land that makes them more open to environmentally sound practices. The Belgian study also found that subsidies were not effective in persuading forest owners to change their management practices. Again, the differences between Belgian forest owners and landowners and stakeholders in the southeast United States may lay in their fundamental environmental concern, which makes them more amenable to changing their operations by working with researchers and receiving subsidies [*Serbruyns and Luyssaert, 2006*].

Another factor in BMP's success may be that they inherently take a systems view, by necessity of dealing with nonpoint pollution, rather than trying to optimize specific parts unless it is absolutely necessary. For example, water quality is normally monitored at the basin level, rather than the farm level. Only if the water quality has not improved do researchers start monitoring at the farm level. At the watershed level in the end, some farms may in fact still be releasing quite a bit of P, while others may have drastically reduced their loads. The average decrease, however, is enough to make a difference in the ecosystem being restored.

### **Simulation of Natural Systems**

The simulacrum is never what hides the truth-- it is truth that hides the fact that there is none. The simulacrum is true.

–Jean Baudrillard (Simulation and Simulacra) [*Baudrillard, 1985*]

In the last 50 years of continually improving computer technology, the use of mathematical models to simulate and help us better understand complex or chaotic natural systems has made incredible progress. A continuing debate in the mathematical modeling community is the relative advantage of using empirical models versus physical models. An empirically based relationship is one based upon directly observed values or experimental data. These models are often based off of statistical or probability theory, and accurately predict observed results from other variables, yet have little to no theoretical reasoning to explain why the relationship works.

Examples of empirical relationships commonly used in hydrological process modeling include the SCS Curve Number method for estimating runoff in an area from precipitation, the original Darcy's Law describing flow through a porous medium (now given a theoretical basis), and Manning's Equation for open channel flow (also recently given a theoretical basis). Often, accurate empirical relationships derived from careful experimentation are later proven to have a theoretical basis as well. This fact can be used to make a strong case for the use of empirical relationships in models, as relationships derived from careful and reproducible experimentation often lead to future understanding of a process. In fact, the Manning equation, derived in 1885, was not formally physically explained until 2002 [*Gioia and Bombardelli, 2002*], using phenomenological turbulence theory. Even the specifics of gravity are not physically explained, yet without using the concept, many of our physically based models would be useless.

One of the main disadvantages of using empirical relationships in models is that the relationship is only as good as the data, which may be limited in spatial or temporal

scope. Additionally, noise and measurement errors can influence the accuracy of relationships. To address these critiques, the model developer must be very aware of potential issues in collected data and prediction uncertainties in the model itself. Accounting for uncertainties in data, model calibration, and model structure is becoming a very sophisticated process, and recent stochastic techniques add to the power of empirical models.

A theoretical or physically based model is one in which specific physical processes are accounted for to make predictions based on accepted laws and theory. Theoretical models simplify the physical system to some extent, and often include empirical components, just as “empirical models” often use relationships based on theory. A main benefit to using a theoretical model is the increased understanding of a process that is being simulated. Another advantage of theoretical models is their ability to be more easily applied to different situations and case studies than empirical models. A theoretically based model should be able to account for the different variables and factors in a process no matter where the location is, as long as certain underlying assumptions are met. An effective empirical methodology may be employed in different situations, although a specific model may be irrelevant.

There are advantages and disadvantages inherent in using each type of modeling system on their own, which is why this dissertation attempts to use both individually and in combination to achieve a more accurate representation of reality. As the post-modern philosopher Jean Baudrillard suggests in his quote, “truth” or reality in the world of simulation is a relativistic term, and using a wide variety of methods to explore reality as we perceive it through time may be the best approach we have. As a

modern scientist, it is essential to understand how your research relates to the greater knowledge base of the world, and how the ultimate goal of scientific thought is not to provide definitive answers, but instead to discover deeper problems using new methods and subject the best answers to ever more rigorous examination. The next sections will detail some relevant models in this dissertation.

### **Global circulation models and ENSO**

Historically, the desire to accurately simulate and predict Earth's climate probably evolved from our desire to forecast weather. Although there is no specific distinction, operational weather forecasting generally extends from hours to days, and climate forecasts pertain to weeks, months, and years. The feasibility of attempting to numerically simulate long-term global climate using computer models was first proved by Norman Phillips in 1956 [*Phillips, 1956*], and the first Global Circulation Models (GCM) used first principles of fluid dynamics rather than energy balances.

Parallel GCM's were developed around the world by different groups incorporating different models, and today there are still many GCM's that are commonly used in conjunction. The presence of multiple models is advantageous, as the current understanding of the extremely complex physics and chaotic dynamics in the ocean and atmosphere is still limited, and having several model outputs allows decisions to be made based on ensemble means or forecasts in which the uncertainty of all models is incorporated.

A key strength of modern GCM's lays in their coupled nature: atmosphere models are coupled with ocean, sea-ice, and land-surface process models incorporating greenhouse gases and carbon sequestration. In turn, these models can be statistical, physical, probabilistic, or a combination of methods. Some more well known models

include the NASA's GISS Model II, the Hadley Center's HadCM3, and NCAR's CCM3. While beneficial for investigating long-term trends and scenarios of climate change, the GCM is not fundamentally well equipped for predicting regional climate impacts, as the area extent of the map grids tends to be of a low-resolution. There is a large body of developing research into GCM downscaling techniques to create more accurate Regional Simulation Models (RCM's) from available GCM forecasts. These downscaling methods may also be statistical or physically based, and are continually evolving to provide better regional climate predictions.

As pertaining to this dissertation, GCM's are of interest because of their relative inaccuracies and disparate predictions in forecasting and simulating ENSO events. Due to the many interacting ocean and atmospheric processes and relative sensitivity to boundary conditions, modeling ENSO accurately in a GCM is a considerable challenge [Bonham *et al.*, 2009]. Only very recently have some GCM's created emergent ENSO-like precipitation and circulation patterns within their simulations, although the future severity and occurrence of ENSO events remains unclear [Bonham *et al.*, 2009; AchutaRao and Sperber, 2002]. The potential socio-economic impacts of changes in ENSO are extensive, making a method that can reduce the uncertainty of ENSO impacts beneficial.

### **Agro-hydrological models**

Compared to a GCM, agro-hydrological models are relatively smaller in scale and scope of output; however, they can simulate details that a GCM has no hope of being able to do. There are a large variety of models to choose from depending on the required local ecology, necessary model complexity, data availability, spatial and temporal simulation extent, and final model performance. Generally, these models can

be grouped in two main categories: those able to operate at a variety of spatial scales that can handle a wide variety of conditions, or those more specifically suited to detailed field scale simulation. It should be noted that a hydrological model does not exist that is able to simultaneously operate at multiple spatial scales, due to the complexity of the land/water processes and interactions. Academic models able to handle a variety of scales include AnnAGNPS [Bingner and Theurer, 2007], BASINS [Duda et al., 2006], SWAT [Neitsch et al., 2005], and WAM [Soil and Water Engineering Technology, Inc., 2004], and MIKE-SHE [DHI, 2004] to name just a fraction. Field scale models include GLEAMS [Leonard et al., 1987], DRAINMOD [Skaggs, 1981], FHANTM [Fraisie and Campbell, 1997], and EAAMOD [Soil and Water Engineering Technology, Inc., 2000]. A commonality of all these models is that they are driven by precipitation and irrigation inputs.

Main tasks that agro-hydrological models should be able to simulate are hydrological processes such as water and solute transport through soil in one or more dimensions, evaporation and transpiration, both ground and surface water flow, vegetation effects which could include agricultural input, pollutant transport such as nutrients, and BMP evaluation. In most models, transport is through a series of cells or basin units whose number and size are decided on by the user, as are many parameters and inputs if not otherwise available as observed data points.

The strength of these large hydrological model packages lies in their broad applicability and the relative ease of generating multiple output scenarios once the model is calibrated. Their weaknesses, however, are the large amount of data required

to accurately calibrate them, and the user subjectivity in many of the parameter input selections and large possibility of human error.

### **Time series models**

A time series is an ordered sequence of observed data, usually through equally spaced time intervals. A time series may be discrete, i.e. taken at specific time intervals such as a daily stock price, or continuous, such as an electric voltage, meaning that it can be recorded continuously in any time interval. In studying a given time series, one can understand the generating mechanism, forecast future values and show the control parameters of a system. Statistics are essential in describing relationships in a system of ordered, correlated data, and the methods that can be used to analyze a time series are generally referred to as time series analysis. Unlike the models previously discussed, time series simulations are purely statistically based, physical interpretations only being assigned subjectively afterwards.

In most areas of research, an observed time series  $(x,t)$  is a realization or sample function from a given stochastic process,  $Z(\omega, t)$ , which in turn is just all realizations  $\{Z_{t1}, Z_{t2}, \dots, Z_{tn}\}$ , of a set of time ( $t$ ) indexed variables. Processes are characterized as being strictly stationary if it is  $n^{\text{th}}$  order distribution functions are each time invariant, but may be characterized as having a lesser order of stationarity. If the distribution function is not time invariant, (for example if the mean function or variance changes over time), then it is called non-stationary. Special measures must be taken to make non-stationary time series stationary before putting them into a model.

The crux of time series modeling theory is based on autocorrelation ( $\rho_k$ ) and autocovariance ( $\gamma_k$ ) functions. If the covariance (Equation 1-1) describes how two variables vary together through time via their expected value,  $\mu$ , the autocovariance

simply describes how one variable varies through time against a time shifted ( $k$ ) version of itself (Equation 1-2).

$$\text{Cov}(X, Y) = E((X - \mu_x)(Y - \mu_y)) \quad (1-1)$$

$$\gamma_k = \text{Cov}(Z_t, Z_{t+k}) = E(Z_t - \mu)(Z_{t+k} - \mu) \quad (1-2)$$

The autocorrelation function, or ACF, is simply the autocovariance normalized by the autocovariance at time zero (Equation 1-3).

$$\rho_k = [\text{Cov}(Z_t, Z_{t+k})] / [\sqrt{\text{var}(Z_t)}\sqrt{\text{var}(Z_{t+k})}] = \gamma_k / \gamma_0 \quad (1-3)$$

The other most used function is the partial autocorrelation function ( $\phi_{kk}$ ), or PACF. The PACF is a measure of the conditional correlation between  $Z_t$  and  $Z_{t+k}$  after their linear dependency upon the variables in-between them has been removed (Equation 1-4).

$$\phi_{kk} = \text{Corr}(Z_t, Z_{t+k} | Z_{t+1}, \dots, Z_{t+k-1}) \quad (1-4)$$

The most basic models can be classified singly or in combination as: autoregressive processes,  $AR(p)$ , moving average processes,  $MA(q)$ , and as integrated  $I(d)$ , or seasonal (S). A model with all the parameters would be  $SARIMA(p, d, q) \times (P, D, Q)_s$ , with capital letters referring to seasonal components and sub-index  $s$  to the seasonal period. Model identification is usually done through quantitative goodness-of-fit measures such as the AIC, Akaike's information criterion, or BIC, Bayesian information criterion, and looking at specific patterns in the graphics of the ACF and PACF at different lag times. However, time series model selection has also been called as much of an art as a science, as there is user subjectivity in sacrificing accuracy for the number of model parameters or vice versa, and recognizing the patterns seen in the ACF and PACF graphs.

Time series models may also be created to describe the relationships in multivariate time series, called vector ARMA( $p,q$ ), or VARMA processes. This type of model will be described in detail in Chapter 5. There have been relatively recent advances in time series model techniques for considering the variance of the current error term as a function of the variances of the previous time periods' error terms. This family of models is called an autoregressive conditional heteroscedasticity (ARCH( $q$ )) or generalized ARCH (GARCH( $p,q$ )) model. These methods are used mainly in finance and economics when dealing with exceptionally volatile time series variables [Bollerslev, 1986].

### **Spectral analysis and models**

The last type of model to be dealt with in this dissertation is spectral models. Though most time series analysis studies relationships in the time domain, an alternative view in the frequency domain describes a variable in terms of its sinusoidal behavior in a range of applicable frequencies, i.e. how often an event happens. The study of Fourier analysis is integral to the study of the frequency domain, as the 18<sup>th</sup> French mathematician Joseph Fourier lent his name to the concept that any periodic function could be represented as harmonically related sinusoids—although the field has vastly expanded since that time. An advantage of studying time series in the spectral domain, especially in geophysical data, is that hidden periodicities may emerge from noisy or chaotic systems that have a clear physical basis. This allows what started as an exercise in empirical modeling to move into becoming a physical model.

In a simple real and finite continuous sequence defined over  $(-P, P)$ , a Fourier series representation,  $f(t)$ , is accomplished using an orthogonal combination of sines and cosines (Equation 1-5).

$$\begin{aligned}
f(t) &= \frac{a_0}{2} + \sum_{j=1}^{\infty} \left[ a_j \cos\left(\frac{-jt\pi}{P}\right) + b_j \sin\left(\frac{jt\pi}{P}\right) \right] \\
a_0 &= \frac{1}{P} \int_{-P}^P f(t) dt \\
a_j &= \frac{1}{P} \int_{-P}^P f(t) \cos\left(\frac{jt\pi}{P}\right) dt \\
b_j &= \frac{1}{P} \int_{-P}^P f(t) \sin\left(\frac{jt\pi}{P}\right) dt
\end{aligned} \tag{1-5}$$

A Fourier transform (Equation 1-6) comes from the study of the Fourier series, involving the use of Euler's formula and complex exponentials to decompose a time series into oscillatory functions. The Fourier transform of a function  $f(t)$  is the integral over all times  $t$  multiplied by Euler's formula representing a basic waveform.

$$F(\omega) = \int_{-\infty}^{\infty} f(t) e^{-2\pi i t \omega} dt, \text{ for every real number } \omega. \tag{1-6}$$

However, when dealing with long-term environmental time series data, there are a number of disadvantages in using Fourier transforms. When doing a Fourier transform using this type of data, one chooses a sliding "window" to extract localized frequency response. The window thereby imposes a scaled "response interval" into the analysis, which effectively blinds the researcher from gaining the whole picture of the power frequency response at all scales through the whole length of record [Kaiser, 1994]. Additionally, Fourier analyses are not prepared to handle non-stationary time series, which makes up much environmental data.

Wavelet analysis is a spectral method which can explore non-stationary environmental data over all frequencies of interest simultaneously [Daubechies, 1990]. The basic concept is that a different "wavelet function",  $\varphi_0(\eta)$ , is a localized, zero-mean

function with a non-dimensional time parameter,  $\eta$ , exists for every time series. Although for our purposes in this dissertation only continuous analysis is used, a wavelet function may be discrete or continuous, orthogonal or non-orthogonal. The wavelet function serves the same purpose as Euler's formula—moving the time series of interest into the frequency domain. The continuous wavelet transform,  $W_n(s)$ , is the convolution of the time series,  $x_n$  with a scaled version of  $\phi_o(\eta)$  (Equation 1-7), where  $s$  is the wavelet scale,  $n$  is the localized time index,  $(^*)$  indicates the complex conjugate.

$$W_n(s) = \sum_{n'=0}^{N-1} x_{n'} \Psi^* \left[ \frac{(n'-n)\partial t}{s} \right] \quad (1-7)$$

By varying  $s$  and translating along the time index,  $n$ , (similar to the sliding window of the Fourier transform), a picture is created against appropriate background spectra showing the amplitude versus the scale, and how this varies through the time of interest or record. More detail on the technical aspects of wavelet transform will be given in the introduction of Chapter 3. Wavelet analyses have been used for data compression and signal analysis in electrical and computer engineering, molecular dynamics and DNA analysis, astrophysics, and turbulence theory [*Chan and Shen, 2005; Askar et al., 1996; Mouri et al., 1999; Zhong and Yang, 2007*], and has more recently been applied to geophysical data such as rainfall, atmospheric pressure, infrared radiance, chlorophyll concentration, river stream flow and sea surface temperatures [*Serrano et al., 1992; Rajagopalan and Lall, 1998; Nezlin and Li, 2003; Labat, 2008; Y. Wang, 1996*]. The application of wavelet transform is growing in popularity, as more scientific fields recognize the powerful information it can provide, coupled with the advantages it has over traditional Fourier types of analysis.

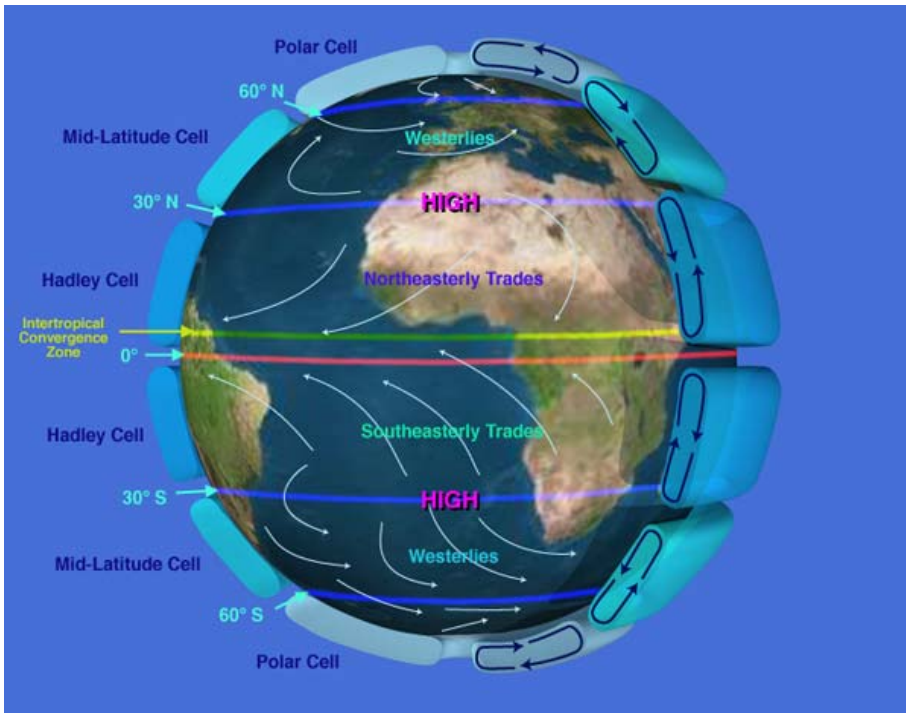


Figure 1-1. Global air circulation patterns are dominated by the trade winds, tropical easterly winds that are found near the equator. Trade winds are responsible for steering the flow of tropical storms that affect North and South America, Asia, and India, and African dust. (from NASA Jet Propulsion Laboratory <http://sealevel.jpl.nasa.gov/overview/climate-climatic.html>)

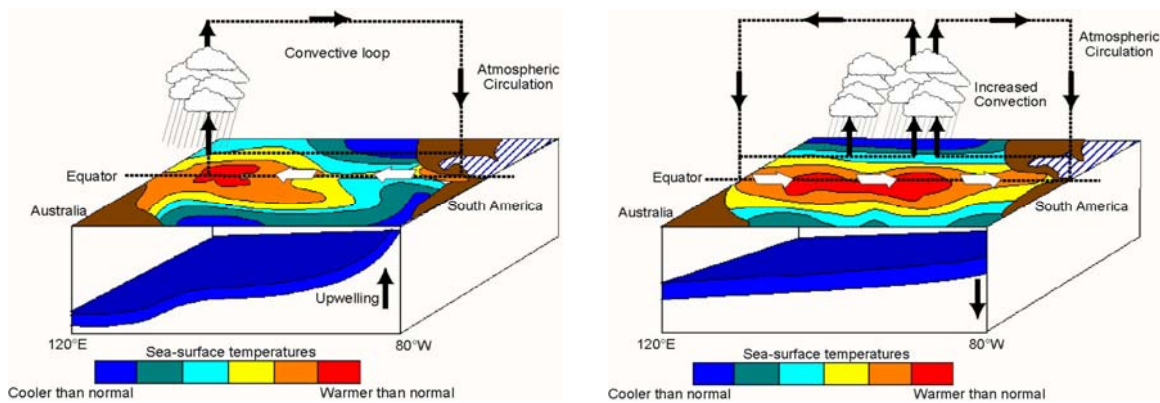


Figure 1-2. As opposed to neutral conditions (left), during an El Niño event (right) sea surface temperatures (SST) in the Pacific equatorial region are warmer than usual, increasing convection of moist air into global circulation. During a La Niña event, cooler water decreases convection.

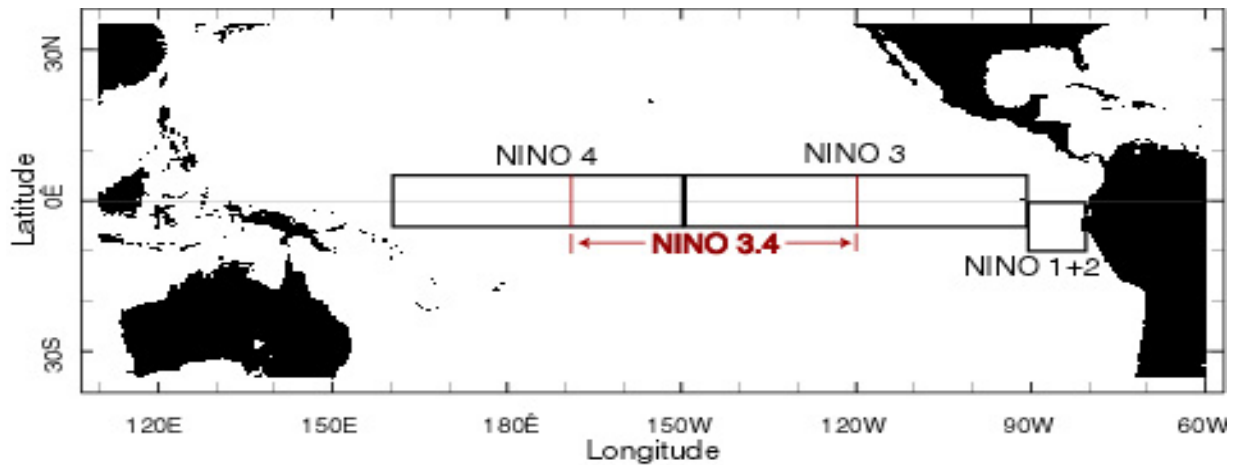


Figure 1-3. The Niño 3 Region is bounded by 90° - 150°W and 5°S - 5°N. The Niño 3.4 Region is bounded by 120° - 170°W and 5°S - 5°N. Niño 4 is bounded by 160°E - 150°W, and from 5°S - 5°N. Niño 1 is defined by 80°- 90°W and 5°- 10°S, Niño 2 by 80°- 90°W and 0°- 5°S. The JMA (not pictured) extends from 4°S - 4°N, 150° - 90°W.

## CHAPTER 2 EFFECTS OF CATEGORICAL EL NIÑO/SOUTHERN OSCILLATION ON SIMULATED PHOSPHORUS LOADING IN SOUTH FLORIDA

### **Introduction**

Indices of climate variability have been monitored regularly for the greater part of the twentieth century. The El Niño/Southern Oscillation (ENSO) phenomenon has emerged as one of the most consistent indices for describing low-frequency climate variability on global and regional scales [*Ropelewski and Halpert, 1986, 1987*]. As the Florida water management agencies are interested in reducing climate-associated risks in managing water resources and agricultural systems, ENSO could provide a basis for correlating water quality, especially nutrient loading, with climate variability.

Different ENSO phases are based on an index of warming or cooling of surface sea temperatures in the equatorial Pacific Ocean and associated pressure and wind pattern changes. ENSO phase classifications used in this research are from the Japan Meteorological Agency (JMA) index [*Japan Meteorological Agency, 1991*], which are based on observed data from 1949 to the present, and a new alternative monthly ENSO classification, which has been initially referred to as the M-ENSO Index. The JMA index is a six-month running average of spatially averaged surface sea temperature anomalies over the tropical Pacific Ocean (4°S to 4°N, 150°W to 90°W). The ENSO year (defined as October through the following September) is classified as El Niño if the running six month surface sea temperatures average, that must include the reference season October to December, is at least +0.5°C higher than average, La Niña if it is -0.5°C lower than average, or neutral (all other values).

A main disadvantage of the annual JMA ENSO classification is that the summer months are determined using the SST conditions from the previous October, as

opposed to more current conditions. The M-ENSO Index still uses the JMA defined six-month duration during a reference season, however, that reference season is from November to January, and the El Niño or La Niña event stops for a given month when the SST anomalies change to a different phase [Gérard-Marchant *et al.*, 2008]. This allows months within an ENSO “year” to be classified as different phases. Using the M-ENSO classification on recorded SST data from 1900-2007, the total number of La Niña months from April to September is 25-35% less than with the annual classification. The number of El Niño months is about 10% less using M-ENSO [Gérard-Marchant *et al.*, 2008].

Much of the southeastern U.S., especially Florida, is strongly affected by ENSO. El Niño winters in Florida tend to be cooler and wetter, whereas La Niña winters tend to be warmer and drier [Hanson and Maul, 1991; Kiladis and Diaz, 1989; Schmidt *et al.*, 2001]. Previous studies have correlated ENSO phase with stream flow [Chiew *et al.*, 1998], rainfall in the western U.S. [Rajagopalan and Lall, 1998], crop yield in Florida [Handler, 1990; Hansen *et al.*, 1997; Hanson and Maul, 1991], and even cholera dynamics worldwide [Pascual *et al.*, 2000].

In Florida, water quality and quantity are important concerns for environmental quality and standard of living. The importance placed on water pollutants is reflected in Florida's policies with respect to ecosystem and Everglades restoration, and in the prevalence of its water management agencies. Although ENSO effects on many environmental data have been explored, there has been no research exploring ENSO effects on nitrogen (N) and phosphorus (P) runoff pollution in Florida. In agro-hydrological watersheds, P and N are important indicators of water quality and best

management practices (BMPs) and are a focus of efforts to reduce nutrient loading in water bodies. In this study, we are focusing on both JMA and M-ENSO effects on simulated nutrient loads rather than historical data because major changes in land use and land management in Florida over the last 50 years make the use of historical data impractical. However, measured P loads were determined to be reasonably represented by model predictions. A major advantage of using simulated nutrient loads is our ability to look for the presence of direct associations between simulated nutrient loads and ENSO phase without confounding land use and management variables.

The agro-hydrological model WAM (Watershed Assessment Model) is a watershed-scale, continuous, spatially distributed simulation model developed by Soil and Water Engineering Technologies, Inc. (SWET) of Gainesville, Florida. Using WAM, scientists and engineers have successfully modeled more than 25% of the watershed areas of Florida [*Jacobson, 2002; Ouyang, 2003*]. Among the most well calibrated and validated processes that WAM simulates are daily stream flow and N and P loads in systems with high water tables [*Soil and Water Engineering Technology, Inc., 2004*]. WAM was specifically calibrated to south Florida's hydrology, as models of specific regions are useful for exploring effects of management on runoff and pollution. Additionally, by assuming that land management has remained constant over time, the effects of climate variability on pollution can be isolated and explored. For these reasons, it is reasonable to use a watershed model, such as WAM, to study the effects of climate variability manifested through ENSO phases on simulated water quality, and to assume future potential in tailoring land management practices to climate prediction.

Nitrogen and P loads into Lake Okeechobee were simulated for 36 years (1965-2001) in basin S-191, a 486.9 km<sup>2</sup> sub-basin directly northeast of Lake Okeechobee in south Florida (Figure 2-1a). Then, we examined potential P load differences at different temporal scales based on historical annual JMA and monthly M-ENSO classifications. Our hypothesis was that there would be statistically significant and quantifiable differences in simulated monthly and/or seasonal P load for the three ENSO phases, and that the M-ENSO index would capture summer climate trends more accurately than the JMA because of the finer temporal resolution. Specifically, we expected to predict greater nutrient loads during El Niño winters and La Niña summers because of the greater precipitation during these phases in south Florida. We also expected nutrient loads in neutral years to be closer to average values. By investigating the trends in nutrient load during the different ENSO phases, the objective was to answer the question of whether or not P loads have climate-based predictability.

In the southeastern U.S., and more specifically the Lake Okeechobee watershed, P loading is more of an issue than N because plant and microbial growth in the lake is most limited by P availability. Traditionally, it had been thought that P applied to soil for crop production would remain in place despite the action of water and independent of soil type. As a result, inorganic phosphate fertilizers often were applied in excess of need because cost was not prohibitive. This was called "banking" phosphorus to insure that it would not be a limiting factor in crop growth. While both N and P are integral life-sustaining components of a biological system, an excess or dearth of either one can create an ecological mess.

Between the early 1970s and mid-1980s, total P loads to the open-water region of the lake nearly tripled [*Flaig and Reddy, 1995*], causing massive hyper-eutrophication and fish kills. Monitoring and managing P loads in Lake Okeechobee are also part of the Lake Okeechobee Water Management Project (LOWP) and the Comprehensive Everglades Restoration Project (CERP), neither of which has yet looked at using climate forecasts to manage nutrient loads. Although WAM simulated both N and P loads, and the consequent analysis was done with both nutrients, this research presents only the P-related results, as N loading is not a problem in Lake Okeechobee. In general, simulated N loads were of a lesser magnitude than P loads, but followed the same trends and patterns over the time series.

## **Data and Methods**

### **The Lake Okeechobee Watershed**

Lake Okeechobee (LO) and its watershed are central components of south Florida's Kissimmee-Okeechobee-Everglades ecosystem, which extends from the headwaters of the Kissimmee River in the north to Florida Bay in the south. The shallow lake is the second largest freshwater body located in the continental United States. It is home to one of the nation's prized bass and speckled perch fisheries, as well as an economically important commercial fishery [*Flaig and Reddy, 1995; Rosen et al., 1996*]. At the same time, it provides habitat for a wide variety of wading birds, migratory waterfowl, and the federally endangered Everglades Snail Kite. Lake Okeechobee can also be a backup water supply for the communities of the lower east coast of Florida. The lake supplies drinking water, irrigation water for the expansive Everglades Agricultural Area (EAA) to the South, and is a critical supplemental water supply for the

Everglades National Park. Given these competing demands, management of the water resource is a major challenge.

### **History and hydrology**

Geological surveys indicate that Lake Okeechobee formed about 6,000 years ago, when ocean waters retreated from covering what is now Florida, leaving a large shallow lake with a maximum depth of about 19-21 feet [*Florida DEP, 2005*]. Much of south Florida remained under sheet flow conditions from the lake's outflow until the late 19<sup>th</sup> century, when real estate developers constructed a canal connecting Okeechobee with Lake Hicpochee, providing another outlet. Additional canals were built in the early 1900s to provide slow continuous drainage for agricultural and flood prevention purposes, with the ultimate goal of draining the entire northern half of the Everglades. With the advent of small farming communities around the lake, a muck levee was constructed around the southern shore. However, two large hurricanes in the 1920s caused major flooding and human casualties, at which point federal help was enlisted through the US Army Corps of Engineers (USACE) to prevent further losses of this nature. The USACE built the Herbert Hoover Dike around Lake Okeechobee, and created a system of canals and levees that artificially controlled all surface inputs and outputs to the lake, except for Fisheating Creek, which remained natural.

This system allowed the lake levels to be monitored and controlled to prevent flooding and measure irrigation allowances, and as a result, much of the land directly surrounding the lake was converted to agricultural uses, with dairy and beef farms in the north and sugar cane and vegetables in the south [*U.S. EPA, 1996*]. These land use changes dramatically increased the loads of N and P inputs into the lake, which resulted in much of the hyper-eutrophication problems being dealt with today. An abundance of

P has caused excessive algal growth in Lake Okeechobee, and hyper-eutrophic P levels cause algal “blooms”, or excesses of growth, in which dissolved oxygen is depleted, in turn killing other aquatic biota and increasing the amount of treatment needed to make the water safe for drinking. Many algal blooms have been shown to be in proximity to areas with high soil P, such as agriculture or poultry and dairy farms, leading researchers concerned with water quality to examine the relationships between soil, hydrology, and land use.

In total, the LO watershed covers a huge area of 12,000 km<sup>2</sup> that extends from Orlando in central Florida, to the Everglades in the southern tip. Except for the natural input of Fisheating Creek, by this point all surface runoff to the lake is directed through man-made canals and gated streams. Hydrological inputs to the lake are mostly from precipitation (39%), the Kissimmee River (31%), S-191, the Taylor Creek/Nubbin Slough (5%) and multiple small inflows such as Fisheating Creek [*Florida DEP*, 2001]. Major outflows are evapotranspiration (66%), the Caloosahatchee River (12%), canals that discharge to the Everglades (18%), and the St. Lucie Canal (4%) [*Florida DEP*, 2001]. Precipitation in Lake Okeechobee is very seasonal; about 75% of the 53 inches/year occur during the summer storm season from May to October [*Purdum et al.*, 1998].

North of LO, elevations in the watershed range from 4 to 23 meters, but south of the lake, the landscape has an even lower gradient that is poorly drained with many marshes and wetlands. Field runoff and nutrient transport in the LO watershed are controlled by water table fluctuation, mostly within one to two meters from the surface [*Knisel et al.*, 1985]. Surface runoff occurs when soil pore spaces are filled with water

and the water table is at the ground surface. This suggests a slow lateral or vertical groundwater infiltration may be an important factor in nutrient transport in areas with more slope [Flaig and Reddy, 1995]. Additional well-field and tracer studies done in basin S-191 indicate that the capacity of a region for sub-surface storage is a better indicator of surface runoff potential than slope [Flaig and Reddy, 1995], however, sub-surface storage capacity is in turn determined by a combination of topography and local boundary conditions. The different P flow-paths and topographical conditions throughout the watershed indicated that non-point source P management and reduction must be done on a case by case basis, rather than an overarching management plan.

### **Geology and soils**

Much of Florida's underlying geology is marine sediment made up of sand, gravel, and clay lenses, with a network of artesian aquifers at depths below 40 meters. The local soils north of Lake Okeechobee are primarily poorly-drained, sandy and naturally infertile Spodosols, or flatwoods, (45%), with some deposits of Entisols and Histosols near the Everglades Agricultural Area (EAA) [USDA-ARS, 2005]. Spodosols in Florida are of the Aquod, or wet type, from 0.5 to 3 m depth, characterized by a shallow and fluctuating water table. Natural vegetation in Aquod soils is water loving, and in the LO watershed includes palms, pines, wet prairie grasslands and wetland species. Most of the soils in the watershed are composed of greater than 90% sand, with high infiltration rates and poor internal drainage due to low permeability of the spodic horizon [Flaig and Reddy, 1995]. The sandy soils in the LO watershed generally do not retain P in their surface horizons, making leaching into ground and surface waters a problem, however, P can be retained in Spodosols given the simultaneous presence of Al- or Fe- rich spodic horizons [Yuan, 1965].

In the 1980s, researchers found that the Taylor Creek/Nubbin slough (S-191) basin of the LO watershed provided only 5% of the water input to the lake, yet 28% of the total P load [*Federico et al.*, 1981]. Specifically, the Taylor Creek/Nubbin Slough basin is mainly comprised of the fine sandy soils Myakka/Immokalee/Waveland and Wabasso/Felda/Pompano, characterized by high hydraulic conductivities of over 16 cm/hr [*Campbell et al.*, 1995]. This and several other high-impact basins were identified as having multiple dairy operations, which were putting high levels of P into the fine sandy soils that have high infiltration rates and do not retain soluble-P well [*Knisel et al.*, 1985]. The lack of deep percolation into spodic horizon soils that could potentially retain the excessive P only compounded the problem [*Yuan*, 1965], resulting in high concentrations of soluble P being transported via lateral seepage above the spodic layer or overland flow from the dairies to adjacent streams and wetlands that ultimately discharge into the lake [*Campbell et al.*, 1995].

### **Ecology and wildlife**

Lake Okeechobee is a naturally eutrophic lake, meaning that its default state is a murky appearance with high levels of nutrients. This serves to make it an extremely productive ecosystem, given that it does not reach the hyper-eutrophic state of the 1970s and 1980s. Additionally, the Okeechobee Basin contains approximately 4,000 km<sup>2</sup> of wetland area, mostly in the Lower Kissimmee River Basin, that are connected via canals and streams to Lake Okeechobee [*Rosen et al.*, 1996]. Both these wetlands and the surrounding watershed areas provide crucial wildlife habitat for birds, fish, and plants.

Lake Okeechobee itself supports a significant largemouth bass and black crappie sport fishery, as well as commercial fisheries for catfish and bream that in 1993 were

generating over \$30 million per year in the local economy [Fox *et al.*, 1993]. There are over 40 recorded species of fish in the lake that depend on macro-invertebrate and zooplankton populations, which in turn provide food for numerous migratory wading birds, raptors, and alligators, including the federally endangered Snail Kite [Havens and Gawlik, 2005]. The lake's natural littoral zone was much larger than what it is today under current levee conditions, and has consequently altered the vegetation, reducing populations of native willow, spikerush, and sawgrass, and encouraging the growth of invasive species such as cattail, torpedograss and hydrilla [Havens and Gawlik, 2005]. Submerged aquatic vegetation populations have also declined causing increases in algal growth and hyper-eutrophication, as there are more available nutrients for algae growth.

### **Management and restoration**

The Lake Okeechobee Protection Bill was passed in the Florida legislature in 2000, which requires several different governing bodies to work together to implement P TMDL regulations. The Bill operates in conjunction with the Comprehensive Everglades Restoration Act (CERP), as outflow from the lake is an input to ecosystems in the Everglades. In 2001, TMDL limits were decided upon for the lake with an overarching adaptive management approach: if newer research and monitoring revealed better load limitations, the TMDL regulations would be changed to reflect that research.

Current TMDL's are based on various combinations of computer model simulations of the lake with an optimal balance between its designated Class 1 uses of urban water supply, agricultural irrigation, Everglades flow, habitat, aquifer recharge, flood control, recreation, and navigation [Florida DEP, 2001], and historical record. Annually, the total allocation for all non-point source inputs to Lake Okeechobee is 140

metric tons of P, with an in-lake P concentration target of 40 ppb in the pelagic zone. In-lake concentrations of P in the water column from 1995-2000 average about 100 ppb or 641 metric tons/year, with recorded concentrations as high as 400 ppb during intense storms or hurricanes that stir up sediments from the lake bottom [*Florida DEP*, 2001].

To achieve the ultimate desired concentration conditions in the lake, researchers calculated that the total annual P load must be less than 423 metric tons/year [*South Florida Water Management District (SFWMD)*, 2001], which has never been close to being met since implementation in 1995. Basin S-191 is a main offender in failing to meet its TMDL targets, with specified basin management action plan (BMAP) goals of 0.18 ppm and 25.1 metric tons/year TP, and recorded rolling averages from 1995-1999 of 0.65 ppm and 91.3 metric tons/year TP [*Florida DEP*, 2001]. There are various committees of researchers, advisors, and managers that monitor and decide on how the LO watershed should be managed and what kinds of BMP's are most effective. To date, reduction strategies have not been effective in meeting the decided upon phosphorus TMDL's, and the results of this research only reinforce that the current limits may not be feasible. Whether this is a problem of BMP implementation and load reduction efforts or realistic P load expectations remains to be seen.

## **Data**

Basin S-191 (Taylor Creek/Nubbin Slough) is a 486.9 km<sup>2</sup> watershed with 85 defined stream reaches in WAM (Figure 2-1b). Stream flow is generally slow-moving and characterized by broad flood-plains with poorly defined stream channels, typical of the Coastal Plain region. Land use has varied historically, but for the purposes of this study, static land use from the year 2000 was used for all simulation years. In 2000, 56% of the watershed area was designated as improved pasture, 6% as scrub/brush

land, 7% as freshwater marsh, 4% as field crops, and all other land uses less than 4% each.

Required WAM inputs such as daily precipitation, daily and mean monthly maximum and minimum temperatures, solar radiation, and wind speed data were obtained online at the SFWMD DBHYDRO browser ([www.sfwmd.gov/org/ema/dbhydro](http://www.sfwmd.gov/org/ema/dbhydro)). Precipitation and water quality stations in S-191 are in 14 locations throughout the basin (Figure 2-1b), which are grouped into spatially distinct "rain zones" within the watershed by WAM. "Rain zones" are user-defined Thiessen polygons within the GIS interface that allow the user to assign different weather stations to represent different areas of a particular watershed. The cumulative annual rainfall averaged yearly over all weather stations from 1967 to 2001 was 115.6 cm, with a minimum of 73.1 cm in 1981, and a maximum of 156.9 cm in 1982. GIS coverages including land use for the year 2000, soils, hydrography, topography, and relevant hydrological structures were provided by the Lake Okeechobee CERP Project Manager. WAM was run using a uniform cell size of 1 ha. Calibration and validation of the model over all 20 basins surrounding Lake Okeechobee (including S-191) was performed by SWET before WAM was provided to the SFWMD, using data from 1991-2000 [Jacobson, 2002].

Historical annual ENSO climate data used in this analysis include 9 JMA El Niño years starting with October of the current year until the following September, (1965, '69, '72, '76, '82, '86, '87, '91, and '97), 10 La Niña years (1967, '70, '71, '73, '74, '75, '81, '88, '98, and '99), and 17 neutral years (remaining years from 1967 to 2001). These data are classified by the Center for Ocean-Atmospheric Prediction Studies (COAPS) based on

the JMA's recording of surface sea temperatures anomalies. Using the M-ENSO classification [Gérard-Marchant et al., 2008], there are 109 El Niño months, 96 La Niña months, and 236 neutral months. The M-ENSO re-classification of this data as compared to the annual method results in about the same number of total El Niño months, a 20% decrease in the number of La Niña months, and a 15% increase in neutral months.

### **Watershed Assessment Model (WAM)**

WAM's function is to serve as a tool for watershed assessment, using the appropriate model components and available data sources [Soil and Water Engineering Technology, Inc., 2004]. WAM includes four nutrient sub-models for different land uses: the Groundwater Loading Effects of Agricultural Management Systems (GLEAMS) model [Leonard et al., 1987], the Everglades Agricultural Area Model (EAAMOD) [Bottcher et al., 1998; Soil and Water Engineering Technology, Inc., 1996], and two sub-models developed by SWET specifically for wetland and urban landscapes [Soil and Water Engineering Technology, Inc., 2004]. For basin S-191, both GLEAMS and EAAMOD were used to simulate daily nutrient loads based on recorded land use, precipitation, and simulated stream flow time series. Stream reaches in the model are routed to the outlet by solving the continuity equation and Manning's equation for uniform channel flow with a variable time step of approximately 15 min, based on the simulated stream velocity (see [Jacobson and Bottcher, 1998], for details). There are no inter-cell interactions in WAM simulations. WAM simulated nutrient loads in 85 user-defined stream reaches of basin S-191, which ultimately merge at a single reach (reach 2), which enters Lake Okeechobee (Figure 2-1b).

For the S-191 watershed, six years (1995-2000) were used as a calibration period for flow and P [Jacobson, 2002], while validation was performed using the years 1991-1994. WAM is a physically based model that utilizes the characteristics of the watershed in the generation of flows and pollutant loadings. Thus, calibration in the classic sense, whereby various parameters are modified until a goodness-of-fit is achieved, is not done. Rather, known data from the watershed are used to verify that the model is appropriately simulating the physical dynamics of the watershed. Measured flow and P concentration for the period 1991-2000 were provided by SFWMD. While daily flow measurements were provided, P measurements were more sporadic, ranging from daily to bi-weekly grab samples. Daily concentrations were calculated by SWET by interpolating between grab samples, which causes errors in actual concentrations and therefore P loads as well. In fact, the flow, concentration, and load data contain measurement uncertainty that can be estimated and incorporated into the performance evaluation of WAM. Using a goodness-of-fit indicator, such as a Nash-Sutcliffe (NS) coefficient [Nash and Sutcliffe, 1970], which can be modified to include measurement uncertainty, allows model evaluation to consider this inherent data uncertainty (Harmel and Smith, 2007). In this analysis, the NS coefficient was used to quantify WAM goodness-of-fit both with (modification 1) and without consideration of measurement uncertainty. The probable error range (PER) values used to compute the modified NS coefficients were based on previous uncertainty estimates [Harmel et al., 2006].

In the initial calibration and validation simulations, the predicted flows were consistently below measured values. Examining the crop coefficients revealed that the leaf area index (LAI) estimates were being reduced too much in the winter for the

regional grasses. Increasing these LAI coefficients improved the match between simulated and measured values [Jacobson, 2002]. The NS coefficients for simulated and measured monthly flows were 0.79 for the calibration period and 0.66 for the validation period, which represent "good" model performance according to [Moriasi et al., 2007]. When measurement uncertainty in the flow data was taken into account using a PER of  $\pm 6\%$ , the modified NS coefficients showed an increase to 0.99 for the calibration period and 0.99 for the validation period. When large differences between simulated and measured P loads occurred, the correctness of land uses of contributing areas was examined. For example, some areas were identified as "improved pasture" when "intensive pasture" was more appropriate. The management practices for the basins were also evaluated to ensure appropriate representation of current practices [Jacobson, 2002]. The NS coefficients for simulated and measured monthly P concentrations were 0.53 for the calibration period and 0.39 for the validation period, which were less accurate than the flows, as expected, and indicate "unsatisfactory" model performance. When uncertainty of concentration data was taken into account using a PER of  $\pm 27.1\%$ , the modified NS coefficients increased to 0.81 for the calibration period and 0.75 for the validation period, indicating that WAM simulated P concentration values that are as good as the uncertain data. The NS coefficients for simulated and measured monthly P loads were 0.73 for the calibration period and 0.63 for the validation period. With a load PER of  $\pm 27.8\%$ , the modified NS coefficients increased to 0.94 for the calibration period and 0.93 for the validation period.

## **Analysis and Statistics**

### **Precipitation and stream flow**

Observed daily precipitation data from all 14 weather stations were averaged and summed into monthly cumulative values, normalized by monthly average, and averaged over all years and by JMA or M-ENSO phase for each month and over all months by year. These anomalies are visualized in both monthly box plots and scatter plots over all years (Figures 2-2, 2-3, and 2-4) in the Results and Discussion section.

Simulated daily stream flow data from WAM were averaged into a monthly rate, normalized by monthly average, and averaged over all years and by JMA or M-ENSO phase for each month and over all months by year. The resulting stream flow anomalies can be seen in monthly and seasonal box plots for each ENSO categorization (Figures 2-5, 2-6 and 2-12) in the Results and Discussion section.

### **Phosphorus concentration and loading: JMA ENSO classification**

Simulated daily sediment and soluble P concentrations were summed and averaged into total daily P, and were then averaged basin-wide into an average value per month and normalized by the monthly average over all years. Simulated average daily total P loads were computed by multiplying daily flow by P concentrations for both sediment and soluble P, and averaged into basin-wide monthly and seasonal values across all sections of stream reaches. Seasons were defined by known southern Florida precipitation and climate regimes and were designated into four categories within their ENSO year: February-April (FMA), May-July (MJJ), August-October (ASO), and November-January (NDJ). Load and concentration anomalies were computed by normalizing loads against the average climatology-based monthly load, which included all ENSO phases (load anomaly = summed monthly load - average monthly load), and

by separation into JMA-defined ENSO phases. Results were visualized in both box plots and scatter plots. Temporal differences in P loads and concentrations were analyzed as "anomalies" rather than actual values, as is commonly done in climate science when the year-to-year variability is high. This procedure normalizes the data to remove bias and effectively see anomalies in the data [*Mason and Goddard, 2001; Rajagopalan and Lall, 1998; Ropelewski and Halpert, 1987*]. Especially when comparing data directly with the JMA index, which is defined by temperature anomalies, it makes sense to analyze precipitation and nutrient variables in the same manner.

Measures of the modeled data's prediction variability at the monthly, seasonal, and JMA phase-based level were calculated and compared via maximum and minimum values, range, and standard deviation. Data are graphically presented in box plots for P load (Figures 2-9 and 2-11) and P concentration (Figures 2-7 and 2-13) in the Results and Discussion section. Differences between nutrient loads and concentrations in JMA ENSO phases and months can be seen, and variability evaluated from the statistics calculated.

The pooled variance between months or different JMA Index ENSO phases was too large, and the sample size (number of ENSO phase events) was too small to identify high probability of formal significance. Thus, statistical tests of significance, such as Student's t-test or classic ANOVA, were not used for assessing variance and significance. Instead, contingency tables were used. This simple and proven alternative to parametric statistics is appropriate for estimating the probabilities of climate anomalies based on ENSO phase [*Mason and Goddard, 2001; Ropelewski and Halpert, 1987; Wilks, 1995*]. This methodology was used to determine whether the events of

interest (high or low nutrient loads) were more or less likely to occur given different values of the independent variable (ENSO phase). Contingency table theory and the hypergeometric probability distribution were used to determine the significance of the number of times that the seasonal simulated nutrient load during each ENSO phase was above or below a pre-defined threshold.

Using the methodology outlined by Mason and Goddard, three-month seasonal normalized predicted mean nutrient load thresholds were calculated for each ENSO year (1965-2001) and then sorted and separated into three terciles: low (T1), mid (T2), and high (T3) for general comparison. Then a TMDL-based categorization of above or below a TP concentration of 0.22 mg/L, as there was no significant probability of any season or phase having a concentration below the current BMAP policy limit of 0.18 mg/L. The low tercile indicates load anomalies dominated by negative values, while the high tercile is dominated by positive values. The mid tercile indicates both positive and negative anomalies of smaller magnitude, and the policy-based table indicates which months and JMA ENSO phases are below an investigatory concentration based on the actual basin S-191 TP target of 0.18 mg/L. The number of times that the simulated nutrient load(concentration) during the separate ENSO phases was in each tercile(concentration level) was tabulated for each season. These frequencies indicate the likelihood of observing a certain tercile(concentration level) of load(concentration) in each ENSO phase and season over all simulated years.

There were a total of 12 contingency tables created for each of the three ENSO phases in each of the four tri-month seasons. Using Fisher's exact test [*Fisher, 1935*], the probability that a certain tally of tercile of load within a given season and ENSO

phase is statistically greater than the other terciles is calculated. This probability is equal to the right tail of the hypergeometric distribution (Equation 2-1), and the information is represented in the contingency table (Table 2-1).

$$P_x(X \geq x) = H(x; r, b, n) = \sum_x^{\min(r,b)} \frac{\binom{b}{x} \binom{n-b}{r-x}}{\binom{n}{r}} \quad (2-1)$$

In Equation 2-1 and Table 2-1, for all calculations there are a total of  $n = 36$  years, of which  $r$  are either El Niño (9), La Niña (10), or neutral (17). The total number of T1 or T3 events counted within a certain ENSO phase across *all* four seasons is represented by  $b$  and  $a$ , respectively. The number of tallied T1 or T3 events within the *particular* season and ENSO phase of interest is represented by  $x$  or  $y$ , respectively. For example, in the November to January season during El Niño,  $n = 36$  total years,  $r = 9$  El Niño years,  $b = 10$  total T1 events across all seasons in El Niño,  $a = 14$  total T3 events across all seasons in El Niño, while the tallied T1 in the NDJ season is  $x = 0$  and the tallied T3 in the NDJ season is  $y = 3$ , leaving the remainder tallied in T2 as  $r-y-x = 6$  (note that the total T1+T2+T3 events equals  $r$ , the total number of El Niño years). According to Fisher's exact test in this example, for the tallied number of events in a tercile to be significantly greater than the other terciles with 95% confidence, there must be at least 5 events. To achieve 99% confidence, there must be at least 6 events. As the test used is right-tailed, we are only identifying those loads which are significantly greater than the others, as high nutrient loads are of more risk and management significance. Therefore, during the NDJ season in El Niño years, the mid-tercile,  $T2 = 6$ , is the only one in which the number of events is greater than what would be expected

from random chance, with 99% confidence. These probabilities indicate the thresholds, pre-defined using the hypergeometric distribution and Fisher's exact test, that must be met or exceeded by the tallied load data to accept a given tercile's (or concentration level's) significance at the 95th or 99th percentile within each ENSO phase, between seasons.

The relevant assumptions for Fisher's exact test and the hypergeometric distribution are similar to those of a Monte Carlo significance test, for which it is assumed that the observation in one year is independent of the observations in all other years. Independence can be confirmed using autoregressive methods [*Mason and Goddard, 2001; Wilks, 1995*]. For our purposes, if the selected ENSO years (the  $r$  sample) are evenly distributed through the entire period ( $n$ ), then autocorrelation and trend effects are not important, and errors will be conservative [*Mason and Goddard, 2001*]. In our relatively short 37-year period, during which ENSO patterns can be considered climatologically and geophysically stable, each ENSO phase was evenly distributed through the tested period with very little clustering. To be certain that the underlying relative frequencies of a particular ENSO phase differ from one-third, the expected probability of any of the three phases occurring due to random chance, for a period of about 40 years within which there are approximately ten La Niña or El Niño years of interest, relative frequencies of 50% or more are needed (for details, [*Mason and Goddard, 2001*]).

The contingency tables were derived from historical JMA and M-ENSO events, and the resulting probabilities are not meant to serve as a forecast. If the probabilities calculated using contingency tables were used to forecast, the table should be

constructed so that the probabilities are contingent on forecasts of ENSO events, rather than observed events. Rather, these contingency table probabilities are only meant to provide a quantitative measure of the significance of the relative seasonal nutrient loads in each ENSO phase.

### **Phosphorus concentration and loading: M-ENSO classification**

The recent Zierden M-ENSO Index [*Gérard-Marchant et al.*, 2008] was used to try and quantify statistically significant differences between months in different ENSO phases. As was previously noted, no statistical difference was found between ENSO phases when a variety of statistical tests were done using yearly ENSO JMA classifications to look at differences in observed precipitation and simulated stream flow and phosphorus concentrations and loads. With the finer temporal resolution of the Zierden Index to better capture the changes in SST, more standard statistical tests could be used, as it has been initially noted that the M-ENSO index is better able to quantify different ENSO events in the southeast United States than the annual JMA index, especially in the summer [*Gérard-Marchant et al.*, 2008].

The finer temporal scale allowed the use of a more standard single-factor ANOVA to determine if there was a statistically significant difference between the means of the three M-ENSO phases, and more specifically, which two ENSO phases were different. ANOVA analysis was performed using a p-level of 0.05 on the observed precipitation data, and the simulated stream flow, P concentration, and P load anomalies.

## Results

### Monthly Precipitation and ENSO Phase

Because certain months in El Niño or La Niña years in Florida can exhibit more rainfall than others, it logically follows that increased precipitation would result in increased runoff and, consequently, increased nutrient loading. The south Florida/Everglades area is semi-tropical in terms of climate patterns, with a general wet season from May to October and a mild dry season from November to April. El Niño winters in Florida are usually wetter than La Niña or neutral years, with southern Florida showing the strongest response [*Livezey and Smith, 1999; Schmidt et al., 2001*]. Our results were consistent with these trends. Summer and fall precipitation trends during El Niño were clearly demarcated, although anomalies tended to be small, and spring in southern Florida can actually be drier than during other phases [*Sittel, 1994*]. La Niña winters and summers were shown to be drier overall across Florida as a whole, while La Niña springs are drier in southern Florida [*Livezey and Smith, 1999; Sittel, 1994*].

Figure 2-2a shows spatially averaged and normalized monthly total precipitation, averaged across all stream reaches for all years and separated by ENSO phase. Error bars are not shown on this graph, as the small ENSO phase sample sizes make error bars large enough to obscure the visible patterns. Straight line segments connect adjacent data points and are not representative of a mathematical function, but they are included to improve visualization of temporal patterns. As expected from previous observed ENSO patterns in south Florida [*Livezey and Smith, 1999; Schmidt et al., 2001*], above-average precipitation was observed in November, December, January, February, and August during El Niño years, and from April to June during La Niña years. Neutral year precipitation was closer to average and had less overall variability.

Figure 2-3 shows total precipitation (cm) anomalies averaged for all precipitation stations, and presents spatially averaged precipitation anomaly means by month and by JMA ENSO phase. In neutral years, monthly precipitation anomalies tended to stay closer to the average (Figure 2-3a), with greater general variability than the nutrient loads, seen in Figure 2-4a with some small ranges, especially in the winter months. However, La Niña and El Niño precipitation trends (Figures 2-3b and 2-3c) did not closely match their corresponding nutrient load trends (Figures 2-4b and 2-4c). Some of this trend is likely due to lags between infiltration and runoff responses, in which extended dry months followed by high-intensity precipitation causes greater P runoff.

In contrast, observed monthly precipitation anomalies classified using the M-ENSO index are shown in Figure 4. While the neutral and El Niño month's precipitation (Figures 2-4a and 2-4c) retains the same general pattern, the La Niña months show major differences (Figure 2-4b). Specifically, the largest differences are seen during the summer months during M-ENSO La Niña months that commonly experience intense convective thunderstorms in Florida: April, May, and June (Figure 2-4b). This information is consistent with previous research on both ENSO in south Florida and the increased accuracy of M-ENSO in the summer months, as it was found that significantly lower La Niña summer precipitation levels were found when comparing the M-ENSO with the JMA [*Gérard-Marchant et al.*, 2008]. The M-ENSO classification both reduces the range and average of the summer months La Niña precipitation, which suggests that perhaps the increase in the precipitation in the rest of an annual JMA La Niña is responsible for the significantly higher precipitations that are commonly expected.

## Monthly Simulated Stream Flow and ENSO Phase

Florida precipitation patterns are altered by ENSO phase, as we have just seen. In the Lake Okeechobee area of south Florida, stream flow has a more complex relationship with ENSO. Generally, stream flow increases during El Niño fall (October-December) and winter (January-March) seasons, while strong La Niña events cause decreases in stream flow for fall through spring, and may even extend into the summer months [*Schmidt et al.*, 2001; *Zorn and Waylen*, 1997]. Stream flow patterns are a complex combination of precipitation, local basin characteristics, human construction, and climate, and while flow patterns smooth out the noise of a rainfall time series, a strong ENSO signal may be lagged or harder to identify.

These seasonal ENSO flow patterns are broadly replicated in the JMA (Figure 2-5) and M-ENSO (Figure 2-6) results seen for basin-wide stream flow in S-191 of the Lake Okeechobee watershed, however, taken month-by-month, the analysis is more complex. In both ENSO designations, neutral months and years look similar to each other (Figures 2-5a, 2-6a) in that they share a pattern marked by more outlier points. Compared to neutral years, El Niño years in the JMA and the M-ENSO (Figures 2-5c, 2-6c) exhibit higher stream flows with greater ranges from January to March, while the fall months are not as different from neutral conditions, as has been shown in south Florida already [*Schmidt et al.*, 2001]. Generally, while winter and fall precipitation is lower than summer precipitation on average, in El Niño years these seasons rainfall can double, resulting in higher stream flows.

In south Florida during La Niña conditions, January through March precipitation and flow tends to be significantly lessened [*Schmidt et al.*, 2001] compared to neutral or El Niño phases, which can be seen in Figures 2-5b and 2-6b. In comparing the JMA and

M-ENSO trends overall, the main difference is again in the La Niña phase, which, like precipitation, has June with a much larger range using the JMA index (Figures 2-5b, 2-6b). The sign of the average June anomaly also changes from positive in the JMA (Figure 2-5b) to negative in the M-ENSO (Figure 2-6b). Again, the finer temporal scale of the M-ENSO index may be better demonstrating south Florida's summer climate and hydrology patterns than the annual JMA.

### **Simulated Monthly P Concentration and ENSO Phase**

In the Lake Okeechobee watershed, concentrations of nutrients are based on both climate and land management factors, and we would not expect them to show ENSO trends as clearly as those in precipitation and stream flow. Depending on the lag from application of fertilizers to entering bodies of water, one could expect a month or two lag of peak concentrations behind months with maximum precipitation. A more detailed correlative lag analysis of different observed data is found in Chapter 3 and Appendix A.

In the analysis of simulated TP concentrations separated by month in the annual JMA ENSO designation (Figure 2-7), some patterns can be distinguished that are more similar to simulated stream flow patterns than precipitation patterns. Like precipitation and flow, TP concentration in neutral years tends to have more consistent, although wide, ranges with means closer to zero (Figure 2-7a). Concentrations in El Niño years mimic flow trends as well, with the anomalous high stream flow and precipitation in the winter months of January to March causing a corresponding possible wide range of positive concentration anomalies (Figure 2-7c). In La Niña years, the low January to March flow and precipitation causes corresponding negative concentration anomalies in the winter (Figure 2-7b). Comparatively, TP concentration separated by the monthly M-

ENSO index (Figure 2-8) shares the same general neutral, El Niño, and La Niña patterns. However, the finer M-ENSO scale creates a more distinct separation between the warm and cool phases. The ranges of P concentration in La Niña months have been restricted to a tighter and smaller band (Figure 2-8b). while the possibility of positive concentration anomalies in El Niño months has increased, with the ranges favoring the positive side, especially in March (Figure 2-8c). Like comparisons between the JMA and M-ENSO precipitation and stream flow series, the M-ENSO separation of P concentration also may demonstrate more accurate fine scale hydrological dynamics in south Florida, especially in wetter El Niño winter months and drier La Niña summers.

### **Simulated Monthly P Load and ENSO Phase**

Figure 2-2b shows the simulated monthly total P load anomalies, averaged across all reaches for all years and separated by ENSO phase. Trends in P loads mostly followed the precipitation trends shown in Figure 2-2a. Figure 2-2 suggests a strong El Niño association with peak loads in the winter months in Florida, and an even stronger association with peak loads in the summer of La Niña years. Error bars are not shown on this graph, as the small ENSO phase sample sizes make error bars large enough to obscure the visible patterns. Instead, the within-period variability is summarized in the statistics of Table 2-2 (by month) and Table 2-3 (by JMA and M-ENSO phase). The degrees of variability were analyzed relative to each other, to ascertain which months or ENSO phases were associated with extreme events in the available data.

The month with the largest variability (as determined by the standard deviation) in load anomalies was June (Table 2-2). September had the greatest range between maximum and minimum loads, and the outlier maximum September load is clearly visible (Figure 2-4a). The month with the smallest standard deviation was December.

While these results suggest that September and June conditions may be the most favorable for high nutrient loading, the large degree of variability of the data must be kept in mind. Conversely, the low variability associated with loads in December suggests that a nutrient load forecast in December of a La Niña year could be considered more reliable.

For both the JMA annual and M-ENSO monthly classifications, the El Niño and neutral phase summary statistics stayed virtually the same (Table 2-3). The largest difference between the monthly and annual ENSO indices was again seen in the La Niña phase. Using the JMA index, La Niña years have the largest standard deviation and range of the ENSO phases, as well as the absolute maximum load anomaly (Table 2-3). This suggests that despite the lower precipitation and stream flow inherent in La Niña years, there is still a large risk for P loading. When ENSO designation is examined by the M-ENSO index, however, La Niña months have by far the lowest standard deviation, range, and mean, as well as the absolute minimum anomaly when compared to the other phases (Table 2-3), which makes more physical sense with what is known about the decreased rainfall and stream flow during La Niña years, and corresponds with research using the M-ENSO classification [*Gérard-Marchant et al.*, 2008].

Figures 2-9 and 2-10 show monthly total P load anomalies averaged across all reaches, and present P load averaged monthly and separated by JMA and M-ENSO phase. Using the JMA index, El Niño years (Figure 2-9c) exhibited more variability and a larger range, while La Niña (Figure 2-9b) and neutral years (Figure 2-9a) had more consistent patterns. The most visible peak load trend occurred in June of La Niña years.

Figure 2-9b shows the large range of P load anomalies in June in JMA La Niña years, which is quite different from neutral and El Niño years, and is similar to trends seen in precipitation, stream flow, and concentration. Major differences between El Niño and La Niña years were again apparent in the larger loads during January to March in El Niño years, and the larger loads in May-July of La Niña years. P load anomalies that were below average in the summer were of similar magnitude in both El Niño and La Niña events, despite large differences in nutrient runoff. These patterns are similar to those found in precipitation and stream flow analyses previously performed in south Florida [Schmidt *et al.*, 2001]. Like the other hydrological variables examined, when P load is separated by the M-ENSO index rather than the JMA annual index, neutral phases look mostly the same (Figure 2-10a), with M-ENSO showing larger loads from January to March of El Niño months (Figure 2-10c), and smaller loads in June through August of El Niño months (Figure 2-10c) and June and July of La Niña months (Figure 2-10b).

### **Simulated Seasonal P Load, Concentration, Stream flow, and JMA ENSO Phase**

Simulations showed that El Niño and La Niña years generally exhibited greater nutrient load range and variability, while neutral years stayed closer to average (Figure 2-11). El Niño years tended to produce greater P load runoff in spring (February-April). La Niña years tended to have larger P loads in the summer (May-July), but the variability was quite large, as indicated by the very strong seasonal signal. Simulated seasonal groupings of nutrient loading temporally match with seasonal simulated stream flow (Figure 2-12) and concentration (Figure 2-13) time series. Seasons with positive flow anomalies and wide ranges of stream flow and P concentrations seem to match with positive P load anomalies and wide ranges of values, such as February to

April (FMA) El Niño flow and concentration (Figure 2-12a and 2-13a) as compared to FMA El Niño P load (Figure 2-11a). Simulated nutrient loading in south Florida is very similar to observed precipitation and stream flow in different ENSO phases. The greatest increases in flow may cause an increased flush of nutrients, increasing P concentration and consequently nutrient load, compared to neutral conditions that occurred in El Niño winter and spring, while only winter precipitation was significantly depressed in La Niña years. As in the literature, during the other seasons, levels were lower than average, but not significant [*Schmidt et al.*, 2001].

Seasonal nutrient loads were analyzed both in box plots and in contingency table significance testing. Table 2-4 summarizes which tercile was dominant in which season, and to what percentage significance level the actual P load for a given season and JMA ENSO phase differed from random chance as calculated (Equation 2-1) with the relevant input parameters. Only one tercile is listed per season, as Fisher's exact test results conveniently had only one tercile significant above 95% in each season and phase. In El Niño years from August-October, no tercile dominated, that is, all were equally likely. Figures 2-11a through 2-11d, which help visualize the tendency of low, typical, and high load anomalies, show the normalized total P load averaged across all reaches, grouped by season and ENSO phase. The potential P runoff or negative load anomaly in each ENSO phase varied widely by season.

The use of “terciles” has been criticized widely in research as being a physically meaningless metric, as the designation of thirds is only relevant to itself. A possible solution to this issue is to use the same contingency table methodology with P limits as defined by BMAP's or TMDL's for basin S-191. The FL DEP has created a BMAP for

basin S-191 that designates a TP concentration limit of 0.18 mg/L and 91,300 kg/year. However, when examined either monthly or seasonally, there were never enough months that were below the 0.18 mg/L limit to be statistically significant at any level. In fact, there were never any springs, summers, or fall seasons below the limit in any of the ENSO phases, and only 4 out of 17 were below the limit during the winter (NDJ) season of both La Niña and Neutral years, making this relatively useless as a management tool to learn which seasons have relatively more risk than others.

When the TP concentration limit is increased to just 0.22 mg/L (merely as an investigatory measure), (Table 2-5), one can better assign some meaning to the temporal analysis of P load risk in different climatic regimes. Since the tables display results for P load and concentration, they are not directly comparable, however, interestingly, the NDJ winter season in all JMA ENSO phases showed a significant chance of being under a 0.22 mg/L P concentration limit, as did the FMA spring season in La Niña years (Table 2-5). All other seasons and ENSO phases did not have a significant chance of being under the P concentration limit.

### **February-March-April**

Positive P load anomalies from February to April (Figure 2-11a) were overwhelmingly associated with El Niño years, which are characterized by higher than normal precipitation, whereas La Niña years showed negative P load anomalies and a tight range. Neutral year anomalies in the February-April season remained centered around zero, as expected, although several large outliers were noted. Both flow and concentration anomalies had the largest ranges in El Niño years as well (Figures 2-12a and 2-13a), implying the possibility of very variable conditions, although their median values were centered on zero or negative anomalies. P Load contingency analysis

(Table 2-4) was consistent with the trend seen in Figure 2-11a, with the highest load tercile being dominant and significant at the 99% level during El Niño years compared to the chance of observing that result generated from a random sample of the underlying population, and low loads dominating during both La Niña and neutral phases. Concentration contingency analysis (Table 2-5) with a 0.22 mg/L investigatory concentration limit showed that only during La Niña years was there a significant chance of coming in under the limit in the FMA season, corresponding with the dominance of T1 during La Niña years. These results are consistent with other analyses of seasonal trends in south Florida, wherein winter precipitation and ENSO phase are strongly linked, and weather stations in south Florida experienced as much as 50% to 150% more rain than typical [*Schmidt et al.*, 2001]. In this case, total average February-April nutrient load in El Niño years was 119% greater than in neutral years and 156% greater than La Niña years.

### **May-June-July**

Conversely, the May-July season (Figures 2-11b, 2-12b, 2-13b) had maximum P load, flow, and P concentration anomalies in La Niña years, with a maximum load surpassing that of any El Niño event. The range of P load, flow, and concentration anomalies in La Niña years was also large, indicating a high degree of variability in May-July loads, which is also consistent with precipitation trends in the present study and in Schmidt et al. (2001). The trends seen (Figure 2-11b) are again consistent with load contingency table analysis (Table 2-4), with the high load tercile significant at the 99% level in La Niña years, and the low load tercile significant at the 99% level during both El Niño and neutral years. El Niño years were associated with negative P load anomalies, and neutral years were centered on zero (Figure 2-11b). May-July total

average P loads were 132% greater in La Niña years than in neutral years and 147% greater than El Niño years. Contingency analysis using the theoretical 0.22 mg/L concentration limit (Table 2-5) showed that there was no significant chance of being under the limit in any of the ENSO phases during the May to July season, even though the load contingency table suggested that relatively lower loads (by tercile) were possible in El Niño and Neutral years. This contradiction shows the relative strength of each method of statistical contingency table analysis (tercile or practical policy based), and that nutrient risk assessment in the summer season of La Niña months or years should be a priority.

### **August-September-October**

August-October is the season with the lowest precipitation in Florida, and this is reflected in the resulting low P load anomalies across all ENSO phases (Figure 2-11c). The low P loads may be due to heavy rains in the previous season having removed much of the soluble P. There was a slight visible trend that La Niña years had a greater negative load than the other ENSO phases and slightly more variability and average higher load in El Niño years. Neutral year total average P load anomaly was 120% greater than El Niño years and 260% greater than La Niña years. Phosphorus concentration (Figure 2-13c) and stream flow (Figure 2-12c) during the fall season were more variable than P load, however still had negative anomaly median values in El Niño and La Niña phases. Load contingency table analysis (Table 2-4) did not identify any tercile as dominant over any other to a significant extent during El Niño years, although it did show that the low tercile was significant at the 99% level during La Niña and the high tercile was significant at the 99% level during neutral years. Concentration contingency analysis did not identify any ENSO phase as having a significant probability

of being under the investigatory 0.22 mg/L TP limit (Table 2-5), meaning that the fall season has a significant possibility of exceeding concentration regulations during all ENSO regimes.

### **November-December-January**

November-January showed a potential for higher P load (Figure 2-11d) and flow (Figure 2-12d) in both El Niño and neutral years, while La Niña years demonstrated more negative load and flow anomalies with a tight range and small variability. These findings are consistent with those of Schmidt et al. (2001); 57% of weather stations in Florida received significantly greater precipitation in November-January of El Niño years than in neutral years, and 65% received significantly less precipitation during La Niña events. Total November-January season nutrient load anomalies averaged 85% greater in El Niño years than neutral years, and 200% greater than La Niña years. Load contingency table analysis (Table 2-4) found that the mid tercile was significant at the 99% level during El Niño years compared to random chance, indicating slightly above average nutrient loading. Looking further into the contingency data analysis, there were zero events tabulated in the lowest load tercile for this season in El Niño years, indicating that, while not overwhelming, the nutrient runoff was consistently higher than average. La Niña and neutral years also had significant mid load terciles and zero events tabulated in the low load tercile, which may suggest that the November-January season is of slightly higher nutrient loading risk for all ENSO phases. This is in contradiction to the concentration contingency table results (Table 2-5) that consistently shows that across all ENSO phases, winter is the only season that has a significant probability of meeting a concentration upper limit of 0.22 mg/L. When concentration is combined with flow data to get nutrient load values, there is a possibility of higher loads

than desirable. Risk assessment using both standard load and concentration based policies is made complex by these dynamics.

### **M-ENSO Statistics (ANOVA) of Monthly Precipitation, Flow, P Concentration and Load**

In single-factor ANOVA analysis performed at the  $p = 0.05$  level for all variables using the monthly M-ENSO classification system, analysis was first performed with all ENSO phases to identify if there were any differences in the variables, i.e., if  $\mu_{\text{Niño}} = \mu_{\text{Niña}} = \mu_{\text{Neutral}}$ . ANOVA identified that there was a significant difference in the three-way means for all variables tested: precipitation, stream flow, P concentration and P load. To specifically identify which pairs of ENSO phases encompassed significant differences for each variable, single-factor ANOVA was repeated for each combination of ENSO phases: El Niño and Neutral, La Niña and Neutral, and El Niño and La Niña (Table 2-6).

Results showed that while no differences significant at  $p = 0.05$  were found between El Niño and Neutral phases, all variables were significantly different between La Niña and Neutral phases. Finally, all variables except for precipitation were also found to be significantly different from each other between El Niño and La Niña phases. This suggests that using the M-ENSO index can in fact find statistical differences between phases that the JMA index could not, and that the major differences between ENSO phases are based upon La Niña months being more different from the other two phases in south Florida. Accordingly, in all the plots and statistics in this research, neutral and El Niño patterns on a whole tend to be more similar to each other than they are to La Niña patterns. Taken as a whole, however, the contingency table analysis and box plots by month and season provide much more information about the timing of loads than the fact that phases are significantly different from each other do. As this

pertains to nutrient risk management in the southeast, La Niña months and years have consistently been identified in this research as having more potential for high summer loads, perhaps suggesting that BMP's that concentrate on summer month load reductions should be a research target.

### **Summary and Discussion**

In Chapter 2, the relationships between two different discrete classifications of ENSO phase, the annual JMA and the new monthly M-ENSO indices, and simulated P loads for a fixed pattern of land use and management in basin S-191 of the Lake Okeechobee watershed are explored. Some ENSO phases tended to produce significantly greater seasonal P loads (February-April of El Niño years, May-July of La Niña years, and August-September of neutral years) or lower seasonal P loads (May-July of El Niño years, February-April and August-September of La Niña years, and February-April and May-July of neutral years). The greater P load potential in certain months was mostly consistent with documented trends in greater precipitation. The determination that ENSO phase was significantly related to P loads suggests the need for future study on use of short-term climate forecasts of ENSO phase to help guide management efforts to minimize nutrient loading not only into Lake Okeechobee but in any area in the southeast similarly affected by ENSO phase. While this study does not provide an accurate simulation of historical nutrient loads in S-191, it is a valid indicator of relationships that can be expected in the southeast United States between ENSO phase and P load.

The comparison between a monthly M-ENSO index and the annual JMA index suggested across P load, concentration, stream flow, and precipitation, that the M-ENSO classification reduces both the range and average of the La Niña summer

months. Consequently, this monthly classification which is more representative of current SST conditions instead of those of the previous October has a more accurate temporal scale that suggests that the previous months (October to April) of an annual JMA La Niña may be erroneously creating patterns in the summer months. Additionally, this finer monthly ENSO scale used to classify even simulated data shows that more accurate local patterns may be discovered using even more temporally downscaled ENSO indices, such as a continuous record of the NIÑO 3.4 temperatures themselves (see Appendix A).

Large flow and nutrient flushes generally followed prolonged periods of lack of precipitation or negative loads. For example, El Niño summers are generally drier than average, producing a nutrient flush during the rainy winters with high stream flows. On the other hand, La Niña winters are generally drier, producing a nutrient flush in the summer. The relationship between previous precipitation and the P load in the following months could be a strong one and is investigated using non-simulated nutrient data in correlation analyses in Chapter 3. Neutral years, which have less consistent trends, showed a smaller range about the normalized average, and more load variability in both summer and winter. Several of the maximum P loads, concentrations, and flows seen, especially during neutral events, could be explained by looking at historical hurricanes affecting Florida. In looking at hurricanes that affected Florida in the past 40 years, there was a relationship between months that hurricanes and peak P loads occurred. The possibility that hurricanes could explain the outlier points and variability seen in several of the neutral year box plots is an interesting question possibility.

Land and water managers can use these data to help make decisions about how to reduce nutrient load runoff in predicted ENSO conditions. Because certain ENSO phases correlate more strongly with increased P runoff in different seasons, the contingency table data could help meet nutrient load limits set by TMDL's, BMAP's, and Florida BMP's. The combination of the relative load based seasonal probabilities using terciles, and the concentration limit contingency tables could be a powerful tool, allowing farmers and other stakeholders to identify particularly risky months for either high P loads or concentrations. The relative load tercile probabilities indicate that the seasons of highest P loading risk include La Niña from May to July and El Niño from February to April, as previously indicated. However, from a policy viewpoint, the November to December season is the only one across all ENSO phases that is close to meeting current BMAP standards. From a land management perspective, this may mean that under realistic conditions (where changing land use is also a factor), the current restoration plans for the Lake Okeechobee watershed area, especially S-191 are not sufficient to meet stated concentration and load goals, and that the winter season may be a good time for BMP staging so that summer loads across all ENSO phases can be reduced.

Focusing on changing land use and BMP effectiveness in different ENSO phases in this area are both questions that are addressed in Chapter 3, to help researchers and stakeholders in making specific management decisions. In the Florida Everglades area specifically, restoration processes focus on allocating the correct quantity and quality of water at the correct time. Knowing that temporally coarse categorical ENSO based climate variability does allow classification and quantification of significant differences in

nutrient loads and local hydrological variables provides a basis for finding a more accurate method of predicting loads from actual sea surface temperature time series in Chapter 5.

Table 2-1. Example of a  $3 \times 2$  contingency table used for verification of a binary forecast within an El Niño ENSO phase. In this table,  $n$  is the total number of years;  $r$  is the number of El Niño, La Niña, or neutral years;  $x$  is the number of T1 events within a specific season and ENSO phase out of  $b$  total T1 events in all seasons within that ENSO phase; and  $y$  is the number of T3 events within a specific season and ENSO phase out of  $a$  total T3 events in all seasons within that ENSO phase.

Tercile	El Niño Years		Total
	Yes	No	
T1	$x$	$b-x$	$b$
T2	$r-x-y$	$n-r-b-a+x+y$	$n-b-a$
T3	$y$	$a-y$	$a$
Total	$r$	$n-r$	$n$

Table 2-2. Total P load (kg) anomaly summary statistics separated by month. Numbers in bold type are the largest and smallest values in each column. All statistics represent anomaly values, except for means.

Event	Std. Dev.	Max.	Min.	Range	Mean <sup>[a]</sup>
January	147	483	-75	558	77
February	291	1479	-103	1582	106
March	245	725	-165	890	168
April	124	<b>390</b>	-76	<b>466</b>	80
May	252	1011	-139	1150	143
June	<b>572</b>	1591	<b>-561</b>	2153	<b>570</b>
July	397	937	-459	1396	474
August	377	878	-469	1346	484
September	489	<b>2467</b>	-447	<b>2914</b>	461
October	510	1732	-358	2090	362
November	285	1110	-133	1243	139
December	<b>108</b>	440	<b>-43</b>	483	<b>48</b>

<sup>[a]</sup> Non-normalized.

Table 2-3. Total P load (kg) anomaly summary statistics separated by JMA and M-ENSO phase. All statistics represent anomaly values, except for means.

	JMA Index			M-ENSO Index		
	El Niño	La Niña	Neutral	El Niño	La Niña	Neutral
Std. Dev.	350	342	346	330	235	382
Maximum	1479	1591	2467	1479	1071	2467
Minimum	-561	-557	-546	-561	-551	1622
Range	2041	2149	3013	2041	1622	3024
Mean <sup>[a]</sup>	263	245	263	287	143	297

<sup>[a]</sup> Non-normalized.

Table 2-4. Seasonal contingency table significance level (compared to random chance) results for P loads for each JMA ENSO phase. Terciles are low (T1), mid (T2), and high (T3). This table represents the results from 12 computed contingency tables.

Season	El Niño		La Niña		Neutral	
	Sig. <sup>[a]</sup>	Tercile	Sig. <sup>[a]</sup>	Tercile	Sig. <sup>[a]</sup>	Tercile
Feb-Apr	99	T3	99	T1	95	T1
May-July	95	T1	99	T3	99	T1
Aug-Oct	--	--	99	T1	99	T3
Nov-Jan	99	T2	95	T2	99	T2

<sup>[a]</sup> Sig. = significance level (%).

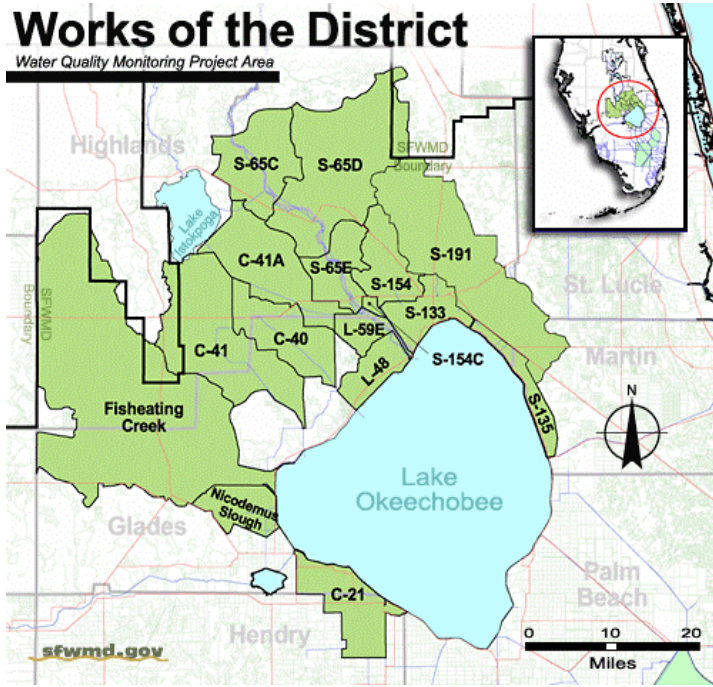
Table 2-5. Seasonal contingency table significance level (compared to random chance) results for P concentrations for each ENSO phase by chance of being under or over a 0.22 mg/L limit in S-191. This table represents the results from 12 computed contingency tables.

Season	El Niño		La Niña		Neutral	
	Sig. <sup>[a]</sup>	<0.22mg/L	Sig. <sup>[a]</sup>	<0.22mg/L	Sig. <sup>[a]</sup>	<0.22mg/L
Feb-Apr	-	Over	99	Under	-	Over
May-July	-	Over	-	Over	-	Over
Aug-Oct	-	Over	-	Over	-	Over
Nov-Jan	90	Under	99	Under	99	Under

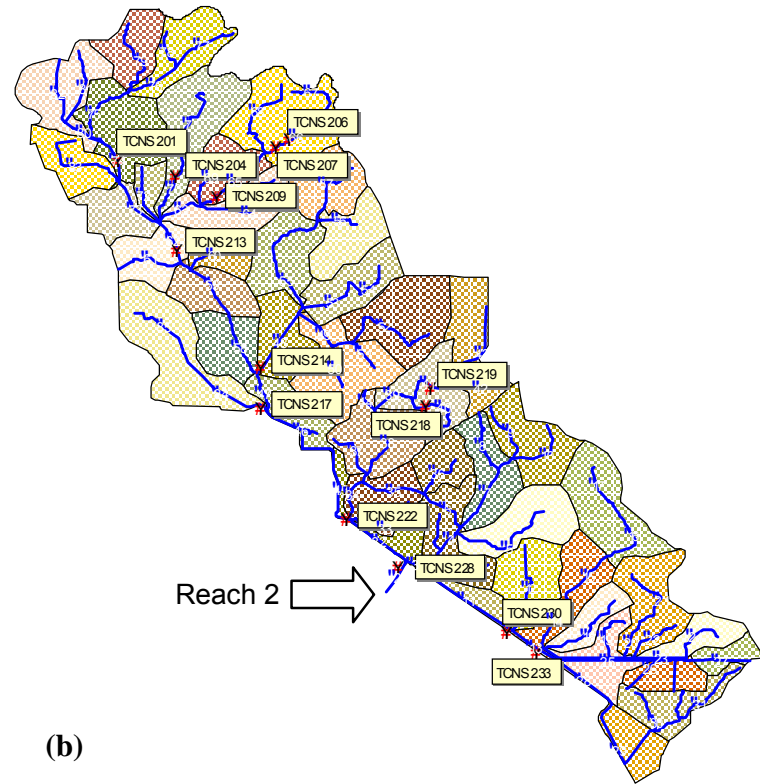
<sup>[a]</sup> Sig. = significance level (%).

Table 2-6. Single factor ANOVA results between M-ENSO phases ( $p = 0.05$ ).  $H_0 : \mu_1 = \mu_2$ , and  $H_A : \mu_1 \neq \mu_2$ . Variables that were found to be significantly different are highlighted in bold text.

Variable	El Niño/Neutral Accept $H_0$ ?	La Niña/Neutral Accept $H_0$ ?	El Niño/La Niña Accept $H_0$ ?
Precipitation	Yes	<b>No</b>	Yes
Flow	Yes	<b>No</b>	<b>No</b>
P (mg/L)	Yes	<b>No</b>	<b>No</b>
P (kg)	Yes	<b>No</b>	<b>No</b>



(a)



(b)

Figure 2-1. (a) Location of Lake Okeechobee, basin S-191, and the surrounding basins (from the South Florida Water Management District), and (b) weather and water quality stations in S-191. Precipitation was spatially averaged over all stations in the basin.

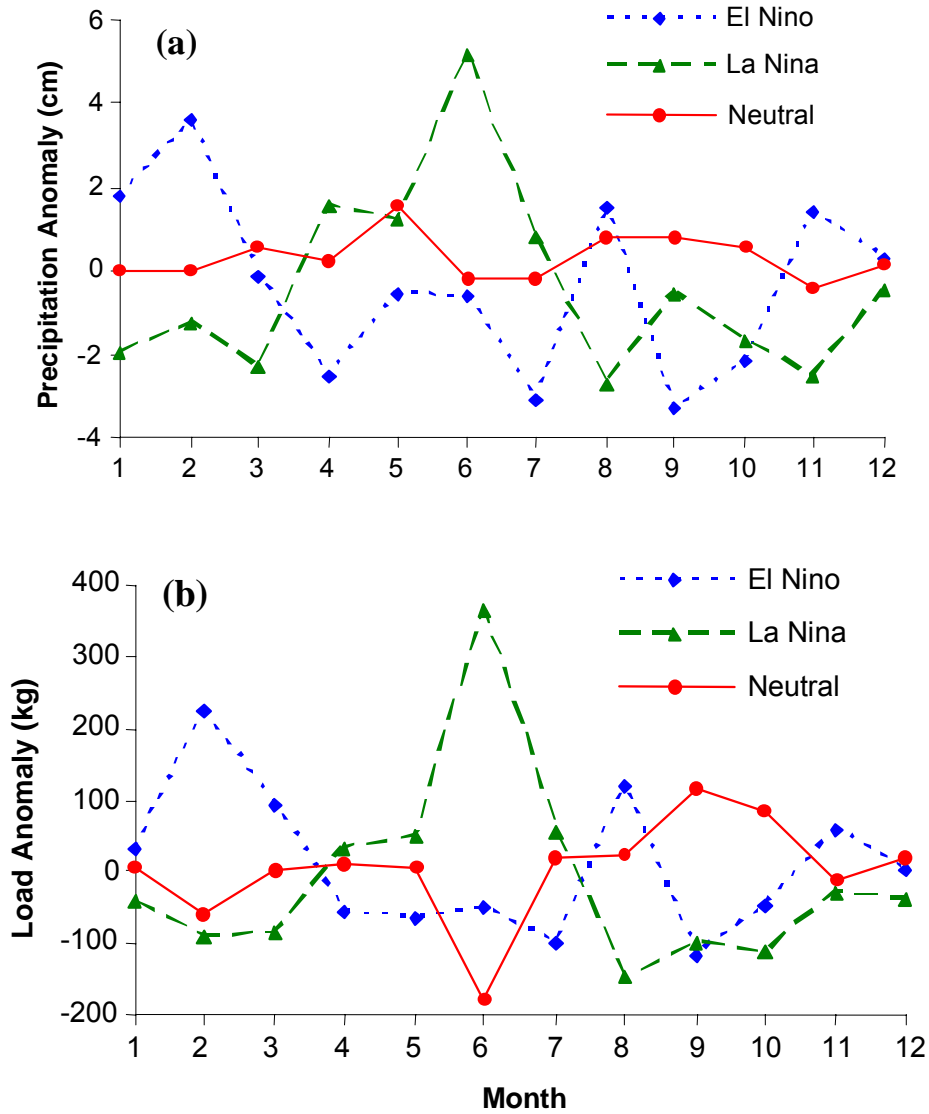


Figure 2-2. Monthly total (a) precipitation (cm) and (b) simulated P load ( $\text{kg month}^{-1}$ ) anomalies, averaged over all reaches, for each ENSO phase (1965-2001). Month 1= January to month 12= December.

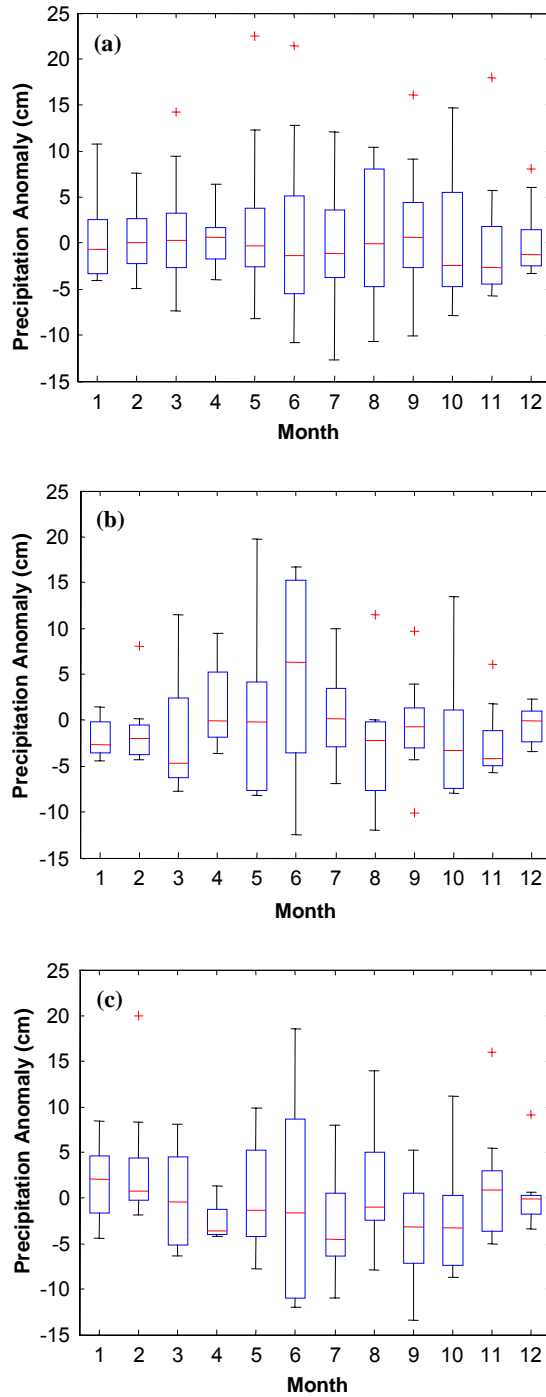


Figure 2-3. Box and whisker plots of observed precipitation anomalies (cm) for JMA (a) neutral years, (b) La Niña years, and (c) El Niño years. Box lines are at the lower quartile, median, and upper quartile values. In all boxplots, whiskers extend from box ends to upper and lower adjacent values, defined as the largest or smallest observation that does not exceed the upper or lower quartile  $\pm 1.5 \times$  interquartile range. Outlier points indicate data that fall outside the whiskers, and are indicated by crosses.

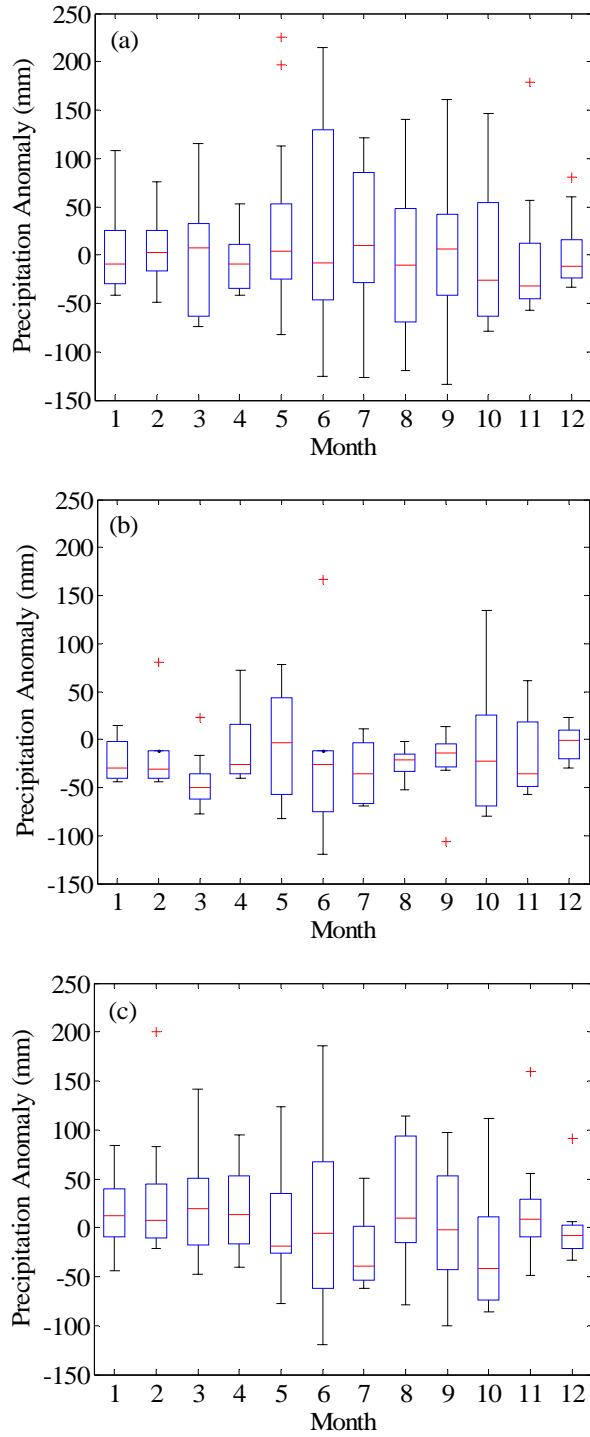


Figure 2-4. Box and whisker plots of observed precipitation anomalies (mm) for M-ENSO (a) neutral months, (b) La Niña months, and (c) El Niño months. Box lines are at the lower quartile, median, and upper quartile values.

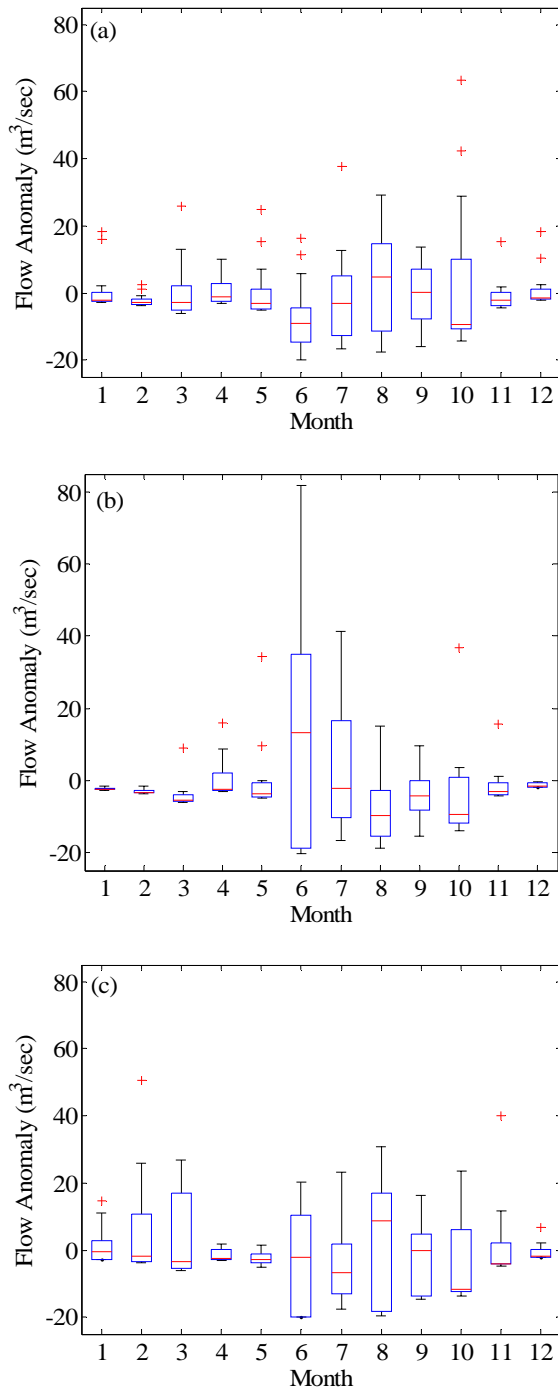


Figure 2-5. Box and whisker plots of simulated monthly stream flow anomalies ( $\text{m}^3/\text{sec}$ ) for JMA (a) neutral years, (b) La Niña years, and (c) El Niño years. Box lines are at the lower quartile, median and upper quartile values.

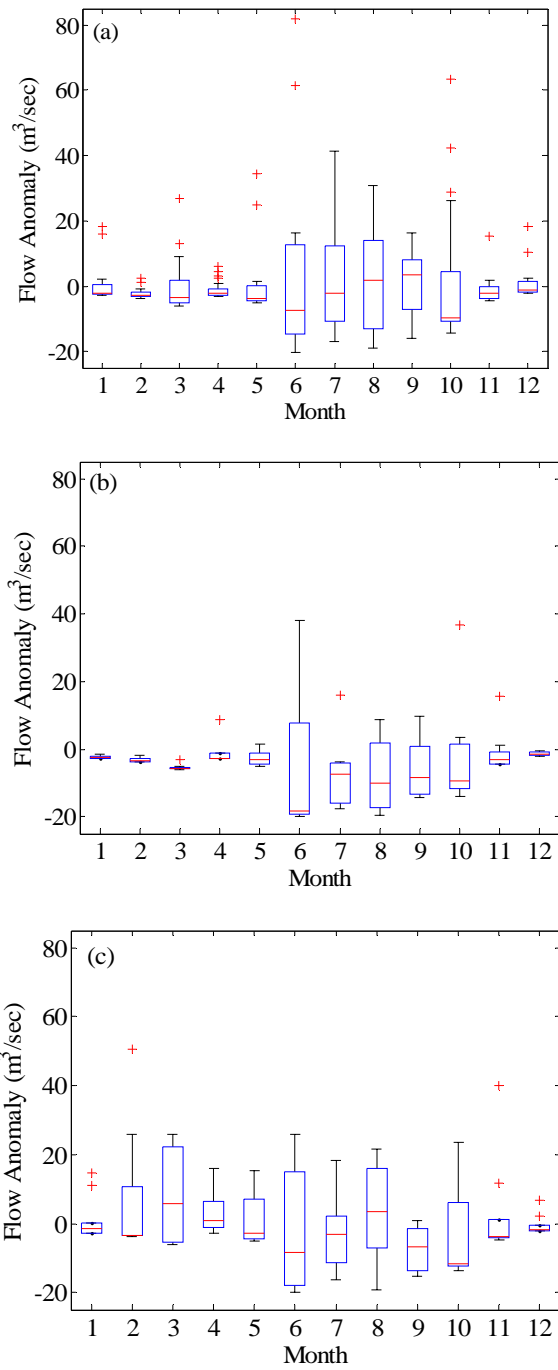


Figure 2-6. Box and whisker plots of simulated monthly stream flow anomalies ( $\text{m}^3/\text{sec}$ ) for M-ENSO (a) neutral months, (b) La Niña months, and (c) El Niño months. Box lines are at the lower quartile, median and upper quartile values.

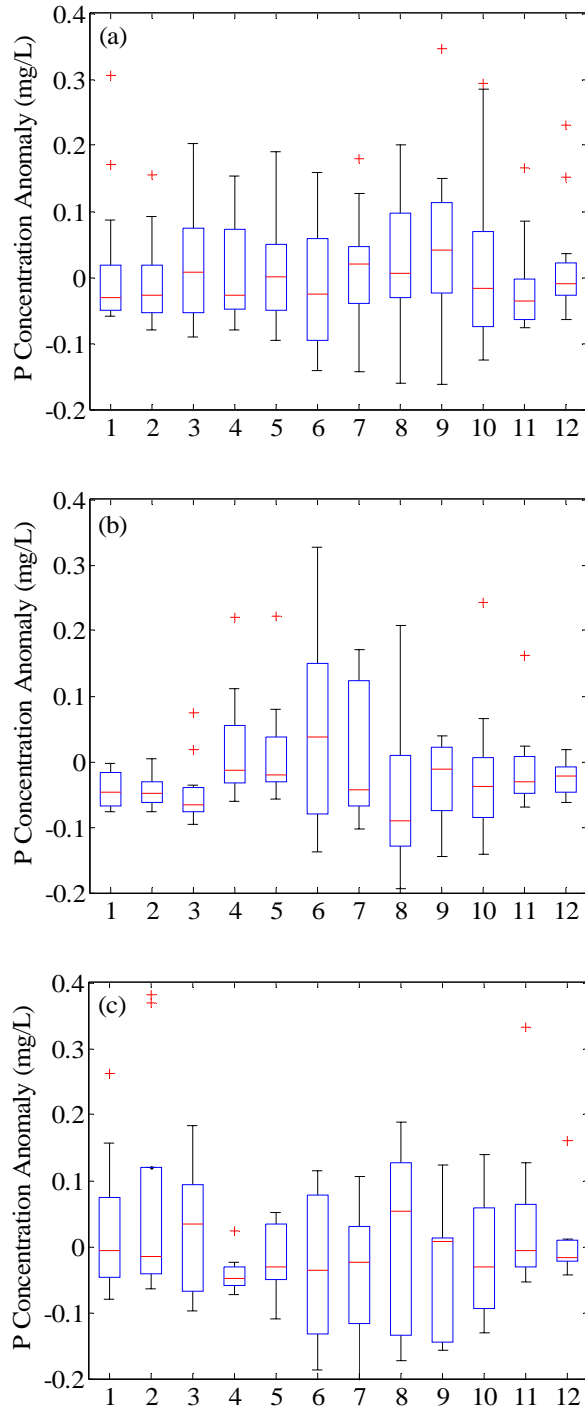


Figure 2-7. Box and whisker plots of simulated TP concentration anomalies (mg/L) for JMA (a) neutral years, (b) La Niña years, and (c) El Niño years. Box lines are at the lower quartile, median, and upper quartile values.

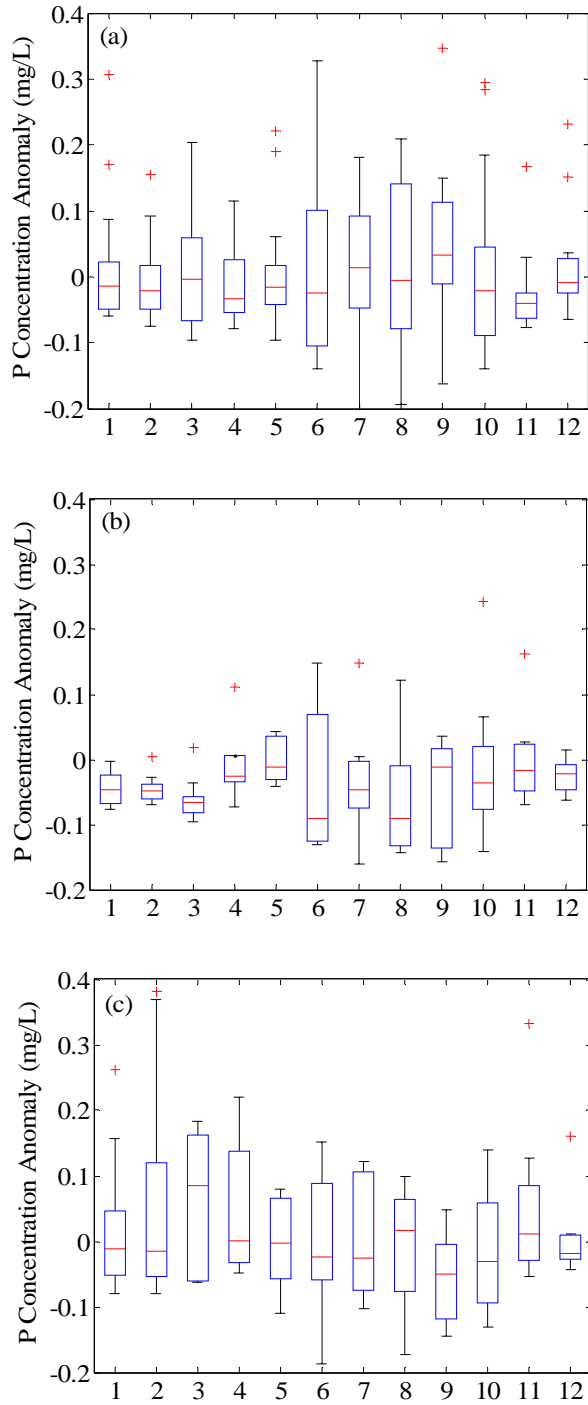


Figure 2-8. Box and whisker plots of simulated TP concentration anomalies (mg/L) for M-ENSO (a) neutral months, (b) La Niña months, and (c) El Niño months. Box lines are at the lower quartile, median and upper quartile values.

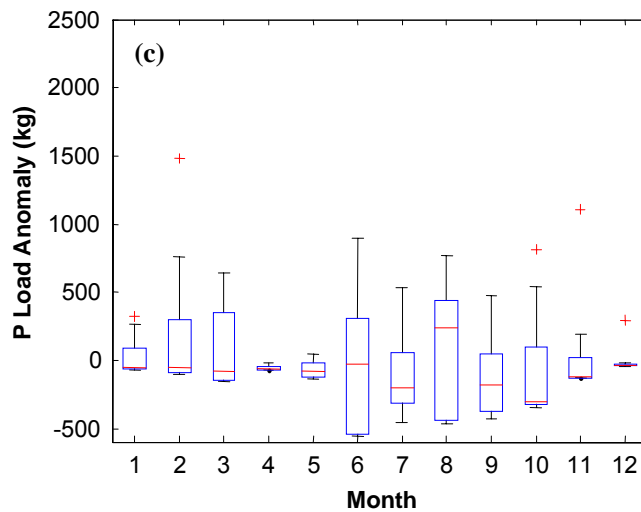
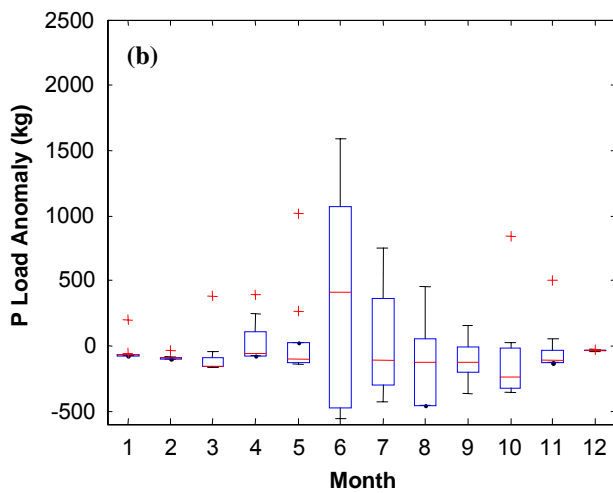
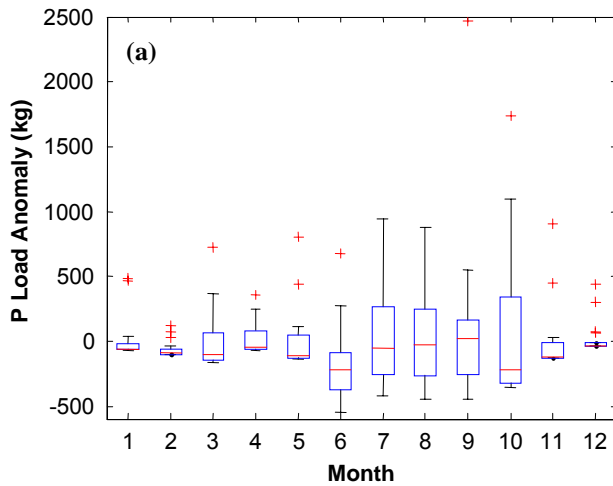


Figure 2-9. Box and whisker plots of monthly P load anomalies (kg) for JMA (a) neutral years, (b) La Niña years, and (c) El Niño years.

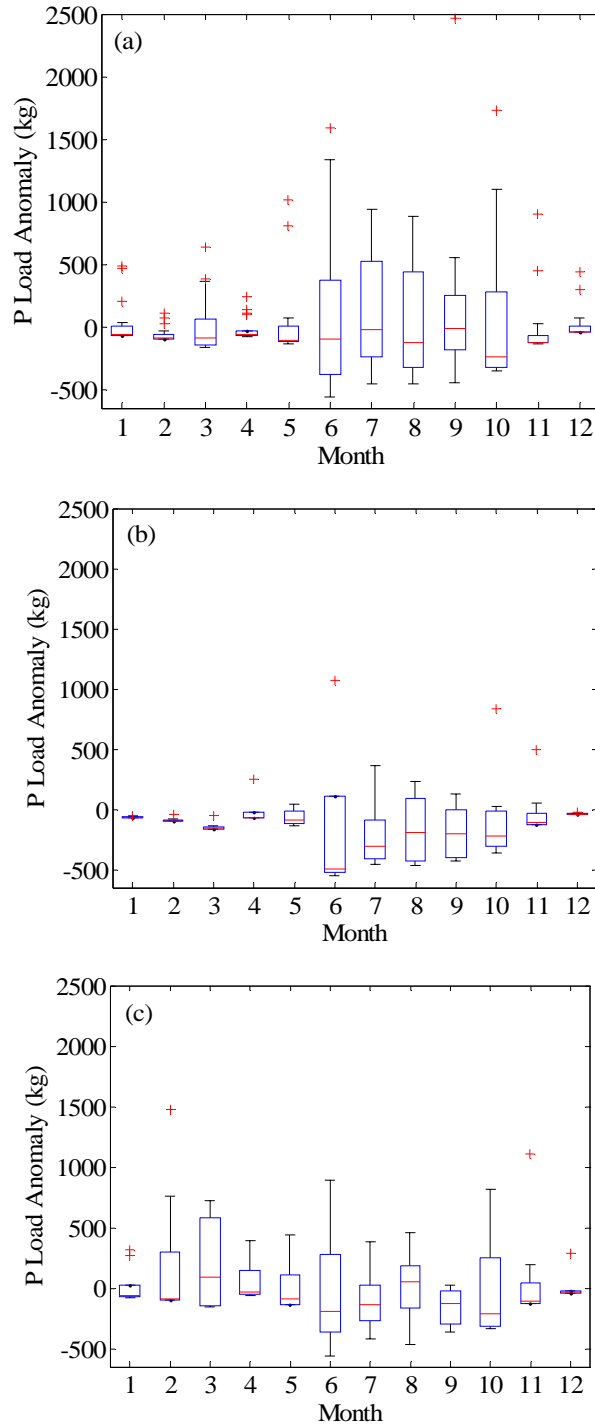


Figure 2-10. Box and whisker plots of monthly P load anomalies (kg) for M-ENSO (a) neutral years, (b) La Niña years, and (c) El Niño years.

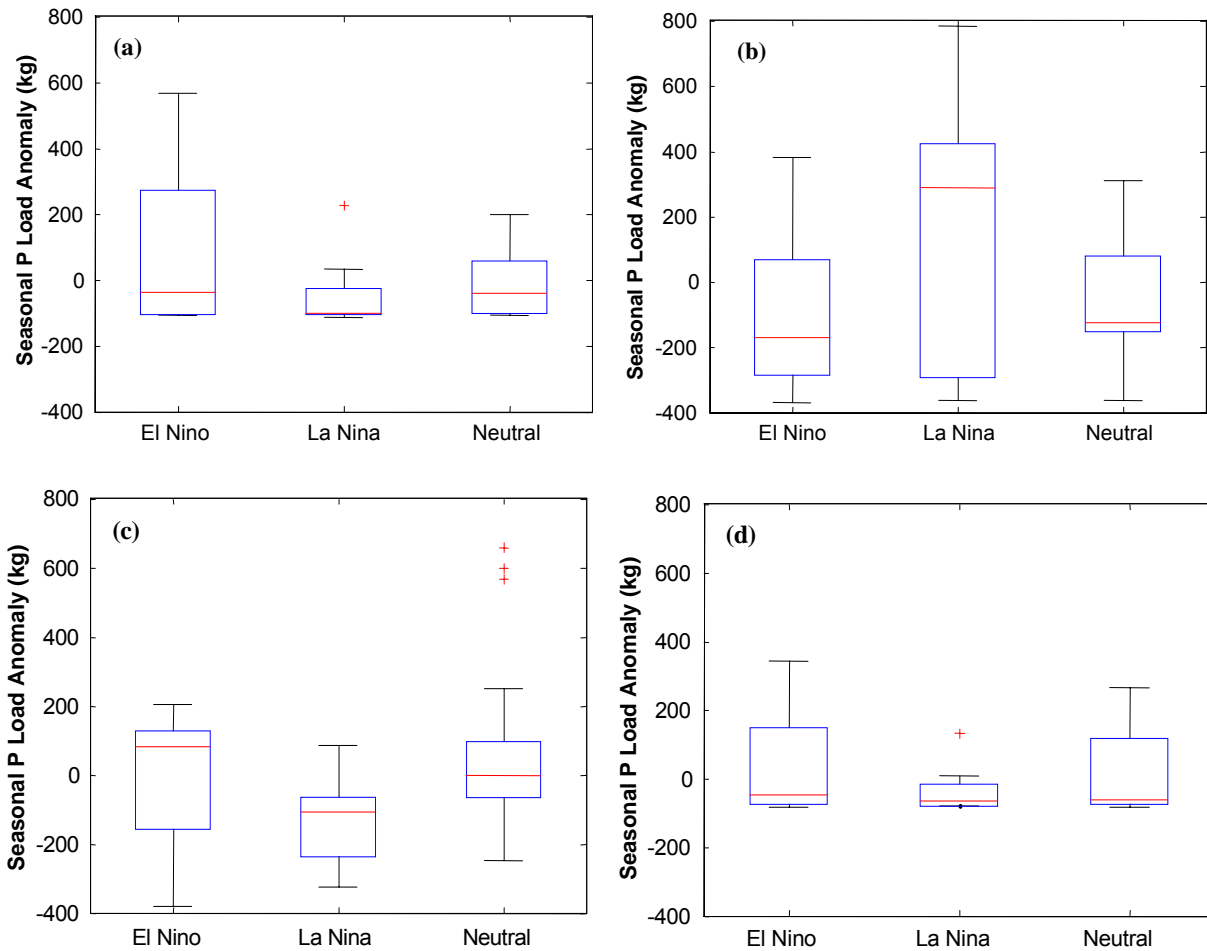


Figure 2-11. Seasonal P load anomaly box plots separated by JMA ENSO phase: (a) February-April, (b) May-July, (c) August-October, and (d) November-January. Box lines are at the lower quartile, median, and upper quartile values. In all boxplots, whiskers extend from box ends to upper and lower adjacent values, defined as the largest or smallest observation that does not exceed the upper or lower quartile  $\pm 1.5 \times$  interquartile range. Outlier points indicate data that fall outside the whiskers, and are indicated by crosses.

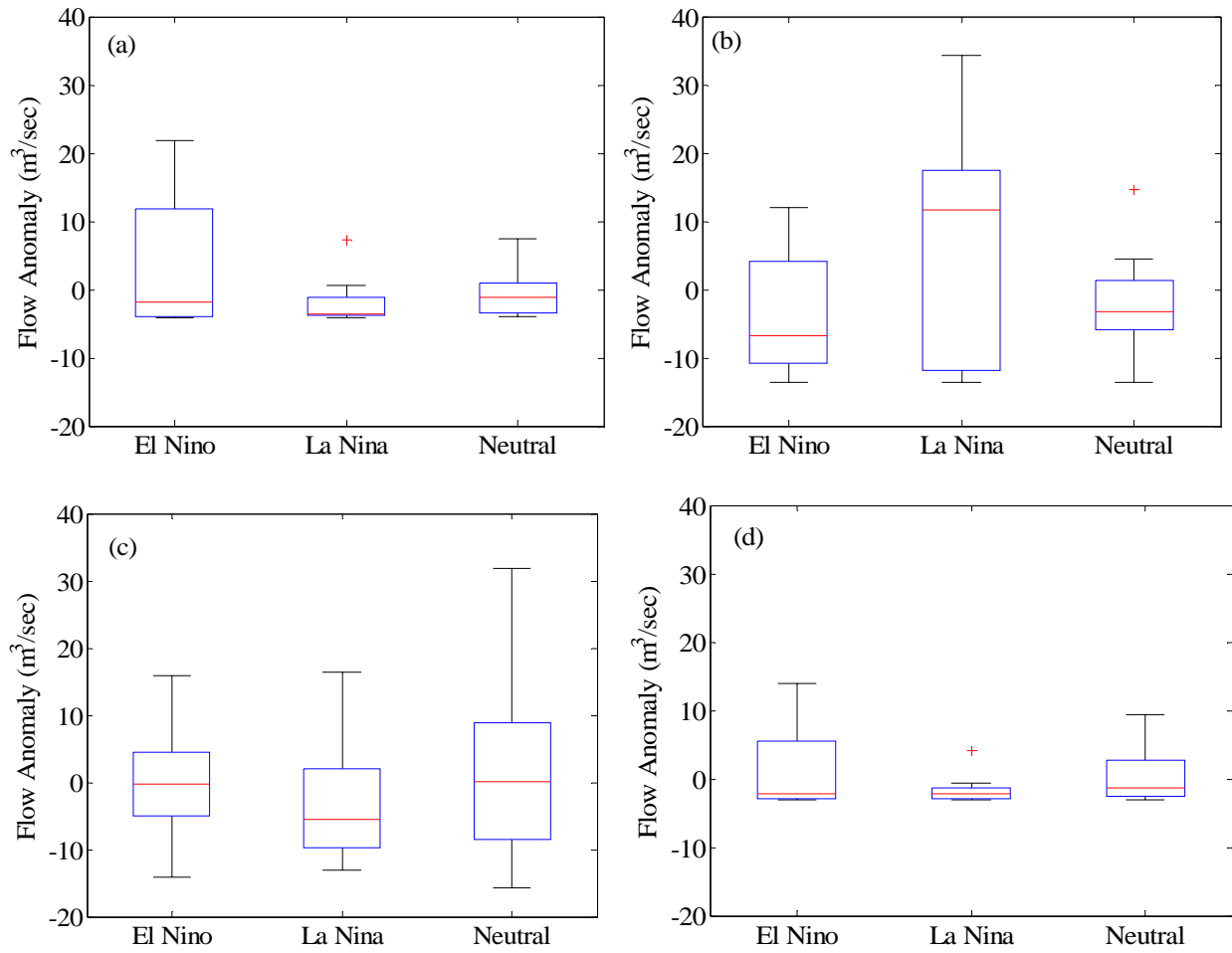


Figure 2-12. Seasonal stream flow anomaly box plots separated by JMA ENSO phase: (a) February-April, (b) May-July, (c) August-October, and (d) November-January.

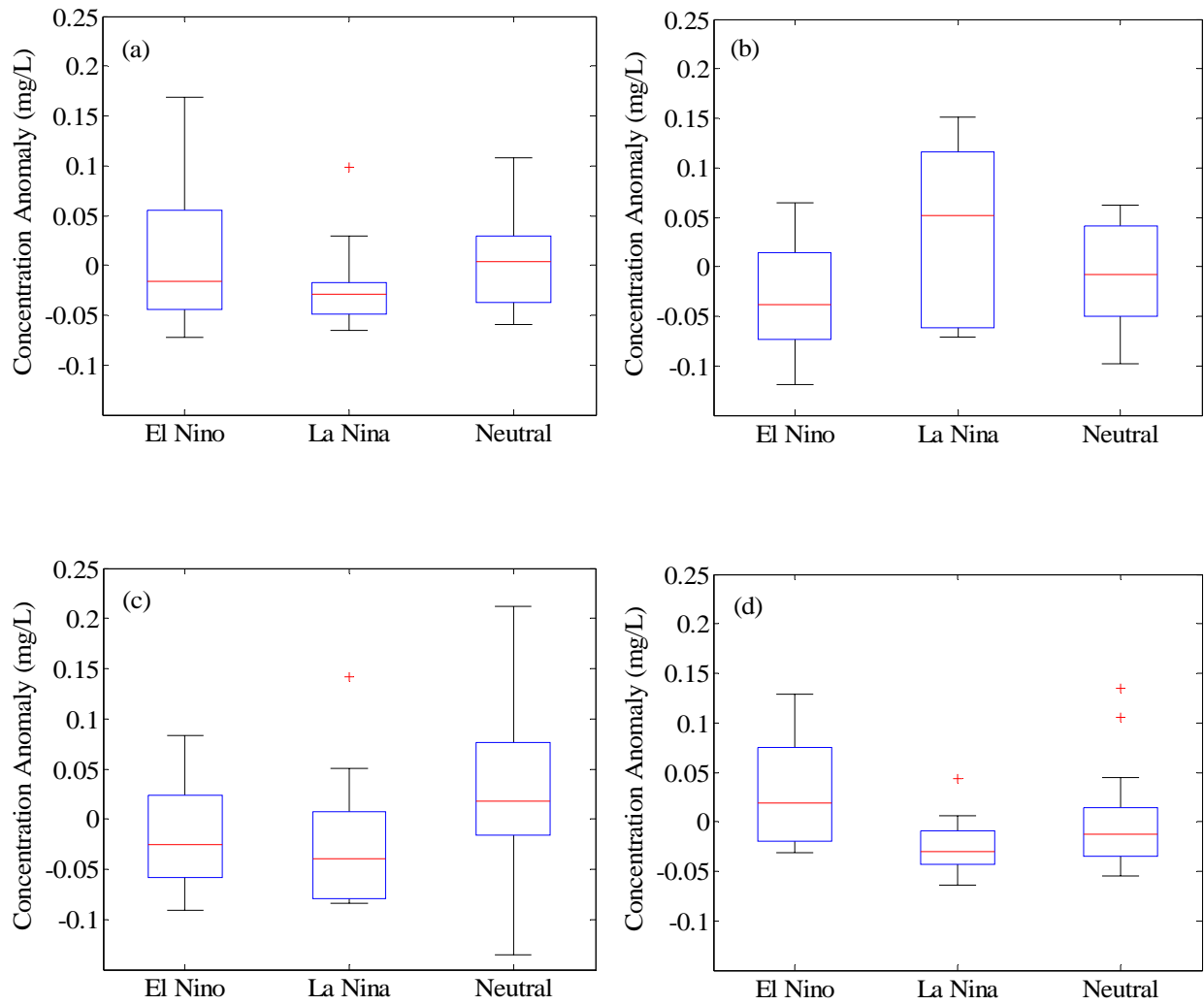


Figure 2-13. Seasonal TP concentration anomaly box plots separated by JMA ENSO phase: (a) February-April, (b) May-July, (c) August-October, and (d) November-January.

CHAPTER 3  
EL-NIÑO/SOUTHERN OSCILLATION (ENSO) INFLUENCES ON MONTHLY NO<sub>3</sub>  
LOAD AND CONCENTRATION, STREAM FLOW AND PRECIPITATION IN THE  
LITTLE RIVER WATERSHED, TIFTON, GEORGIA.

**Introduction**

In Chapter 2, we used model simulations of hydrological and nutrient data to investigate ENSO related climate variability. The categorical ENSO classifications, however, while they were able to find significant differences in phase, were not on a scale fine enough to capture the inherent variability and dynamics of the hydrology. Additionally, the goal of creating a predictive model for nutrient loads based on ENSO indices would not be as accurate using categorical labels. Chapter 3 explores the relationship of continuous measures of ENSO variability with hydrologic data observed over the last 35 years. Climate variability and change are areas of high priority research both locally and globally. Recent research has shown that extremes of climate such as heat waves, droughts, floods and tropical cyclones may be becoming more common [IPCC, 2007]. Climate variability directly affects a range of hydrological variables, such as precipitation and water quantity. By extension, climate variability also may affect water quality as seen in pollutants, although these concerns are often overlooked in favor of focusing on stream flow amounts and timing. However, volumes of stream flow may not be the most important factor if water quality is lowered to a point where the utility in natural or manmade ecosystems is compromised. There is a need to identify climate non-stationarities and their links to watershed outcomes. In particular, for risk management, inter-annual modes of climate variability and their seasonal expression are of interest.

The analyses in Chapter 3 are some of the first analyses to link water quality parameters to these non-stationary climate modes. The recent IPCC technical paper 'Climate Change and Water' suggests with high confidence that the increase in global climate variability and extremes may exacerbate some types of water pollution, leading to declines in water quality that could affect food availability, human health, water infrastructure operating costs, and ecosystem health [Bates *et al.*, 2008]. This research is targeted at exploring the relationship between climate variability at the inter-annual level via the El Niño/Southern Oscillation (ENSO) and hydrology and water quality at the small basin scale in the Little River watershed, Georgia. By quantifying the relationships between inter-annual climate and water quality, it may be possible to use this information to reduce pollutant loads into target watersheds during high risk months using short-term climate predictions.

The ENSO is a periodic ocean and atmospheric phenomenon with strong effects on the climate of the southeast United States. The tri-state region especially (FL, GA, AL) experiences strong ENSO effects. El Niño winters tend to be cooler and wetter than those in neutral years; whereas La Niña winters tend to be warmer and drier [Kiladis and Diaz, 1989; Hanson and Maul, 1991; Schmidt *et al.*, 2001]. Different ENSO phases are identified using indices of sea surface temperatures (SST) in the equatorial Pacific Ocean and associated pressure and wind pattern changes. Generally, an ENSO year is classified as El Niño if the 6-month spatially averaged mean is at least +0.5°C greater than average, La Niña if it is -0.5°C lower than average, and neutral otherwise, although the precise definition has changed over time and varies by study [Trenberth, 1997]. In this research, categorical definitions such as the Japan Meteorological Agency's "El

Niño” or “La Niña” will not be used to define entire years [*Japan Meteorological Agency*, 1991]. Instead, the continuous SST anomaly time series averaged over the region bounded by 5°N to 5°S, from 170°W to 120°W and called the NINO 3.4 index is used to encompass finer temporal variability within the ENSO signal [*Trenberth*, 1997]. ENSO phase has previously been shown to have predictable effects on stream flow, precipitation, monsoon occurrence, crop yield, cholera occurrence, flood frequency, and simulated water quality data in different regions around the world [*Chiew et al.*, 1998; *Rajagopalan and Lall*, 1998; *Hansen et al.*, 1997; *Pascual et al.*, 2000; *Piechota and Dracup*, 1999; *Keener et al.*, 2007]. In monitoring and research efforts during the 20th century, ENSO indices have emerged as one of the most consistent for describing inter-annual climate variability on both global and regional scales [*Ropelewski and Halpert*, 1986].

Often in research, hydrological processes over long periods of time are assumed to be stationary. Observed data for many different variables provide evidence to the contrary. Spectral analysis methods have been used to investigate the frequency relationships between large scale climate indices such as the ENSO, North Atlantic Oscillation (NAO) and Pacific Decadal Oscillation (PDO) and hydrologic variables such as stream flow and precipitation [*Rajagopalan and Lall*, 1998; *Enfield et al.*, 2001; *d'Arrigo et al.*, 2001]. Spectral wavelet methods allow one to explore non-stationary aspects of time series within the frequency domain.

The ENSO phenomenon is recognized as having an approximate periodicity of 3-7 years [*Rasmusson and Wallace*, 1983], which has various affects on global climate. If relationships shown in other locations between observed precipitation, stream flow, and

the ENSO index [*Rajagopalan and Lall, 1998; Labat, 2008; Piechota and Dracup, 1999*] are valid in the Little River watershed in Georgia, it may be possible to use the NINO 3.4 anomalies as a predictor for high risk monthly nutrient loading, and thus as part of a best management practice (BMP) or BMP selection tool. The wavelet analysis allows the characterization of the low-frequency oscillations and amplitudes associated through time with geophysical data such as rainfall, SST [*Torrence and Compo, 1998; Y. Wang, 1996*] and nutrient loading. Coherence and cross wavelet analysis then allows the direct comparison of two time series, SST and precipitation, stream flow, or nutrients, for the purpose of identifying areas in which they co-vary with high power [*Grinsted et al., 2004*]. Investigating and identifying significant oscillation periods in precipitation, stream flow, and nutrient loads in the southeast United States that correspond to ENSO oscillations is a crucial first step in ultimately reducing risks associated with climate variability in managing water resources and agricultural systems. The result is an understanding of both recurrent, episodic phenomena, and also a method of quantitatively describing climate risk that is changing in time.

Hydrological relationships involving storm runoff and infiltration rates that apply in much of the US do not apply for the coastal plain [*Sheridan et al., 2001*], and it is therefore often necessary to create new models with specific hydraulic relationships for the region. Existing models often rely on empirical algorithms to represent processes that are not well understood, making wavelet analysis appealing, in which long term, high, or low frequency patterns can be found and used to advance understanding of these processes. Inclusion of the impacts of the large riparian zones in the LRW on flow and water quality is critical to accurate physical hydrological modeling [*Sheridan et al.,*

1983]. Evidence exists that seasonal precipitation in the region may be shifting, with more rainfall from September to March, and less during the growing season from April to August [Baigorria *et al.*, 2007; Knisel *et al.*, 1985]. The southeast United States is an important region both economically, agriculturally, and socially, because of its rapidly growing population that will add water demand and environmental stress to currently stressed or degraded ecosystems. To address the multitude of issues associated with the changing climate in the southeast, finding new methods of making predictions for hydro-climatic variables based on periodic non-stationary phenomena such as the El Niño Southern Oscillation is an important tool. In this research, wavelet analysis explores the link between nutrient loading, hydrology, and ENSO in the Little River Watershed near Tifton, Georgia. This study is a step in ultimately modeling how flushes of nutrient loading in the southeast may be reduced via management based on current or short-term predictions of ENSO phase.

## **Data and Methods**

### **Field Site: Little River Watershed**

The Little River Watershed (LRW) in Tifton, southeast Georgia, is an example of a stereotypical rural coastal plain watershed. Occupying a large area in the southeast US, the LRW is part of the Suwannee River Basin of Florida and Georgia, characterized by broad, flat alluvial flood plains with low-gradient, poorly defined channels, sandy soils, and slow moving streams (Figure 3-1a). The LRW covers 334 km<sup>2</sup>, of which approximately 40% of the southern half and 30% of the northern half are agricultural cropland [Bosch *et al.*, 2004]. It is comprised of eight sub-basins of size varying from 9 to 115 km<sup>2</sup> (Figure 3-1b), and has extensive riparian buffers and gentle stream slopes ranging from 0.1 to 0.5%. The Little River drains into the Withlacoochee River, which in

turn drains into the Suwannee River and ultimately empties into the Gulf of Mexico. All analyses were done on sub-basin K, a 16.8 km<sup>2</sup> area with 106-146 m elevation in the watershed uplands with the most comprehensive nutrient data available of the basins. Maintaining environmental quality in rural landscapes often depends on buffering natural ecosystems from non-point pollution derived from agriculture. In the Suwannee River Basin and the LRW, these non-point pollutants include irrigated crops that receive additional nutrient fertilizer and pesticides, animal production that releases high levels of nutrient and pathogen rich waste, and animal production that mechanically impacts the condition of riparian, stream, or wetland ecosystems through trampling or grazing.

### **History and monitoring**

In 1967, the United States Agricultural Research Service (ARS) installed hydrologic and climate monitoring systems in the LRW, so as to create a data-rich site to better research and understand the hydrology and agricultural impacts on the southern Coastal Plain. The instrumentation was put in throughout the early 1960s, and has been continuously monitored and upgraded since that time, leading the LRW to become the primary experimental agricultural watershed in the Coastal Plain [Bosch *et al.*, 1999]. The extensive rain gauge network was designed to provide a correlation coefficient of 0.9 between measurements of the nearest gauges, indicating the predictability of one measurement based on one from another location [Bosch *et al.*, 1999]. Since they were installed, some gauges that were deemed redundant were removed to save costs, and the digital weighing-type gauges have been replaced by tipping-bucket type gauges, which tip after each 0.254 mm of precipitation, and record each accumulated measurement after 5 minutes [Bosch *et al.*, 1999].

Eight stream flow measurement devices were constructed throughout the entire LRW watershed between 1967 and 1972. Because of the slow-moving and low gradient nature of streams within the LRW, engineers used Virginia V-notch weirs to provide the needed accuracy of measurement without upstream ponding [*Bosch and Sheridan, 2007*]. Each weir was constructed with steel-sheet piling cutoff walls across the stream channel, wing walls to direct flow across the measurement device, a concrete apron to dissipate the energy downstream from the notch, and stilling wells on either side of the weir [*Bosch and Sheridan, 2007*]. The stilling wells compensate for potential periods of no-overfall over the weir crest, measuring elevation every 5-minutes on two Fischer-Porter digital stage recorders synchronized across the entire LRW hydrologic network until 1993, and strain gauge pressure-transducer digital loggers after that [*Bosch and Sheridan, 2007*]. Sub-basin K in particular uses a horizontal weir with a V-notch center section measuring 17.8 m in length with a notch depth of 44.2 cm [*Bosch and Sheridan, 2007*]. Data were checked for accuracy by SEWRL USDA-ARS researchers, and are maintained in public databases.

The water-quality monitoring program was started in the LRW in 1973 in basin K, with an automatic sampler taking three samples per day from the flow monitoring location to test for in-stream chloride, nitrate and nitrite [*Lowrance et al., 1984*]. In 1974, an additional limited duration rainfall water-quality sampling program was started to gather baseline nutrient concentrations [*Lowrance and Leonard, 1988*]. In 1979, total kjeldahl nitrogen and total phosphorus were added to the list of analytes monitored [*Feyereisen, Lowrance, et al., 2007*]. Over the years, sample collection methodology and timing has varied according to research objectives, funding, and technological

advances. Collection methodology has varied from manual grab-sample, automated timed discrete, and automated flow-weighted composite refrigerated or non-refrigerated, while the place of collection has varied from weir overfall to the upstream stilling well area [Feyereisen, Lowrance, et al., 2007]. Sampling times range from every 5-minutes, to several hours, to weekly. Analyte loads were calculated by summing the product of concentration and stream flow for a given time step, and are also available in the website database.

### **Soils and geology**

All of the Little River Watershed study area is in the outcrop era of the Hawthorn Formation, a Miocene Age geological structure that can obstruct regional interactions between surface and groundwater systems [Stringfield, 1966]. In the northern LRW, including basin K, the Hawthorn Formation consists mainly of non-marine, cross-bedded gravelly sands mixed with indurated sandy clays, with a total thickness of approximately 21 meters [Stringfield, 1966]. The lower 6.5 meters are mainly sandy claystone, with a second identified rock type of sandy gray-green clay in the lowest 3 meters. The Hawthorn Formation was subsequently overlain by a 0-6 meter highly permeable Quaternary and Recent eolian and fluvial sediments over older marine sediments [Asmussen, 1971]. The soils of sub-basin K are mainly sandy loam and loamy sand with characteristically high infiltration capacity [Rawls et al., 1976].

In fact, 85% of the soils within the LRW have infiltration rates of 5 cm/hr or greater [Calhoun, 1983]. Infiltration at the surface layer from 0-6 meters is restricted by a plinthic layer of clay/sandy clay loam with low hydraulic conductivity generally less than 0.01 cm/hr [Feyereisen et al., 2008]. Upland soils generally have good internal drainage, while lowland drainage can be very poor, with isolated standing water for

extended times in winter and spring [Calhoun, 1983]. Phosphorus tends to be fixed in the soils, making it less leachable than nitrate. As a result, while neither pollutant is specifically problematic in the LRW, phosphorus levels are extremely low.

### **Climate and hydrology**

Climate in the LRW region is humid sub-tropical, characterized by long and hot summers, short and mild winters, and an average growing season of 245 days [Sheridan, 1997]. Annually, the area's average precipitation (1922-1988) is 1208 +/- 214 mm [Sheridan and Knisel, 1989], with variable monthly distribution. As in much of the southeast US, summer rainfall is characterized by convective storms with shorter individual events that occur with greater frequency and intensity than in other seasons. In this regard, summers in the LRW usually have greater total rainfall than other seasons [Sheridan, 1997]. Typically, the fall months have the least total rainfall, but are more likely to have extended storms with longer average duration between precipitation events [Feyereisen et al., 2008]. Late summer and fall months may also receive heavy rainfall from tropical storms. Winter and spring seasons receive more total rainfall than the fall season, and continue to be characterized by variable low-intensity storm events. Average temperatures range from a monthly minimum of 4.2°C in January to a maximum of 32.7°C in August, with an annual average of 19.1°C [Sheridan, 1997].

Shallow, groundwater flow is the primary runoff component in uplands, accounting for up to 80% of stream flow [Sheridan, 1997]. Groundwater flow is also the primary flow route for soluble nutrients [Lowrance et al., 1984]. Groundwater recharge to aquifers below the surficial aquifer is restricted by the Hawthorn formation, which makes up the confining layer for the artesian Florida Aquifer under the watershed [Stringfield, 1966]. In areas of the LRW, the Hawthorn formation is continuous, creating relatively

impermeable subsurface horizons that impede deep seepage and groundwater recharge, instead promoting lateral movement. The shallow lateral subsurface flow and groundwater flow from the surficial aquifer contribute seasonally to stream flow as shallow return flow to surface drainage [*Sheridan, 1997*].

There have been water balance studies at both the field and watershed scale in the LRW. Basin K specifically was measured from 1967-1977 as having mean surface runoff of 42.8 cm with 75% of that taking place between January and May, and a consistent but virtually negligible sub-surface runoff of 0.0008 cm, while 33% of the recorded precipitation flowed from the basin as surface flow and relative subsurface flow only 1/100<sup>th</sup> of a percent of rainfall input [*Lowrance et al., 1983*].

### **Land use, management and policies**

Sub-basin K in 1968 was defined as mixed-use agricultural, and vegetative mapping showed land use as 39% agricultural (mostly peanuts, corn, cotton, soybean, tobacco), and 61% woodland (mostly slash and longleaf pine with wiregrass or broomsedge, some hardwood pine, swamp hardwood, and pine/oak) [*Sheridan et al., 1983*]. In 2003, the land use had changed to approximately 29% agricultural and 57% woodland [*Feyereisen, Strickland, et al., 2007*]. The Southeast Watershed Research Lab (SEWRL) in Tifton has collected hydraulic and climatic data continuously for the entire watershed since 1965, and water quality data in sub-basin K beginning in the mid-1970s [*Feyereisen et al., 2008*]. There are also historical land-use and fertilizer records starting in the late 1970s.

Historically, the environment and water quality of the LRW has not been overly adversely affected by agricultural practices, due to the effect of large riparian filters throughout the heavily forested watershed. However, the cultivated agricultural area in

sub-basin K has been increasing since the early 1990s with a related decline in upland and riparian areas, meaning that the ecology and water quality are being increasingly impacted. Because of the large amount of data available for the LRW, analysis of this impact is possible. Within the 30% of cultivated area in sub-basin K in 2004, cotton is the major crop grown, comprising 68% of all cultivated area with peanut next with only 29%. As one of the more upland sub-basins, field studies in 1984 showed that K was accumulating the most nutrients in the LRW, which suggested that more intensive cropping of the upland fields could lead to more efficient use of nutrients by having actively growing crops for more of the growing season [Lowrance *et al.*, 1984]. Currently, almost year round production of row crops has led to extensive and sustained use of fertilizer and pesticides on the watershed (Bosch *et al.*, 2004) On the other hand, less intensive agriculture coupled with increased forest and riparian area could have similar effects on efficient use of nutrients.

In past studies done by SEWRL, the LRW has shown the highest overall stream flow concentrations of nitrate ( $\text{NO}_3$ ) and total phosphorus (P) from January to March, and minimums from July to September [Lowrance *et al.*, 1984]. Low rainfall and low evapotranspiration, decreased denitrification and decreased uptake in the upland and riparian zones may contribute to higher nutrient concentrations in the winter, while crop nutrient uptake and low leaching may cause low concentrations in the summer [Lowrance *et al.*, 1984]. Decreased  $\text{NO}_3$  and P concentrations were observed during April to June even though runoff was still high and fertilizer application occurred, in part because of biological effects such as nutrient uptake, transpiration, and utilization. Nitrate loads are highest when stream flow is highest, from December through

February, and lowest when flow is least, from September to November. Nutrient loads are disproportionately low from June to August while flow is still relatively high, as crops are utilizing the most nutrients in this season [Lowrance *et al.*, 1984, 1985]. Over the past 25 years, there have been numerous studies by SEWRL documenting the hydrology, ecology and stream chemistry of the LRW [Bosch *et al.*, 2004; Feyereisen *et al.*, 2008], yet nothing investigating the relationship between the hydrology and local ENSO effects.

### **Little River Watershed Data**

Observed precipitation and stream flow data from sub-basin K of the LRW used in this study ranges from February of 1968 to June of 2005, and have been recorded and compiled by researchers at SEWRL in Tifton, Georgia (Table 3-1). Details on the daily flow and precipitation data collection, quality, and processing are thoroughly discussed in Bosch *et al.*, 1999, 2007a and 2007b. Flow in the LRW is measured at eight concrete v-notch weirs built between 1967 and 1971, one of which lies at the outlet of sub-basin K. There are currently 46 active rain gauges in the LRW, 13 of which are within and surrounding sub-basin K, and were used to calculate the weighted watershed area daily precipitation [Bosch, Sheridan, and Marshall, 2007]. Daily precipitation data within sub-basin K were created from watershed weighted data using the methods of Dean and Snyder [Bosch, Sheridan, and Marshall, 2007; Dean and Snyder, 1977], summed into monthly cumulative values, and then normalized by monthly average to remove annual cycles for each month of the record. Processed daily stream flow data [Bosch and Sheridan, 2007] for all 37 years were summed into monthly cumulative values and normalized by monthly average as well.

Nitrate and total phosphorous concentration datasets contain varied collection frequencies from 1974 to the present, ranging from every five minutes to once a week. Researchers at SEWRL have in-filled the nutrient data to the daily level using a variety of methods based on the sampling method that was used (i.e. automatic sample, manual grab). The in-filling provided complete daily time series of 24 years of total P concentration (from January, 1979 to December, 2003), and 29 years of NO<sub>3</sub> concentration (from January, 1974 to December, 2003). The detailed methods and reasoning behind stream chemistry in-filling are discussed in Feyereisen et al [Feyereisen, Lowrance, et al., 2007] , and additionally located on the LRW public database website, located at <ftp://www.tiftonars.org/>, under the file “streamchemistry\_readme.txt”. Daily concentration data were converted to loads by multiplying daily flow by nutrient concentration. Nutrient concentrations and loads were averaged into basin-wide monthly values and normalized by median monthly values, creating time series of average monthly anomalies with the annual cycle removed. Median values were used to normalize nutrient concentrations and loads to minimize difficulties associated with the different methods of nutrient data in-filling.

Sea Surface Temperature anomalies were calculated from the Kaplan extended NINO 3.4 index (27.5°E to 22.5°E, 87.5°S to 87.5°N), which is available from the Lamont-Doherty Earth Observatory data library (Table 1) [Kaplan et al., 1998]. The SST data are gridded by 5° × 5° delineations, and range from 1856 to the present, although only the 1968 to 2005 data are used in this study. Temperatures were converted to monthly average and seasonal average anomalies by being normalized against the total

month's average. All variables' raw time series were plotted against time (month and year) to provide an initial visualization of the data trends (Figure 3-11).

All hydrological and climatic data normalized by monthly medians are shown in boxplots (Figures 3-6 to 3-10) separated by M-ENSO phase (see Chapter 2 introduction for M-ENSO details) and month.

### **Wavelet Analysis**

Wavelet analysis is a spectral method of decomposing a time series into time and frequency space, allowing the identification and analysis of dominant localized variations of power, i.e., where the variance of the time series is largest for a given frequency. In this context, a main purpose of using the wavelet analysis technique is to quantify and visualize statistically significant changes in the ENSO SST and nitrate load variance over a multi-decadal time scale. The windowed Fourier transform is typically used to analyze a signal in frequency space at a global level, however, it is scale-dependant, and is hence inefficient and inaccurate when attempting to perform an analysis on non-stationary environmental data sets with different signal powers that evolve through time [Torrence and Compo, 1998]. A well known and relevant example is that of SST's in the equatorial Pacific Ocean, where the dominant mode of variability is ENSO, shown by frequency signals on a time scale of 3-7 years [Rasmusson and Wallace, 1983]. Superimposed on this signal are much longer inter-decadal fluctuations, visible in the wavelet power spectrum over time as the evolution of the SST signal power. The inter-decadal fluctuations have the effect of modulating the amplitude and frequency of occurrence of El Niño events. Torrence and Compo (1998) have written a comprehensive guide to wavelet use for geophysical data, the basic theory they discuss will be summarized here.

With any time series,  $x_n$  ( $n = 0 \dots N-1$ ) with time spacing  $\delta t$ , there is a corresponding wavelet function,  $\psi_0(\eta)$ , with zero mean and localized in time and frequency space, that depends on a non-dimensional time parameter,  $\eta$ , and the non-dimensional frequency,  $\omega_0$ . In this analysis, the Morlet wavelet (Equation 3-1), consisting of a plane wave modulated by a Gaussian, is used for all time series, the frequency of which, in practice, is given the default value of  $\omega_0 = 6$  for all analyses [Farge, 1992]:

$$\Psi_0(\eta) = \pi^{-1/4} \exp i\omega_0\eta \exp -\eta/2 \quad (3-1)$$

A Morlet wavelet is a non-orthogonal, complex function that can be used with the continuous wavelet transform,  $W_n(s)$ . The continuous wavelet transform (Equation 3-2) of a discrete sequence  $x_n$ , is the convolution of  $x_n$  with a scaled and translated version of  $\psi_0(\eta)$ :

$$W_n(s) = \sum_{n'=0}^{N-1} x_{n'} \psi^* [(n'-n)\delta t / s] \quad (3-2)$$

Where (\*) is the complex conjugate,  $s$  is the wavelet scale,  $n$  is the localized time index,  $n'$  is the translated time index, and  $\psi$  is the normalized wavelet. An approximate value of  $W_n$  can be found by performing the convolution  $N$  times for each scale, where  $N$  is the number of points in the time series. All convolutions can then be done in Fourier space using a discrete Fourier transform of  $x_n$ , (Equation 3-3), which in our case, is:

$$\hat{x}_k = (1/N) \sum_{n=0}^{N-1} x_n \exp^{-2\pi i k n / N} \quad (3-3)$$

Where  $k = (0 \dots N-1)$  is the frequency index. By the convolution theorem, the wavelet transform (Equation 3-4) is the inverse Fourier transform of the product of the discrete Fourier transform of  $x_n$  and  $\Psi^*$ , with angular frequency  $\omega_k$ :

$$W_n(s) = \sum_{k=0}^{N-1} \hat{x}_k \hat{\psi}^*(s\omega_k) \exp^{i\omega_k n \delta t} \quad (3-4)$$

Finally, the wavelet power spectrum is defined as  $|W_n(s)|^2$ , and the amplitude at each point,  $|W_n(s)|$  and phase,  $\tan^{-1} [\text{I}\{W_n(s)\} / \text{R}\{W_n(s)\}]$  can be found. Significance levels for wavelet spectra are found by comparison against a random background distribution, which, for geophysical spectra, are modeled as either white or red noise (increasing power with decreasing frequency). In this study, red noise is used [B. Wang, 1995; Torrence and Compo, 1998], and modeled as a univariate lag-1 autoregressive (AR-1) process.

The wavelet variance is indicated by the Global Wavelet Spectrum (GWS), calculated by the integration of the squared transform coefficients at different scales for all data points. Areas of global wavelet significance are shown as a dashed blue line, above which indicates a 95% confidence limit above red noise. Continuous Morlet wavelet transforms and wavelet power spectra were computed and visualized for all monthly normalized time series in Table 1 to find significant periodicities that correspond to ENSO signals. All univariate wavelet analysis was done using the WAVETEST Matlab script for WAVELET, [Torrence and Compo, 1998], which can be downloaded from: <http://paos.colorado.edu/research/wavelets/>.

## Cross Wavelet and Coherence Transforms

A detailed explanation of cross wavelet transform (XWT) can be found in Torrence and Compo [*Torrence and Compo*, 1998]. Given two different time series, X and Y, with different wavelet transforms  $W_n^X(s)$  and  $W_n^Y(s)$ , the cross wavelet transform is  $W_n^{XY}(s) = W_n^X(s) W_n^{Y*}(s)$ , where (\*) denotes the complex conjugate. The spectrum is complex, thus the cross-wavelet power can be defined as  $|W_n^{XY}(s)|$ . The cross wavelet transform finds regions in time frequency space where the two time series show high common power, and thus, significance. In particular, this transform examines whether regions in time frequency space with large common power have a consistent phase relationship, and therefore are suggestive of causality between the time series [*Grinsted et al.*, 2004].

Computing the wavelet coherence transform (WTC) finds regions in time frequency space where the two time series co-vary, but do not necessarily have high power. For this reason, both the cross wavelet transform and the wavelet coherence transform are necessary when analyzing two time series to assess both causality and local covariance. Generally, a WTC will have more significant areas than an XWT spectrum, as the significance is sacrificed for the desirable visualization of shared power in the XWT. The wavelet coherence transform of two time series [*Grinsted et al.*, 2004] is defined as:

$$R_n^2(s) = \frac{|S(s^{-1}W_n^{XY}(s))|^2}{S(s^{-1}|S(W_n^X(s))|^2) \cdot S(s^{-1}|S(W_n^Y(s))|^2)} \quad (3-5)$$

Where S is a smoothing operator defined by the wavelet type used and the entire expression is similar to that of a traditional correlation coefficient localized in time-

frequency space. The statistical significance level of the wavelet coherence is estimated using Monte Carlo methods, and then the significance level for each scale is calculated using only values outside the cone of influence.

Cross-wavelet and coherence transforms were done on normalized NINO 3.4 SST time series with precipitation, stream flow, NO<sub>3</sub> concentration and NO<sub>3</sub> load, all calculated to 95% significance levels. Wavelet coherence and cross wavelet software used was via the XWT and WTC scripts written by Aslak Grinsted for Matlab, © 2002-2004, downloadable at <http://www.pol.ac.uk/home/research/waveletcoherence/>.

### **Cross-Correlation Time Series Analysis**

The lagged cross correlation between the ENSO index and the hydrological time series,  $x(i)$  and  $y(i)$ , at different delays ( $d = 0 \dots N-1$ ) were computed as:

$$R = \frac{\sum_i [(x(i) - \mu_x) * (y(i-d) - \mu_y)]}{\sqrt{\sum_i (y(i-d) - \mu_y)^2} \sqrt{\sum_i (x(i) - \mu_x)^2}} \quad (3-6)$$

In which N is the length of the time series and  $\mu_x$  and  $\mu_y$  are the respective means. A positive correlation is associated with the series correlated in their current configuration, while a negative correlation indicates a relationship with the inverse of one of the time series. The delay at which maximum correlation is seen describes the most significant time lag relationship between the two data series. Cross correlations were calculated between the NINO 3.4 SST time series and precipitation, stream flow, NO<sub>3</sub> concentration and NO<sub>3</sub> load for delays from zero to 24 months. Significance was calculated at 95% confidence corrected for time series autocorrelation [*World Meteorological Organization*, 1966].

## Results

### Wavelet Analysis

The monthly wavelet power spectra for the NINO 3.4 SST, precipitation, stream flow, and NO<sub>3</sub> concentration and load time series are shown in Figures 3-2a-e. As previously demonstrated [Y. Wang, 1996; Torrence and Compo, 1998], when the annual cycle is removed, SST power (Figure 3-2a) is concentrated within the ENSO periodicity band of 3-7 years, although the amplitude and dominant modes tend to shift through time. From 1911-60, a 5-7 year period is strongest, while a 4-5 year period dominates from 1972-92 [Y. Wang, 1996]. Longer decadal variations cannot be assessed with significance given the limited length of record. The annual cycle of ENSO is associated with observing strong La Niña power in the wavelet spectrum [Y. Wang, 1996], as well as normal seasonal variations or possible manifestations of the Quasi-Biennial Oscillation (QBO) [Baldwin et al., 2001; Reed et al., 1961]. The enhancement of annual power by La Niña, and respective weakening during El Niño, has been hypothesized to be due to the thermocline becoming shallower and the trade winds strengthening, which reinforces the ocean upwelling effect that modulates the annual SST cycle [Gu and Philander, 1995]. Therefore, by removing the annual cycle, we are able to more easily visualize powerful El Niño events in the 3-7 year band. The most pronounced SST variability within the wavelet power spectrum is observed during the strongest El Niño phenomena encompassed within this time series, namely the 1982-83 and 1997-98 events—the latter of which is the strongest El Niño recorded in the 20<sup>th</sup> century [Chavez et al., 1999]. In the time domain, NINO 3.4 SST anomaly trends are easy to discern, as they form the basis for classification of ENSO phases (Figure 3-6). All ENSO phases have relatively low variability, while neutral months are close to zero

(Figure 3-6a); La Niña years are slightly below zero (Figure 3-6b) and El Niño years are slightly above zero (Figure 3-6c).

Precipitation in the southeast US and the LRW has distinct seasonality. In the coastal plain region and more specifically the LRW, the most intense precipitation events are in the spring and summer months, associated with convective or cyclonic storms [Sheridan, 1997]. Summer events are shorter, smaller in area, and more frequent and intense, while fall and winter events are frontal in nature, milder, but longer in duration. The time domain boxplots and wavelet power spectrum of monthly precipitation anomalies from 1968-2004 is shown in Figures 3-7 and 3-2b, respectively. Normalized precipitation time series show large variability for all months in the neutral phase (Figure 3-7a), more summer month positive anomalies and September to December negative anomalies dominate in the La Niña phase (Figure 3-7b), and a larger Sept-Dec and summer variability in El Niño phase (Figure 3-7c). Low frequency precipitation information corresponding to the 3-7 year ENSO signal has been demonstrated in the Florida Everglades via wavelet analysis, as well as in the western US [Kwon *et al.*, 2006; Rajagopalan and Lall, 1998], and the Little River Watershed shares that signal. Regions of high power relative to the noise background are seen in the precipitation record in the same 3-7 year periodicity as for the NINO 3.4 series (Figure 3-2b), although the signal is not powerful enough for statistical significance, nor is it as clear as the SST record in Figure 3a. Since a 4-5 year quasi-periodicity dominates ENSO from 1972-92 as seen in longer SST wavelet analyses [B. Wang, 1995; Y. Wang, 1996], this may explain the 4-5 year period visible in the precipitation time series. Again, the strongest power at that frequency is seen from 1981 to 1992 and

surrounding the 1997-98 El Niño event, which implies that ENSO variability clearly is associated with precipitation in basin K of the LRW (Figure 3-2b). The high power still visible at the 1-2 year period, despite removal of the annual cycle, may represent the variability from a seasonal anomaly. Analyzing summer and winter seasons separately with each hydrological variable showed slightly stronger 3-7 year ENSO wavelet power in winter months, although not enough to be statistically significant.

In basin K of the LRW, average annual stream flow depth is approximately one-third of annual precipitation [*Sheridan, 1997; Feyereisen et al., 2008*], a figure comparable to similar statistics from other coastal plain watersheds. As such, the inter-annual component of the wavelet power spectrum (Figure 3-2c) for the stream flow record for 1974-2003 shares much of the power and variability pattern seen in the precipitation spectrum, although the signal is actually stronger as it is less noisy than the precipitation record. The M-ENSO monthly plots of stream flow show similar trends in the neutral and El Niño phase (Figures 3-8a and 3-8c) of particularly low flows from June to October, with most flow from December through April. The La Niña M-ENSO anomalies show relatively higher flows from May to September, and greater January to April variability (Figure 3-8b). In the wavelet spectrum, the ENSO periodicity is seen again as high power in stream flow for the 3-7 year period, surrounding the 1982-83 and 1997-98 El Niño events (Figure 3-2c). High power is again seen in the 1-2 year period, perhaps related to intense summer storms or the QBO. Clearly, the observed 3-7 year periodicity in the stream flow spectrum demonstrates that while ENSO signals have been found in large rivers around the world [*Chiew et al., 1998; Labat, 2008*], the

relationship is valid for small, slow-moving coastal plain streams and rivers in the LRW as well.

Wavelet power spectra of nitrate concentration (mg/L) and load (kg) are shown in Figures 3-2d and 3-2e, respectively. While it has been shown that categorical ENSO signals exist in model simulated nutrient loads in south Florida [Keener *et al.*, 2007], observed and continuous data have not been analyzed in the literature. Both nutrient series extend from 1974 to 2003. M-ENSO boxplots of NO<sub>3</sub> concentration show a more uniform spread and lack of trend through all months during the neutral phase (Figure 3-9a), increased potential for positive anomalies from May to July and low variability negative anomalies from August to December in the La Niña phase (Figure 3-9b). During El Niño, anomalies are present from June to August larger than those seen in La Niña, with upward anomalies trending from January to May (Figure 3-9c). NO<sub>3</sub> concentration exhibits less marked high power in the ENSO periodicity than either precipitation or stream flow, which is expected due to a less direct relationship with the atmosphere. There is also high power centered on the 1988-1989 La Niña, at 1-2 year periodicity, and may signify an anomalous event. These regions of high variability imply that NO<sub>3</sub> concentration is more sensitive to the high intensity rains characteristic of La Niña summers or hurricane in the southeast, although no periods are significant at the 90% level as manifested in the global wavelet spectra. The minimal concentration power visible indicates that the concentration signal does not change in a significant or systematic way, and that flow and load should remain the main focus.

Nitrate load (Figures 3-10 and 3-2e) is a combination of stream flow and concentration time series. Accordingly, there is a broader band of ENSO-related high

power in the 3-7 year period centered on the 1982-83 El Niño, and only medium power visible in the cone of influence around the 1997-98 El Niño. A longer time series may reveal more about the load structure during the latter El Niño. High power is seen in nitrate load in the 1-2 year periodicity centered around 1986-89, which may reflect the stream flow's modulation of the concentration, and the La Niña event of 1998-99, the pattern of which is also reflected in high power seen in precipitation, stream flow, and SST spectra. This may again be related to the high annual power noted in some strong La Niña events [Y. Wang, 1996]. Load boxplots show the main differences in M-ENSO phase are increased January to March variability in both El Niño and La Niña phases as compared to neutral (Figure 3-10a-c), with very high load anomalies possible in February and March of El Niño (Figure 3-10c). Summer loads in La Niña are not higher than usual according to these metrics (Figure 3-10b).

### **Cross-Wavelet Analysis**

Although one can see regions in the wavelet power spectra in the previous section where two time series show high common power, a more direct analysis of two series is needed. Significance levels of the cross-spectra power are calculated against a red noise background, indicated by thick black outlines in the cross wavelet transform spectra (Figure 3-3) to the 5% level. The cross wavelet transform between SST and precipitation (Figure 3a) shows that areas that were picked out as possibly sharing power in the single wavelet spectra, do indeed share significant power in the 3-7 year periodicity surrounding the 1982-83 and 1997-98 El Niño. The significant areas within the 3-7 year period are phase-locked positively, which when considered with the fact that ENSO is a main driver of global climate variation, suggests a causal relationship between SST and precipitation in the LRW that was already suspected. The same

patterns of shared power, phase, and 3-7 year periodicity are seen in the cross wavelet transform between SST and stream flow (Figure 3-3b).

The cross wavelet transform relationship between  $\text{NO}_3$  concentration and SST (Figure 3-3c) shows less significant shared power, although there is a small area from 1985-90 around 3-4 year periodicity. The general 3-7 year period area shows high power, but too little for significance at the 5% level. The lack of definitive relationship between SST and concentration is explained by nutrient concentrations being very much an extraneous variable, dependent on both local agricultural activities and rainfall or river flow. Nutrient load, on the other hand, takes stream flow into account. The cross wavelet transform of  $\text{NO}_3$  load and SST (Figure 3-3d) shows the same significant area as the cross wavelet transform with stream flow and precipitation, a shared 3-7 year in-phase periodicity extending from 1980-90, and a 1-2 year periodicity in the area around the 1998-99 La Niña.

### **Wavelet Coherence Analysis**

Compared with the cross wavelet transform, a larger area in the wavelet coherence spectra is marked as significant. However, neither the significance of the wavelet coherence transform nor the cross wavelet transform on their own do not necessarily imply causality, as any two variables can be significantly correlated by chance. Small areas of wavelet coherence transform significance are unlikely to be causal taken on their own. More extensive areas of significance, however, are less likely to be due to chance, and should be examined carefully for additional relationships to a physical mechanism. The wavelet coherence transform between SST and precipitation (Figure 3-4a) and SST and stream flow (Figure 3-4b) show very similar sustained significant areas from 1979-2000 in the 3-7 year period, indicating high correlation

between SST and each time series in the area relating to ENSO signal. Longer time series would be desirable for every variable to further investigate the changing periodicities; however within the cone of influence, there is a sustained ENSO signal.

The wavelet coherence transform between  $\text{NO}_3$  concentration and SST is shown in Figure 3-4c. There are arguably no areas of causal significance, especially when considered with respect to the importance of variables outside of this analysis such as fertilizer application or land-use changes. Practically, this means that the two time series do not show any significant correlation at any periodicities of interest to this study, although there is a small area of ENSO related significance in the XWT. The concentration significance in the XWT may be a remaining artifact from the much stronger stream flow signal (Figures 4b and 5b), showing up despite the stochastic nature of the concentration series. When analyzed in conjunction with the WTC, it becomes clear that this is probably an artifact and should not be assigned any causal explanation. Nitrate load, however, (Figure 3-4d) shows a very high correlation with SST throughout all the years within the cone of influence at 3-7 year periodicity. This correlation reflects a combination of the strong stream flow ENSO signal with the weak concentration ENSO signal, but should not be discounted as non-causal, as stream flow response is directly related to precipitation and SST. The in-phase correlation and power of SST and  $\text{NO}_3$  load suggests that a model based upon the 3-7 year periodicity of ENSO could have predictive skill for LRW nitrate loads. Across all the wavelet power analyses, the ENSO signal appears in sustained and common 3-7 year frequency bands. This frequency structure is replicated across the NINO 3.4, precipitation, stream flow, and  $\text{NO}_3$  load time series, and is moreover found within the cross-wavelet and

wavelet coherence spectra, supporting this ENSO structure and demonstrating that the ENSO climate teleconnection extends to precipitation, hydrology, and observed NO<sub>3</sub> loads in the small streams of the LRW.

### **Cross Correlation Analysis**

As common frequency bands and high or significant power were found in wavelet analysis of SST and precipitation, stream flow, and NO<sub>3</sub> load, time series cross correlation analysis was performed to temporally quantify how these relationships actually manifest during the year. After the removal of annual trends from each variable considered, significant monthly correlations were found between SST and all hydrological variables (Figure 3-5a-c). The correlation of highest magnitude is between SST and NO<sub>3</sub> load (Figure 3-5c), which is reinforced by the wavelet coherence transform analysis. All cross-correlations were dominated by positive significant correlations with the ENSO 3.4 index. Precipitation and stream flow had maximum cross-correlation function values of 0.139 and 0.342 with SST at a four month and two month lag, respectively, and NO<sub>3</sub> load a maximum of 0.360 at a three month lag. This means that high or low precipitation and stream flow are correlated with high or low sea surface temperature observed four and two months earlier, while NO<sub>3</sub> load is positively correlated with SST three months prior—observations that are supported by the cross wavelet transform and wavelet coherence transform spectral analyses.

Additional cross-correlation analyses were done to determine the strength of the lag relationship between precipitation and stream flow, precipitation and NO<sub>3</sub> load, and stream flow and NO<sub>3</sub> load. In each relationship, the most significant lag was at zero months, suggesting that a smaller time-step may be needed to assess the correlative lag more accurately. However, the strongest CCF value of 0.663 (Figure 3-5d) was

seen between precipitation and flow at lag zero, followed by stream flow and NO<sub>3</sub> load with a CCF of 0.472, and finally precipitation and load with 0.268. These values show that the NO<sub>3</sub> load is most directly correlated with flow, which supports the previous wavelet analyses.

### **Summary and Discussion**

Chapter 3 uses wavelet analysis to identify and quantify the significance of a teleconnection between sea surface temperatures associated with the NINO 3.4 index and precipitation, stream flow, and nitrate concentration and load in the Little River Watershed in Georgia. We found common areas of high power and time series inter-annual variability manifested in the ENSO signal for 36 years of LRW monthly precipitation data, and 29 years of stream flow, nitrate concentration and nitrate load data. Areas of the highest power for all hydrological variables were observed in the 3-7 year periodicity known to be related to ENSO modes of variability. Temporally, the area of greatest variability was centered on the 1997-98 El Niño event, which is on record as the strongest anomaly in the 20th century. Sea surface temperatures dramatically decreased from the transition of the 1997-98 El Niño to the 1998-99 La Niña, which may be reflected in the anomalous variability visible in the wavelet power spectra of the hydrologic variables. Nitrate concentration was the variable with the weakest ENSO signal power, which is due to it being more dependent on extraneous variables such as human-caused agricultural activities. High or significant power was seen in precipitation, stream flow, and nutrient loads in the 1-2 year period centered on the 1998-99 La Niña, and may be related to a signal from the QBO and strong seasonal signals. The stronger power seen in nitrate load time series, rather than concentration or precipitation, suggest that stream flow variability dominates the trends seen in loads.

Regions of shared power were found between the NINO 3.4 index and the hydrological variables of interest. There was common high power and phase in the 3-7 year mode of variability for strong El Niño events, as well as in the 1-2 year mode of variability for strong La Niña episodes for SST and precipitation, stream flow, and nitrate load. High time series covariance exists in the same 3-7 year period for SST and precipitation, stream flow, and nitrate loads. The cross wavelet transform and wavelet coherence transform confirm that the known physical mechanism of ENSO teleconnection in the southeast United States [*Schmidt et al.*, 2001; *Ropelewski and Halpert*, 1986] is causally linked to inter-annual variability within precipitation, stream flow, and nitrate load signals in the LRW. The high shared power and significant correlation between these variables confirms that the ENSO teleconnection seen in the precipitation and stream flow signals in large river and watershed systems around the world [*Chiew et al.*, 1998; *Rajagopalan and Lall*, 1998; *Handler*, 1990; *Kulkarni*, 2000; *Hansen et al.*, 1997; *Piechota and Dracup*, 1999; *Pascual et al.*, 2000] extends to the hydrology and, more interestingly, nitrate loads in a small basin of the Little River Watershed.

Mechanistically, El Niño (La Niña) events result in increased (decreased) sea surface evaporation. The mid-latitude jet is displaced equatorially (poleward), increasing (decreasing) winter frontal precipitation in the southeast United States. Additional winter moisture is advected into the southeast from the tropical Pacific by the subtropical jet stream [*Ropelewski and Halpert*, 1987]. Precipitation in El Niño winters typically increase as a result, and as seen in the large El Niño events centered around 1985 and 1997-98 in the LRW, resulted in increased river discharge and pollution transport. It is

unusual that the ENSO signal is more visible in the stream flow and nitrate loads of the LRW than in the precipitation signal. Although the thirteen weather stations used to form the precipitation series in this research are well distributed across the 16.8 km<sup>2</sup> area of basin K in the LRW, spatial variability of rainfall in the southeast United States is great, and still does not encompass all of the variability inherent in the watershed. For this reason, the ENSO signal present in the precipitation record may be somewhat damped, especially when considered next to the stream flow record. In addition to being a smoothed function of precipitation, stream flow in the Little River Watershed may be strengthening the correlation with the ENSO signal. As has been previously discussed, groundwater flow in the LRW is responsible for up to 80% of the total stream flow [Sheridan, 1997], as well as comprising the main route for movement of soluble nutrients [Lowrance et al., 1984]. The ENSO signal in stream flow may increase in power due to the significance of the role of groundwater, and additionally due to the presence of the Hawthorn confining layer, restricting flow into the aquifer system and increasing the amount of lateral groundwater flow represented in the stream flow record.

The nature of the strong ENSO power visible in the wavelet analyses demonstrates that in the LRW during anomalous ENSO phases, BMP's and crop management practices could be more effectively applied to reduce the risk of high nutrient runoff resulting from the increased precipitation and stream flow. Best Management Practices in the LRW have mainly been comprised of crop rotations designed to more effectively use available water and prevent nutrient leaching. At this point, conservation tillage or crop cover practices have not been implemented in sub-basin K. Some BMP modeling work with SWAT has been done in sub-basin K as a part

of the national Conservation Effect Assessment Project (CEAP), in which a simulated increase of 30% cultivated area with better crop management showed a 17% reduction in total nitrogen load [Cho *et al.*, 2010], suggesting that BMP's could in fact be quite effective in generally reducing loads.

While sometimes it is both economically as well as environmentally in a farmer's best interest to implement BMP's, it can be difficult to quantify the effectiveness of the results and for farmers to know when best to apply them. The strong ENSO signal in the nitrate load and stream flow, coupled with the cross-correlation analysis of SST's suggests that when an anomalous ENSO phase is predicted or is occurring, BMP's could be put in place to control the risk of high nutrient runoff. The ability to make management decisions months in advance with reduced uncertainty of the BMP's not being needed could save the farmer both time and money, and result in environmental and water quality improvements. Implementing and monitoring the effectiveness of different BMP's in the LRW in different seasons and ENSO phases would take additional time and effort, but would be worth verifying if BMP application by ENSO phases would actually save time and money for watershed managers, farmers, or other stakeholders.

In this study, more than 29-36 years of data would have been informative as to how inter-decadal variability affects hydro-climatic events. However, short-term inter-annual climate variability is a crucial factor affecting climate in the southeast US, and therefore must be understood in how it ultimately relates to water quality. Additional large El Niño and La Niña anomalies within the hydrological time series record will also help to confirm patterns in the time and frequency domain. As a correlation has been

established linking ENSO to precipitation, stream flow, and nutrient load in the LRW, the significant 3-7 year modes of variability can be extracted from the signal and reconstructed into a predictive time series model for nitrate load based on the NINO 3.4 sea surface temperatures. By analogy, time series of different pollutant loads affecting water quality could be analyzed using these methods. Generating a forecast system for nutrient loads or other pollutants based on low frequency ENSO phenomena will be useful, feasible, and could avoid uncertainty associated with possible misrepresentation of physical processes and used in conjunction with hydrological models for the southeast coastal plain.

Table 3-1. LRW time series data and sources used.

Variable	Years	Source	Comments
NINO 3.4 SST (°C)	1968- 2005	Kaplan extended index, <a href="http://ingrid.ldeo.columbia.edu/SOURCES/.KAPLAN/.EXTENDED/.ssta/">http://ingrid.ldeo.columbia.edu/SOURCES/.KAPLAN/.EXTENDED/.ssta/</a>	Anomaly data averaged monthly
Precipitation (mm)	1968- 2005	<a href="ftp://www.tiftonars.org/databases/LREW/Precipitation/Daily">ftp://www.tiftonars.org/databases/LREW/Precipitation/Daily</a>	Summed, averaged and normalized monthly. Some in-filled values.
Stream Flow (m <sup>3</sup> )	1968- 2005	<a href="ftp://www.tiftonars.org/databases/LREW/streamflow/daily">ftp://www.tiftonars.org/databases/LREW/streamflow/daily</a>	Daily values averaged and normalized monthly. Some in-filled values.
NO <sub>3</sub> Concentration (mg/L)	1974- 2003	<a href="ftp://www.tiftonars.org/databases/LREW/stream_water_quality/long_term_water_quality">ftp://www.tiftonars.org/databases/LREW/stream_water_quality/long_term_water_quality</a>	Daily/weekly values averaged and normalized by median monthly. Some In-filled data.
NO <sub>3</sub> Load (kg)	1974- 2003	<a href="ftp://www.tiftonars.org/databases/LREW/stream_water_quality/long_term_water_quality">ftp://www.tiftonars.org/databases/LREW/stream_water_quality/long_term_water_quality</a>	Daily/weekly values averaged and normalized by median monthly.

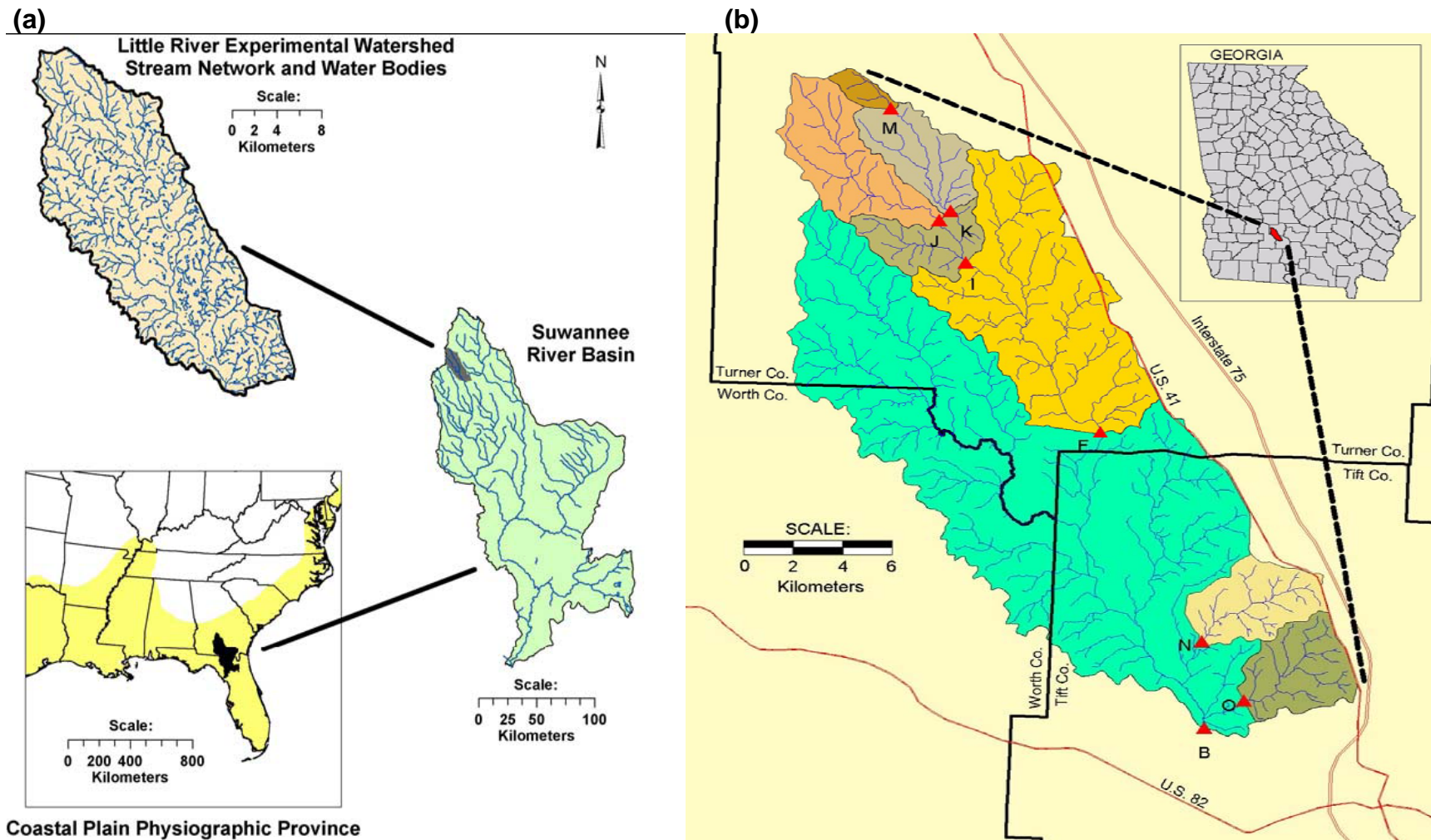


Figure 3-1. The Little River Watershed and sub-basins, Tifton, Georgia. (a) Position relative to the entire Suwannee River Basin [Bosch, Sheridan, Lowrance, et al., 2007]. (b) The total area is 334 km<sup>2</sup>. All analysis was done with data from upland sub-basin K, with an area of 16.8 km<sup>2</sup>. Triangles indicate weir/stream flow measurement locations for each sub-basin.

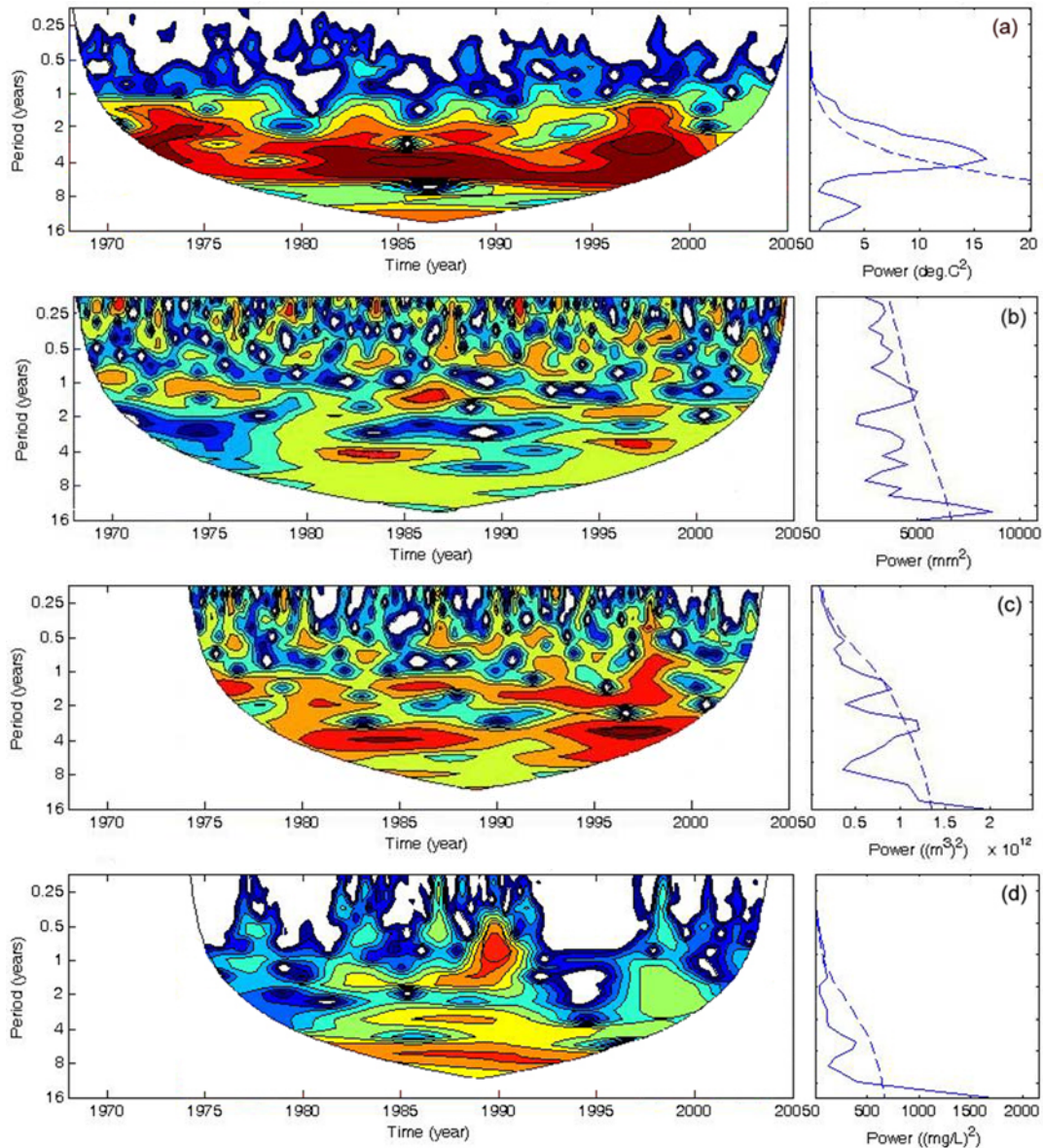


Figure 3-2. Significant Wavelet Power Spectra are shown within the cone-of-influence, which depends on time series length and degrees of freedom. Figures are color-mapped to indicate high wavelet power with reds and oranges, and low powers in blue and white. The Global Wavelet Spectrum (GWS) at the right of each figure shows power integrated over all scales and times. The 95% confidence limit is shown on the GWS (dashed blue line), the periodicities above which show significance. (a) Monthly NINO 3.4 ( $^{\circ}\text{C}$ ) Sea Surface Temperatures, (b) Monthly precipitation anomaly (mm), (c) Monthly stream flow anomaly ( $\text{m}^3$ ), (d) Monthly  $\text{NO}_3$  concentration anomaly (mg/L), (e) Monthly  $\text{NO}_3$  load anomaly (kg).

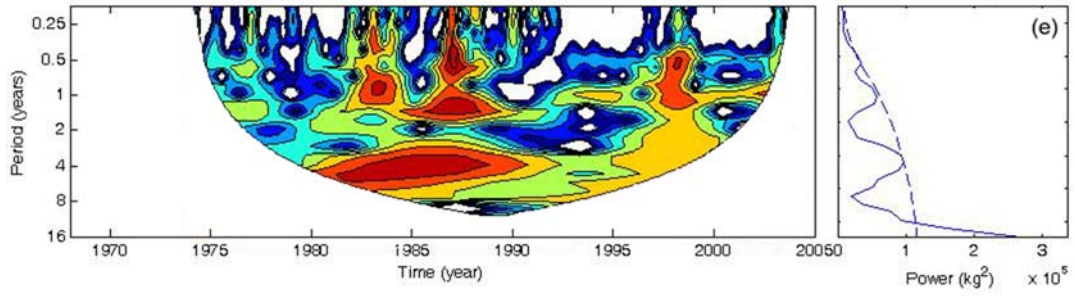


Figure 3-2. Continued.

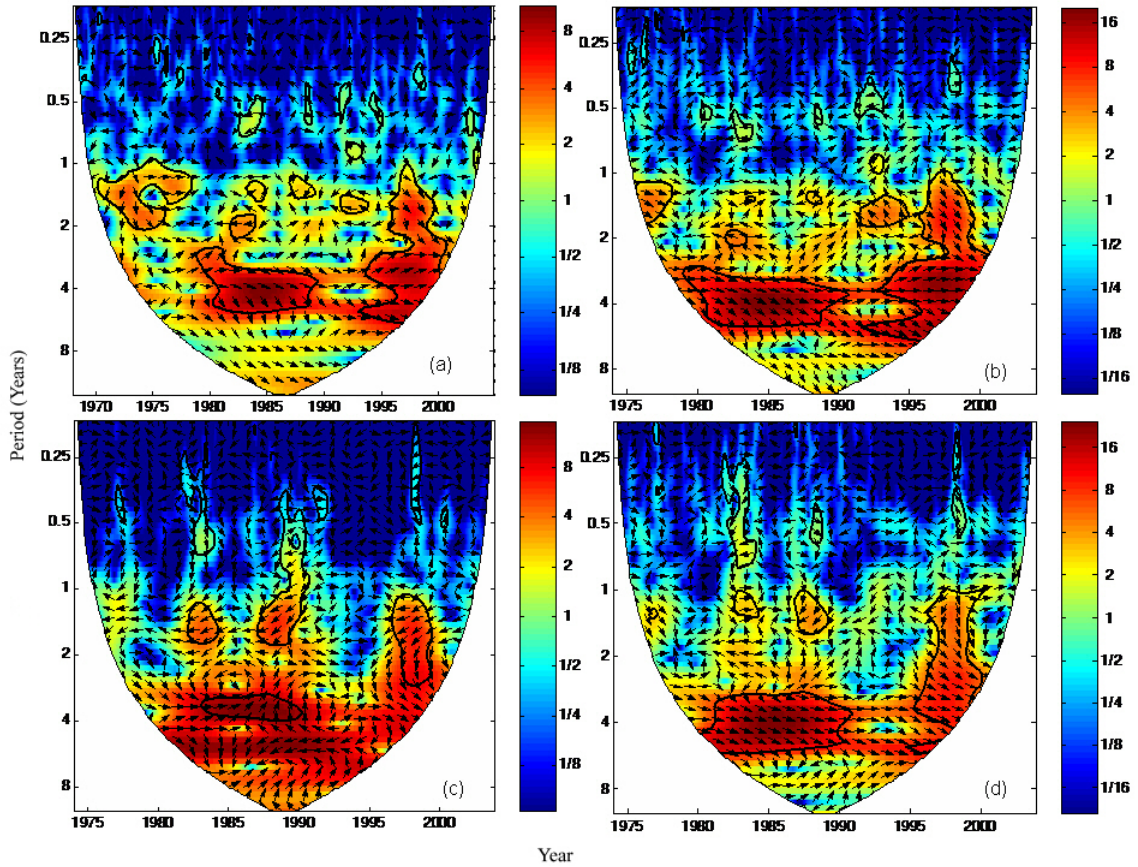


Figure 3-3. Cross Wavelet Spectrum between (a) monthly SST and Precipitation, (b) monthly SST and stream flow ( $m^3$ ), (c) monthly SST and  $NO_3$  concentration ( $mg/L$ ), (d) monthly SST and  $NO_3$  Load ( $kg$ ). Black figure outlines indicate areas significant to 95% confidence, while arrows represent variables' phase relationship. Arrows pointing clockwise indicate in-phase behavior, while counter clockwise arrows indicate anti-phase behavior.

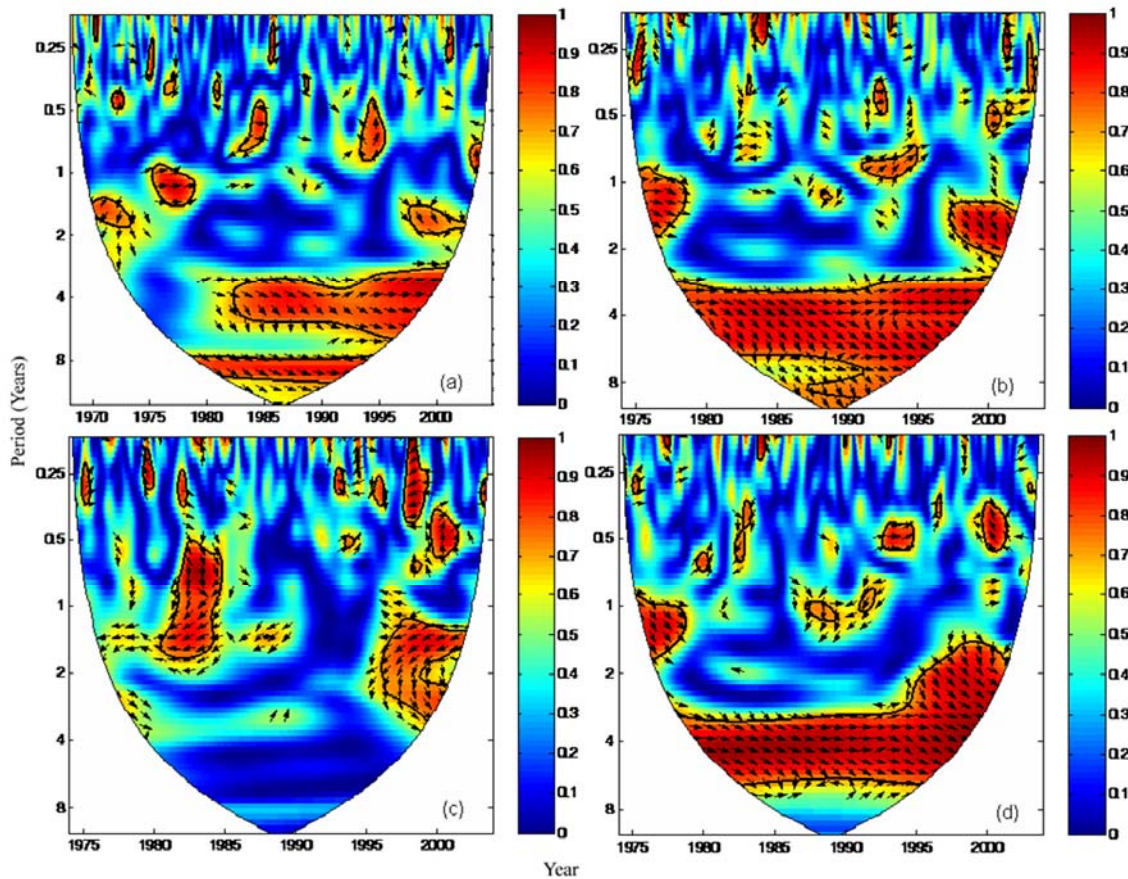


Figure 3-4. Wavelet Coherence Analysis between (a) monthly SST and Precipitation, (b) monthly SST and stream flow ( $\text{m}^3$ ), (c) monthly SST and  $\text{NO}_3$  concentration ( $\text{mg/L}$ ), (d) monthly SST and  $\text{NO}_3$  load ( $\text{kg}$ ). Black figure outlines indicate areas significant to 95% confidence, while arrows represent variables' phase relationship. Arrows pointing clockwise indicate in-phase behavior, while counter clockwise arrows indicate anti-phase behavior.

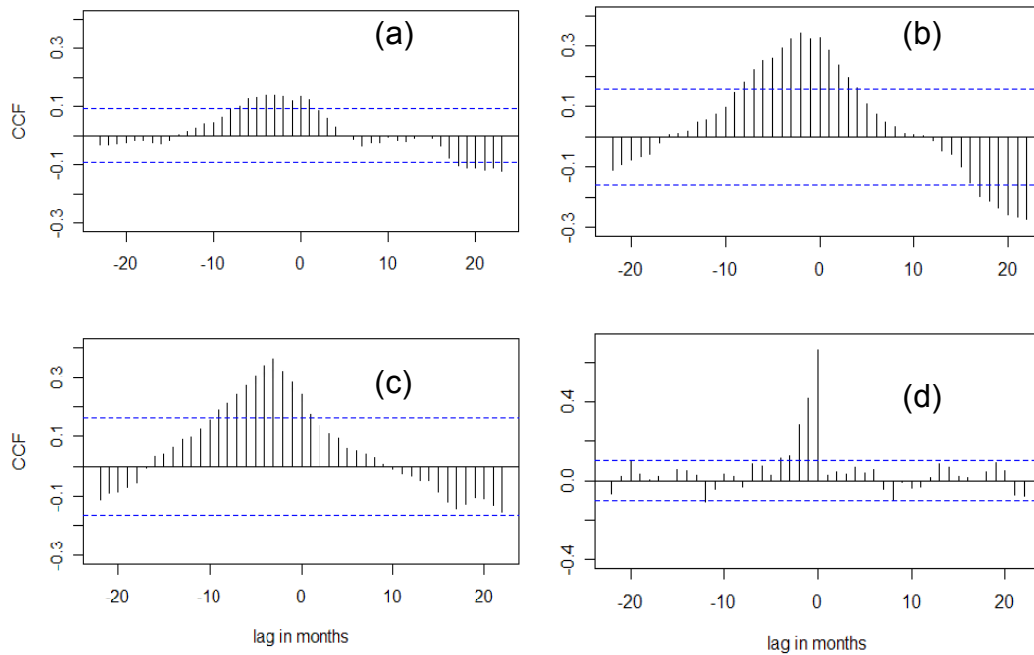


Figure 3-5. Cross-correlation analysis between NINO 3.4 ( $^{\circ}\text{C}$ ) and LRW sub-basin K (a) precipitation (mm) (b) stream flow ( $\text{m}^3$ ) (c)  $\text{NO}_3$  (kg), and between (d) precipitation (mm) and stream flow ( $\text{m}^3$ ). A negative lag indicates months that the NINO 3.4 SST leads the variable in question. The strongest Cross-Correlation Function (CCF) relationship within the NINO 3.4 index is SST leading stream flow by two months, while the strongest hydrologic relationship overall is between precipitation and stream flow. Values above or below dashed lines indicate significant correlation above 95% confidence, corrected for autocorrelation.

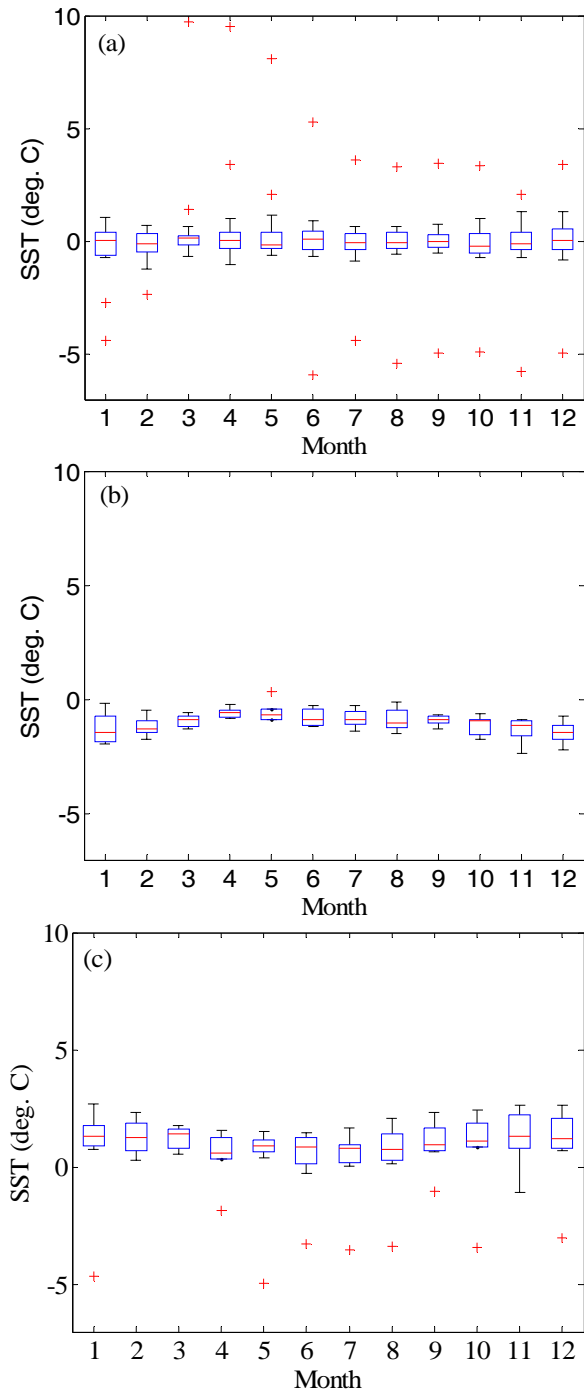


Figure 3-6. Box and whisker plots of observed NINO 3.4 SST anomalies ( $^{\circ}\text{C}$ ) for M-ENSO (a) neutral years, (b) La Niña years, and (c) El Niño years. Box lines are at the lower quartile, median, and upper quartile values. Whiskers extend from box ends to upper and lower adjacent values, defined as the largest or smallest observation that does not exceed the upper or lower quartile  $\pm 1.5 \times$  interquartile range. Outlier points indicate data that fall outside the whiskers, and are indicated by crosses.

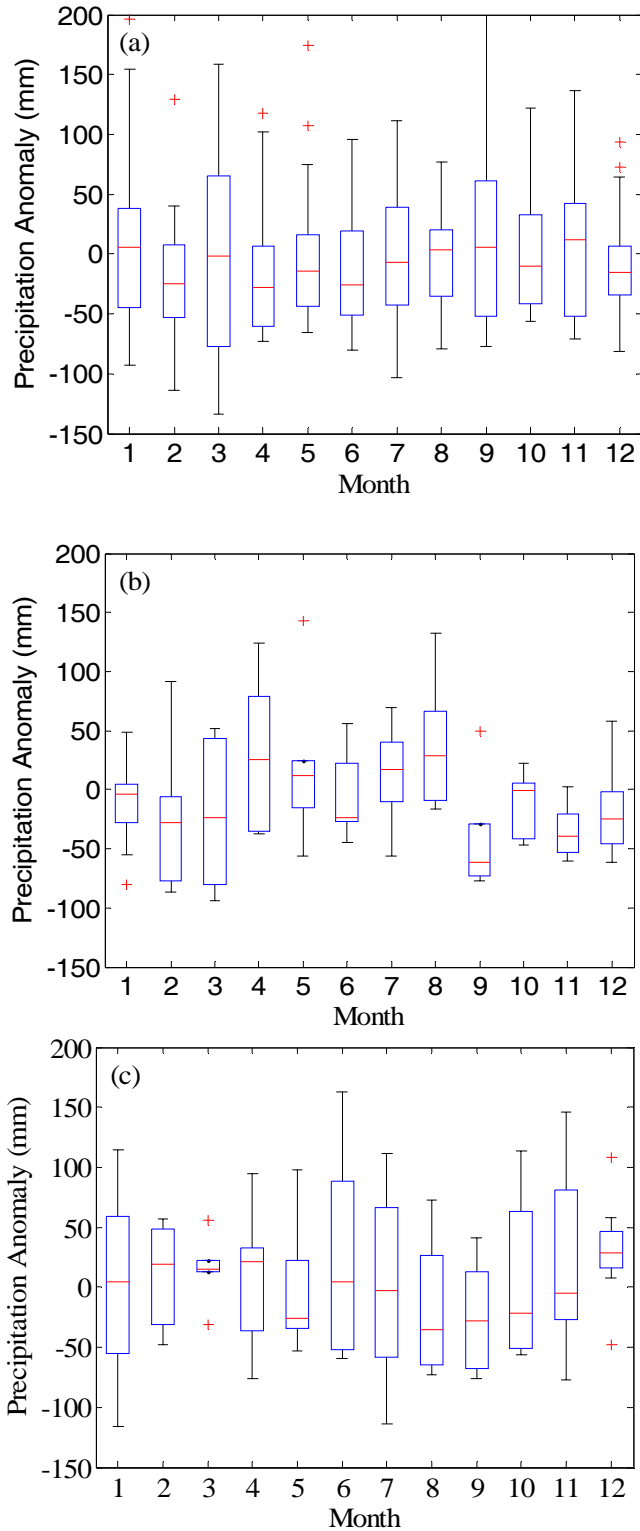


Figure 3-7. Box and whisker plots of observed precipitation anomalies (mm) for M-ENSO (a) neutral years, (b) La Niña years, and (c) El Niño years. Box lines are at the lower quartile, median, and upper quartile values.

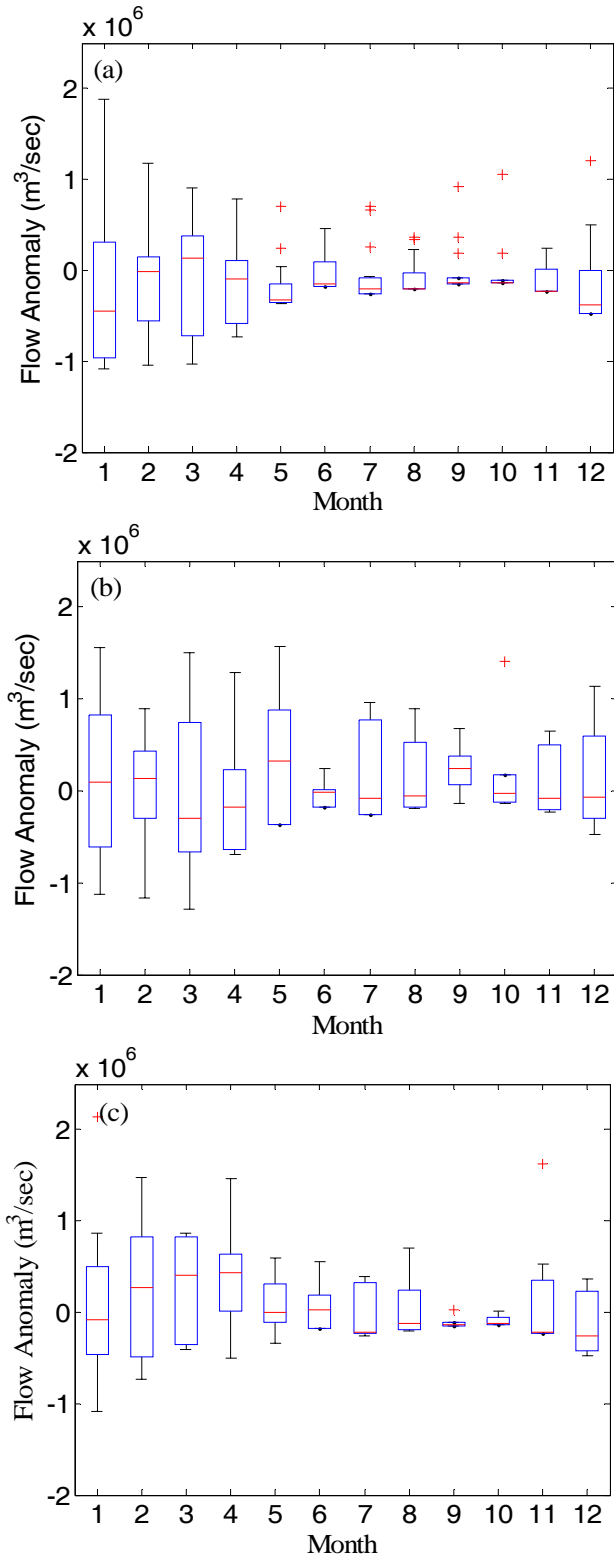


Figure 3-8. Box and whisker plots of observed stream flow anomalies ( $\text{m}^3/\text{sec}$ ) for M-ENSO (a) neutral years, (b) La Niña years, and (c) El Niño years. Box lines are at the lower quartile, median, and upper quartile values.

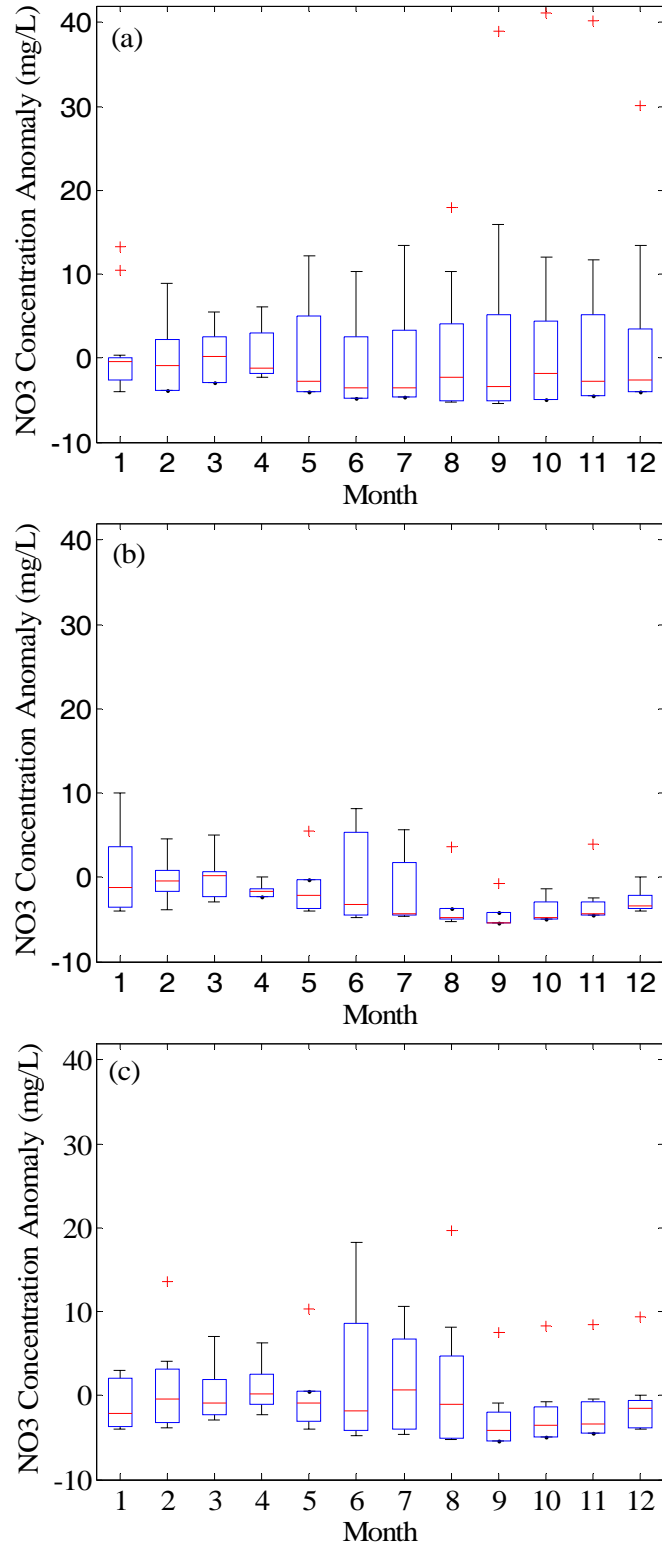


Figure 3-9. Box and whisker plots of observed NO<sub>3</sub> concentration anomalies (mg/L) for M-ENSO (a) neutral years, (b) La Niña years, and (c) El Niño years. Box lines are at the lower quartile, median, and upper quartile values.

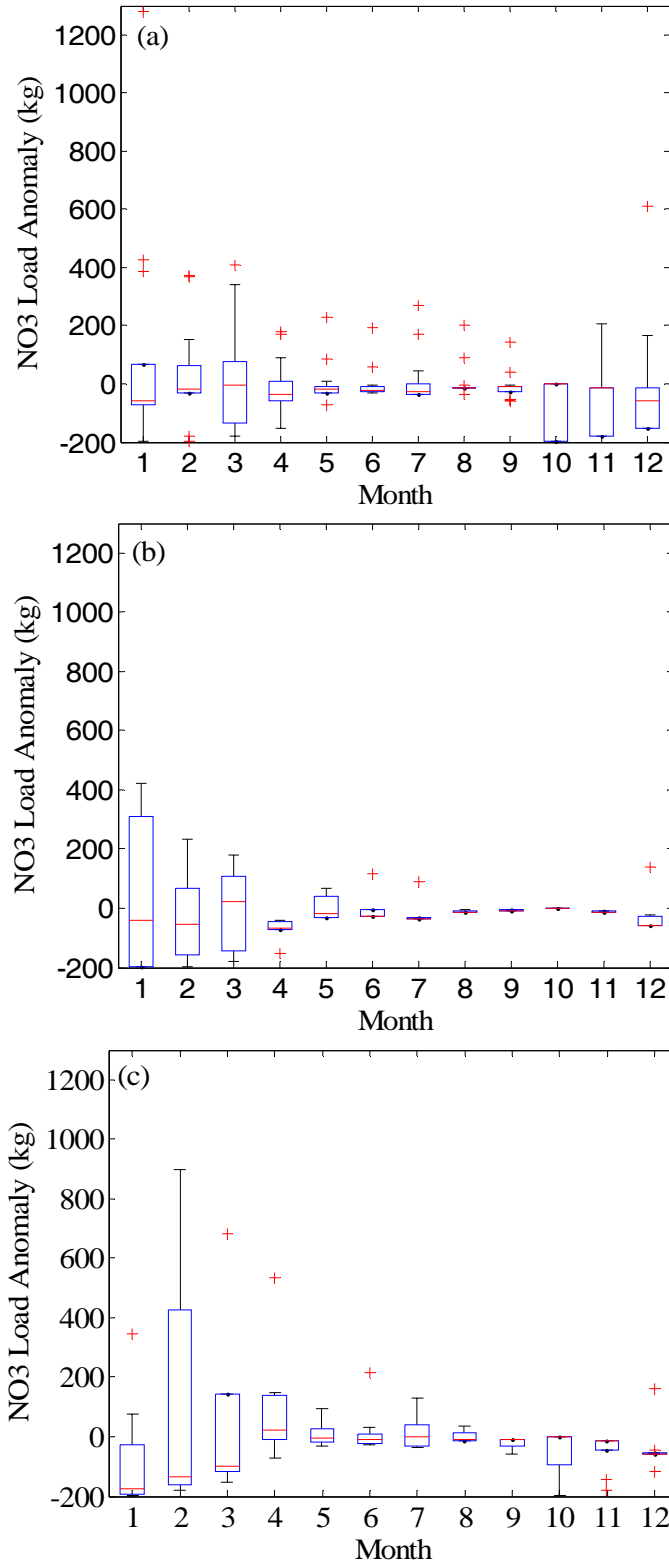


Figure 3-10. Box and whisker plots of observed NO<sub>3</sub> load anomalies (kg) for M-ENSO (a) neutral years, (b) La Niña years, and (c) El Niño years. Box lines are at the lower quartile, median and upper quartile values.

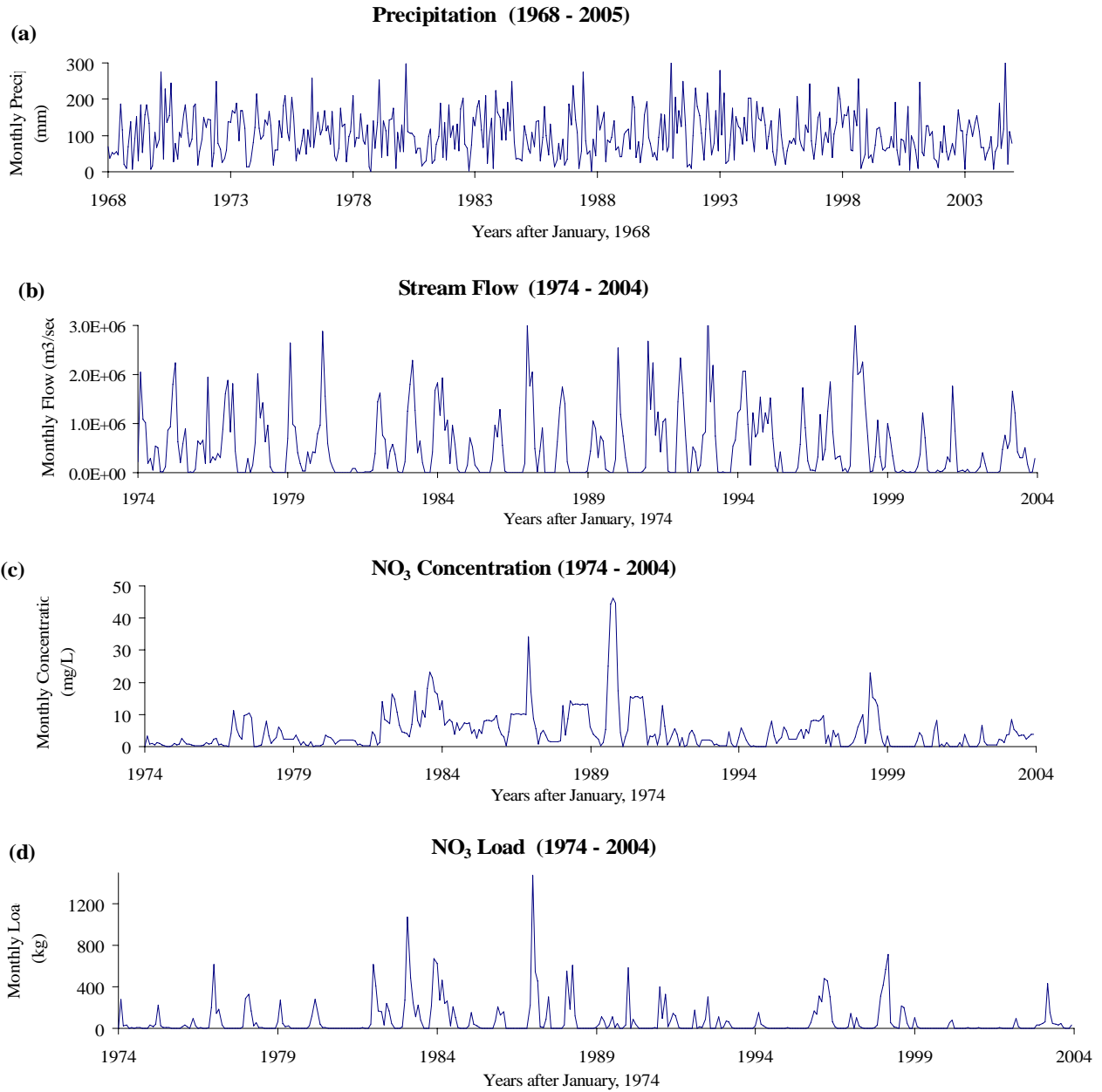


Figure 3-11. Raw monthly time series of (a) precipitation (mm), (b) stream flow (m<sup>3</sup>/sec), (c) NO<sub>3</sub> concentration (mg/L) and (d) NO<sub>3</sub> load (kg)

## CHAPTER 4 INTEGRATION OF ENSO SIGNAL POWER THROUGH HYDROLOGICAL PROCESSES IN THE LITTLE RIVER WATERSHED

### Introduction

When the relationship of the El-Niño /Southern Oscillation (ENSO) to hydrology is commonly discussed, it is typically in terms of the ability to separate significantly different hydrologic variable responses depending on the type of ENSO anomaly that has taken place. Using this kind of analysis, ENSO phase has been shown to have predictable effects on precipitation, stream flow, monsoon occurrence, crop yield, cholera occurrence, flood frequency, phytoplankton growth, and water quality data in different regions around the world [*Chiew et al.*, 1998; *Rajagopalan and Lall*, 1998; *Hansen et al.*, 1997; *Pascual et al.*, 2000; *Piechota and Dracup*, 1999; *Keener et al.*, 2007, 2010; *Nezlin and Li*, 2003; *Chiew and McMahon*, 2003]. From a research standpoint, most of the work relating ENSO trends to proxy variables had been done on precipitation records until the mid 1990s, at which point increasing numbers of studies started to focus on ENSO relationships with stream flow as well as other environmental variables [*Cayan et al.*, 1999; *Charles et al.*, 1997; *Fraedrich and Muller*, 1992; *Gutierrez and Dracup*, 2001; *Ropelewski and Halpert*, 1987; *Zorn and Waylen*, 1997]. The signals in stream flow are typically complex, representing the integration of both climatic, landscape, and anthropological responses that are able to increase the power of the inherent ENSO signal in regional precipitation data.

With increasing research on ENSO and stream flow relationships, it has been observed in case studies around the world that the complex relationships in a hydrological system can serve to increase the inherent ENSO signal power within precipitation in other hydrologic variables. For example, increased atmospheric CO<sub>2</sub>

levels representing greenhouse gas global warming scenarios have been shown to have a doubling effect on winter stream flow signal in El Niño years in north California [Maurer *et al.*, 2006], while stream flow responses to ENSO in the western United States have generally been shown to be accentuated over precipitation due to differences in the duration of wet phases in different ENSO regimes [Cayan *et al.*, 1999]. Multiple studies at both the regional and global scale have discovered that the relationship between ENSO and stream flow response can be stronger than that with its relationship to precipitation, likely due to stream flow effectively spatially and temporally integrating the signal in rainfall and reducing the noise [Chiew and McMahon, 2003; Keener *et al.*, 2010; Whiting *et al.*, 2004; Dettinger and Diaz, 2000].

This non-intuitive relationship strength could prove to be quite useful in terms of making seasonal climate predictions based on climate indices such as ENSO, as a geographic area with a seemingly weak ENSO precipitation signal could have a stronger stream flow or other proxy variable climate signal that could be used for predictive purposes. The use of seasonal forecasts of both flows and other hydrologic variables could also more immediately benefit water resource managers or farmers, as decisions on irrigation and allocation would be able to incorporate additional climate information, and would not be predictions made so far in the future as to render them virtually unusable in typical policy-based management plans.

In Chapter 3, both univariate and multivariate wavelet analysis were used to quantify the significance of a teleconnection between the continuous NINO 3.4 index of sea surface temperatures (SST) and observed precipitation, stream flow, and nitrate concentration and load in the Little River Watershed (LRW) in Georgia. Mechanistically,

El Niño (La Niña) events result in increased (decreased) sea surface evaporation. The mid-latitude jet stream is displaced equatorially (poleward), increasing (decreasing) winter frontal precipitation in the southeast United States. Additional winter moisture is advected into the southeast from the tropical Pacific by the subtropical jet stream [Ropelewski and Halpert, 1987]. Precipitation in El Niño winters typically increases as a result, and as seen in the large El Niño events centered around 1985 and 1997-98 in the LRW, resulted in increased river discharge and nutrient pollution transport [Keener et al., 2010].

In Chapter 4, hydrological simulation using the Soil and Water Assessment Tool (SWAT) and observed data is used to explore the ENSO signal power in stream flow time series compared to precipitation. Although the thirteen weather stations used to form the precipitation series in this research are well distributed across the 16.8 km<sup>2</sup> area of basin K in the LRW, spatial variability of rainfall in the southeast United States is high, and the weather stations still do not encompass all of the precipitation variability inherent in the watershed [Baigorria et al., 2007]. Specifically, it is shown how: (1) the observed and SWAT simulated stream flow signal in the LRW has a more powerful relationship with ENSO than that of observed precipitation, (2) validated SWAT simulations of groundwater dynamics can help us identify what is causing the climate and stream flow signal power increase, and (3) wavelet analysis can be used in a novel way to elucidate not only changes in spectral strength over time, but also to identify mechanistic similarities in simulated data.

We hypothesize that there are several mechanisms of ENSO/stream flow signal power increase: If groundwater flow in the LRW is responsible for up to 80% of the total

stream flow [Sheridan, 1997], as well as comprising the main route for movement of soluble nutrients [Lowrance *et al.*, 1984], then the power of the ENSO signal in stream flow may be strengthened by the significant role of groundwater and the presence of the Hawthorn confining layer, both restricting flow into the deep aquifer system and increasing the amount of interflow in the root zone represented in the stream flow record [Stringfield, 1966; Sheridan, 1997]. Another possibility is that in anomalous ENSO phases, the potential evapotranspiration (ET) is affected enough to significantly influence stream flow. For example, if in an El Niño winter in southern Georgia and the LRW, temperature decreases and precipitation significantly increases; then conversely, ET may significantly decrease due to less solar radiation and less of a vapor pressure deficit. In turn, this could increase the stream flow signal.

To elucidate what is mechanistically happening to the climate signal in the LRW, a SWAT model of basin K that is calibrated and validated for hydrology, phosphorus and total nitrogen nutrient cycles was used to look at simulated surface and groundwater movement and runoff from 1979 to 2005, with observed land use input from LandSat images and observed crop rotations and management [Bosch *et al.*, 2004, 2006; Cho *et al.*, 2010; Feyereisen, Strickland, *et al.*, 2007]. Using a validated SWAT model of the LRW enables us to analyze detailed continuous simulations of the entire water budget, and more specifically the groundwater budget records to look for ENSO trends that may be visible in the groundwater hydrology time series. Additionally, simulated and observed potential ET records can be analyzed in the same manner.

Simulated hydrological cycle components are visualized using an average annual water budget and as a percentage of observed annual average precipitation. They were

then analyzed using exceedance curves to show the 10, 50, and 90% probabilities that a specific variable was equaled or exceeded, separated by monthly ENSO phase dynamics and compared to the LRW observed climatology during all phases. The exceedance probabilities in the observed ENSO precipitation were found to be even more pronounced in the SWAT simulated flow and groundwater variables, demonstrating the various flows increasing inter-annual variability signal power as compared to rainfall.

Wavelet analysis, a spectral method of decomposing a time series into time and frequency space that allows the identification and analysis of dominant localized variations of power, was used as in Chapter 3. There, it was used to analyze the NINO 3.4 SST index and observed hydrological and nutrient data in the LRW basin K. Here, wavelet analysis is used to analyze and compare various simulated SWAT components of the hydrological cycle with the NINO 3.4 index. In this way, we can quantify components of the hydrological cycle that are strengthening the ENSO related stream flow signal. Patterns found in the observed rainfall are more spectrally powerful in the observed and simulated stream flow, and these shared patterns are identified as powerful signals of interest in the SWAT simulated groundwater dynamics that increase the oscillatory climate-related signals.

## **Data and Methods**

### **Field Site and Data: The Little River Watershed**

The same field site, the Little River Watershed (LRW), basin K, is used as is described in Chapter 3, Data and Methods, section Field Site: Little River Watershed. The same observed precipitation from 13 spatially distributed weather stations, stream flow, and nutrient data from basin K is also used as described in Chapter 3, Data and

Methods, section Little River Watershed Data, as input and calibration data for SWAT. Additional weather input, including minimum and maximum daily air temperatures, solar radiation, and relative humidity data were obtained from a University of Georgia weather station that is 1 km northeast of LRW-K [Bosch *et al.*, 2004; Cho *et al.*, 2010]. A digital elevation model (DEM) with a 30 meter grid size was used in SWAT to specify sub-basins, stream networks, and topography, and digital soil data from the USDA-NRCS Soil Data Mart were used to derive the soil related parameters [Cho *et al.*, 2010].

Agricultural land boundaries and non-row crop land cover were input from one meter resolution USGS orthoquadrangle aerial pictures, and while the land boundaries were assumed to be constant during the period of simulation, changes in crop rotations and management within the fields were input using observed harvested crop area data from the University of Georgia Cooperative Extension service [Bosch *et al.*, 2004; Cho *et al.*, 2010; Feyereisen, Strickland, *et al.*, 2007].

Delineations of ENSO phase are done via the categorical monthly M-ENSO index [Gérard-Marchant *et al.*, 2008], and from the continuous NINO 3.4 SST monthly index as described in the introductions of Chapter 2 and Chapter 3, respectively.

### **SWAT Model Hydrologic Calibration and Validation**

The Little River Watershed is a part of the USDA-ARS Watershed Assessment Study and the national Conservation Effects Assessment Program (CEAP), which has the aim of quantifying the effects and successes of soil and water conservation and management procedures around the country to support sound policy implementation [USDA-ARS, 2005]. To gather data for this national assessment, researchers at the SEWRL in the Little River Watershed have performed a calibration and sensitivity analysis on basin K's hydrologic and subsequently its nutrient parameters in SWAT that

could provide guidance for future SWAT calibration in the southeastern U.S [Feyereisen, Strickland, et al., 2007; Cho et al., 2010]. SWAT is a versatile agro-hydrologic, geochemical process model that can simulate hydrologic budgets and nutrient processes at either field or watershed scales [Neitsch et al., 2005]. SWAT is spatially semi-distributed, as it first delineates sub-catchments via topography and a designated threshold area, and then further divides the sub-catchments into Hydrological Response Units (HRU) based on unique inputs of management, soil, and vegetation parameters. Each HRU is modeled individually, then aggregated at the sub-catchment level and routed to the associated stream reach. Groundwater flow is also spatially semi-distributed, and considers specific hydraulic conductivities and storage coefficients at the HRU level only. Full theoretical documentation of SWAT is available online in Neitsch et al, 2005. In its various incarnations, SWAT has been successfully tested and modified for different environmental conditions throughout the world [White and Chaubey, 2005]. The version of SWAT used in these modeling studies is AVSWATX, which is the same process based model with a GIS interface implemented in ArcView 3.2.

For hydrological calibration between 1979-1994 and validation from 1995-2004, the manual calibration procedure outlined in the 2000 SWAT user manual was followed to maximize the Nash-Sutcliffe Efficiency and minimize the sum-of-squared differences of the water budget calculation ( $SSD_{WBC}$ ) [Feyereisen, Strickland, et al., 2007; Neitsch et al., 2002]. First, annual surface flow was balanced by adjustment of the NRCS runoff curve number, followed by groundwater baseflow adjustment to observed values [Shirmohammadi et al., 1986]. Model evapotranspiration (ET) output was calibrated to

match observed ET, minimizing the  $SSD_{WBC}$ , and finally, parameters influencing baseflow speed, shallow aquifer depth and surface runoff lag were adjusted to maximize the Nash-Sutcliffe efficiency (NSE) [Feyereisen, Strickland, et al., 2007]. These calibrated parameters were used as the base values for the sensitivity analysis on the 16 selected SWAT hydrologic parameters covering surface, sub-surface, and overall basin flow response. Input parameters chosen for calibration and sensitivity analysis were based on a combination of knowledge from the results of simulations in different basins adjacent to K within the Little River Watershed [Van Liew et al., 2007; Bosch et al., 2004], and several investigatory soil parameters of interest.

Local sensitivity was calculated using the sensitivity coefficient,  $S$  (Equation 4-1), which quantifies the ratio between the rate of change of a model output ( $O$ ) and the rate of change of model input parameter ( $P$ ) of interest.

$$S = \frac{\partial O}{\partial P} \quad (4-1)$$

Relative sensitivity, the unit-less variable  $S_r$ , was then calculated as equation 4-2 [Haan, 2002], where  $O_{P+\Delta P}$  and  $O_{P-\Delta P}$  are parameter outputs plus or minus 25% of the input parameter base value, normalized by the model output with the parameter at the base value,  $O_P$ , and the absolute change in the value of the input parameter,  $\Delta P$ , with respect to its initial value,  $P$ .

$$S_r \cong \frac{[(O_{P+\Delta P} - O_{P-\Delta P}) / O_P]}{2\Delta P / P} \quad (4-2)$$

This measure of local relative sensitivity, while it does measure parameter influence on model output, does not take parameter interactions into account, and does not simultaneously vary parameters in a global sense. Feyereisen et al (2007) achieved a final model monthly NSE of 0.88 and a daily NSE of 0.56. Relative sensitivity analysis

results showed that surface response parameters were much more sensitive than basin and sub-surface parameters. The five most sensitive hydrologic input parameters for total water yield, storm flow, and base flow proved to be mainly the CN for cropped land (CN = 76), followed by the CN for forested land (CN = 50), soil evaporation compensation factor, soil available water content, and soil bulk density, while insensitive to the other 11 parameters tested [Feyereisen, Strickland, et al., 2007]. Overall, the CN for cropped land and the soil available water content were the parameters that dominated the SWAT calibration for the Little River Watershed basin K.

The dominance of the curve number for cropped land on the model output was surprising, given that 30% of the area in basin K is agricultural in nature [Bosch et al., 2004; Feyereisen, Strickland, et al., 2007]. However, a change in only 1% of the base value of the CN for cropped land would result in a 74% increase in total water yield output, and a 422% increase in storm flow output [Feyereisen, Strickland, et al., 2007]. This sensitivity is in part due to the increased surface runoff from even average-sized precipitation events on cropped land.

Studies have been done on the entire LRW to evaluate the hydrologic impacts of observed land-use change over the past 35 years. As part of the USDA's Conservation Reserve Program (CRP), over 13 million ha of erodible and environmentally sensitive agricultural land has been converted into non-tilled land since 1985 [Bosch et al., 2006], including 261,511 ha of trees planted in Georgia alone [Moorhead and Dangerfield, 1996]. The potential for the CRP program to cause dramatic changes in forested land-use within many watersheds is large, with resulting change in ET, stream flow, and infiltration regimes. Using SWAT on LRW-K, it was found that the land-use changes that

occurred between 1975 and 2003 did not significantly affect the stream flow or other hydrological regimes of the basin, although the land-use percentages did not drastically change from agriculture to forest during the dates monitored (Figure 4-1) [Bosch *et al.*, 2006]. In the whole time period analyzed, there was only a 1% decrease in total upland and riparian forest acreage, with a 3% increase between 1985 and 2003 when the CRP effects would have been expected to appear. As seen in Figure 4-1, a 12% decrease in fallow, 7% increase in agriculture, and 5% increase in pasture acreage was observed over the whole watershed [Bosch *et al.*, 2006].

SWAT partitions groundwater into two aquifers: a shallow, unconfined aquifer that may interact with surface soil layers, and a deep, confined aquifer in which the contributed flow is assumed to exit the watershed. In the SWAT representation of LRW-K, deep aquifer recharge is only 1% of total precipitation due to the confining Hawthorn layer, and therefore almost negligible [Rawls *et al.*, 1976]. To investigate certain processes in the watershed, specific variables were isolated within SWAT (Figure 4-2). For the LRW in SWAT, simulated surface runoff is calculated from the empirical SCS Curve Number method, based on precipitation, soil parameters and water content [USDA, 1972]. Simulated potential ET is computed via the Priestly-Taylor method [Priestley and Taylor, 1972]. Percolation of groundwater occurs when the field capacity of the soil layer is exceeded and the layer below is not saturated. If percolated water passes through the last root zone layer, it enters the unsaturated vadose zone before becoming shallow aquifer recharge.

In SWAT, interflow is called “lateral flow”, and is defined as sub-surface flow within the root zone. Interflow is significant in areas with soils having high hydraulic

conductivity in the surface layers, and an impermeable layer at shallow depths, which occurs in some areas of the LRW in which the Hawthorn Formation is either at or very close to the surface. Groundwater flow represents baseflow that originates from the vadose zone and shallow aquifer of the SWAT model, and is dependent on the particular watershed's storage capacity and physical characteristics. All flows are routed to the open stream channel, at which point they are routed using Manning's Equation and a variety of open channel hydrodynamic methods [Neitsch *et al.*, 2005].

### **Water Budget and Exceedance Curves**

An annual hydrologic budget of relevant variables is a simple method of comparing relative amounts of water simulated by SWAT in the LRW. In this case, since we are interested in the relationship between hydrology and ENSO climatology, the annual average water budget for each variable has been calculated for all years, and for each defined M-ENSO year. The SWAT simulated variables SUR\_Q (surface runoff), PERC (percolation past the root zone), GW\_Q (baseflow contribution to stream flow), LAT\_Q (root zone flow contribution to stream flow), Q (total stream flow), and total ET (evapotranspiration) were compared as single yearly average values over the simulation period 1979 to 2004 in different categorical ENSO phases. The observed actual precipitation record was also used as a point of comparison. The water budget was represented as the total annual average water yield for each variable for all years, and as a percentage of total annual observed precipitation for each of the three ENSO phases.

The same SWAT simulated variables listed above and observed precipitation were also utilized in probability of exceedance graphs. An exceedance curve is a backwards cumulative form of a probability density curve, showing what percentage of area under

the probability density curve lies to the right of the value of the variable on the x-axis. In this case, the probability of exceeding each value for each variable was calculated for four different cases: all available data, or the “climatology” (black dots), El Niño (blue dots), La Niña (red dots) and Neutral ENSO phase (green dots). One then can compare the curves in each ENSO phase with both the whole climatology and against each other. For example, a tendency toward drier than normal precipitation conditions in La Niña would be indicated if the red curve lies to the left of the black curve. Exceedance curves should not be read as forecasts. If the red and black curves overlapped, it would not indicate a forecast for average conditions in a La Niña phase, but that there are equal probabilities in a La Niña phase for anything to occur that has happened during the total climatological period. The values for each variable at the 10, 50, and 90% probability of exceedance were compared across ENSO phases and climatologies.

### **Wavelet Analysis**

All technical wavelet methodology is the same as detailed in Chapter 3, Data and Methods sections Wavelet Analysis and Cross Wavelet and Coherence Transforms. Typically, as in Chapter 3, wavelet analysis is used in conjunction with geophysical data to visualize how dominant frequency structures in non-stationary data change over time. In a more novel use, here we use wavelet analysis to observe whether SWAT simulated components of the hydrological cycle share the climate-based significant spectral variability we identified in the observed stream flow record. By analyzing SWAT simulated surface runoff, groundwater and interflow, percolation past the root zone and evapotranspiration, patterns can be identified that are shared with those seen in the wavelet spectra of observed surface runoff.

Hydrological components that may be strengthening the ENSO signal power in stream flow time series as compared to precipitation would be expected to share more spectral power with the NINO 3.4 SST index. Simulated individual variables with significant visible ENSO inter-annual power were then analyzed by cross-wavelet and wavelet-coherence analysis with the NINO 3.4 index to confirm areas of shared significant power and localized correlation. In this way, we were able to visualize components of the hydrological cycle that strengthen the ENSO related stream flow signal. Univariate wavelet analysis, and multivariate cross-wavelet (XWT) and wavelet coherence (WTC) analyses were done on observed NINO 3.4 SST records and the simulated SWAT variables total flow, groundwater flow, interflow, percolation past the root zone, and evapotranspiration from 1979-2005. Processed daily SWAT simulated flow, groundwater components, and ET were summed into monthly cumulative values and normalized by monthly average for input into the wavelet analysis.

## **Results**

### **Observed Precipitation and Stream Flow**

In Chapter 3, an interesting result found through wavelet analysis was that the significant spectral climate-based signal in the observed stream flow data was stronger than that seen in the corresponding precipitation data (Figure 4-3). This can be seen in the fact that the areas of high spectral power, areas of red and orange in the wavelet spectra, are more widespread and cohesive throughout the wavelet spectrum of observed stream flow records (Figure 4-3b) than precipitation (Figure 4-3a), as well as in known ENSO periodicities sustained around 3-7 years and surrounding times of high El Niño abnormalities in 1997 and 1983.

Additionally, the global wavelet spectrum (GWS) on the right side of each wavelet spectrum figure shows the more standard spectral visualization of time-integrated variance of the energy coefficients at every scale throughout the wavelet transform (Figure 4-3). In the GWS, scales that are significant above the 95% level against a red noise background exceed the dashed line. While the observed precipitation time series only shows 95% significance within the cone-of-influence from the 1.2 to 1.7 year period, the observed stream flow signal shows significance both from the 1.5-1.8 and 3.3- 4.4 year period. Observed stream flow also shared more significant areas in cross-wavelet and wavelet coherence analysis with the NINO 3.4 index than it did with precipitation (Chapter 3), reinforcing that the inter-annual climate signal is indeed stronger in flow.

### **SWAT Water Budget and Exceedance Curves by ENSO Phase**

Simulated hydrologic variables were compared in the water budget as single yearly average values over the simulation period from 1979 to 2004, and compared to their values when separated by M-ENSO phase. The SWAT simulated variables examined in detail were SUR\_Q, PERC, GW\_Q, LAT\_Q, Q, and total ET. The observed precipitation record was also used as a point of comparison. The water budget is first visualized as the total annual average water yield for each variable for all years, and for each of the three ENSO phases (Figure 4-4).

Figure 4-4 shows that in the El Niño phase in the LRW-K, there is more total precipitation than in other ENSO phases, while there is less precipitation in the La Niña phase. When this is visualized in the water budget, we see that the trend of greater precipitation in El Niño years is also reflected in greater simulated surface runoff, stream flow, interflow, groundwater flow, and percolation in El Niño years, with the greatest

disparity in groundwater flow and percolation. On the other hand, total average evapotranspiration remains fairly consistent through each ENSO phase.

When the same data are analyzed in terms of the simulated hydrologic variables as a percentage of the total observed precipitation (Figure 4-5), the picture can be explained further. As a percentage of total precipitation, ET in El Niño years was less than all other ENSO phases, while it was greater in La Niña years. This implies that the increased (decreased) precipitation and decreased (increased) temperature in El Niño (La Niña) ENSO phases does in fact decrease (increase) the relative percentage of total ET. Combined with the observation that the relative increase or decrease in precipitation during El Niño or La Niña years is mirrored in the simulated groundwater flow and percolation, it appears that mechanistically, both groundwater flow and ET amounts respective to precipitation are contributing to the increased power of the ENSO signal seen in observed stream flow records.

The probability of exceedance curves are shown in Figure 4-6. The general trends plotted as monthly values separated by M-ENSO phase follow the same patterns that are present in the water budgets (Figure 4-4 and 4-5). In the curves for all variables (Figure 4-6 a-g), the total climatological distribution overlays with the neutral M-ENSO year distribution very well, meaning that neutral and average observed conditions have the same basic probabilistic distribution for all variables. The values of the given variables at 10, 50, and 90% probability of exceedance during the different M-ENSO phases are listed in Table 4-1. Quantitatively as well, the climatology and neutral values for all variables are either exactly the same or very close to being the same, for both 10, 50 and 90% probabilities (Table 4-1). It should be noted, however, that the

climatological distribution is only based on the available data, and therefore may not capture extreme historical events if they were not in this data record.

For observed precipitation (Figure 4-5a), there was a general pattern of greater probability of observing lower(higher) than normal values in La Niña(El Niño) phases, and slightly higher(lower) than average values in El Niño(La Niña) phases. These patterns are reflected in the distribution skew, that at 10% probability of exceedance El Niño rainfall was 107% of and La Niña was 74% of neutral rainfall, while at 90% probability of exceedance El Niño was 64% and La Niña was 101% of neutral rainfall (Table 4-1).

The observed precipitation patterns were reflected in the SWAT simulated total stream flow (Figure 4-5b), groundwater flow (Figure 4-5c), interflow (Figure 4-5d), and percolation (Figure 4-5e) to more significant extents, again showing the increase of the relative flows signal power. In the case of total flow, groundwater and interflow and percolation, the exceedance curves during El Niño were skewed towards higher values. The most extreme differences at the 10% probability of exceedance between El Niño and La Niña years were seen in simulated total flow (141% and 54% of neutral flow) and even more in groundwater flow (143% and 44% of neutral flow), in which both magnitudes of difference are greater than those seen in observed precipitation. Less extreme climatic differences were seen in interflow, percolation, surface runoff and ET records (Table 4-1). Practically, this means that historically, there was a 10% probability in El Niño of exceeding high relative values of total stream flow and groundwater flow relative to neutral conditions.

## Univariate Wavelet Analysis

The monthly wavelet power spectra for the NINO 3.4 SST and SWAT simulated groundwater flow, interflow, surface runoff, percolation, and ET time series are shown in Figure 4-7a-f. As previously demonstrated [Y. Wang, 1996; Torrence and Compo, 1998; Keener *et al.*, 2010], when the regular annual cycle is removed, SST power (Figure 4-7a) is concentrated within the ENSO periodicity band of 3-7 years, although the amplitude and dominant modes tend to shift through time. From 1911-60, a 5-7 year period is strongest, while a 4-5 year period dominates from 1972-92 [Y. Wang, 1996]. Longer decadal variations cannot be assessed with significance given the limited length of record.

Precipitation in the southeastern United States has distinct seasonality. In the coastal plain region and more specifically the LRW, the most intense precipitation events are in the spring and summer months, associated with convective or cyclonic storms [Sheridan, 1997]. Summer events are shorter, smaller in area, and more frequent and intense, while fall and winter events are frontal in nature, milder, but longer in duration. Spectral precipitation information corresponding to the 3-7 year ENSO signal has been demonstrated in the Florida Everglades via wavelet analysis, as well as in the western US [Kwon *et al.*, 2006; Rajagopalan and Lall, 1998], and the Little River Watershed shares that signal (Figure 4-3a). Regions of high power relative to the noise background were seen in the observed precipitation, flow, and nutrient record in the same 3-7 year periodicity as for the NINO 3.4 series (Chapter 3, [Keener *et al.*, 2010]).

In basin K of the LRW, total average annual stream flow depth is approximately one-third of annual precipitation [Sheridan, 1997; Feyereisen *et al.*, 2008], a figure comparable to similar statistics from other coastal plain watersheds. In a typical cool,

wet winter in the LRW, which is more associated with El Niño events, the shallow aquifer and the vadose zone are nearly fully saturated, with the water table directly below the root zone [Bosch *et al.*, 2004]. Additionally, detailed field studies in the watershed have found the shallow aquifer to vary from being 0 to 7 meters below the surface throughout the year [Bosch *et al.*, 2003], making it quick to become fully saturated. As a consequence, almost all precipitation in El Niño winters is received as stream flow (Figure 4-7b), enhancing the overall ENSO signal in the groundwater (Figure 4-7c). This pattern is especially enhanced by the confining Hawthorn formation underlying the entire area of basin K, which under these saturated conditions allows even the interflow component (LATQ) to exhibit a strong signal power (Figure 4-7d) that joins the total stream flow. Conversely, warm and dry winters associated with La Niña events exhibit measured water table conditions that are well below saturation [Shirmohammadi *et al.*, 1986; Bosch *et al.*, 2004]. Precipitation events received in these conditions in the LRW can infiltrate very quickly, with little to none reappearing as stream flow, as no-flow conditions can occur in the LRW [Shirmohammadi *et al.*, 1986; Bosch *et al.*, 2004; Feyereisen, Strickland, *et al.*, 2007].

As seen in the wavelet power spectra of these SWAT simulated time series, 3-7 year periodic ENSO power significant at the 95% level against a red noise background is visible in the stream flow and mirrored through the groundwater and interflow spectra (Figure 4-7c and d). This strong inter-annual power in the groundwater and interflow, denoted by reds and oranges in the wavelet spectrum, have both a more powerful inter-annual periodicity than the stream flow signal and a larger integrated area of 95% significance in the global wavelet spectra (GWS) to the right of each wavelet spectra

figure, despite the interflow component having a much smaller magnitude than the other flows. In the GWS, simulated total flow has significant peak spectra at 3.2 to 4.0 years (Figure 4-7b), while groundwater has peaks from 1.0-1.6 and 2.4-3.6 years (Figure 4-7c) and interflow from 1.1-1.8 and 2.8-3.6 years (Figure 4-7d), both of which show more significant periodicities than observed precipitation as discussed earlier.

Simulated percolation past the root zone (Figure 4-7e) also exhibits a significant 3-7 year ENSO signal; however, the strength of the signal is not as strong (signified by strong patterns of reds and yellows) as the flow or groundwater components. This is possibly because during wet El Niño winters, the soil remains consistently saturated, obscuring dynamics that could enhance the ENSO signal, although percolation still exceeds the 95% GWS significance from 1.1-1.8 and 3.3-4 years. Finally, the wavelet power spectrum of the SWAT simulated evapotranspiration time series (Figure 4-7f) does not show any significant periodicities in the GWS graph, nor does it show the familiar powerful patterns in the inter-annual climate based periodicities that are recognized in the other spectra of Figure 4-6.

This fact implies that while ET is in fact different in El Niño and La Niña years from neutral conditions, it does not exhibit a spectral pattern showing a strong teleconnection between ENSO sea surface temperatures and evapotranspiration in the LRW. The observations of patterns of strong inter-annual groundwater and interflow power with greater significant 95% periodicities in the GWS lend support to the hypothesis that groundwater and interflow are more responsible for increasing the power of the total stream flow ENSO signal relative to precipitation, than ET dynamics and percolation. To

determine whether NINO 3.4 SST and these SWAT simulated variables varied together and shared spectral power, cross wavelet and wavelet coherence analyses were done.

### **Cross Wavelet and Wavelet Coherence Analysis**

To directly analyze whether or not two time series share common wavelet power and localized correlation, cross wavelet (XWT) and wavelet coherence (WTC) analyses were performed on the NINO 3.4 SST record and the SWAT simulated variables of interest, groundwater flow, interflow, percolation, and evapotranspiration. Significance levels of the cross-spectra power are calculated against a red noise background, indicated by thick black outlines in the cross wavelet transform spectra (Figure 4-8a-d) to the 5% level.

The cross wavelet transform between SST and simulated groundwater flow (Figure 4-8a) shows that areas that were selected as possibly sharing power in the single wavelet spectra also share significant power in the 3-7 year periodicity centered around 1982-83 (it is difficult to see the exact center since it is outside of the cone of significance) and 1997, two El Niño, high precipitation and high flow years in the LRW. These same areas of high common power were also seen between SST and interflow (Figure 4-8b), and SST and percolation (Figure 4-8c). The relationship between SST and interflow had the most areas of significant high shared power. Evapotranspiration and SST had the least shared significant power (Figure 4-8d).

The areas with 95% significance were phase-locked positively in the case of SST and groundwater flow, interflow, and percolation (Figure 4-8a, b, c), meaning they vary together. The significant areas in Figure 4-8d, SST and evapotranspiration, were out of phase, implying an opposite relationship between the two variables. Compared to the XWT between NINO 3.4 SST and observed stream flow seen in the results of Chapter

3, (Figure 3-8b), there was less significant area in the simulated groundwater flow and interflow cross-spectra. However, there were also fewer visible years in the analysis which narrows the cone of influence, and while groundwater flow and interflow account for nearly 80% of stream flow in the LRW [Sheridan, 1997; Lowrance et al., 1984], they do not account for all of it, which may slightly weaken the oscillatory signal. Based on the cross-wavelet transforms, we are able to say that the NINO 3.4 index shares significant 3-7 year spectral power with SWAT simulated groundwater and interflow time series, some power with percolation, and little explanatory power with evapotranspiration. This furthers the hypothesis that the ENSO signal in stream flow is enhanced by the role of groundwater and interflow as restricted by the Hawthorn formation.

As was the case with the observed LRW time series in Chapter 3, a larger area in the WTC spectra of SWAT simulated data (Figure 4-9a-d) was marked as significant as compared to the XWT spectra. These areas of significant wavelet coherence are indicative of localized correlation strength, not shared time series wavelet power. With a short record of simulated hydrological data, it is difficult to attribute even areas of sustained significance visible in the WTC as implying causality; however, it is still possible to compare them to significant regions in the XWT to verify a simulated variable's covariance with the NINO 3.4 index. Compared to the observed stream flow record visualized via WTC in Chapter 3 (Figure 3-4b), all simulated variables had less significant power, which is expected given that these are components of the stream flow itself.

Of the SWAT simulated variables, NINO 3.4 SST and groundwater flow had the most significant wavelet coherence pattern in the 3-7 year oscillatory period (Figure 4-9a). This was followed closely in significant area by simulated interflow (Figure 4-9b), with much less significant covariance between SST and percolation (Figure 4-9c) and evapotranspiration (Figure 4-9d). The areas of sustained WTC significance in the groundwater and interflow spectra were both most likely centered around 1982-84, and also showed a positive in-phase relationship with SST. It is curious that the 1997 El Niño event does not show up on any of the WTC spectra, as it does on both the observed data from Chapter 3 (Figure 3-4), and in the XWT (Figure 4-8). The lack of a signal in 1997 means that these variables were not showing localized covariance with SST, which may be due to the nature of the SWAT simulation, or may have implications for the covariance of the groundwater dynamics with climate variability during this large El Niño event. The shared wavelet significance of the NINO 3.4 index seen in the XWT and the WTC for groundwater and interflow in the 3-7 year ENSO periodicity, and lack thereof in the evapotranspiration time series, again supports the hypothesis of groundwater and interflow enhancing the stream flow ENSO signal in basin K of the Little River Watershed.

### **Summary and Discussion**

Hydrological simulation of the Little River Watershed basin K via the Soil and Water Assessment Tool (SWAT) and observed data are used to determine the mechanism that is strengthening the correlation of the spectral ENSO signal with observed stream flow and loading time series compared to observed precipitation. Using a calibrated and validated SWAT model of LRW-K, the detailed surface and

groundwater hydrology was continuously simulated on a daily basis from 1979 to 2004, and aggregated into monthly average values for use in analysis.

The clear increase in the power of the inter-annual climate signal was demonstrated by shared patterns in water budget and exceedance curves, as well as qualitatively and quantitatively in high ENSO related energy in the wavelet spectral analyses and the 95% significant periodicities against a red noise background for each variable both analyzed alone and with the NINO 3.4 SST index. We found that in the Little River Watershed basin K, in Tifton, Georgia, the power of the climatological teleconnection to the El-Niño/Southern Oscillation was increased in both the observed and simulated stream flow through the mechanisms of groundwater and interflow, as they are confined by a geological layer, the Hawthorn Formation.

The Hawthorne formation in the Little River Watershed forms a nearly perfect aquaclude, so although infiltration is very fast, soil saturation can be reached relatively quickly while recharge into the deep aquifer is extremely slow [Rawls *et al.*, 1976; Sheridan, 1997]. This results in the increased significance of groundwater and interflow contributions to both soluble nutrient movement into outlet stream flow, and the stream flow itself. In the LRW, perhaps much more than other watersheds without a ubiquitous confining layer and lack of topography, the power of the El-Niño/Southern Oscillation 3-7 year signal that was found in precipitation is increased in the observed and simulated stream flow signal. The entire explanation of the strengthened ENSO power may have as much to do with the groundwater, interflow and Hawthorn Formation, as with the land use of the watershed itself. In turn, this raises the question of what the actual physical properties of the watershed are that lead to this potentially unique increased ENSO

signal power in the simulated and observed surface and sub-surface flow regimes of the LRW-K. By gathering physical properties of this relatively small coastal plain watershed such as the total area and depth to the surficial aquifer, transmissivity and porosity in the sandy soils, residence times of groundwater and surface water, and hydraulic conductivities, it may be possible to create an analytic function describing exactly how the precipitation based integration of stream flow through time and space in the entire hydrological system occurs.

Calibration and validation of the SWAT model for LRW-K generally showed that while the model predicted the hydrologic trends in the observed data, there were inconsistencies in the magnitude and duration of simulated daily stream flows. Generally, in La Niña-like conditions, flow was over-predicted in summer months when zero-flow conditions were observed, as was persistence of interflow [Bosch *et al.*, 2004; Feyereisen, Strickland, *et al.*, 2007]. This discrepancy in stream flow may help explain why the ENSO related SWAT simulated stream flow wavelet spectrum (Figure 4-7b) was not as strong as that of the observed data (Figure 4-3b). El Niño winters in the LRW tend to be cooler and wetter, resulting in near saturation of the shallow aquifer and vadose zone, and an increased stream flow signal from precipitation events. SWAT simulated storm flow rose and fell too rapidly in response to winter storms, while interflow did not recede rapidly enough relative to observed events. Despite these discrepancies, however, the univariate and cross-wavelet spectral ENSO signals were still visible and significant in the groundwater and interflow SWAT simulations, which suggest that we could expect to see an even more powerful signal if the flow data were

simulated more precisely with a fully spatially-distributed model or there was continuous detailed observed groundwater data.

Relative sensitivity analysis and calibration of SWAT simulated LRW-K hydrology previously showed that surface response parameters were significantly more sensitive than those pertaining to sub-surface hydrology [*Feyereisen, Strickland, et al., 2007*]. The most sensitive parameter to overall water yield, storm flow, groundwater flow and interflow was the curve number for agricultural land, partly due to the increased surface runoff from even average precipitation events on cropped land. In relationship to the future of the Little River Watershed, this implies that an increase in land area used for agricultural purposes may serve to strengthen the ENSO signal in stream flow even more than it currently is, while a significant decrease in cropped area could cause the teleconnection and predictive relationship between ENSO and flow, and consequently other variables such as pollutant loads, to weaken. As such, this ENSO teleconnection and its relationship with agricultural area could hold for other Coastal Plain watersheds as well.

The specific mechanism by which the ENSO signal power is increased via ground water hydrology and a confining layer in the Little River Watershed is by no means the only way in which a watershed could increase a climate signal delivered primarily through precipitation [*Cayan et al., 1999; Maurer et al., 2006*]. However, the spatial integration and reduction of noise in precipitation that the stream flow signal effectively accomplishes is most likely a primary method of signal power increase in different watersheds, as research on river flows from around the world have shown significant spectral signals corresponding to multiple climate indices [*Labat, 2008*]. This non-

intuitive relationship between ENSO signal strength and stream flow could prove to be helpful for making seasonal climate predictions in a geographic area with a weaker than desirable ENSO/precipitation signal, as a predictive relationship could be found between stream-flow or other proxy hydro-climatic variables. The exploration of additional non-precipitation hydrologic variables as they correlate to ENSO could expand how climate data could be used for more practical hydrologic prediction and for municipal water supply management, as well. The use of seasonal forecasts based on ENSO teleconnection with both surface and ground water flows and pollutant and nutrient loads could also more immediately benefit water resource managers or farmers, as decisions on irrigation, allocation, and runoff management would be based on actual climate information, and would not be predictions made so far in the future as to render them virtually unusable in normal management plans. In Chapter 5, this question is explored using a time series model to predict nitrate-N loads in the Little River Watershed based on the NINO 3.4 sea surface temperature index.

Table 4-1. Reference 10, 50, and 90% probabilities from all M-ENSO separated exceedance curves. This table indicates the probability that during a given ENSO phase, a certain variable will be above the number indicated. The largest differences between ENSO phases are seen in the 10% exceedance probabilities for stream flow and groundwater flow; compared to neutral, EN stream flow is 141% greater, while LN is only 54% of neutral flow, while groundwater flow is 143% greater in EN, and 44% of neutral groundwater flow in LN.

	Exceedance Probability	Climatology	Neutral	El Niño	La Niña
Precipitation (mm)	10%	188.4	190.0	203.7	141.2
	50%	91.4	89.6	106.9	68.3
	90%	29.5	29.9	19.1	30.2
Stream Flow (mm)	10%	89.7	89.7	126.4	48.1
	50%	8.9	8.1	11.0	3.6
	90%	0.8	0.8	0.5	1.1
Surface Runoff (mm)	10%	16.6	16.6	20.3	14.1
	50%	2.1	2.2	3.0	0.8
	90%	0.1	0.2	0.1	0.1
Groundwater Flow (mm)	10%	68.9	69.3	99.2	30.6
	50%	5.0	5.0	6.4	1.6
	90%	0.2	0.2	0.1	0.3
Interflow (mm)	10%	6.0	6.0	6.2	4.3
	50%	2.4	3.7	2.6	1.7
	90%	0.6	1.9	0.5	1.0
Percolation (mm)	10%	87.9	87.9	101.2	46.8
	50%	5.9	6.6	6.1	3.3
	90%	0.2	0.2	0.1	0.3
ET (mm)	10%	126.7	126.7	133.2	123.2
	50%	61.5	61.5	66.4	39.6
	90%	20.5	21.5	19.1	21.9

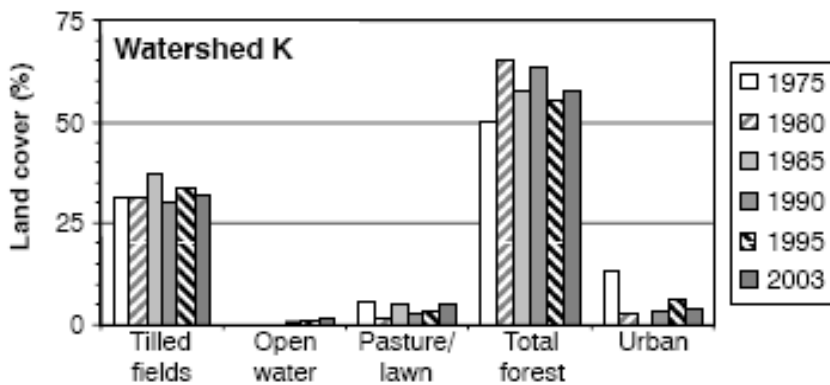


Figure 4-1. Observed land-use from 1975-2003 at 10 km resolution from LandSat images in Little River Watershed basin K [Bosch *et al.*, 2006].

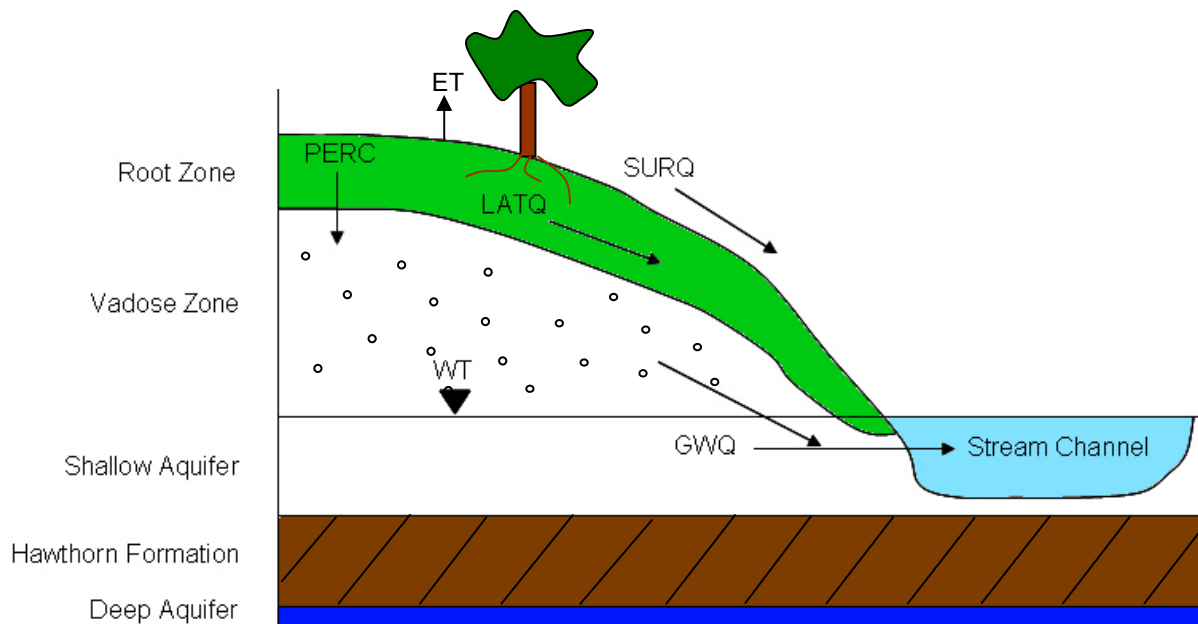


Figure 4-2. Cartoon cross-section of relevant SWAT simulated surface and sub-surface hydrological processes in an HRU of the LRW. SURQ is non-infiltrated surface runoff to the open stream channel, ET is potential evapotranspiration, PERC is percolation past the root zone soil layers into the vadose zone, LATQ is interflow from the root zone to the open stream channel, and GWQ is baseflow from the vadose zone and shallow aquifer to the open stream channel. The Hawthorn Formation is a confining layer above the deep aquifer, which receives negligible recharge from the area.

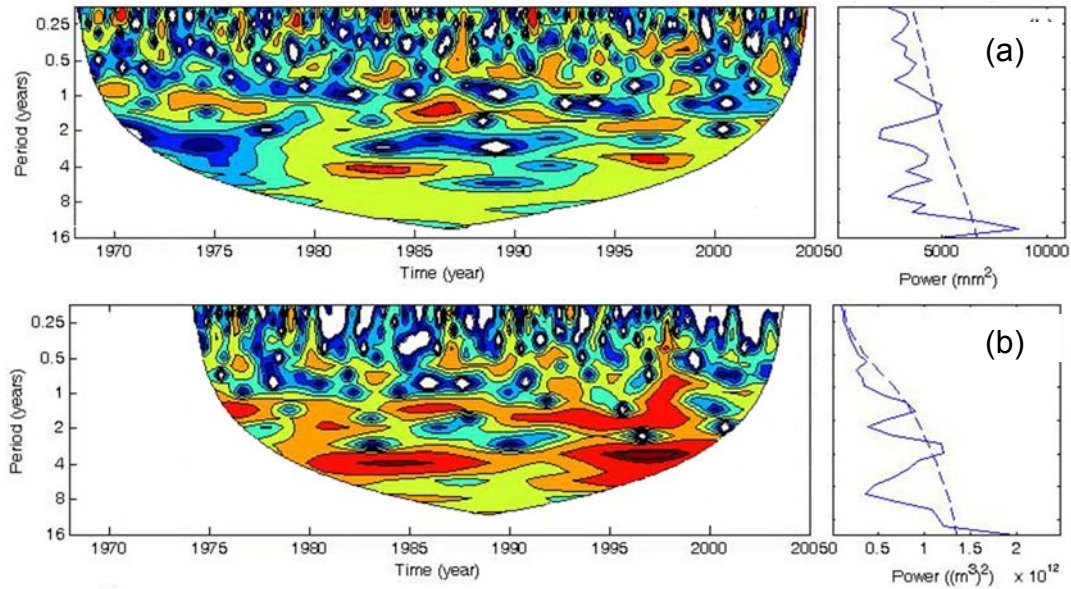


Figure 4-3. Significant Wavelet Power Spectra are shown within the cone-of-influence, which depends on time series length and degrees of freedom. Figures are color-mapped to indicate high wavelet power with reds and oranges, and low powers in blue and white. The Global Wavelet Spectrum (GWS) at the right of each figure shows power integrated over all scales and times. The 95% confidence limit is shown on the GWS (dashed blue line), the periodicities above which show significance. (a) Observed precipitation (mm) and (b) observed stream flow (m<sup>3</sup>). [Keener et al., 2010]

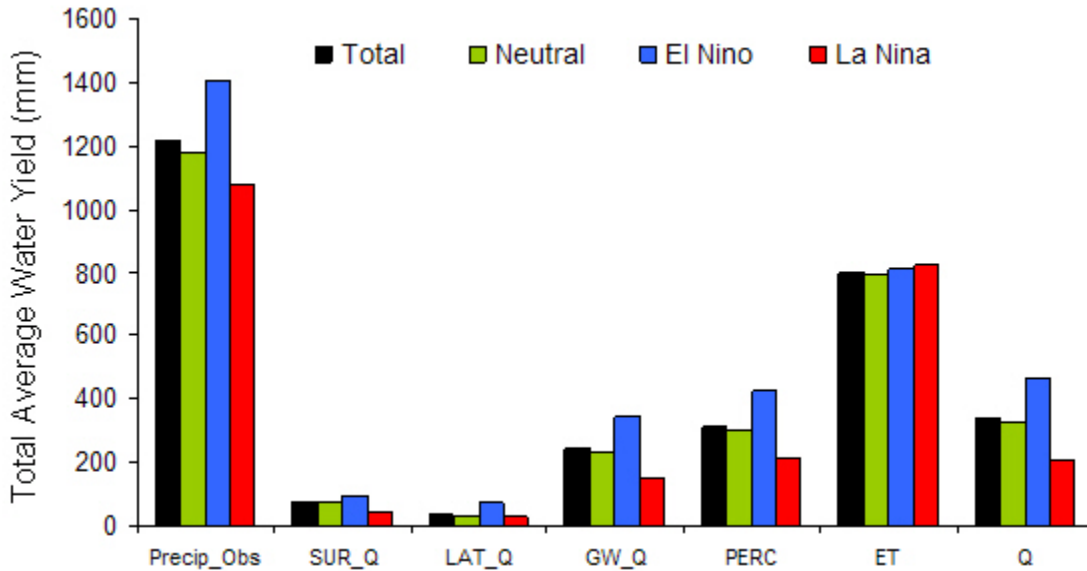


Figure 4-4. Average annual water yield (mm) of selected SWAT hydrologic variables in different M-ENSO phases, including: observed precipitation (Precip\_Obs) and SWAT simulated surface runoff (SUR\_Q), interflow (LAT\_Q), total groundwater flow (GW\_Q), percolation past the root zone (PERC), evapotranspiration (ET), and total flow (Q).

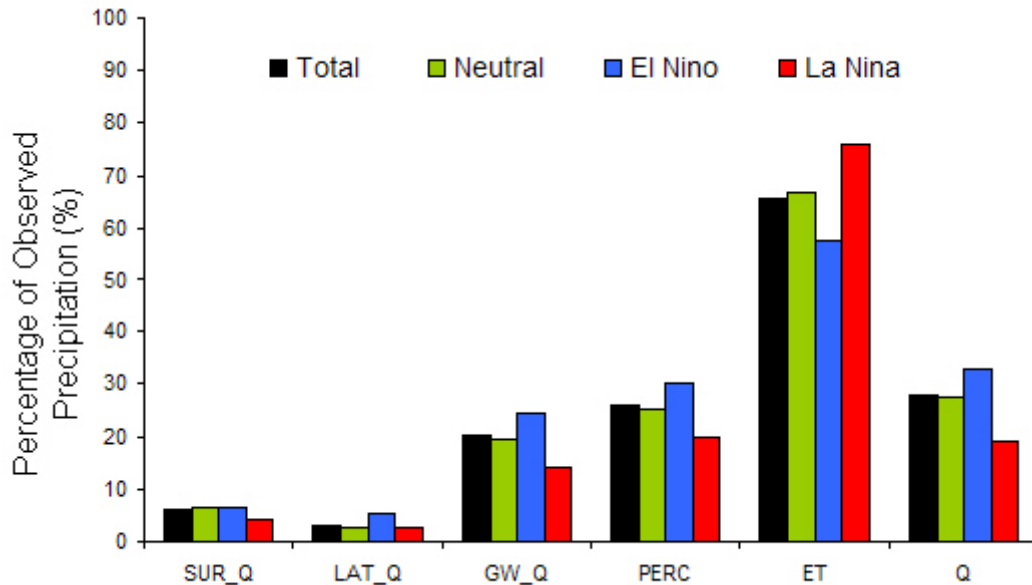


Figure 4-5. Average annual water yield as percentage of observed annual average precipitation of selected SWAT hydrologic variables in different M-ENSO phases, including: SWAT simulated surface runoff (SUR\_Q), interflow (LAT\_Q), total groundwater flow (GW\_Q), percolation past the root zone (PERC), evapotranspiration (ET), and total flow (Q).

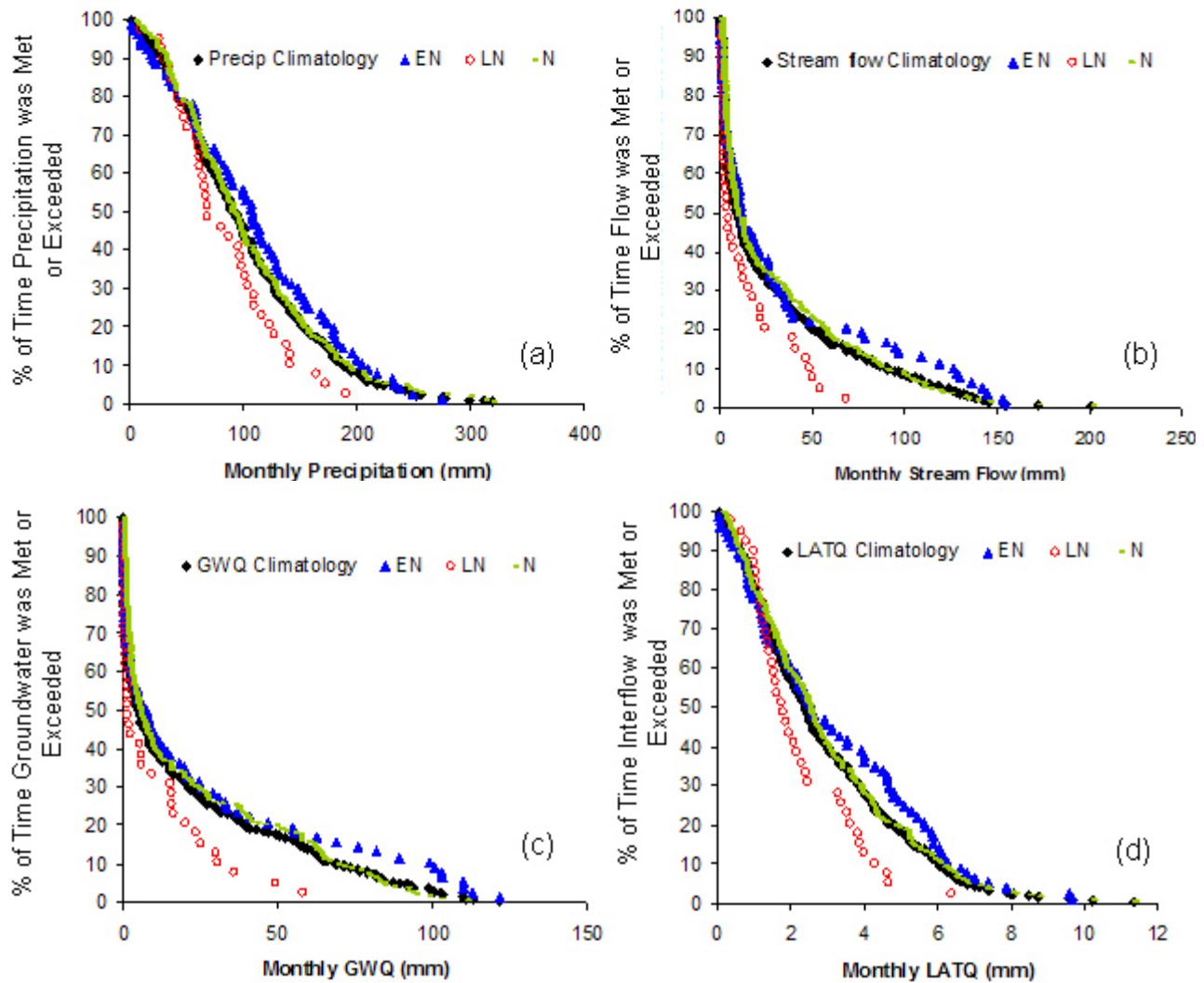


Figure 4-6. Probability of exceedance curves in different M-ENSO phase and observed climatological record for monthly (a) Observed Precipitation, and SWAT simulated (b) stream flow (c) groundwater flow (GWQ) (d) interflow (LATQ) (e) percolation past the root zone (PERC), (f) evapotranspiration (ET), and (g) surface runoff (SURQ). An exceedance curve is a backwards cumulative probability density curve, showing what percentage of area under the probability density curve lies to the right of the value of the variable on the x-axis. For example, a tendency toward drier than normal precipitation conditions in La Niña would be indicated if the red curve lies to the left of the black curve. Exceedance curves should not be read as forecasts.

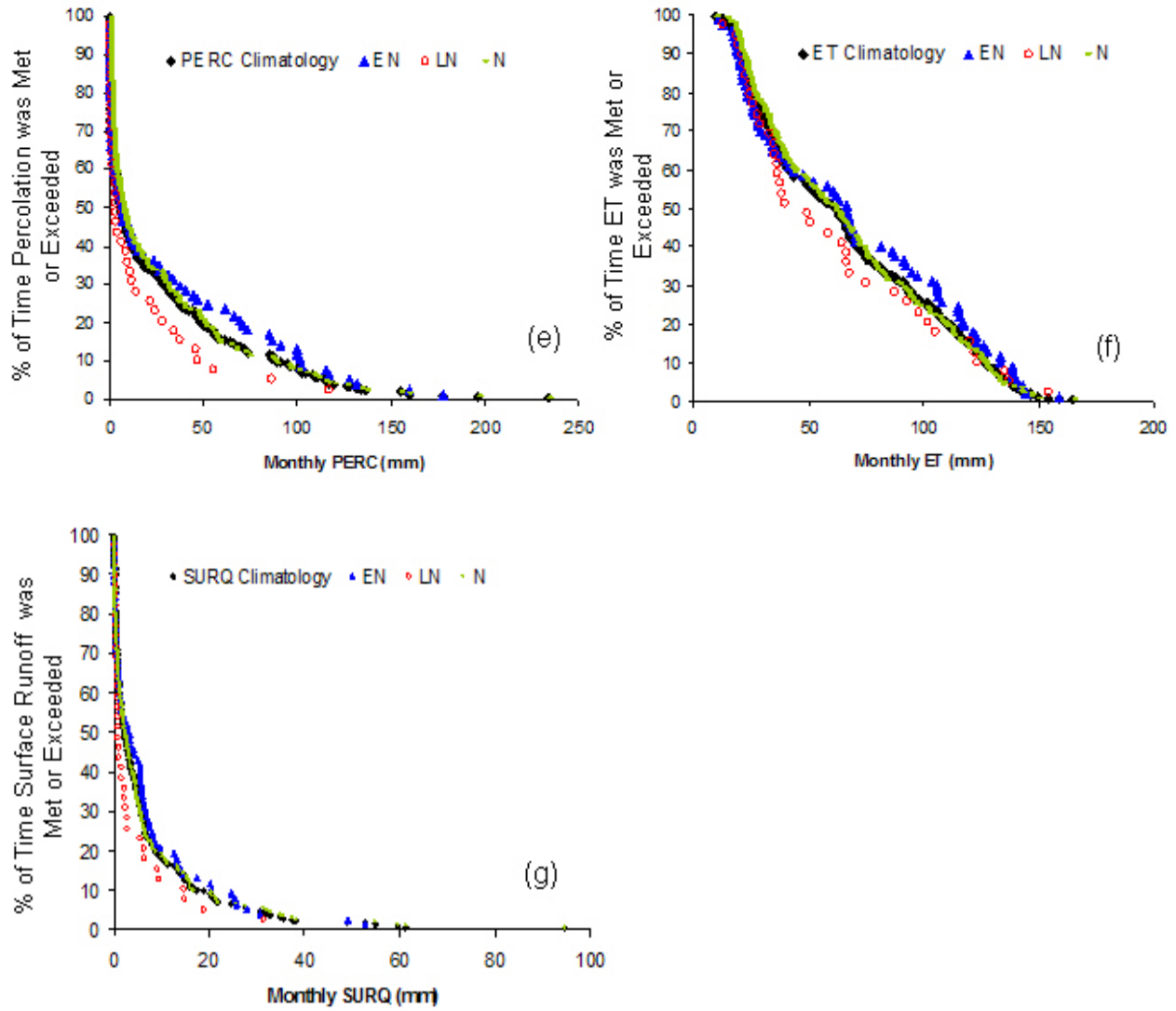


Figure 4-6. Continued.

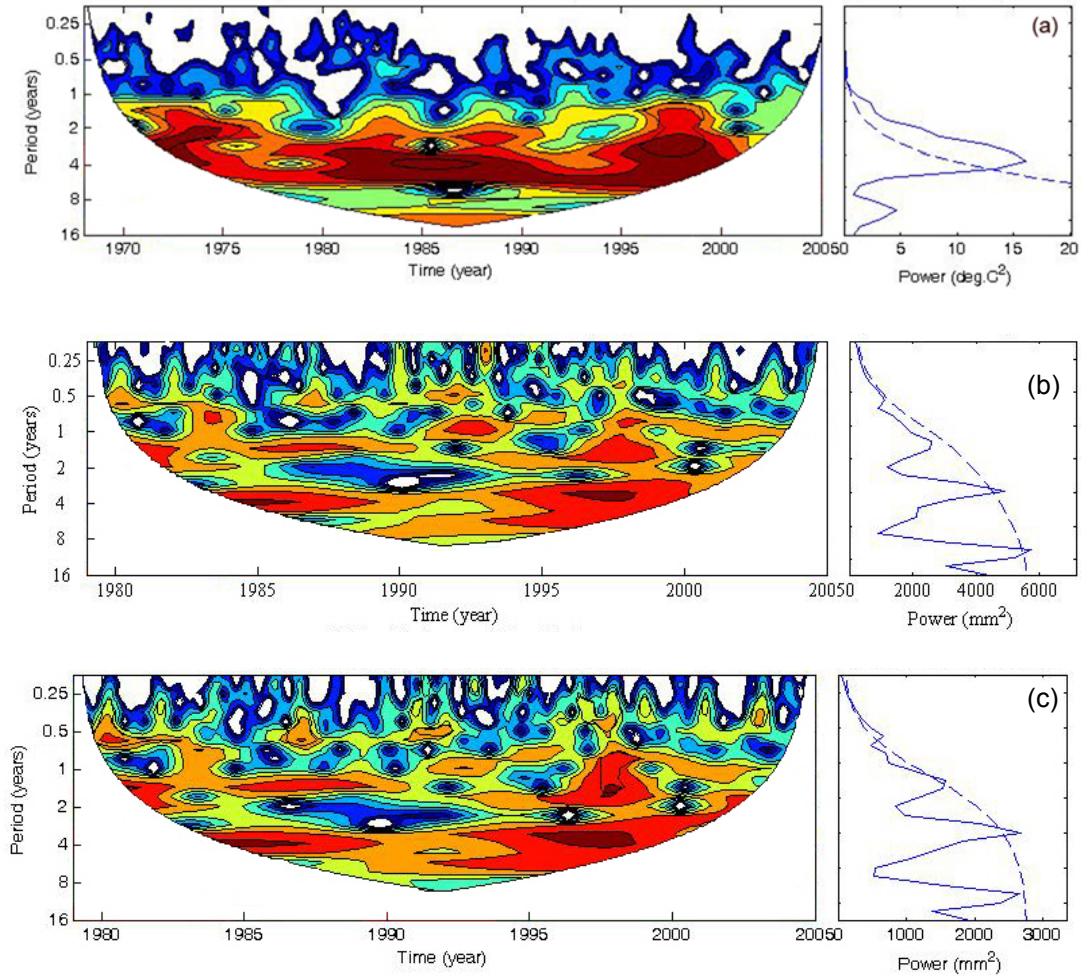


Figure 4-7. Significant Wavelet Power Spectra are shown within the cone-of-influence, which depends on time series length and degrees of freedom. Figures are color-mapped to indicate high wavelet power with reds and oranges, and low powers in blue and white. The Global Wavelet Spectrum (GWS) at the right of each figure shows power integrated over all scales and times. The 95% confidence limit is shown on the GWS (dashed blue line), the periodicities above which show significance. (a) NINO 3.4 SST index (°C) (b) SWAT Simulated Stream Flow (mm) (c) Groundwater Flow (mm) (d) Interflow (mm) (e) Percolation (mm) (f) Evapotranspiration (mm)

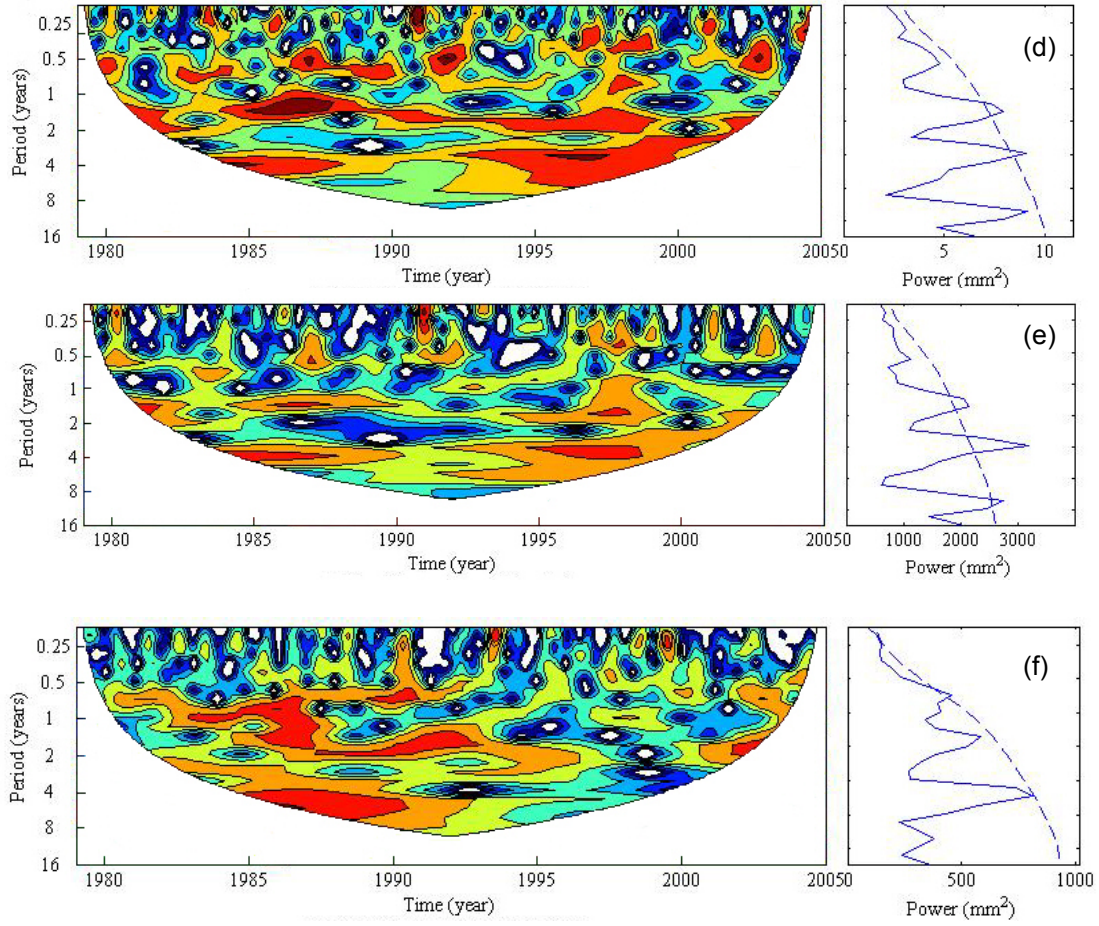


Figure 4-7. Continued.

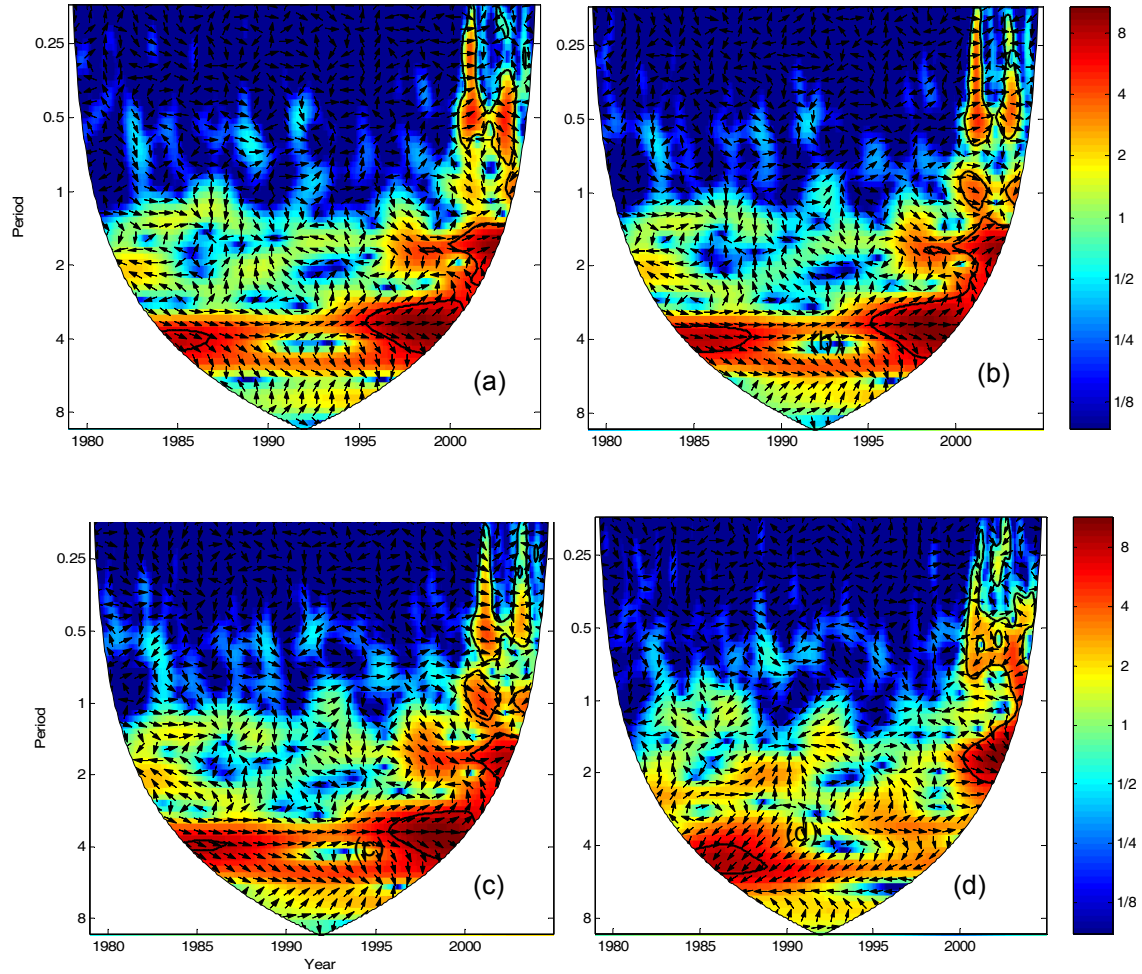


Figure 4-8. Cross Wavelet Spectrum between monthly NINO 3.4 SST ( $^{\circ}\text{C}$ ) index and (a) groundwater flow (mm) (b) Interflow (mm) (c) Percolation (mm) (d) Evapotranspiration (mm). Black figure outlines indicate areas significant to 95% confidence, while arrows represent variables' phase relationship. Arrows pointing clockwise indicate in-phase behavior, while counter clockwise arrows indicate anti-phase behavior.

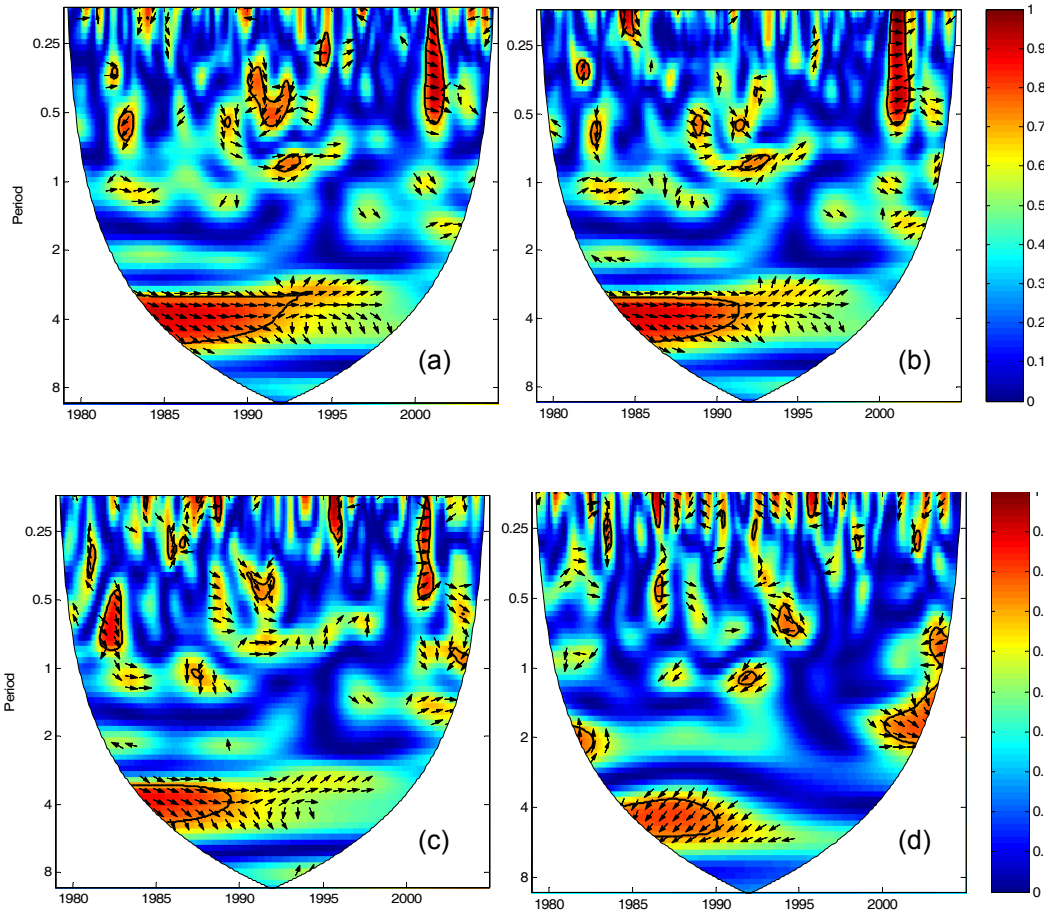


Figure 4-9. Wavelet Coherence Transform between monthly NINO 3.4 SST ( $^{\circ}\text{C}$ ) index and (a) groundwater flow (mm) (b) Interflow (mm) (c) Percolation (mm) (d) Evapotranspiration (mm). Black figure outlines indicate areas significant to 95% confidence, while arrows represent variables' phase relationship. Arrows pointing clockwise indicate in-phase behavior, while counter clockwise arrows indicate anti-phase behavior.

CHAPTER 5  
AN ENSO BASED MULTIVARIATE TIME-SERIES MODEL FOR FLOWS AND  
NITROGEN LOADS IN THE LITTLE RIVER WATERSHED

**Introduction**

In socio-economic and political affairs of the late 20<sup>th</sup> and 21<sup>st</sup> centuries, the concept of using Global Circulation Models (GCM's) to extrapolate the Earth's changing climate in the next 50 to 200 years has been a highly controversial issue. While still thoroughly discussed, there is not nearly as much debate in the scientific community as in the public arena about the core issue: that the Earth's climate is changing and we as a species urgently need to address and ultimately adapt to these changes to ensure the well being of as many people as possible. What has become very clear, especially in the wake of recent global meetings such as the United Nations Climate Change Conference in Copenhagen (December, 2009), is that despite mostly good intentions, it is virtually impossible for the global community to come together and make meaningful changes in their day-to-day policies using the predictions from these 50-200 year forecasts of global climate using model ensembles.

Aside from the socio-political obstacles to using long-range GCM predictions in a practical manner, there are scientific uncertainties as well. For example, it has been stated that using outputs from averaged ensembles of GCM runs to extrapolate a non-linear system with corresponding non-linear interactions, such as Earth's climate, into the future only increases uncertainty and introduces bias shifts into model outputs [Rajagopalan *et al.*, 2002]. The use of these outputs as boundary conditions and inputs to other models such as hydrological packages for making future simulations of hydrology changes may be very biased and uncertain. Even the estimate of global climate sensitivity, an important climatological reference number defined as the

estimated change in global mean surface air temperature that would result from a doubling of atmospheric CO<sub>2</sub> concentration, changes regularly, with the most recent IPCC estimate ranging from 2 to 4.5°C [IPCC, 2007], a relatively uncertain range. For both political and scientific reasons, it may be more beneficial and practical to concentrate more research efforts on predicting hydrological consequences using seasonal and inter-annual climate variability, as we can learn from our mistakes by observing if we are correct, predict and prepare for catastrophic events in the near term, and perhaps have an easier time effecting faster policy changes.

In Chapter 3, a known climatological signal was identified in the 3-7 year ENSO spectral range through univariate and multivariate wavelet analysis which was reflected in the observed monthly precipitation, stream flow, nitrate concentration and nitrate load of the Little River Watershed (LRW) in Tifton, GA [Keener *et al.*, 2010]. This periodic ENSO signal power that is visible in the hydrologic variables in the LRW is representative of a climatological teleconnection that is known to exist between sea surface temperatures in the equatorial Pacific Ocean, ENSO, and the southeast United States [Ropelewski and Halpert, 1986, 1987; Schmidt *et al.*, 2001]. Chapter 3 was the first study to extend the observation of the ENSO signal down the hydrologic chain to in-stream nutrient loads. It was found that the strongest wavelet power was seen in ENSO correlations with the monthly stream flow and monthly nitrate load. Both of these relationships were stronger than that between ENSO and monthly precipitation, which was shown in Chapter 4 to be because of spatial integration of the stream flow signal as opposed to the chaotic precipitation time series, and because of the Hawthorn Formation, a nearly perfect aquaclude that forms a confining layer under LRW-K

[Feyereisen, Strickland, et al., 2007; Stringfield, 1966]. In addition to representing a smoothed function of precipitation, stream flow in the Little River Watershed has a strengthened correlation with the ENSO signal (Chapter 4). Groundwater flow in the LRW is responsible for up to 80% of the total stream flow [Sheridan, 1997], as well as comprising the main route for movement of soluble nutrients [Lowrance et al., 1984]. The ENSO signal power in stream flow is strengthened by the significance of the role of groundwater, and additionally increased due to the presence of the Hawthorn confining layer, restricting flow into the deep aquifer and increasing the amount of interflow represented in the stream flow record (Chapter 4). As nutrient concentration is dependent on both natural climatological phenomena as well as anthropological effects such as agriculture and urbanization, a less significant ENSO correlation was seen in its wavelet power spectrum relative to stream flow. For these reasons, stream flow and nutrient load were targeted as the main time series of predictive interest.

Wavelet analysis in both its univariate and multivariate forms has been accused of being comprised of interesting, colorful pictures and little substantial, quantitative data [Grinsted et al., 2004]. In this research, we have built upon the identified significant relationships in the hydrologic variables of the LRW and then isolated, extracted, and rebuilt the wavelet oscillatory signals for use in a local monthly predictive time series stream flow and nutrient load model. Time series models are used in municipal water supply management such as by Tampa Bay Water [Asefa and Adams, 2007], and forecasting of flows and precipitation in different locations, although they are not widely published in academic journals. This may be because of the relative subjectivity of determining the appropriate parameterization for time series models, or simply because

they are not able to answer larger questions having to do with land-use changes or long term simulation. In our case, however, a time series model that simply provides short-term flow and nitrogen load forecasts that can be easily updated with additional data is a useful option for a decision support tool.

This study investigates the periodicity and variability in stream flow, nitrate and total nitrogen loading as a non-stationary process, by quantifying and comparing the effects of spectrally significant components on the predictability of flows and water quality in the LRW. Our hypothesis is that the wavelet time series models will outperform standard time series models in forecasting one to three month nutrient loads in the LRW, while SWAT will be more accurate in simulating hydrology on an annual basis. The wavelet decomposition models will also contain higher-orders of parameters than the time-domain models. However, for this research we are examining these models for future pragmatic forecasting, making minimizing the number of parameters less crucial.

Chapter 5 evaluates the effectiveness of a series of wavelet (W-VAR) and non-wavelet based (VAR and VARX) vector time series models with different types of inputs in predicting flows, total nitrogen, and nitrate loads in the LRW basin K, including possible inputs of observed  $\text{NO}_3$  load, wavelet reconstructed components (RC) of  $\text{NO}_3$  load, observed stream flow, wavelet RC of stream flow, observed and SWAT simulated TN load, observed and SWAT simulated wavelet RC of TN load, SWAT simulated wavelet RC of stream flow, and an exogenous variable in the non-wavelet models of either observed or forecasted NINO 3.4 SST. All models were trained using data from 1968-2002, and validated using predicted and observed data from 2003.

The resulting slew of time series models gives insight into the different advantages and disadvantages of different types of time series models, and into using spectral inputs as opposed to those in the time domain. In theory, the time series models that are based on the wavelet extracted significant oscillations will retain both the marginal distributions of all involved variables, as well as the spectral signature including the amplitude and frequency over time of the variables. These spectral time series models may excel at reproducing quasi-periodic long memory behavior and non-linear dynamics that give rise to both persistent regimes of behavior and stochastic regime transitions without *a priori* modeling specifications [Kwon *et al.*, 2007], such as the various ocean-atmosphere climate indices affecting the southeast Coastal Plain. While SWAT and time series models theoretically serve very different purposes, in conjunction their abilities are magnified. A time series model is not meant to and cannot simulate spatially distributed, long-term and theoretical future conditions based on changing land uses, a use at which SWAT excels. The W-VAR models can provide shorter term monthly and seasonal predictions of high risk nutrient loads and high or low flows with very minimal input once the initial model has been set up. The forecasts of one to three month outlooks of stream flows and nutrient loads can provide general advice for stakeholders and natural resource managers that are concerned with or trying to actively manage and reduce their loading risk in certain seasons and months as part of a BMP or even an adaptive management plan.

## **Data and Methods**

### **Field Site and Hydro-Climate Data**

The same field site, the Little River Watershed (LRW), basin K, is used as is described in Chapter 3, Data and Methods, section Field Site: Little River Watershed. The same precipitation, stream flow, and nutrient data from basin K are also used as described in Chapter 3, Data and Methods, section Little River Watershed Data, for obtaining spectral reconstructed components. All data delineating continuous observed measures of the El-Niño/Southern Oscillation are from the observed NINO 3.4 sea surface temperature index, as described in Chapter 3, Data and Methods section Little River Watershed Data.

For evaluation of time series models, in some cases a year of hindcast values of the NINO 3.4 SST index from 2003 were used for comparison as an exogenous variable input. These past forecasts of anticipated NINO 3.4 were obtained from the IRI/LDEO Data Library ([http://iridl.ldeo.columbia.edu/SOURCES/.IRI/.FD/.SSTA\\_FCST/.ASST/.version01/.sst/L/data.html](http://iridl.ldeo.columbia.edu/SOURCES/.IRI/.FD/.SSTA_FCST/.ASST/.version01/.sst/L/data.html)), and are from the NCEP coupled ENSO forecast model; they are presented as the mean of the NOAA NCEP coupled ENSO Climate Forecast System (CFS) [*Saha et al.*, 2006], LDEO model [*Cane et al.*, 1986; *Zebiak and Cane*, 1987], and CPC constructed analogue (CA) [*van den Dool and Barnston*, 1995; *van den Dool et al.*, 2003] models, meant to give the best ensemble estimate of expected NINO 3.4 SST behavior at the time.

### **SWAT Nutrient Calibration and CP Implementation**

Using the results of the hydrologic parameter SWAT calibration as described in Chapter 4, Data and Methods, section SWAT Model Hydrologic and Nutrient Calibration and Validation, a subsequent calibration and validation of nutrient parameters and

effects of BMP implementation and conservation practices (CP) on agricultural areas in basin K was performed [Cho *et al.*, 2010]. Again, AVSWAT-X, SWAT 2005 with a GIS interface, was used to simulate the hydrology of the Little River Watershed basin K, and calibrated for water quality and conservation practice scenarios. Based on the SWAT settings, 26 sub-basins and 452 hydrologic response units (HRU's) were created for LRW-K. As a spatially semi-distributed model, SWAT individually models each HRU response, aggregates them at the sub-basin level, and then routes each sub-basin to the appropriate stream reach within the watershed.

The water quality and CP were calibrated for eight years from 1979 to 1986, and validated from 1987 to 2004 [Cho *et al.*, 2009, 2010]. Calibration was manually performed as outlined in the SWAT manual [Neitsch *et al.*, 2002]. While the hydrological parameters remained as they had under the previous analysis, additional parameters affecting biomass of crops, upland sediment erosion, and in-stream processes were calibrated. Crop rotations that were calibrated and validated were three year rotations of corn-corn-peanut and cotton-cotton-peanut, and a six year rotation of corn-peanut-corn-peanut-cotton-peanut, while non-cropped area management was kept constant. An observed phenomenon in the LRW is the significant removal and transformation of nitrogen from nitrate-N to organic-N in the riparian forested buffers [Lowrance, 1992; Lowrance *et al.*, 1984]. Since SWAT is unable to simulate dynamic nutrient transformations within riparian zones [Li *et al.*, 2004], only total nitrogen (TN) and phosphorus (TP) at the watershed outlet were calibrated [Cho *et al.*, 2009].

Previous detailed studies of nutrient processes within the LRW have shown that overall, approximately 40% of annual natural and anthropological TN inputs are

removed during harvest, while approximately 57% either remain in the watershed or are lost in an unspecified way [Lowrance *et al.*, 1985]. In other basins of the LRW, 94% of TN was observed to be transported from the uplands to the stream channel through sub-surface flow, while 67% of groundwater TN and 37% of TN in surface runoff was removed through the riparian filters [Lowrance *et al.*, 1984, 1983; Lowrance and Sheridan, 2005]. Since there is no option in SWAT to calibrate nitrogen reduction separately within surface and sub-surface riparian regimes, all nitrogen reduction was simulated through adjusting the riparian filter width (FILTERW) and the half-life of nitrate in the shallow aquifer (HLIFE\_NGW) variables [Cho *et al.*, 2009]. Within the simulation, nutrient processes were calibrated such that simulated in-stream TN reduction at the outlet matched observed values for basin K of 3.9% of TN input, or 3.34 kg/ha of TN load [Cho *et al.*, 2009; Lowrance *et al.*, 1985].

Percent error (PE) was used to quantitatively compare observed and simulated total runoff and pollutant load for the entire simulation period. Monthly RMSE-observations standard deviation ratio (RSR) [Moriassi *et al.*, 2007] and Nash-Sutcliffe Efficiency Index (NSE) [Nash and Sutcliffe, 1970] were used to calculate error statistics and a monthly correlation statistic [Cho *et al.*, 2009]. Simulation performance is considered satisfactory if monthly NSE > 0.5, and monthly RSR  $\leq$  0.7, which Cho *et al.* achieved, with a PE of 14.4%, RSR and NSE of 0.62 for TN load (Table 5-1).

From 1985 to 2003, approximately 11% of the total land area in the LRW had undergone a conservation practice of some kind [Sullivan and Batten, 2007]. Of those implemented conservation practices, the most common were nutrient management (13.1%), pest management (12.9%), and grassed waterways (9.6%) [Sullivan and

*Batten, 2007*]. The entire SWAT simulated stream flow (Figure 5-1) and TN load (Figure 5-2) from 1979 to 2004 was converted to monthly average values and can be seen as compared to observed flows and TN loads. For the purposes of this research, daily SWAT simulations for 2003 were grouped into monthly values to be compared to the forecasts made by the various time series models. It should be noted that the simulations produced by SWAT use observed weather data, and are not forecasts. By comparing the time series models with the SWAT simulated data, we are able to see how well a simple time series model can forecast flows and loads in the short-term, and if looked at over several years of forecast and simulation, could identify years in which the SWAT simulations are not capturing climate variability adequately.

### **Wavelet Reconstruction**

Every vector in a vector space can be written as a linear combination of the basis vectors in that vector space, specifically by multiplying the vectors by some constants, and then taking the summation of the products. The analysis of the signal involves the estimation of these constants (Fourier coefficients or wavelet coefficients for example). Reconstruction of the original signal amounts to extracting the relevant coefficients and computing the linear combination equation. The wavelet transform is analogous to a band-pass filter with a response function corresponding to the original mother Morlet wavelet function used (Equation 3-1). Since the mother wavelet is known, it is possible to reconstruct the entire time series using deconvolution or the inverse filter [*Torrence and Compo, 1998*]. In the case of the continuous wavelet transform used in this analysis, the original time series,  $X_n$ , can be reconstructed using a different “synthesizing” wavelet, the easiest of which is a delta ( $\delta$ ) function [*Farge, 1992*]. The

reconstructed time series,  $R_{jn}$ , is then the sum of the real part of the wavelet transform over all scales of interest,  $a$  (Equation 5-1):

$$R_{jn} = \frac{\delta_j \delta_t^{0.5}}{C_\delta \Psi_0(0)} \sum_{j=0}^J \frac{\Re\{X_n(a_j)\}}{a_j^{0.5}} \quad (5-1)$$

The factor  $\Psi_0(0)$  (Morlet =  $\pi^{-0.25}$ ) removes the energy scaling,  $a_j^{0.5}$  converts the wavelet transform to energy density, and  $C_\delta$  is a constant from the reconstructed delta function from the particular mother wavelet used (Morlet = 0.776), and can be looked up in appropriate tables [Farge, 1992; Torrence and Compo, 1998].

For this study, the 95% significant reconstructed components as identified from the Global Wavelet Power (GWP) were extracted from the wavelet transforms of the observed data described in Chapter 3 in the Little River Watershed, and summed into a single time series representing inter-annual oscillatory variability. The scales for which the GWP spectrum is higher than the 95% red noise significance level were selected for time series reconstruction. This process was done for monthly precipitation, stream flow, SWAT simulated total nitrogen (TN) load and observed nitrate ( $\text{NO}_3$ ) load. Nitrate concentration was not considered as a relevant reconstructed time series in this analysis, as it did not meet relevant significance criteria in Chapter 3.

### **Wavelet Time Series Model: VARX(p,s)**

In many research studies involving geophysical data, there are observations from several different variables that relate to the overall system being analyzed. In our case, we have identified several hydrologic and climate based time series in Chapters 2 through 4 that have a significant relationship with the nitrate nutrient loads we want to forecast, primarily, stream flow and the NINO 3.4 SST index [Keener *et al.*, 2010].

Expanding on the general introduction to time series analysis in Chapter 1, Literature Review section Time Series Models, this section will more specifically discuss vector time series models. The vector time series model is a natural extension of a univariate model to multivariate dynamic time series, while an exogenous variable outside the system of interest ( $X$ ) can be added to increase forecasting power. For example, if a single variable is denoted by  $Y_t = (y_1, y_2 \dots y_t)$  to form an autoregressive AR( $p$ ) model of lag  $p$ , then by extension, a vector model with  $Y_t = (y_{1t}, y_{2t} \dots y_{nt})'$  denotes a ( $n \times 1$ ) dimensional vector of variables in a vector autoregressive (VARX( $p, s$ )) model of lag  $p$  with exogenous variable  $X$ :

$$Y_t = \Pi_1 Y_{t-1} + \dots + \Pi_p Y_{t-p} + \Gamma_1 X_{t-1} + \dots + \Gamma_s X_{t-s} + \varepsilon_t, \quad \text{from } t = 1 \dots T \quad (5-2)$$

In which  $\Pi_i$  are ( $n \times n$ ) coefficient matrices,  $X_t$  is a ( $m \times n$ ) matrix of exogenous variables,  $\Gamma_s$  is a parameter matrix estimated via regression, and  $\varepsilon_t$  is a zero-mean white noise vector process. A VAR( $p$ ) model without the exogenous variable simply lacks the corresponding matrix of parameters that include  $X$ . The following assumptions are made:

- $E(\varepsilon_t) = 0$ ,  $E(\varepsilon_t, \varepsilon_t') = \Sigma$ , a positive-definite,  $m \times m$  matrix of the residual covariances, and  $E(\varepsilon_t, \varepsilon_t') = 0$  for  $t$  not equal to  $s$ .
- The VAR and VARX processes are stationary, i.e. the roots of  $\det[\Gamma(x)] = 0$  are outside the unit circle.
- Explanatory (independent) variable(s)  $x_t$  are not correlated with the residuals  $\varepsilon_t$ .

In abbreviated summation notation, the VARX( $p, s$ ) model (Equation 5-3) can be written as:

$$Y_t = \sum_{i=0}^s \Gamma_i x_{t-i} + \sum_{i=1}^p \Pi_i y_{t-i} + \varepsilon_t \quad (5-3)$$

Optimal lag selection for each model is done by minimizing the Akaike information criterion (AIC) (Equation 5-4) and/or the Bayesian information criterion (BIC) (Equation 5-5). Each method of model selection has advantages and disadvantages. Typically, the AIC will choose the best model even if the number of parameters is unreasonably large, which may result in over-fitting. The BIC incorporates a penalty term for the number of parameters in the model, often resulting in optimal fits with fewer terms than the AIC, but less overall predictive accuracy. Theoretically, the AIC for vector models gives a quantifiable estimate of the relative amount of information lost when balancing a statistical model's bias versus variance, in which  $p$  is the number of parameters in a given  $m$ -dimensional model of  $n$  time points, and  $\hat{\Sigma}_p$  is the residual covariance matrix without degree-of-freedom corrections from the VAR( $p$ ) model, representing the estimated error variance  $\varepsilon_t$ .

$$\begin{aligned}
 AIC(p) &= -\frac{2}{n} \ln(\max \text{ likelihood} ) + \frac{2}{n}(p) \\
 &= \frac{2m^2 p}{n} + \ln\left(\hat{\Sigma}_p\right)
 \end{aligned}
 \tag{5-4}$$

The BIC penalty for additional parameters is in the second term (Equation 5-5), making BIC an increasing function of both  $p$  and the variance of the error term.

$$\begin{aligned}
 BIC(p) &= \ln(\sigma_e^2) + \frac{p}{n} \ln(n) \\
 &= \ln\left(\det \hat{\Sigma}_p\right) + \frac{m^2 p \ln(n)}{n}
 \end{aligned}
 \tag{5-5}$$

where  $\hat{\Sigma}_p = n^{-1} \sum_{t=1}^n \hat{\varepsilon}_t \varepsilon_t'$

In this research, the vector components include observed raw and wavelet reconstructed LRW monthly stream flow, and monthly nitrate-N and total-N load time series, while both observed and hindcast NINO 3.4 SST index values are used as the exogenous variable. To achieve stationarity and variance stabilization, the raw stream flow and TN load data were transformed via first-order differencing (i.e.,  $y_{it} = y_{it} - y_{it-1}$ ), while the  $\text{NO}_3$  load was log transformed and then first-order differenced. Wavelet RC and NINO 3.4 exogenous variable time series were not transformed. AIC was used to select the best lag for VAR( $p$ ) and VARX( $p,s$ ) models, while BIC was used for W-VAR( $p$ ) models to keep the maximum number of parameters in check.

### Forecasting and Uncertainty

Forecasting is a main objective of time series analysis, and forecasting from a vector model is very similar in theory to forecasting from a univariate model. The optimal minimum mean squared error (MSE)  $h$ -step-ahead forecast of  $Y_{t+h}$  at time  $t$  is (Equation 5-4) when the parameters  $\Pi_j$  have been estimated as  $\hat{\Pi}_j$  is found recursively with a forecast error covariance matrix (Equation 5-5),

$$\hat{Y}_{t+h|t} = \hat{\Pi}_1 \hat{Y}_{t+h|t} + \dots + \hat{\Pi}_p \hat{Y}_{t+h-p|t} + \varepsilon_{t+h} \quad (5-4)$$

$$\hat{\Sigma}(h) = \sum_{o=0}^{h-1} \hat{\Psi}_o \hat{\Sigma} \hat{\Psi}_o'$$

$$\text{where } \hat{\Psi}_o = \sum_{j=1}^o \hat{\Psi}_{o-j} \hat{\Pi}_j \quad (5-5)$$

The  $h$ -step forecast error (Equation 5-6) now includes the part of the forecast error due to estimating the parameters of the VAR or VARX model.

$$\hat{Y}_{t+h} - \hat{Y}_{t+h|t} = \sum_{s=0}^{h-1} \psi_o \varepsilon_{t+h-o} + \left( Y_{t+h} + \hat{Y}_{t+h|t} \right)$$

where the matrices  $\psi_o = \sum_{j=1}^{p-1} \psi_{o-j} \Pi_j$  (5-6)

In this study, confidence intervals for the forecasts are provided at the 95% level. The confidence level is inferred from the empirical forecast error covariance matrix (Equation 5-5). Cones of forecast uncertainty are also typically generated by adding multiples of the prediction standard error estimates at each time step, illustrating the growing uncertainty the farther one gets from the last observed data point. This method is not used to illustrate the uncertainty in this research.

### **Tercile Analysis**

After generating one to twelve month forecasts for nitrate load, TN load, and stream flow anomalies in the year 2003, forecast accuracy was tallied using terciles. In this case, monthly forecasts made using different VAR and VARX models with exogenous input of the NINO 3.4 index and monthly SWAT simulations are counted if they are in the correct observed tercile of the observed time series variable in question. Counts of the correct tercile prediction of each model were made at one, three, six, and twelve month intervals to observe how each model's accuracy changed over time.

### **Results**

Reconstructed components (RC) were extracted from the univariate wavelet transform of normalized observed monthly precipitation, stream flow, NO<sub>3</sub> load and SWAT simulated TN load and stream flow. The reconstructed components in the spectrum for each variable that were above the 95% GWS significance level were isolated and summed into a single component representing the wavelet-extracted inter-

annual climate variability within a given time series (Figure 5-3). The number of significant RC for each variable are seen in Table 5-2, as well as the percentage of variance that the extracted RC comprise relative to the original anomaly time series and the optimal lag chosen by AIC and BIC for each time series model type. Observed stream flow and nutrient load anomalies were chosen as vector inputs, as they exhibit the most significant RC's as well as the largest percentage of representative variance and cross-correlative power with the NINO 3.4 index [Keener *et al.*, 2010], while observed and hindcast NINO 3.4 SST's were used as the exogenous input variable. From both the conclusions drawn in Chapter 3, the relevance of the significant RC calculated here, and time series modeling results that are not shown with poor predictive power in the vector models, observed precipitation and NO<sub>3</sub> concentration are not included in the subsequent time series modeling section. As such, the vector inputs to the model are observed monthly NO<sub>3</sub> or TN load, stream flow, and SST.

### **VAR, VARX, and W-VAR Time Series Models**

Two main classes of time series models predicting monthly N-nutrient load anomalies in the LRW basin K are compared and contrasted in this study: VAR models with and without an exogenous input (VARX) of the NINO 3.4 index, and wavelet-VAR (W-VAR). Theoretically, the W-VAR models should not require the addition of the exogenous variable of NINO 3.4 SST to perform better, as they inherently encompass inter-annual climate-based variability as manifested in the significant reconstructed components. More interestingly, the W-VAR models do not only include NINO 3.4 based climate signals, as all significant reconstructed components were included in the analysis, not only those in the 3-7 year oscillatory period corresponding to ENSO. The reconstructed W-VAR model could encompass inter-annual oscillatory climate

information from any of a number of periodic ocean-atmospheric indices that affect different aspects of the southeast United States, some of which have been initially identified as affecting cotton yields more than ENSO [*Pathak*, 2010], such as the Tropical Northern Hemisphere (TNH) index [*Mo and Livezey*, 1986] and the North Pacific Pattern (NPP). This gives the W-VAR models a distinct advantage in the amount of climate-based information they are able to incorporate without the addition of exogenous variables which can introduce additional model or forecast uncertainty.

The optimal number of lags chosen via AIC and BIC was one month for all VAR and VARX models using different exogenous input types, five for W-VAR NO<sub>3</sub> load and stream flow, and seven for W-VAR TN load and stream flow (Table 5-2). By necessity, the wavelet based models contain significantly more parameters than those constructed in the time domain, as they are expected to capture the inter-annual oscillatory character in the respective time series data, given a representative group of reconstructed components. While the number of parameters selected in the W-VAR models is not excessive, it does introduce another source of potential model uncertainty.

Figures 5-4 through 5-11 show the different time series model types and the monthly observed and predicted values of nutrient load and stream flow for 2003. With any model used for forecasting, it is expected that prediction accuracy decreases as the model gets further from the last observed data point. Time series models are generally used to forecast only a few steps in advance at a given time, and are routinely updated with new data to generate new forecasts through time. In these time series models, 12 months of forecasts were made for exploratory analysis, however, practically, only

forecasts at the one to three month level would likely be used for their potential decision making abilities. It should also be noted that using the monthly M-ENSO categorical index, January and February of 2003 were classified as El Niño months, while the rest of the calendar year was Neutral. This was preceded by nine months of El Niño conditions from April to December of 2002. These ENSO categorizations could have effects on the models prediction abilities, as transition regimes from wetter to drier seasons can have effects on watershed storage potential and saturation levels, and further forecasts and evaluations need to be done on years representing different climate regimes.

Upon visual inspection of the VAR(1) models of NO<sub>3</sub> load and stream flow (Figure 5-4) and TN load and stream flow (Figure 5-8), it is clear that these models are not adequately simulating the dynamics of either variable, as the entire year of predictions remains nearly static around the mean with wide confidence intervals. The VAR models also show the fewest correct predictions of load and flow terciles, especially in the 1-3 month forecasts (Table 5-3), and some of the highest RMSE estimates, especially for NO<sub>3</sub> and TN loads (Table 5-4). Methods to improve the fit of using only the raw time series for forecasting could include incorporating a seasonal dimension to the model to add dynamics that the current model is missing. In this research, however, we are interested in looking at the ways in which a wavelet model compares with a time-domain model, not in methods of producing a “best-fit” time series model. For these reasons, these simple VAR models are used without any climate information incorporated as a baseline to compare with our models that use climate data either directly or implicitly.

The next incarnation of models are VARX(1) forecasts using observed NINO 3.4 sea surface temperatures as an exogenous input. Theoretically, these models create a more dynamic simulation by directly incorporating climate data. Indeed, visual inspection of the NO<sub>3</sub> load and flow (Figure 5-5) and TN load and flow (Figure 5-9) shows a more dynamic forecast, which does much better during the first three months of forecasting in 2003. The VARX models using observed SST's show reduced RMSE values for all variables as compared to the straight VAR model, especially in months 1-3. The number of correctly predicted load and flow terciles also increases from the VAR model, again concentrated in months one through three, with 2/3 months correctly forecast for the TN load and flow model, and 1/3 and 2/3 months respectively for NO<sub>3</sub> load and flow (Table 5-4).

To recreate a more realistic representation of how this type of model would be used in forecasting situations, we then used VARX(1) models to predict flows and loads in 2003 using predicted NINO 3.4 sea surface temperatures as an exogenous input. Once again, the forecasts flatten out and lose their dynamic nature for both the NO<sub>3</sub> load model (Figure 5-6) and the TN load model (Figure 5-10), and begin to resemble the VAR models. The numbers of correctly predicted flow and load terciles are almost the same as the numbers seen for the VAR model (Table 5-3), and the RMSE estimates (Table 5-4) again increase, and are even slightly greater than those seen in the VAR model for some variables. The lack of dynamic simulation seen by using the predicted SST's is odd, as we would expect to see the same dynamic results as the observed NINO 3.4 model, only less accurate. Similar results have been seen in regional cotton yield data [*Baigorria et al.*, 2008]. Comparing the observed and predicted monthly NINO

3.4 SST values for 2003 produces an  $R^2$  of 0.6. These results show that uncertainty in predicted values of SST degrade forecasts of flow and loads, and in actual management scenarios, observed SST's for model input will not be available.

Finally, the W-VAR models are shown for  $\text{NO}_3$  load and flow (Figure 5-7) and TN load and flow (Figure 5-11). It is immediately apparent that the W-VAR models are more dynamic and accurate in their forecasts of both load and flow. In the suite of exploratory time series models, the W-VAR models have the lowest RMSE estimates for  $\text{NO}_3$  load, TN load, and stream flow associated with each model (Table 5-4). With the exception of the flow forecast associated with TN load, the W-VAR models also generate the correct tercile of flow and load for 3/3 months (Table 5-3). Given these statistics and trends, the W-VAR models are seemingly doing a much better job of incorporating climate information into the seasonal forecasting models, despite not directly using any external climate data. The immediate advantage of this is that forecasts based on this wavelet method are not dependent on an additional variable that must be forecast, introducing another source of uncertainty and error, and at the same time this method manages to use implicit inter-annual climate data.

A reason that the W-VAR models do better than the VARX models using observed NINO 3.4 SST data is that the spectral information included in the model is not limited to ENSO relationships, but any significant frequencies that were identified in the global wavelet spectra. This is also advantageous in the sense that even the ENSO signal can be considered a non-stationary variable, as there are arguments that anthropogenic climate forcing may in fact be changing the nature of ENSO oscillation regularity and strength [Park and Mann, 2000; Tsonis and Swanson, 2009]. By not limiting the

reconstructed components to a narrow band of pre-determined 'valid' frequencies, we allow both different climate indices and a possibly changing ENSO itself to be included in the signal reconstruction.

In the case of nitrate load and stream flow, this included five RC's, and seven from the total nitrogen load. However, the number of total significant RC's was limited by the length of record and degrees of associated freedom with the analyzed data. Although over 30 years of nutrient and load data were used, the cone-of-influence of the wavelet power spectra only reached half of that, about 15 years, as the maximum periodicity that was able to be analyzed in a significant way. As a result, only reconstructed components from 1-15 years were able to be included as candidates for reconstruction, and any lower-oscillation climate signals were not captured in the W-VAR forecast time series models. It should also be noted that while these models are based on relatively temporally extensive data, they are not spatially distributed, only simulating loads and flows in one place—the stream outlet of a small forested upland basin of the Little River Watershed.

### **Bi-monthly updated W-VAR forecasts and SWAT simulations**

To represent how the W-VAR models would be used more realistically, forecasts were made for every two months of 2003, updated with the past two months of observed data and then re-forecast for the following two months. This updating and re-forecasting of the flows and nitrate loads (Figure 5-12) and total nitrogen loads (Figure 5-13) was done until December of 2003. Since SWAT was unable to simulate the NO<sub>3</sub> loads, we cannot directly compare the updated W-VAR model with it. However, compared to the other time series models, the bi-monthly updates for the nitrate do much better in both the short and long term. After 12 months, the updated W-VAR

model had predicted 10 nitrate load and 8 flow terciles correctly, while the un-updated W-VAR model only predicted 6 months correctly for both flow and load (Table 5-3). Additionally, the RMSE values through the entire year as compared to the un-updated W-VAR model were slightly decreased (Table 5-4).

When compared to SWAT simulated flow and TN load for 2003, the updated W-VAR models are quite competitive for the first three months of prediction, with tallies of correctly forecast terciles equal for the first three months (Table 5-3), and RMSE values that are only slightly different than the SWAT estimates for overall stream flow, and comparable with respect to TN load. In fact, the updated W-VAR models match SWAT in the number and distribution of correctly forecast TN loads through all of 2003, with 10/12 months in the correct tercile for both models, and 6/10 correct flow W-VAR updated flows compared to 8/10 correct flow terciles for SWAT. The ability of the W-VAR models to match a calibrated and validated simulation of flows and loads through SWAT shows that the use of these conceptually simpler statistical models for short and middle term management and decision making can save time and provide equally accurate information.

Although SWAT replicates the entire year of flows more accurately than any of the time series suite of models, this is to be expected, given that a properly calibrated and validated physically based model with extensive input land use data, and topography is a model that is expected to perform well for at least a year. It should also be noted that the SWAT input weather data used to simulate 2003 was observed. Together, the SWAT and time series models theoretically serve very different purposes. A time series model is not meant to and cannot simulate spatially distributed, long-term and

theoretical future conditions based on changing land uses, a use at which SWAT excels. The W-VAR models can provide shorter term monthly and seasonal predictions of high risk nutrient loads and high or low flows with minimal input once the initial model has been set up. Using the tercile methodology, one to three month outlooks of stream flows and nutrient loads can provide general advice for stakeholders and natural resource managers that are concerned with or trying to actively manage and reduce their loading risk in certain seasons and months as part of a BMP or even an adaptive management plan.

### **Summary and Discussion**

Using the knowledge from Chapters 2 through 4, we have utilized the ENSO teleconnection to the Little River Watershed basin K in Tifton, Georgia, that extends from climate to a strong inter-annual oscillatory signal in the stream flow and nutrient loads in several time series models that can forecast and identify months of high loading risk. As wavelet analysis can be likened to a band-pass filter, this can be exploited to extract and rebuild the component signals at different scales according to the desired specifications. We found that stream flow and nutrient loads were identified as having the most significant NINO 3.4 SST correlation and spectral signature [Keener *et al.*, 2010]. Although precipitation is the major driver of the hydrological cycle, it was not included as an input in these time series models. The non-inclusion of rainfall as a variable can be considered an advantage, as in the southeast, precipitation has high spatial variability even within a relatively small area such as basin K of the LRW. This high degree of variability and corresponding noise in the signal can add uncertainty to an already uncertain signal, the exclusion of which gives us interesting insight into hydro-climate processes in the LRW without a direct precipitation input.

For these reasons, observed  $\text{NO}_3$  and TN load and stream flow monthly anomalies were used as inputs to a multivariate time series model. Data in the time-domain was combined with observed NINO 3.4 values input as an exogenous independent variable to create models that incorporated ENSO information in a non-spectral way. This was contrasted with wavelet time series models that used significant reconstructed frequency components of  $\text{NO}_3$  and TN load and stream flow to inherently encompass ENSO climate variability without the addition of an exogenous variable.

In the VARX models, it was interesting that the inclusion of an ensemble hindcast of NINO 3.4 SST's versus the observed SST's in most cases made the prediction accuracy worse, yet in the case of forecast nitrate loads, actually made it better. This may be an artifact resulting from possibly erroneous 1992-1995 observed nitrate data, however, it decreases the amount of trust one is able to put in the VARX models as effectively including climate information into the time series model framework. In almost all cases, though, forecast error was reduced even by using the VARX and hindcast NINO 3.4 data as compared to the straight VAR models.

In general, the W-VAR models did a much better job than time-domain VAR and VARX models of reproducing and encompassing the monthly and seasonal climate variability trends in the LRW basin K, while theoretically maintaining the spectral signature of the inter-annual climate-based oscillations that are within each time series. The bi-monthly updated W-VAR models, more similar to how such a forecasting system might actually be implemented, demonstrated increasingly accurate monthly load predictions, correctly predicting 10/12 load terciles for both  $\text{NO}_3$  and TN, and 6/12 and 8/12 correct flow terciles with reduced RMSE values. However, the modeling adage of

“garbage in, garbage out” applies here, as problems with the nutrient data could be revealed by SWAT that are ignored by statistical modeling. Indeed, it appears as if the observed nitrate loads between 1992 and 1995 may exhibit measurement error, as the anomalies do not make sense with the observed or SWAT simulated total nitrogen loads (Figure 5-3c, 5-3d). Additionally, it is impossible for any of the time series models to specifically incorporate land-use change information in their predictions other than in the most inherent way, although SWAT simulations reflecting land-use changes in the last three decades in the LRW did not show any major changes or influences on the hydrology or nutrient loads. In a watershed in which there were major land-use changes in a short period of time, the W-VAR method may not perform as accurately.

In all non-updated time series models, forecast accuracy declined precipitously after the first three months of prediction, as would be expected from this type of model. These time series models are designed to be shorter-term tools for natural resource managers and farmers, who could use them to implement BMP's more quickly and appropriately as to reduce nutrient runoff risk by managing periods of high stream flows. This method has an advantage over time consuming processes of continually re-calibrating, adding huge amounts of weather and land-use data, and validating large and complex agro-hydrological models such as SWAT to make management predictions that are necessarily more short term. As of 2007, 16% of the land area in the entire LRW had implemented a BMP of some sort, of which 13.1% was devoted to nutrient management [*Sullivan and Batten, 2007*]. The implementation of these management practices were either established as a component of a federally funded cost share conservation program, or were paid by an individual who was provided

technical support free of charge. Nutrient management and water quality BMP's implemented within the watershed include grassed waterways, contour farming and terraces, seasonal residue management, improved grazing and animal management, and fertilizer and crop rotation optimization [Sullivan and Batten, 2007]. While some of these BMP's are implemented once (such as grassed waterways or fencing cattle out of stream tributaries), some are also implemented seasonally or annually, and could be positively influenced by one to three month advance knowledge of climate-based risk for high stream flows and the associated risk of flushing out high nutrient loads into the greater watershed area.

These prediction tools do not address the root causes of nutrient pollution, which is application of chemical fertilizers on agricultural land, or increasing animal production operations. In fact, the prediction tools are based on high or low stream flows flushing out nutrients from the watershed, which is in turn dependent on anthropogenic agricultural practices, surface and groundwater residence times, and nitrogen residence time in the LRW. In choosing to more carefully manage times of high stream flow, we are effectively managing how much nutrient pollution is let into the watershed during a period of time, not reducing the total amounts of pollutants that are input to the system. However, by using these models to more effectively manage stream flows and their nutrient pollution, the overall health of the water body and surrounding ecosystem would still be positively affected. If by managing a high flow season predicted using the climate based W-VAR model the amount of nutrient load is reduced, there would be less chance of eutrophication and ecosystem damage. While the current W-VAR model is based on data from one outlet in basin K of the LRW, it is feasible that climatic trends in

the region would hold similar patterns, and that warnings from one location could be extended to many. This would need to be tested in several other basins of the LRW, however.

Ideally, monthly time series models of high stream flows and nutrient loading risk would be used for shorter term seasonal and annual management, in conjunction with a larger hydrological package such as SWAT for any longer term simulation studies about more general land-use change or hydrology effects. This kind of analysis could easily be extended to other chemical pollutants in runoff, to create models of how other indicators of water quality and determinants of human health are influenced and predicted by inter-annual or longer climate variability.

Table 5-1. Summary of model performance measures for calibration period from 1979 to 1986 on LRK total runoff, sediment yield, and total nitrogen (TN) [Cho *et al.*, 2009]. Monthly RSR refers to the root mean squared error-observations standard deviation ratio, while NSE refers to the Nash-Sutcliffe Efficiency.

Evaluation Measures	Runoff (mm/year)	Sediment (ton/year)	TN (kg/year)
Observed total	342	60.0	4,975
Simulated total	354	62.2	5,691
Percent Error (%)	3.6	3.8	14.4
Monthly RSR	0.28	0.68	0.62
Monthly NSE	0.92	0.53	0.62

Table 5-2. Time series descriptions and attributes for both wavelet-VAR and VARX models for precipitation, nitrate load and concentration, stream flow, and total nitrogen load. Dashes (--) indicate that calculations were not done because of lack of significance of variable. Flow series with n/a do not have optimum lag indicated because the lag is shared with the associated nutrient load.

	Precipitation (mm)	NO <sub>3</sub> (kg)	NO <sub>3</sub> (mg/L)	Stream Flow (mm)	TN (kg)
Duration (mo/yr)	1/74-12/02	1/74-12/02	1/74-12/02	1/74-12/02	1/79-12/02
Number of sig. RC	3	6	0	5	6
% RC	34.5%	54.5%	20.8%	45.1%	48.8%
Variance					
Optimum lag W-VAR	--	5	--	n/a	7
Optimum lag VARX	--	1	--	n/a	1

Table 5-3. Number of times each vector autoregressive (VAR) or SWAT model correctly predicted the observed tercile of 2003 monthly TN load, NO<sub>3</sub> load, and corresponding stream flow, at different time steps away from t<sub>0</sub>. O-SST refers to observed NINO 3.4 values, P-SST refers to predicted hindcast NINO 3.4 values, W-VAR to wavelet based VAR, and updated W-VAR to the model updated with observed data every two months. SWAT values that are not applicable (n/a) either were not simulated (NO<sub>3</sub>), or only have one simulated value (flow).

	VAR	VARX + O-SST	VARX + P-SST	W-VAR	Updated W-VAR	SWAT
TN (kg):						
1 month	0	1	1	1	1	1
3 months	0	2	1	3	3	3
6 months	0	4	1	5	6	6
12 months	2	6	3	6	10	10
Flow (mm):						
1 month	0	1	0	1	1	1
3 months	0	2	0	2	2	3
6 months	1	3	1	3	4	4
12 months	4	4	4	5	6	8
NO <sub>3</sub> (kg):						
1 month	0	0	1	1	1	n/a
3 months	0	1	3	3	3	n/a
6 months	0	3	5	4	5	n/a
12 months	4	5	6	6	10	n/a
Flow (mm):						
1 month	0	1	0	1	1	n/a
3 months	0	2	1	3	3	n/a
6 months	1	4	2	5	5	n/a
12 months	4	5	4	6	8	n/a

Table 5-4. Summary of forecast vector autoregressive (VAR) time series model and SWAT performance by root mean squared error (RMSE) for one, three, six, and twelve month forecasts for NO<sub>3</sub>, TN load, and stream flow. O-SST refers to observed NINO 3.4 values, P-SST refers to predicted hindcast NINO 3.4 values, and W-VAR to wavelet based VAR models. For each predicted load model, the predicted stream flow RMSE's are listed under the loading of interest.

	VAR	VARX + O-SST	VARX + P-SST	W-VAR	Updated W-VAR	SWAT
RMSE at:	NO <sub>3</sub> (kg)					
1 month	59.7	47.7	3.5	2.1	2.1	n/a
3 months	111.1	92.1	52.1	26.5	10.6	n/a
6 months	110.9	81.2	59.4	62.9	31.7	n/a
12 months	105.8	117.2	103.0	98.3	47.7	n/a
	Flow (mm)					
1 month	35.9	4.5	47.5	7.8	7.8	n/a
3 months	29.7	14.5	38.1	9.7	11.0	n/a
6 months	26.2	27.6	29.0	13.1	11.9	n/a
12 months	20.4	46.5	23.0	13.8	12.2	n/a
	TN (kg)					
1 month	654.6	199.4	442.1	186.7	186.7	12.6
3 months	499.9	415.4	451.8	167.4	138.8	165.0
6 months	411.2	330.7	402.8	188.8	130.8	132.0
12 months	349.4	380.8	344.7	248.0	138.9	162.5
	Flow (mm)					
1 month	33.4	4.9	37.9	11.8	11.8	0.2
3 months	28.6	32.1	31.2	12.5	14.5	10.4
6 months	25.8	30.0	26.9	10.6	18.0	8.2
12 months	20.1	37.5	21.6	15.0	19.3	10.2

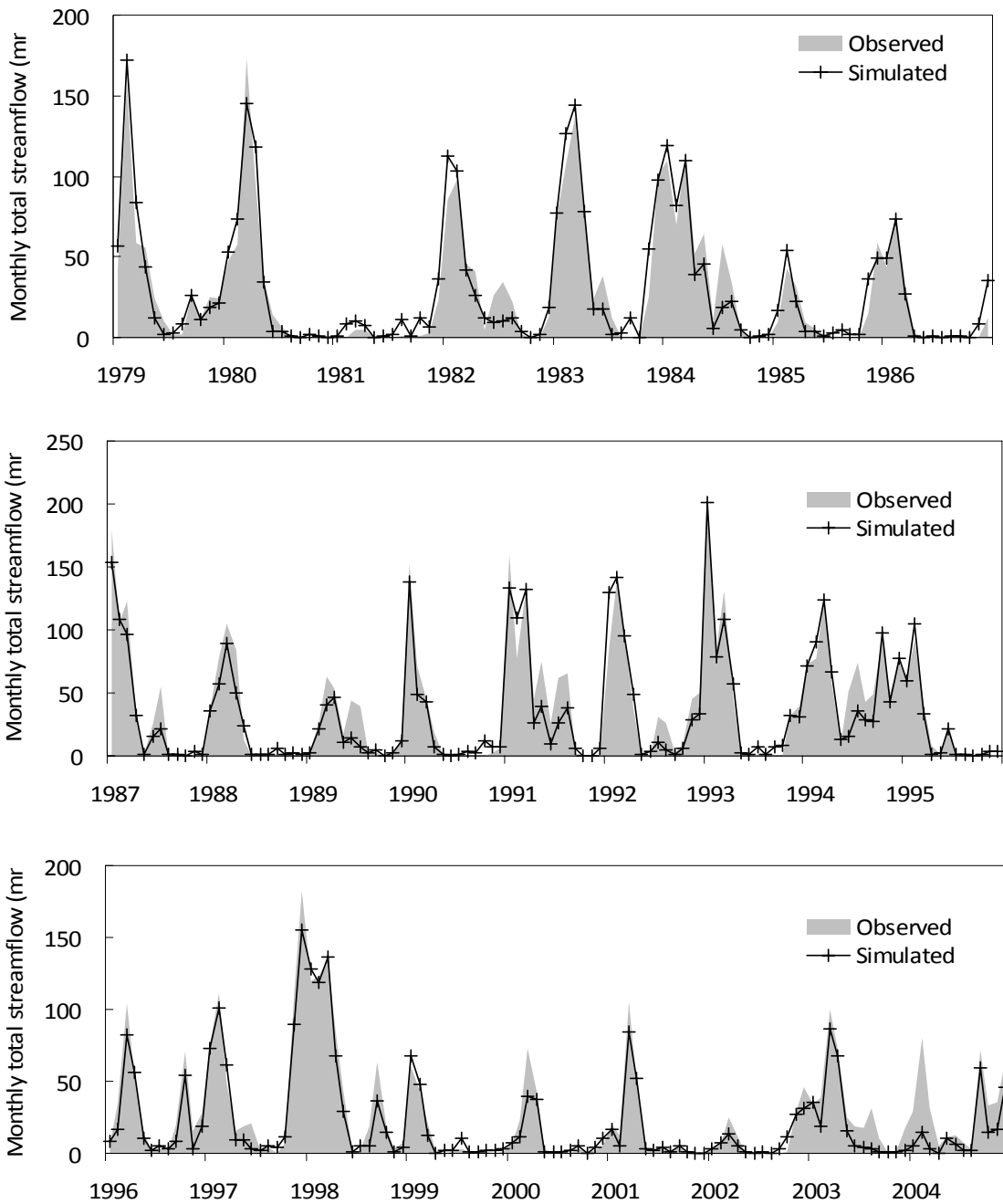


Figure 5-1. SWAT simulated total monthly stream flow (mm) in LRW basin K. Calibration is from 1979 to 1986, and validation is from 1987 to 2004. [Cho et al., 2009]

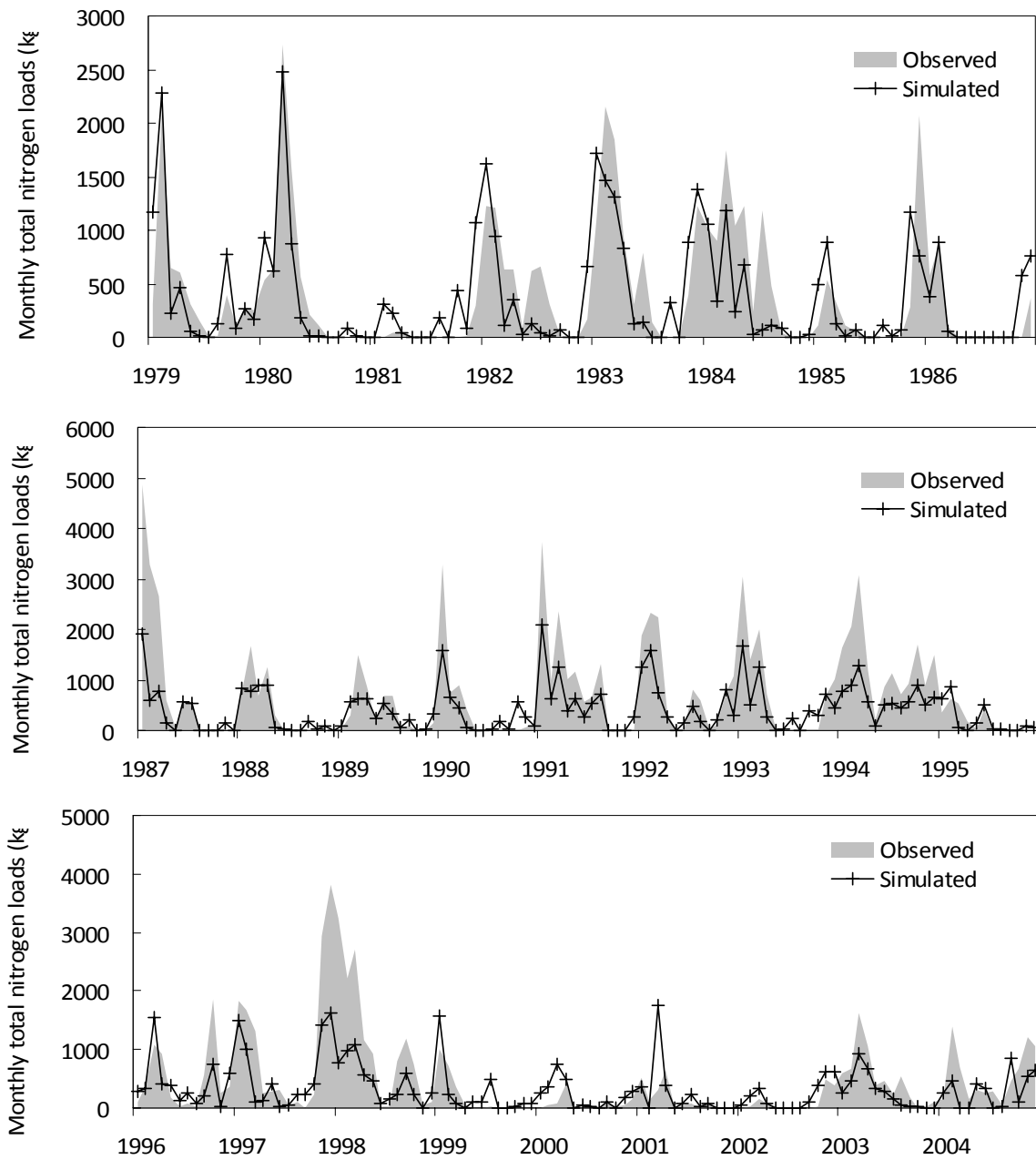


Figure 5-2. SWAT simulated total monthly total nitrogen load (kg) in LRW basin K. Calibration is from 1979 to 1986, and validation is from 1987 to 2004. [Cho et al., 2009]

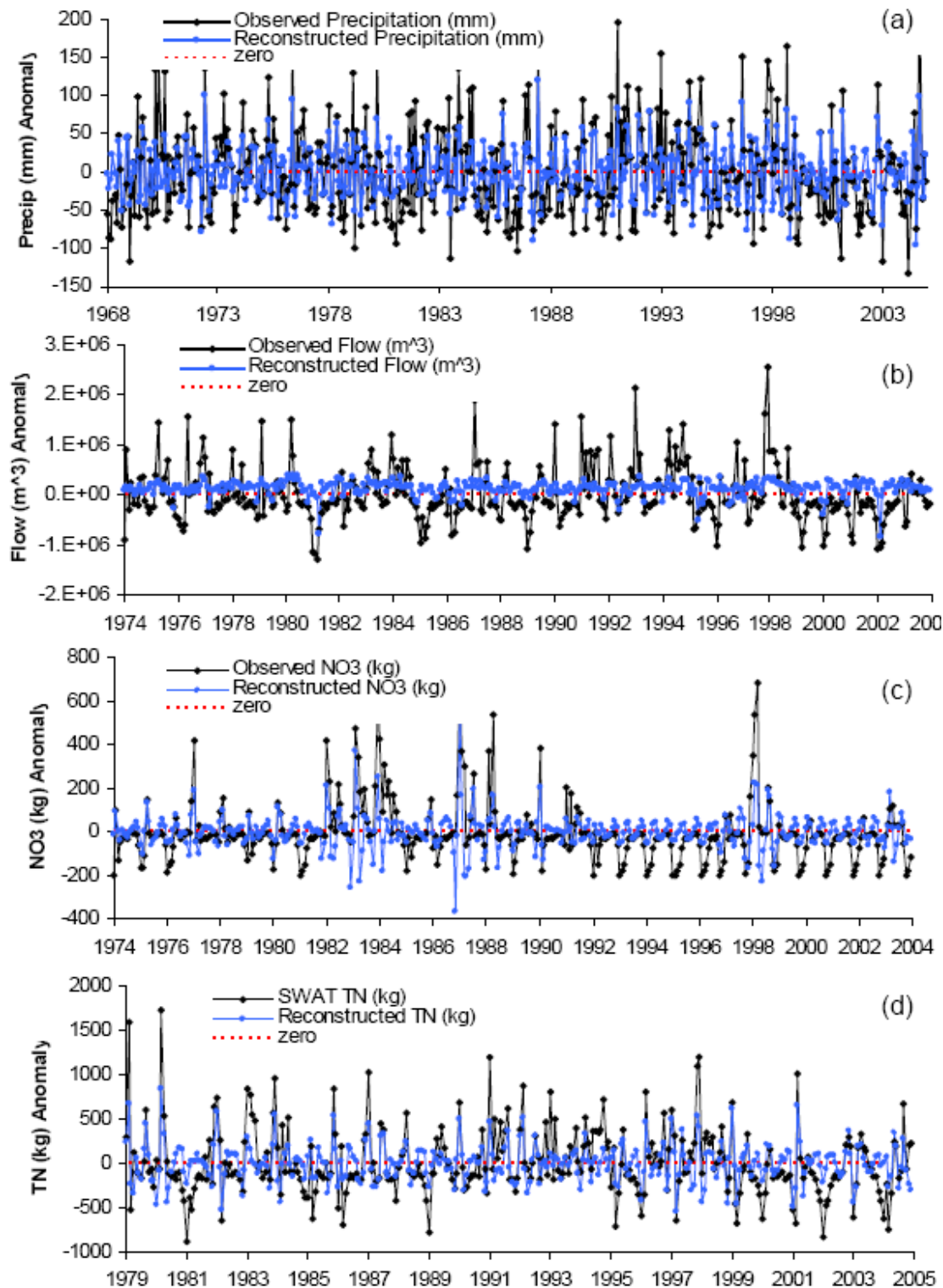


Figure 5-3. Original observed time series (monthly anomaly) and 95% significant wavelet reconstructed components for (a) precipitation (mm) (b) stream flow (m<sup>3</sup>) (c) nitrate load (kg) (d) total nitrogen load (kg). Red-dashed horizontal line indicates zero-line.

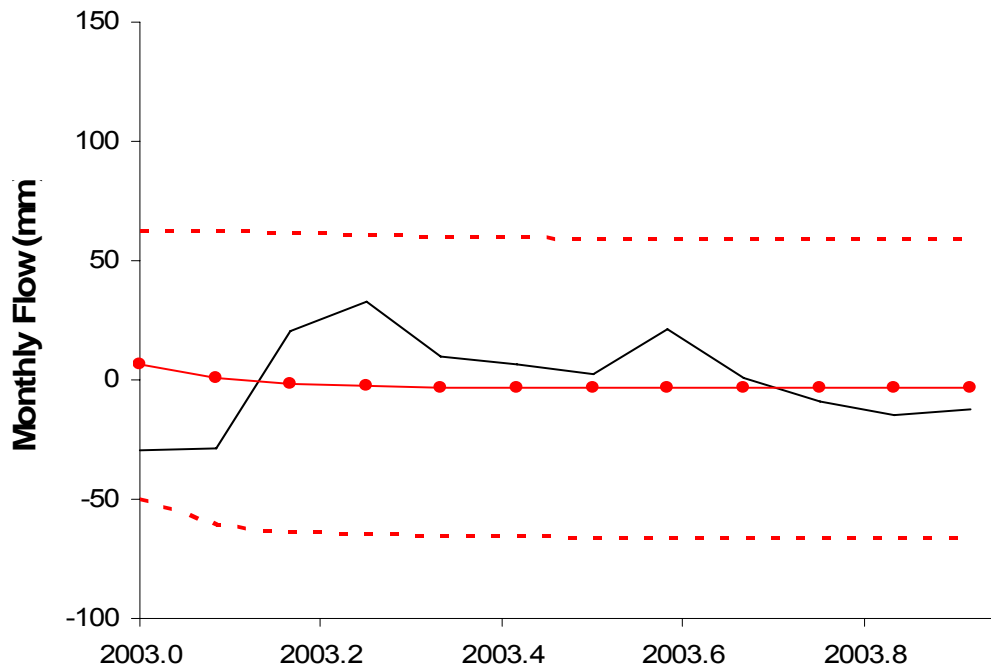
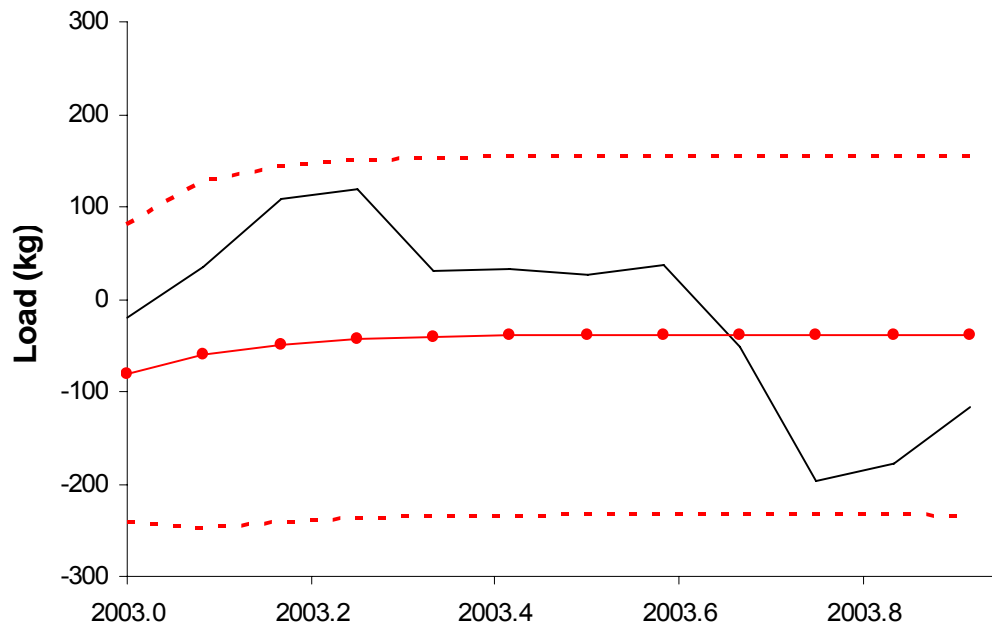


Figure 5-4. VAR(1) time series model with 95% CI (red dashed lines) of monthly nitrate load anomaly (kg) and streamflow (mm). Models are trained using data from 1974-2003, and validated using observed 2003 monthly data. Solid black line indicates observed data, while red lines with circles indicate forecast.

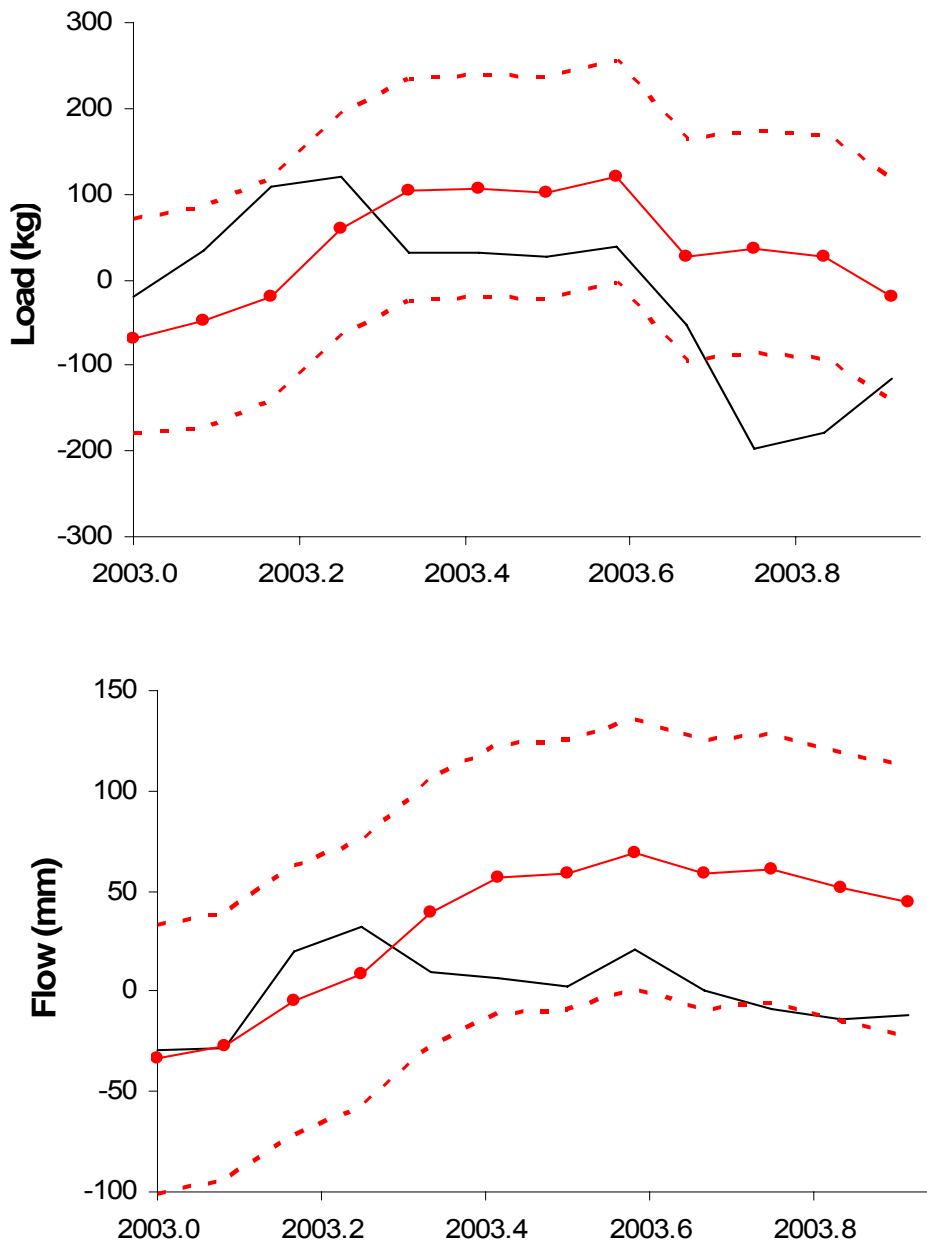


Figure 5-5. VARX(1) + Observed NINO 3.4 SST time series model with 95% CI of monthly nitrate load anomaly (kg) and streamflow (mm). Models are trained using data from 1974-2003, and validated using observed 2003 monthly data. Solid black line indicates observed data, while red lines with circles indicate forecast.

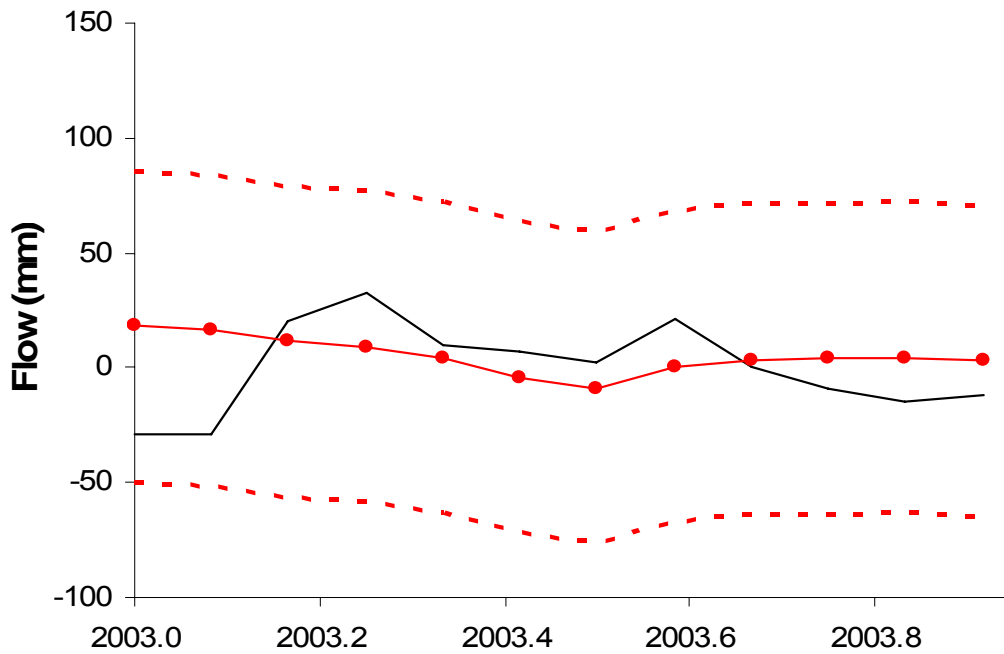
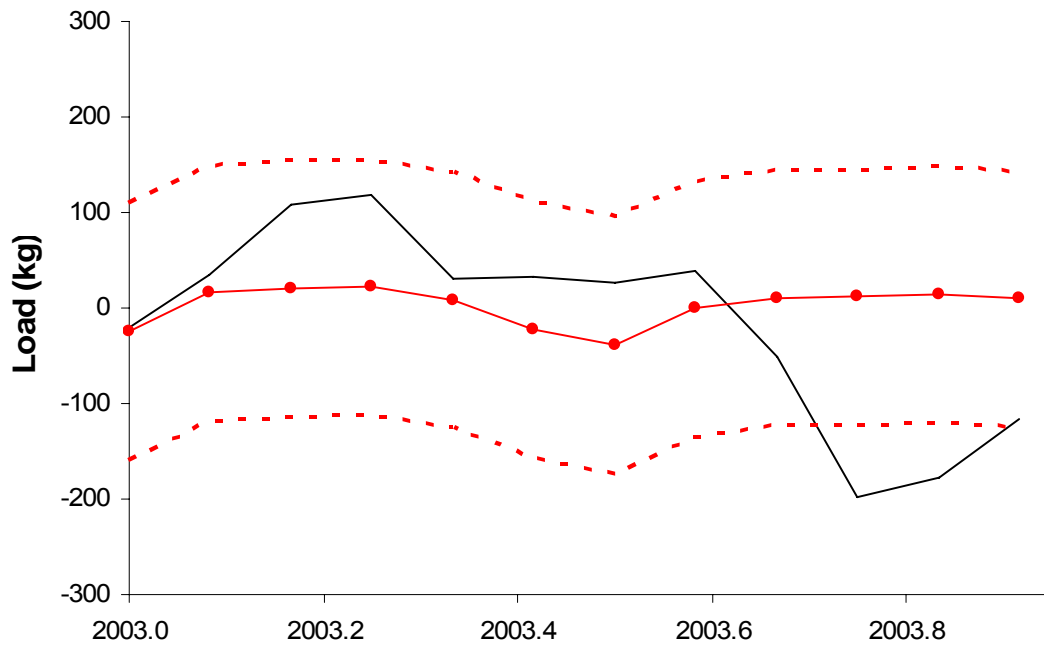


Figure 5-6. VARX(1) + Predicted NINO 3.4 SST time series model with 95% CI of monthly nitrate load anomaly (kg) and streamflow (mm). Models are trained using data from 1974-2003, and validated using observed 2003 monthly data. Solid black line indicates observed data, while red lines with circles indicate forecast.

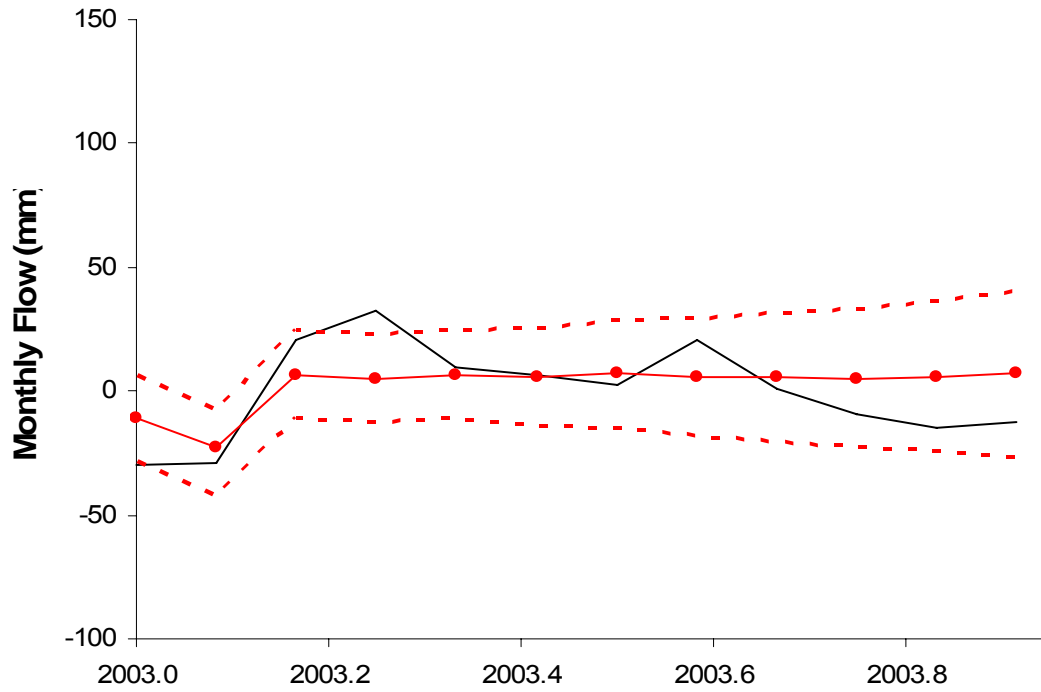
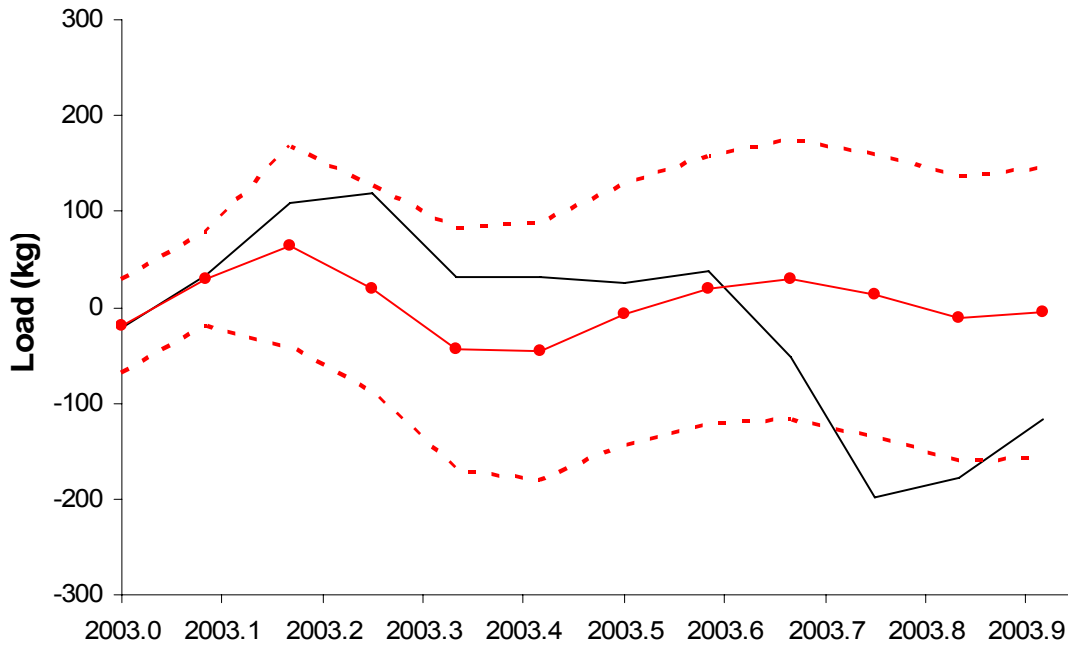


Figure 5-7. W-VAR(5) time series model with 95% CI of monthly nitrate load anomaly (kg) and streamflow (mm). Models are trained using data from 1974-2003, and validated using observed 2003 monthly data. Solid black line indicates observed data, while red lines with circles indicate forecast.

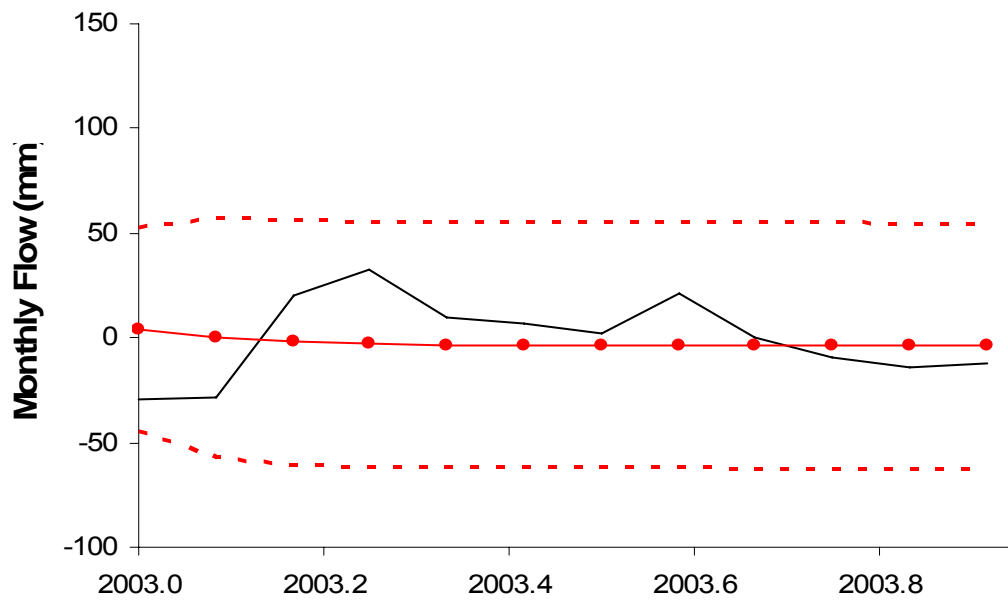
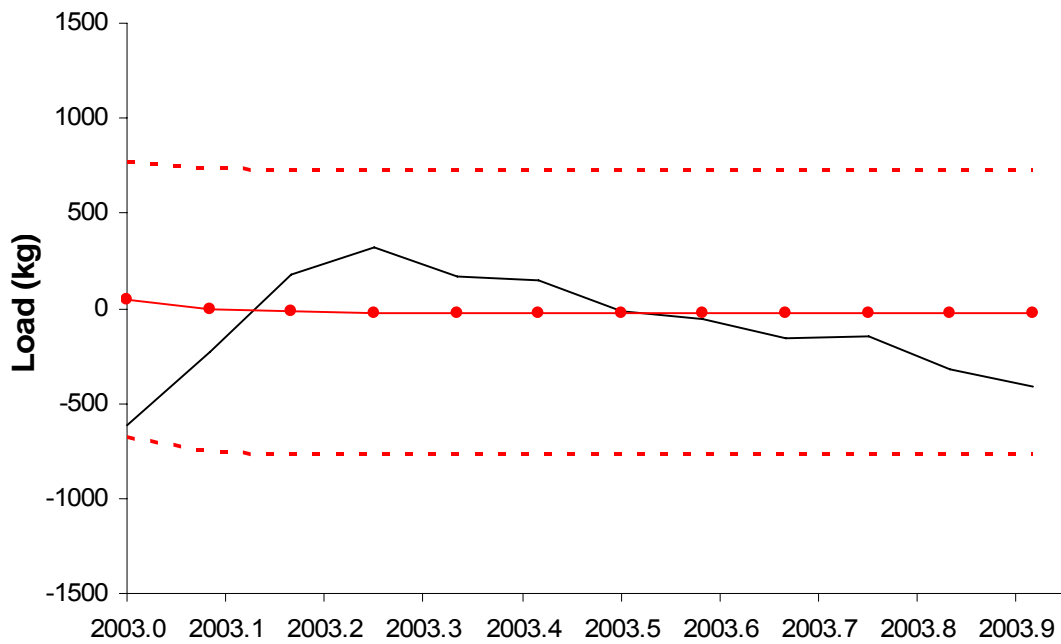


Figure 5-8. VAR(1) time series model with 95% CI of monthly TN load anomaly (kg) and streamflow (mm). Models are trained using data from 1974-2003, and validated using observed 2003 monthly data. Solid black line indicates observed data, while red lines with circles indicate forecast.

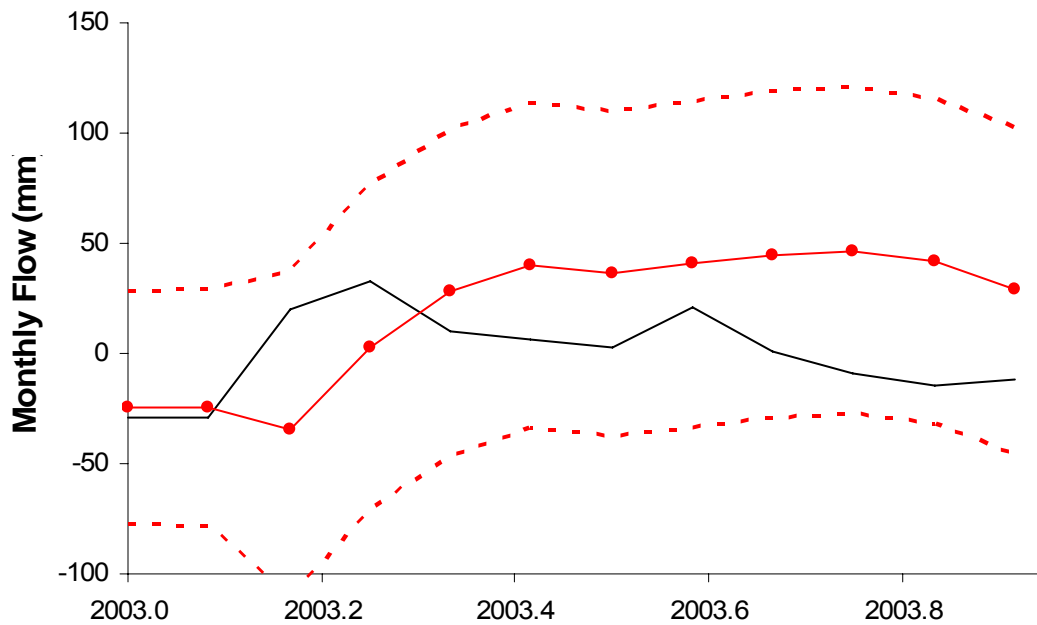
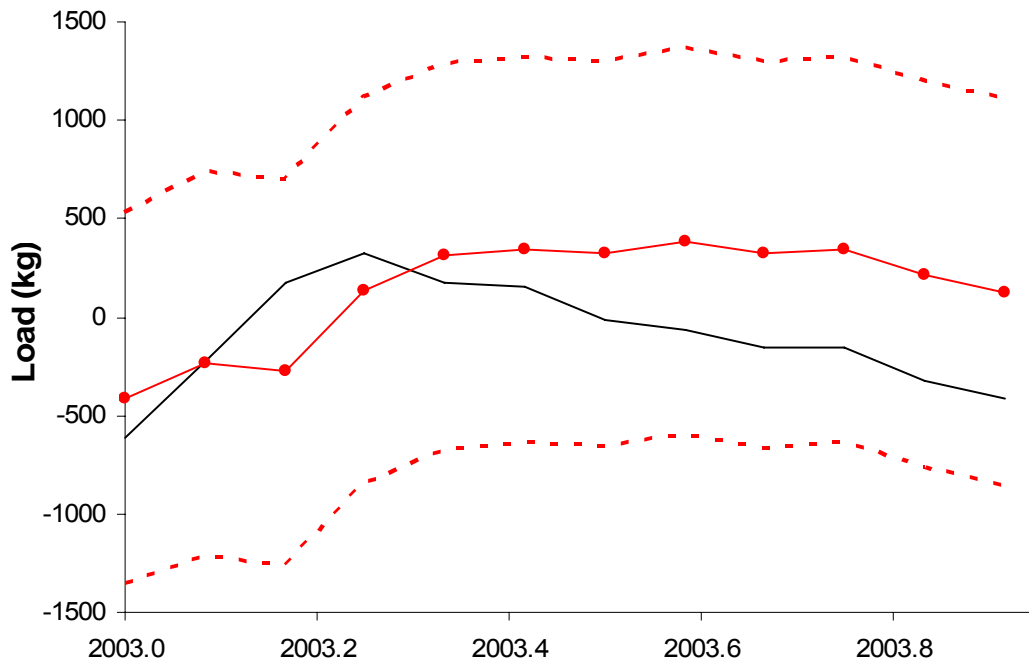


Figure 5-9. VARX(1) + Observed NINO 3.4 SST time series model with 95% CI of monthly TN load anomaly (kg) and streamflow (mm). Models are trained using data from 1974-2003, and validated using observed 2003 monthly data. Solid black line indicates observed data, while red lines with circles indicate forecast.

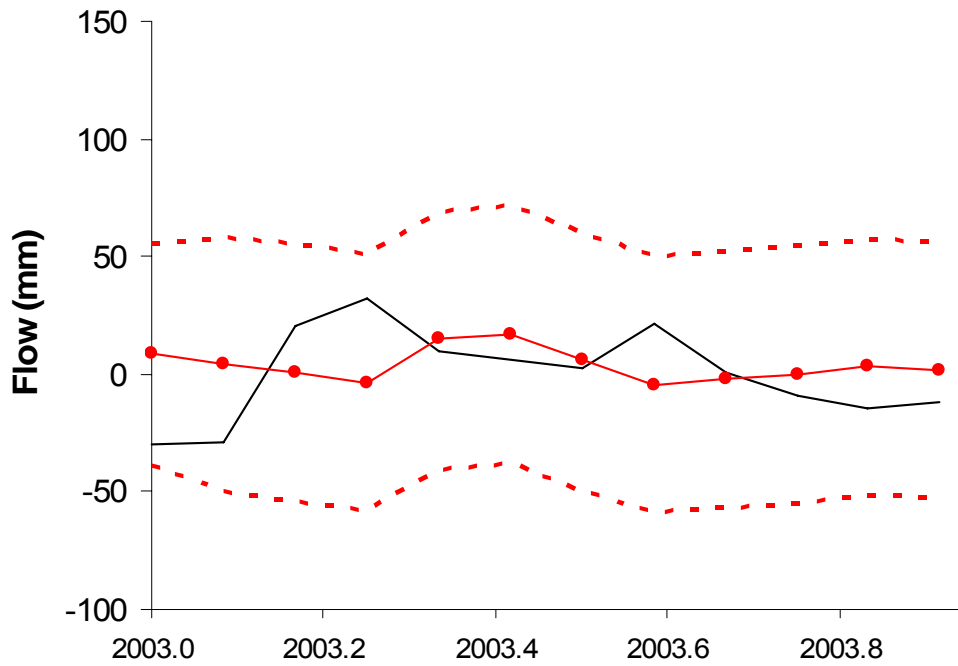
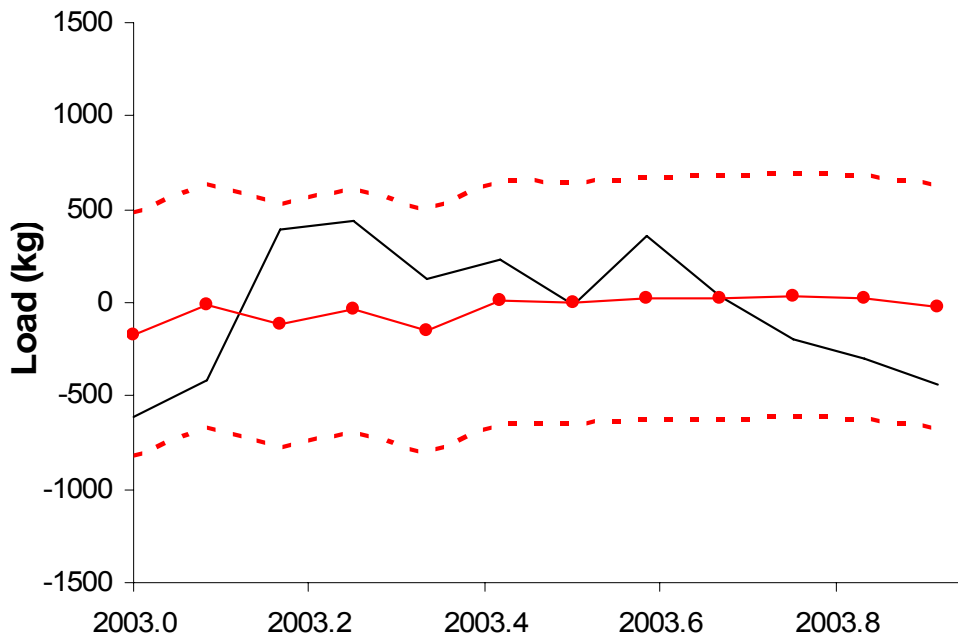


Figure 5-10. VARX(1) + Predicted NINO 3.4 SST time series model with 95% CI of monthly TN load anomaly (kg) and streamflow (mm). Models are trained using data from 1974-2003, and validated using observed 2003 monthly data. Solid black line indicates observed data, while red lines with circles indicate forecast.

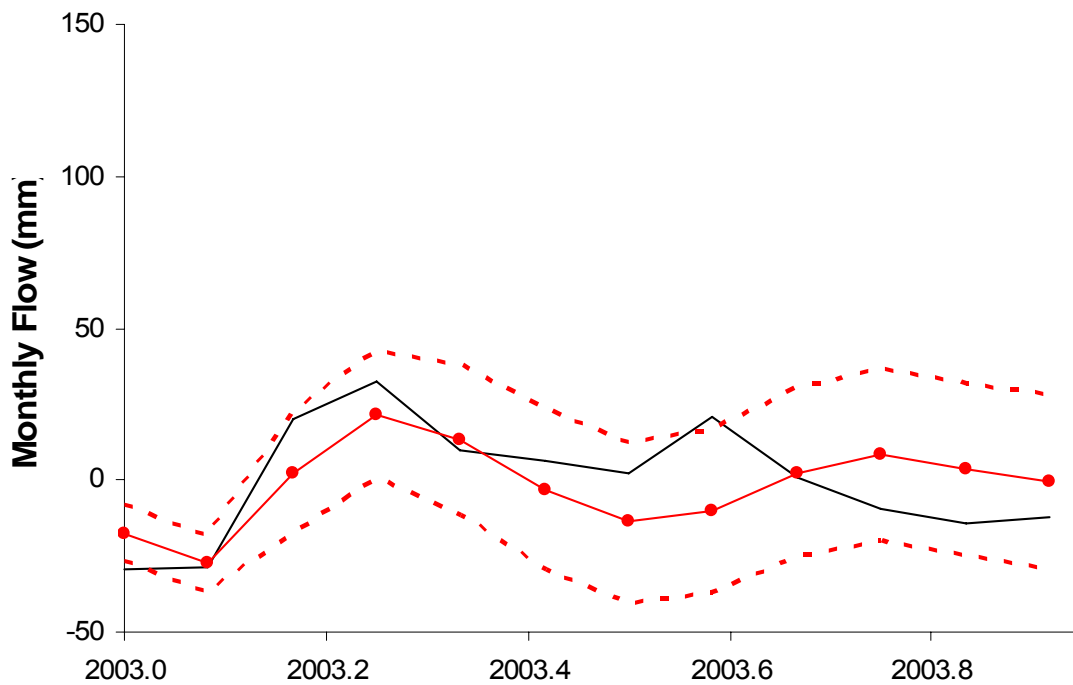
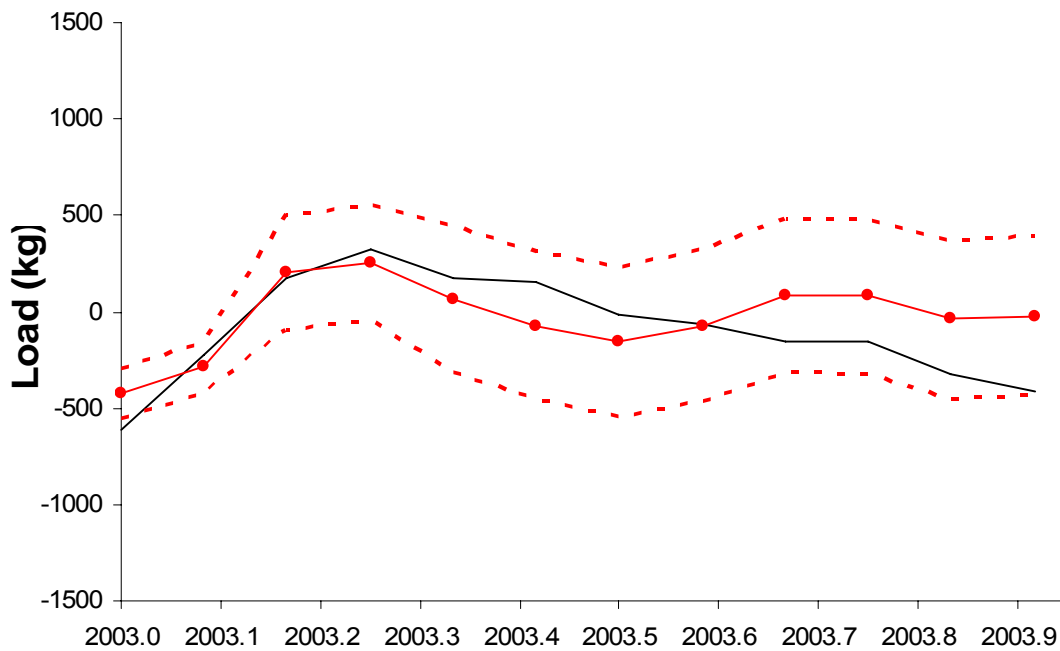


Figure 5-11. W-VAR(7) time series model with 95% CI of monthly TN anomaly (kg) and streamflow (mm). Models are trained using data from 1974-2003, and validated using observed 2003 monthly data. Solid black line indicates observed data, while red lines with circles indicate forecast.

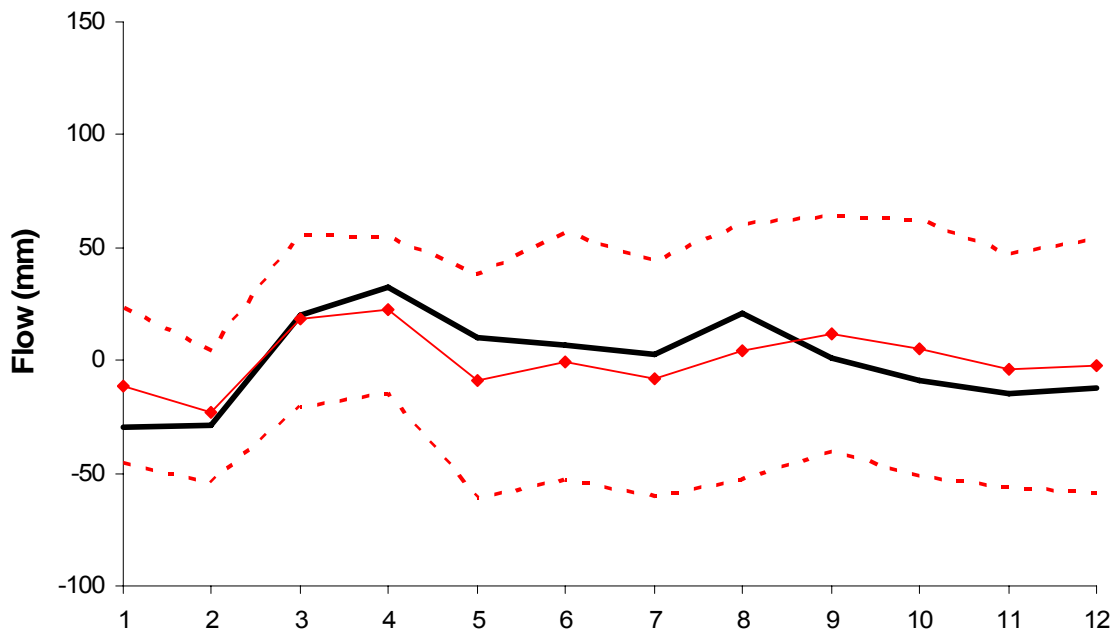
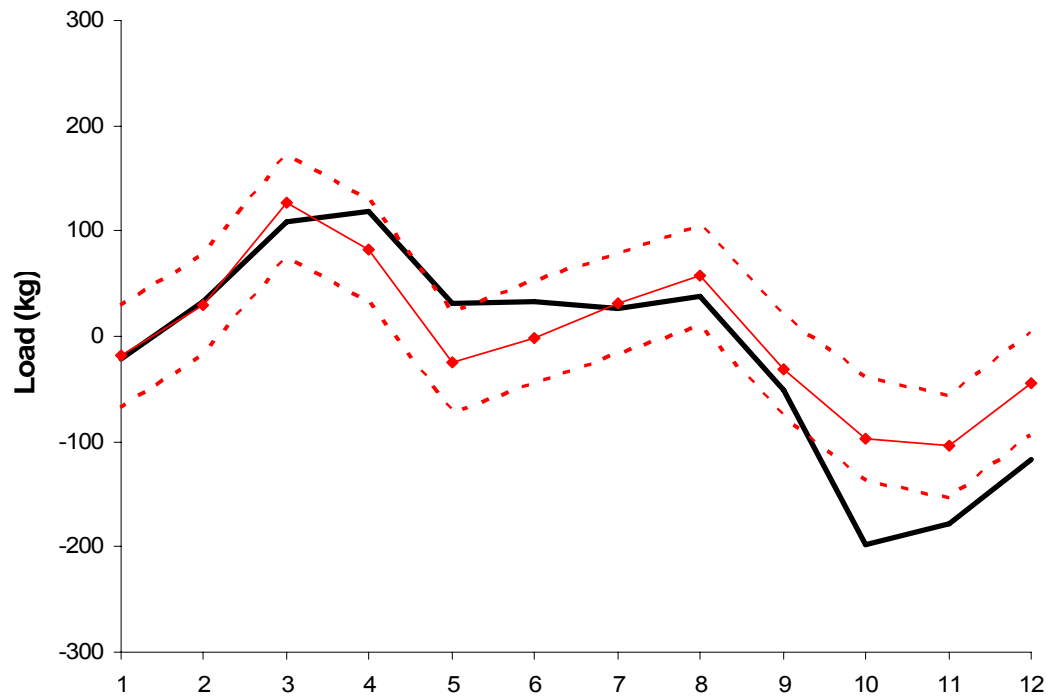


Figure 5-12. Bi-monthly updated W-VAR(5) time series model for 2003 with 95% CI of monthly nitrate anomaly (kg) and stream flow (mm). Month 1:12 (Jan: Dec) is indicated on the x-axis. Solid black line indicates observed data, while red lines with circles indicate forecast.

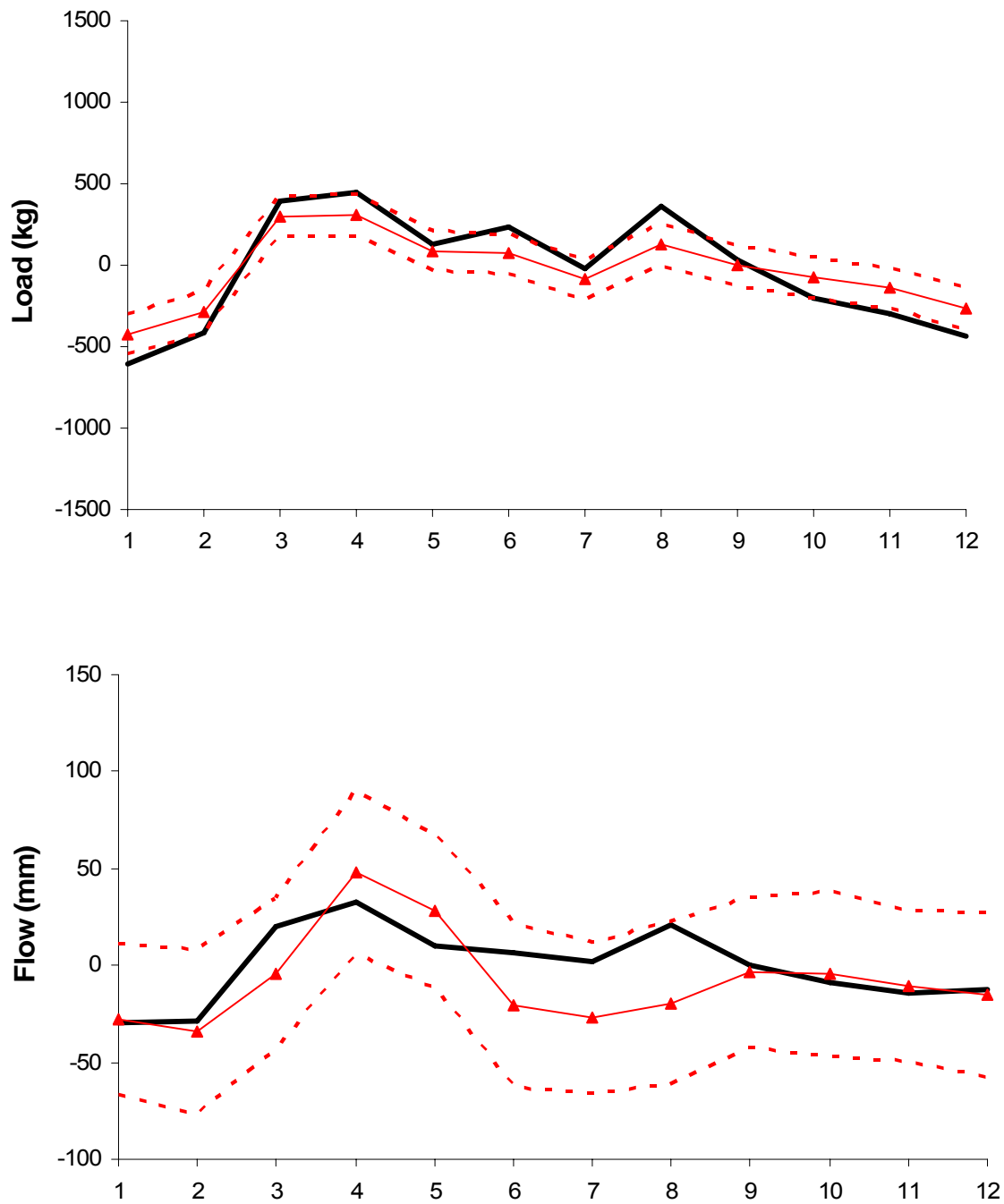


Figure 5-13. Bi-monthly updated W-VAR(7) time series model for 2003 with 95% CI of monthly total nitrogen anomaly (kg) and streamflow (mm). Month 1:12 (Jan: Dec) is indicated on the x-axis. Solid black line indicates observed data, while red lines with circles indicate forecast.

## CHAPTER 6 CONCLUSIONS

Global climate change has been called the socio-economic, environmental, and energy challenge of our lifetime. The possible consequences of a changing climate are both far-reaching and severe, making research that can help us better understand, adapt to, mitigate, or stop and reverse its consequences a crucial part of modern environmental science. Warming of the average global climate over the past century has been proven unequivocally [*IPCC et al.*, 2007], and because the hydrological cycle is linked closely to variations in climate, citizens and water resource managers both will have to deal with new challenges associated with both water quantity and quality. Over the past several decades, research into global warming has revealed significant changes in precipitation patterns, weather extremes such as floods, droughts and storms, snow-pack duration and amount, increased evaporation, increased wildfire risk, and changes in soil moisture and runoff [*Mote et al.*, 2005; *Stewart et al.*, 2005; *Westerling et al.*, 2006]. These relatively sudden changes make it increasingly difficult to efficiently adapt current anthropological practices such as large-scale agriculture and maintaining a municipal water supply, while continuing to provide clean, safe drinking water and adequate food to an ever increasing population.

Specifically, it is difficult to say exactly what climate change effects will be, as climate signals are fairly chaotic and noisy, encompassing annual, inter-annual, decadal, or much longer periods of variability. This climate variability combined with the effect of exogenous variables and the lack of extensive monitoring systems, both spatially and temporally, can make extracting short or long term climatic patterns an uncertain process. For both short and middle term risk management planning, inter-

annual modes of climate variability and their seasonal expression are of interest. There is a need to identify climate non-stationarities and their links to watershed water quality outcomes. In this dissertation, we isolated, modeled and forecasted the effects of inter-annual climate variability on hydrology and water quality in the southeast United States.

To explore whether there was a basis for correlating ENSO phase, hydrology, and water quality in the southeast United States, we used over 30 years of hydrological data simulated by the Watershed Assessment Model (WAM) for basin S-191 of the Lake Okeechobee watershed in south Florida. By doing both monthly and seasonal contingency table analyses of hydrology and phosphorus (P) loads in the watershed as delineated by annual JJA categorical ENSO phase, we found that some ENSO phases tended to produce significantly greater seasonal P loads (February-April of El Niño years, May-July of La Niña years, and August-September of neutral years) or lower seasonal P loads (May-July of El Niño years, February-April and August-September of La Niña years, and February-April and May-July of neutral years). The greater P load potential in certain months was mostly consistent with documented trends in greater precipitation.

As it was difficult to assign statistical significance using annual designations of ENSO, a newer monthly M-ENSO index was also used to examine the results on a finer temporal scale. Across all variables of simulated P load, concentration, stream flow, and observed precipitation, the M-ENSO classification reduced both the range and average of the La Niña summer months, and allowed more standard methods of identifying formal significance. Consequently, this monthly classification which is more representative of current SST conditions instead of those of the previous October has a

more accurate temporal scale that suggests that the previous months (October to April) of an annual JMA La Niña may be erroneously creating patterns in the summer months. Because of the discrepancies in significance between annual and monthly ENSO phase, we concluded that using a continuous record of NINO 3.4 sea surface temperatures themselves would allow the identification of more accurate local trends and patterns using observed data.

In Chapter 3, univariate and multivariate wavelet analysis is used to identify and quantify the significance of a teleconnection between SST associated with the NINO 3.4 index, and observed precipitation, stream flow, and nitrate concentration and load in the Little River Watershed in Georgia. The results confirm that the known physical mechanism of ENSO teleconnection in the southeast United States [*Schmidt et al.*, 2001; *Ropelewski and Halpert*, 1986] is causally linked to inter-annual variability within precipitation, stream flow, and nitrate load signals in the LRW. The high shared power and significant correlation between these variables confirms that the ENSO teleconnection seen in the precipitation and stream flow signals in large river and watershed systems around the world [*Chiew et al.*, 1998; *Rajagopalan and Lall*, 1998; *Handler*, 1990; *Kulkarni*, 2000; *Hansen et al.*, 1997; *Piechota and Dracup*, 1999; *Pascual et al.*, 2000] extends to the hydrology and nitrate loads in a small basin of the Little River Watershed. We found common areas of high, shared power and time series inter-annual variability manifested in the NINO 3.4 SST index and 36 years of LRW monthly precipitation data, and 29 years of stream flow, nitrate concentration and nitrate load data. Areas of the highest power for all hydrological variables were observed in the 3-7 year periodicity known to be related to ENSO modes of variability. Temporally, the

area of greatest variability was centered on the 1997-98 El Niño event. Nitrate concentration was the variable with the weakest ENSO signal power, which is due to it being more dependent on extraneous variables such as human-caused agricultural activities. High or significant power was seen in precipitation, stream flow, and nutrient loads in the 1-2 year period centered on the 1998-99 La Niña, and may be related to other climate indices and strong seasonal signals. The stronger power seen in nitrate load time series, rather than concentration or precipitation, suggest that stream flow variability dominates the trends seen in loads.

A finding of note from the work in Chapter 3 was that the ENSO signal is more visible in the stream flow and nitrate loads of the LRW than in the precipitation signal. Although the thirteen weather stations used to form the precipitation series in this research are well distributed across the 16.8 km<sup>2</sup> area of basin K in the LRW, spatial variability of rainfall in the southeast United States is great, and still does not encompass all of the variability inherent in the watershed. For this reason, the ENSO signal present in the precipitation record may be somewhat damped, especially when considered next to the stream flow record. In addition to being a smoothed function of precipitation, stream flow in the Little River Watershed may be strengthening the correlation shared with the ENSO signal. To determine what the mechanism for this increased ENSO signal power correlation with flow rather than precipitation is, in Chapter 4 we again turned to a physical hydrology simulation model, the Soil and Water Assessment Tool (SWAT).

Using a calibrated and validated SWAT model of LRW-K, the detailed surface and groundwater hydrology was continuously simulated on a daily basis from 1979 to 2004,

and aggregated into monthly average values for use in analysis. The clear increase in the power of the inter-annual climate signal is demonstrated by shared patterns in water budget and exceedance curves, as well as qualitatively and quantitatively in high ENSO related energy in the wavelet spectral analyses and the 95% significant periodicities against a red noise background for each variable both analyzed alone and with the NINO 3.4 SST index. As has been previously discussed, groundwater flow in the LRW is responsible for up to 80% of the total stream flow [Sheridan, 1997], as well as comprising the main route for movement of soluble nutrients [Lowrance et al., 1984]. In the Little River Watershed basin K, in Tifton, Georgia, the power of the climatological teleconnection to the El-Niño/Southern Oscillation is strengthened in both the observed and simulated stream flow through the mechanisms of groundwater and interflow, as they are confined by a geological layer, the Hawthorn Formation. Both the univariate and multivariate spectral ENSO signals were visible and significant in the groundwater and interflow SWAT simulations, which suggest that we could expect to see an even more powerful signal if the flow data were simulated more precisely with a fully spatially-distributed model or there was continuous detailed observed groundwater data.

The Hawthorne formation in the Little River Watershed forms a nearly perfect aquaclude, so although infiltration is very fast, soil saturation can be reached relatively quickly while recharge into the deep aquifer is extremely slow [Rawls et al., 1976; Sheridan, 1997]. This results in the increased significance of groundwater and interflow contributions to both soluble nutrient movement into outlet stream flow, and the stream flow itself. In the LRW, perhaps much more than other watersheds without a ubiquitous confining layer and lack of topography, the power of the 3-7 year ENSO signal that is

found in precipitation is increased in the observed and simulated stream flow signal. The entire explanation of the strengthened ENSO power may have as much to do with the groundwater, interflow and Hawthorn Formation, as with the land use of the watershed itself. In turn, this raises the question of what the actual physical properties of the watershed are that lead to this potentially unique increased ENSO signal power in the simulated and observed surface and sub-surface flow regimes of the LRW-K. By gathering physical properties of this relatively small coastal plain watershed such as the total area and depth to the surficial aquifer, transmissivity and porosity in the sandy soils, residence times of groundwater and surface water, and hydraulic conductivities, it may be possible to create an analytic function describing exactly how the precipitation based integration of stream flow through time and space in the entire hydrological system occurs.

Relative sensitivity analysis and calibration of SWAT simulated LRW-K hydrology previously showed that surface response parameters were significantly more sensitive than those pertaining to sub-surface hydrology [*Feyereisen, Strickland, et al., 2007*]. The most sensitive parameter to overall water yield, storm flow, groundwater flow and interflow was the curve number for agricultural land, partly due to the increased surface runoff from even average precipitation events on cropped land. In relationship to the future of the Little River Watershed, this implies that an increase in land area used for agricultural purposes may serve to strengthen the ENSO signal in stream flow even more than it currently is, while a significant decrease in cropped area could cause the teleconnection and predictive relationship between ENSO and flow, and consequently other variables such as pollutant loads, to weaken. As such, this ENSO teleconnection

and its relationship with agricultural area could hold for other Coastal Plain watersheds as well.

The specific mechanism by which the ENSO signal power is increased via ground water hydrology and a confining layer in the Little River Watershed is by no means the only way in which a watershed could increase a climate signal delivered primarily through precipitation [Cayan *et al.*, 1999; Maurer *et al.*, 2006]. However, the spatial integration and reduction of noise in precipitation that the stream flow signal effectively accomplishes is most likely a primary method of signal power increase in different watersheds, as research on river flows from around the world have shown significant spectral signals corresponding to multiple climate indices [Labat, 2008]. This non-intuitive relationship between ENSO signal strength and stream flow could prove to be helpful for making seasonal climate predictions in a geographic area with a weaker than desirable ENSO/precipitation signal, as a predictive relationship could be found between stream-flow or other proxy hydro-climatic variables. The exploration of additional non-precipitation hydrologic variables as they correlate to ENSO could expand how climate data could be used for more practical hydrologic prediction and for municipal water supply management, as well. The use of seasonal forecasts based on ENSO teleconnection with both surface and ground water flows and pollutant and nutrient loads could also more immediately benefit water resource managers or farmers, as decisions on irrigation, allocation, and runoff management would be based on actual climate information, and would not be predictions made so far in the future as to render them virtually unusable in normal management plans.

As a significant hydrologic and water quality teleconnection between ENSO and the LRW basin K has been identified, quantified, and mechanistically explained, Chapter 5 explored using a novel wavelet-based time series model (W-VAR) to predict monthly stream flows and nitrogen (N) loads in the Little River Watershed based on the NINO 3.4 sea surface temperature index. As wavelet analysis can be likened to a band-pass filter, this can be exploited to extract and rebuild the component signals at different scales according to the desired specifications. Although precipitation is the major driver of the hydrological cycle, it was not included as an input in these time series models. The non-inclusion of rainfall as a variable can be considered an advantage, as in the southeast, precipitation has high spatial variability even within a relatively small area such as basin K of the LRW. This high degree of variability and corresponding noise in the signal can add uncertainty to an already uncertain signal, the exclusion of which gives us interesting insight into hydro-climate processes in the LRW without a direct precipitation input.

For these reasons, observed  $\text{NO}_3$  and TN load and stream flow monthly anomalies were used as inputs to a multivariate time series model. Data in the time-domain was combined with observed NINO 3.4 values input as an exogenous independent variable to create models that incorporated ENSO information in a non-spectral way. This was contrasted with wavelet time series models that used significant reconstructed frequency components of  $\text{NO}_3$  and TN load and stream flow to inherently encompass ENSO climate variability without the addition of an exogenous variable.

In general, the W-VAR models did a much better job than time-domain VAR and VARX models of reproducing and encompassing the monthly and seasonal climate

variability trends in the LRW basin K, while theoretically maintaining the spectral signature of the inter-annual climate-based oscillations that are within each time series. The bi-monthly updated W-VAR models, more similar to how such a forecasting system might actually be implemented, demonstrated increasingly accurate monthly load predictions, correctly predicting 10/12 load terciles for both NO<sub>3</sub> and TN, and 6/12 and 8/12 correct flow terciles with reduced RMSE values. However, the modeling adage of “garbage in, garbage out” applies here, as problems with the nutrient data could be revealed by SWAT that are ignored by statistical modeling. Indeed, it appears as if the observed nitrate loads between 1992 and 1995 may exhibit measurement error, as the anomalies do not make perfect sense with the observed or SWAT simulated total nitrogen loads (Figure 5-2c, 5-2d). Additionally, it is impossible for any of the time series models to specifically incorporate land-use change information in their predictions other than in the most inherent way, although SWAT simulations reflecting land-use changes in the last three decades in the LRW did not show any major changes or influences on the hydrology or nutrient loads. In a watershed in which there were major land-use changes in a short period of time, the W-VAR method may not perform as accurately.

In all non-updated time series models, forecast accuracy declined precipitously after the first three months of prediction, as would be expected from this type of model. For that reason, it should be remembered that these models should not be used to make predictions more than three months in the future, as the uncertainty is magnified each month farther from where the observations end, even beyond what is shown in the 95% confidence intervals in the forecasts. These time series models are designed to be shorter-term tools for natural resource managers and farmers to use to implement

BMP's more quickly and appropriately as to reduce nutrient runoff risk by managing periods of high stream flows, instead of continually re-calibrating, adding huge amounts of weather and land-use data, and validating large and complex agro-hydrological models such as SWAT to make management predictions that are necessarily more short term.

These prediction tools do not address the root causes of nutrient pollution, which is application of chemical fertilizers on agricultural land, or increasing animal production operations. In fact, the prediction tools are based on high or low stream flows flushing out nutrients from the watershed, which is in turn dependent on anthropogenic agricultural practices, surface and groundwater residence times, and nitrogen residence time in the LRW. In choosing to more carefully manage times of high stream flow, we are effectively managing how much nutrient pollution is let into the watershed during a period of time, not reducing the total amounts of pollutants that are input to the system. However, by using these models to more effectively manage stream flows and their nutrient pollution, the overall health of the water body and surrounding ecosystem would still be positively affected. If by managing a high flow season predicted using the climate based W-VAR model the amount of nutrient load is reduced, there would be less chance of eutrophication and ecosystem damage. While the current W-VAR model is based on data from one outlet in basin K of the LRW, it is feasible that climatic trends in the region would hold similar patterns, and that warnings from one location could be extended to many. This would need to be tested in several other basins of the LRW, however.

Ideally, monthly time series models of high stream flows and nutrient loading risk would be used for shorter term seasonal and annual management, in conjunction with a larger hydrological package such as SWAT for any longer term simulation studies about more general land-use change or hydrology effects. This kind of analysis could easily be extended to other chemical pollutants in runoff, to create models of how other indicators of water quality and determinants of human health are influenced and predicted by inter-annual or longer climate variability.

In the course of researching effects of inter-annual climate variability as manifested in the ENSO phenomenon on hydrology and water quality in the southeast United States, we have arrived at predictive models to forecast the near future. Through these models, we thereby add knowledge to how we understand global non-stationary climate modes and their regional consequences at the watershed level. However, this work does bring about questions of how we as a society will deal with the fact of environmental and hydrological non-stationarity as a whole. A recent topic generating much discussion in the academic environmental sciences is that of “The Death of Stationarity” [*Pielke Jr.*, 2009; *Rial et al.*, 2004]. In this case, the general term “stationarity” refers to our ability to predict the future based on recorded or reconstructed averages, variances, and statistics accurately describing the past.

If global climate change is in fact partly or significantly anthropogenic in nature, then humans are changing the global climate cycle at a faster rate and in different ways than the Earth has ever experienced before. Additionally, the Earth’s climate system in geologic time has always been non-linear in nature [*Rial et al.*, 2004], with chaotic inputs and outputs, fuzzy boundaries, and multiple equilibria that can cause seemingly

unforeseeable sudden shifts and abrupt changes. In light of these realizations, we can reasonably say that environmental stationarity has always been dead, and perhaps it is just recently, with anthropogenic influences putting the final nail in its coffin, that the research community as a whole is beginning to accept it and deal with it in models and forecasts. There are those advocating the use of models to predict a wide range of future conditions so as to be able to enable robust policy related decision-making and test the limits of human adaptation as a method of dealing with system non-stationarities [Dessai *et al.*, 2009]. There are also those who, equally importantly, continue to advance the understanding of physical systems informing the models in order to make forecasts increasingly accurate despite unforeseen non-linearities.

In the end, however way we as a global community choose to deal with climate and hydrological non-stationarities, we must first recognize that they exist, both in our short-term planning of municipal water supplies and reservoirs, environmental flows and restoration, agricultural systems, and even coastal management. The original research presented in this dissertation is a step towards recognizing and incorporating climate and hydrological non-stationarities into management on the regional watershed scale, and demonstrates that it can be done both practically and informatively. By using inherent climate variability to our advantage in hydrological forecasts, we will increase our ability to effectively adapt to the unpredictable challenges of the future.

APPENDIX A  
WAVELET ANALYSIS OF LAKE OKEECHOBEE BASIN S-191 MONTHLY OBSERVED  
PRECIPITATION AND WAM SIMULATED STREAM FLOW, TOTAL P LOAD AND  
CONCENTRATION

**Introduction**

To provide continuity to the analyses performed on the data in Chapter 2 and the methods in Chapter 3, Appendix A discusses the results of univariate and multivariate wavelet analyses performed on the Watershed Assessment Model (WAM) simulated data in S-191 of the Lake Okeechobee watershed. The objective in analyzing the WAM simulated data in this way is to ascertain if the ENSO variability and predictability inherent in the hydrological variables discovered via contingency table analysis [Keener *et al.*, 2007]; Chapter 2) is also present in the frequency structure of the WAM simulated data. While hydrological simulation may be able to accurately re-create and predict magnitudes and general timing of stream flows and water quality, we are interested to see if data simulated by hydrology mechanisms and soil physics as currently understood are able to maintain certain climate based spectral signatures such as the 3-7 year periodicity of ENSO.

In Chapter 3, wavelet analysis was used to extract the 3-7 year ENSO periodicities as reflected in the NINO 3.4 sea surface temperature index from observed precipitation, stream flow, and nutrient parameters in the Little River Watershed in Georgia. Taken by themselves, the strongest ENSO signal in the LRW mirrored in the monthly hydrological variables was seen in stream flow, then subsequently in nitrate load, nitrate concentration, and finally, least of all in precipitation. In the multivariate cross-wavelet (XWT) and wavelet coherence (WTC) analyses, the most shared in-phase high power was seen between the NINO 3.4 index and stream flow, while the

highest covariance between series was between the NINO 3.4 and nitrate load. Physically, this is explained by the inherent noise in these variables time series. While we may have expected to see the most ENSO signal in the variable most directly related to the El Niño phenomenon, precipitation, it is also an extremely noisy series (Chapter 3, Figure 11a). While stream flow is an additional step away, mechanistically, it ultimately has a stronger ENSO signal in the frequency spectrum than that of precipitation, as it is a smoothed version of the noisier rainfall signal. As nutrient in-stream loads are mainly dependent on stream flow, and flow variability is largely based on precipitation in the LRW, it is not surprising that nutrient load has the next strongest ENSO power. Since nutrient concentration may be more dependent on agricultural activities than natural or climatic processes, the least visible spectral signal in the concentration variable is also unsurprising.

ENSO signal is generally regarded as being more strongly manifested in south Florida, where Lake Okeechobee is located, than in southern Georgia, where the LRW is found [*Ropelewski and Halpert, 1986, 1987; Schmidt et al., 2001*]. Therefore, if the spectral signature of the hydrologic variables is maintained in the simulated data, we could expect even more 3-7 year power representative of ENSO trends in the Lake Okeechobee data than in the LRW. From the wavelet results for the simulated data in S-191, however, it appears as if the relative spectral signatures of the simulated variables is not maintained as powerfully as they are in observed data in the LRW, where the ENSO signal is known to be weaker.

## Data and Methods

### Data: WAM, Basin S-191 and the NINO 3.4 Index

Site description and history of Lake Okeechobee, basin S-191 are discussed in Chapter 2, Data and Methods section The Lake Okeechobee Watershed. Data used from Lake Okeechobee is identical to that in Chapter 2, Data and Methods section Data: observed daily precipitation from 1967-2001 over 14 weather stations was summed into monthly cumulative averages and normalized by monthly average [Keener *et al.*, 2007]. Variables simulated by WAM from 1967-2001 include daily stream flow; total P concentration (mg/L) and total P load (kg). WAM calibration and validation procedures are also identical to those described in Chapter 2, Data and Methods section Watershed Assessment Model [Jacobson, 2002; Keener *et al.*, 2007; Soil and Water Engineering Technology, Inc., 2004]. The continuous measure of sea surface temperature (SST) used representing ENSO phase, the NINO 3.4 index, is identical to that discussed in Chapter 3, Data and Methods, section Little River Watershed Data, with the exception that the SST data used was extended back to 1967.

### Wavelet Analysis

Univariate wavelet analysis was performed on monthly observed precipitation data and simulated total P concentration, total P load, and stream flow. The methods are identical to those as indicated in Chapter 3, Data and Methods section Wavelet Analysis [Torrence and Compo, 1998]. Multivariate cross-wavelet (XWT) and wavelet coherence (WTC) analysis was performed on monthly NINO 3.4 SST and observed precipitation, simulated total P concentration, total P load, and stream flow. These methods are identical to those described in Chapter 3, Data and Methods section Cross Wavelet and Coherence Transforms [Grinsted *et al.*, 2004].

## **Cross-Correlation Analysis**

Cross-correlation analysis was performed on the monthly NINO 3.4 index and observed precipitation, simulated P load, P concentration, and stream flow. It was also performed between all hydrologic variables: precipitation, stream flow, P concentration, and P load. The methodology used is as described in Chapter 3, Data and Methods section Cross-Correlation Time Series Analysis.

## **Results**

### **Univariate Wavelet Analysis**

The monthly wavelet power spectra for the NINO 3.4 SST, observed precipitation, and simulated stream flow, and total P concentration and load time series are shown in Figure A-1. As discussed in Chapter 3, main power in the NINO 3.4 spectrum is concentrated within the 3-7 year period (Figure A-1a). Precipitation in the Lake Okeechobee region is seasonal, and previous wavelet analysis on Everglades annual rainfall [Kwon *et al.*, 2006] shows a figure of similar signal strength to that done with the S-191 basin's observed precipitation data (Figure A-1b). Precipitation shows a relatively high power within the 3-7 year period, centered around 1980-1985. This relative period of signal power is visible in precipitation from 1980-1985 in the LRW as well (Figure 3-2b), and may be indicative of the large 1982-1983 El Niño effects.

Now analyzing the WAM simulated data, we can see from the stream flow wavelet spectrum that while the signal strength has about the same magnitude and 3-7 year periodicity as that of the observed precipitation surrounding 1980-1985 (Figure A-1c), it does not share the strengthened ENSO spectral signature that was observed in the LRW. While the flow spectrum in the LRW demonstrated a stronger ENSO signal than precipitation in the LRW because of a less noisy, smoothing effect, this is not seen

in the simulated flow to the same extent. However, the flow 3-7 year periodicity is still powerful and statistically significant above the red noise background, indicating that the ENSO signal is very much present in the simulated data. This finding is not directly comparable to the LRW results, as the hydrologic system is most definitely different in each site.

Strangely enough, although the observed nitrate concentration (Figure 3-2d) had the least wavelet ENSO power of all hydrologic variables examined, the simulated total P concentration in basin S-191 (Figure A-1d) demonstrates both the highest 3-7 year ENSO signal power, and the most temporally prolonged in all the simulated Lake Okeechobee data. While in the LRW, it was reasoned that concentration had the least correlation with the NINO 3.4 index because of its dependence on anthropological activities such as agriculture, this is not the demonstrated case in the simulated S-191 concentration spectrum. This could be for several reasons: it may be impossible to compare the two field sites in any respect, or the anthropological fertilizer inputs may be timed differently in either the model simulation or in actuality, despite the fact that the LRW as a general rule has a much smaller problem with water quality, while basin S-191 is a nutrient hot-spot for providing phosphorus inputs to the Lake.

In basin S-191, the opposite relationship with nutrient load holds than in the Little River Watershed; while the strongest ENSO wavelet relationship was seen in nitrate load in the LRW, in S-191, total simulated P load (Figure A-1e) shows the weakest 3-7 year signal power, although it is still statistically significant against the background noise. In Chapter 2, we found that simulated load trends seemed to follow observed trends in precipitation in the Lake Okeechobee watershed. The lack of signal strength in

total P load here could again be related to the fact that the two field sites may be impossible to compare in terms of signal strength. However, it could also signify a weakening spectral signal that is inherent in the WAM simulations of hydrological data. Since the flow signal and the P concentration signal both appear to have greater spectral 3-7 year power than the P load, it is unlikely that this is the case. It must be noted, though, that the precipitation used in this analysis (Figure A-1b) is observed actual data, not simulation. Therefore, it is possible that the WAM simulations are simply maintaining the ENSO spectral signal in the flow and water quality data, rather than recognizing or generating them.

### **Cross-Wavelet and Wavelet-Coherence Analysis**

The cross-wavelet transform (XWT) identifies shared frequencies between two variables with high common power. Regions with shared high power, and thus, significance against a red noise background also indicate a consistent in or out of phase relationship. In the XWT between the NINO 3.4 SST index and observed S-191 precipitation (Figure A-2a), significant areas of shared in-phase high power are visible centered around the 3-7 year period from 1980-90, and slightly less power around the 2-3 year period from 1970-75. In fact, all the other XWT analyses performed between NINO 3.4 and simulated stream flow (Figure A-2b), P concentration (Figure A-2c), and P load (Figure A-2d) show basically the same strength, length, and periodicity of shared power with the same phase relationship. This basically identical relationship seems unlikely, and, while the univariate wavelet analyses implied that there were differences in the ENSO signal strength in the simulated S-191 hydrological variables, these multivariate analyses show that the variability is less than we were lead to believe.

What the XWT analyses demonstrate is that the shared time series significant modes of ENSO variability established between the NINO 3.4 index and observed precipitation is replicated almost exactly in the simulated hydrological data. In real, observed data, such similar areas of common power and significance are rarely seen. Of course, it is possible that this could be a real relationship, although, given the simulation circumstances, it seems more likely to assume that the variability inherent in the rainfall data was replicated in the stream flow and P concentration and load time series almost identically using empirical and deterministic relationships in WAM, and that some measure of ENSO related variability is missing from the simulated data.

The wavelet coherence transform (WTC) analyses, however, do not measure shared power, but time series co-variance. In Chapter 3, it was shown that more area was given significance in WTC than in XWT analysis, reflecting the likely causal mechanism between ENSO and precipitation, stream flow, and nutrient data in the Little River Watershed. In the S-191 WTC analysis, however, less area is significant than in the XWT figures (Figure A-3). It has been previously noted that the less area that is marked significant in a WTC analysis, the less likely that the shared power is causal in nature [*Grinsted et al.*, 2004]. In fact, while the WTC relationship between Lake Okeechobee observed precipitation and NINO 3.4 shows a weakly significant co-variance in 3-7 year ENSO periodicities (Figure A-3a), both simulated stream flow (Figure A-3b) and total P load (Figure A-3d) show similar and stronger co-variance relationships, while total P concentration (Figure A-3c), the strongest 3-7 year univariate wavelet signal, has almost no areas of co-variance with the NINO 3.4 SST record.

In Chapter 3, in the Little River Watershed, on the other hand, stronger 3-7 year ENSO bands of high power were reinforced even more strongly in wavelet coherence transform analyses. A relatively weak WTC coherence between SST and precipitation in the LRW gave way to very strong and sustained co-variance for flow and especially for nitrate load. The collective lack of significant high power areas in the WTC (Figure A-3) imply that while univariate ENSO power and some shared multivariate power may be present in simulated hydrologic variables in the Lake Okeechobee basin S-191, there is a lack of co-variance between the NINO 3.4 SST index and the simulated hydrological data that may be representative of a deficiency in replicating climate variability in the multi-decadal timescale.

### **Cross Correlation Analysis**

Time-series cross-correlation analysis was performed between monthly hydrological data and with NINO 3.4 SST to investigate the maximum lag relationships throughout the simulation. Although significant monthly lag correlations were identified between SST and all hydrological variables, they were only very weakly above the confidence bounds. The NINO 3.4 SST and observed precipitation had a significant but small maximum correlation of 0.156 at zero months lag (Figure A-4a). Sea surface temperatures lead stream flows by 2 months, with a maximum correlation of 0.125 (Figure A-4b). Total P concentration lead SST by 1 month, with a maximum correlation of 0.179 (Figure A-4c), while SST lead P load by one month, with a maximum correlation of 0.110 (Figure A-4d). While these cross-correlations are relatively small, the results again show the greatest connection of SST with P concentration, as was seen in the univariate wavelet analysis (Figure A-1d). However, the confusing maximum lag times that alternate between SST leading or following a hydrologic variable tend to

make me skeptical of these results, as a causal relationship of nutrients leading sea surface temperatures does not make sense.

Finally, cross-correlation analyses were performed between the hydrologic variables themselves, separate from the influence of SST, of precipitation and stream flow (Figure A-4e), stream flow and P load (Figure A-4f), and P load and P concentration (not shown). All relationships had a maximum correlation at zero months lag, indicating that a smaller time step would be needed to identify precise hydrologic relationships. The strongest correlation was between flow and P load (0.977), followed by P concentration and load (0.805), and finally precipitation and flow (0.704). The high correlations between precipitation, flow, and load are to be expected, based on the mechanistic hydrology simulations done by WAM, which uses precipitation as its driving input.

### **Summary and Discussion**

It is difficult to make sensible connections between the Lake Okeechobee and Little River Watershed field sites, not only because of the difficult in comparing simulated and observed data from two different places, but also because of the differences in the field sites themselves, despite their presence in the Coastal Plain. In and of itself, however, univariate wavelet analysis of basin S-191 shows that probably due to the input of the driving force of the model, observed precipitation, the 3-7 year ENSO modes of wavelet variability are conserved in simulated stream flow, P concentration, and P load. It is a credit to WAM's validity that it can maintain the spectral signature of low-frequency ENSO precipitation variability in its simulated stream flow and water quality data.

Given that the ENSO signal in south Florida is known to be stronger than it is in Georgia and in the Little River Watershed, it is probably not wise to put too much faith in the univariate or multivariate wavelet analyses performed on the simulated data, as they show a stronger signal in the LRW than in the Lake Okeechobee region. Specifically for our cases, the nutrient load in basin S-191 is shown to have a relatively weak correlation to the NINO 3.4 index as compared to the other simulated hydrologic variables and to the LRW analyses done in Chapter 3. This may be because the field site is simply different, or it may be because of the increased mechanistic distance of load from observed precipitation as compared to stream flow, which is highly mechanistically correlated, or concentration, which is less related to natural climate and more dependent on agricultural activities.

It is questionable whether or not a simulated precipitation time series produced by re-sampling or a weather generator would retain ENSO's spectral signature throughout water quality WAM simulations. Forcing WAM with different generated precipitation inputs in order to test which one maintained spectral ENSO signals would in fact be an interesting experiment that could be of some use to climatologists and modelers in places that are affected significantly by phenomena such as ENSO or different climatological indices.

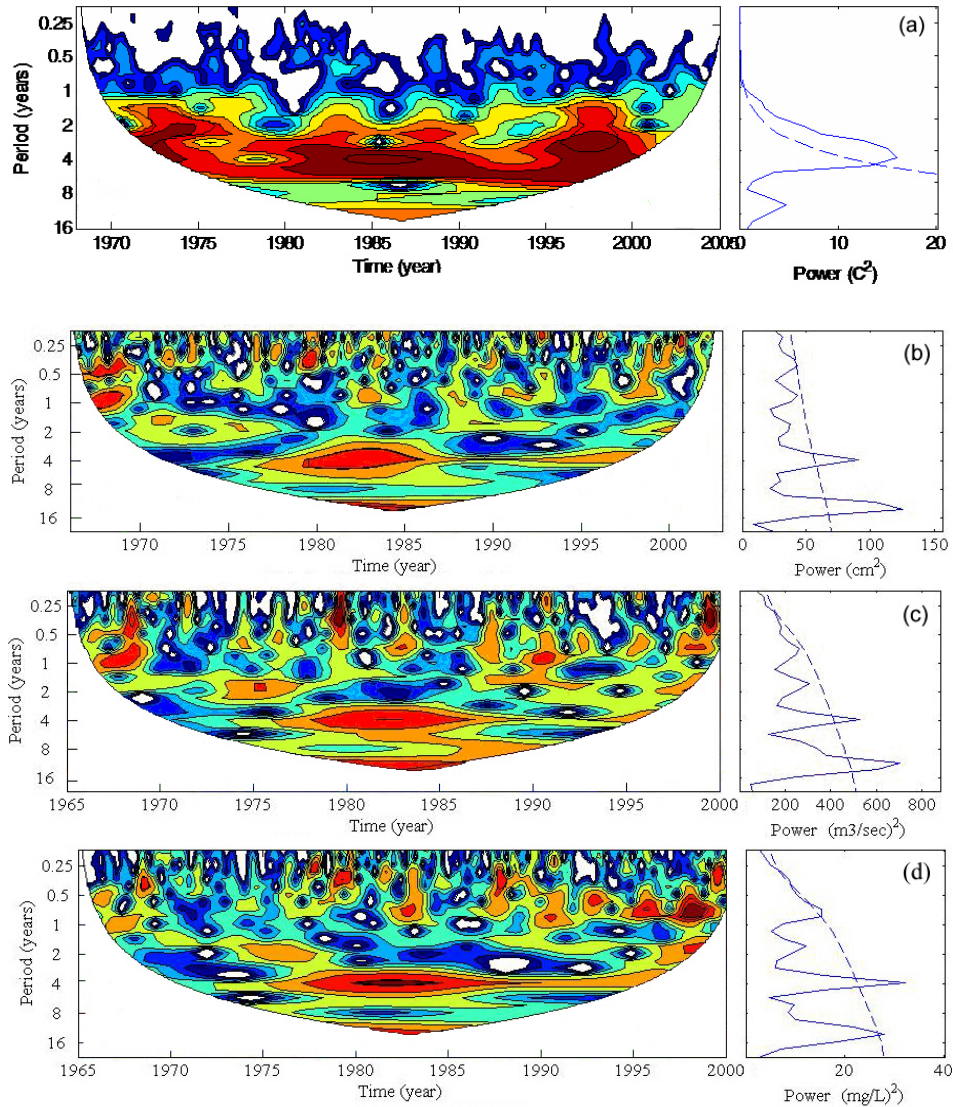


Figure A-1. Significant wavelet power spectra are shown within the cone-of-influence, which depends on time series length and degrees of freedom. Figures are color-mapped to indicate high wavelet power with reds and oranges, and low powers in blue and white. The Global Wavelet Spectrum (GWS) at the right of each figure shows power integrated over all scales and time. The 95% confidence limit is shown on the GWS (dashed blue line), the periodicities above which show significance. Monthly (a) NINO 3.4 ( $^{\circ}\text{C}$ ) SST, (b) precipitation anomaly (cm), (c) stream flow anomaly ( $\text{m}^3$ ), (d) total P concentration anomaly ( $\text{mg/L}$ ), and (3) total P load anomaly (kg).

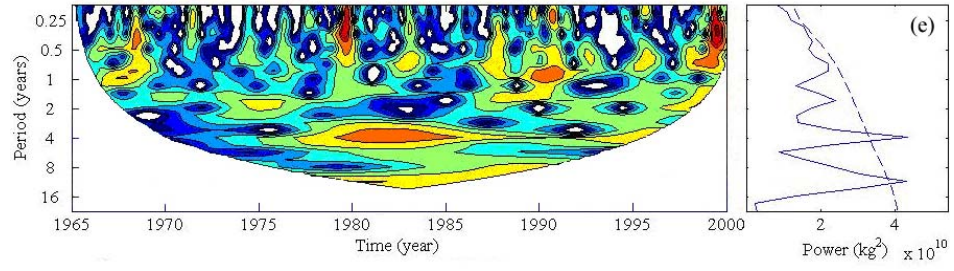


Figure A-1. Continued.

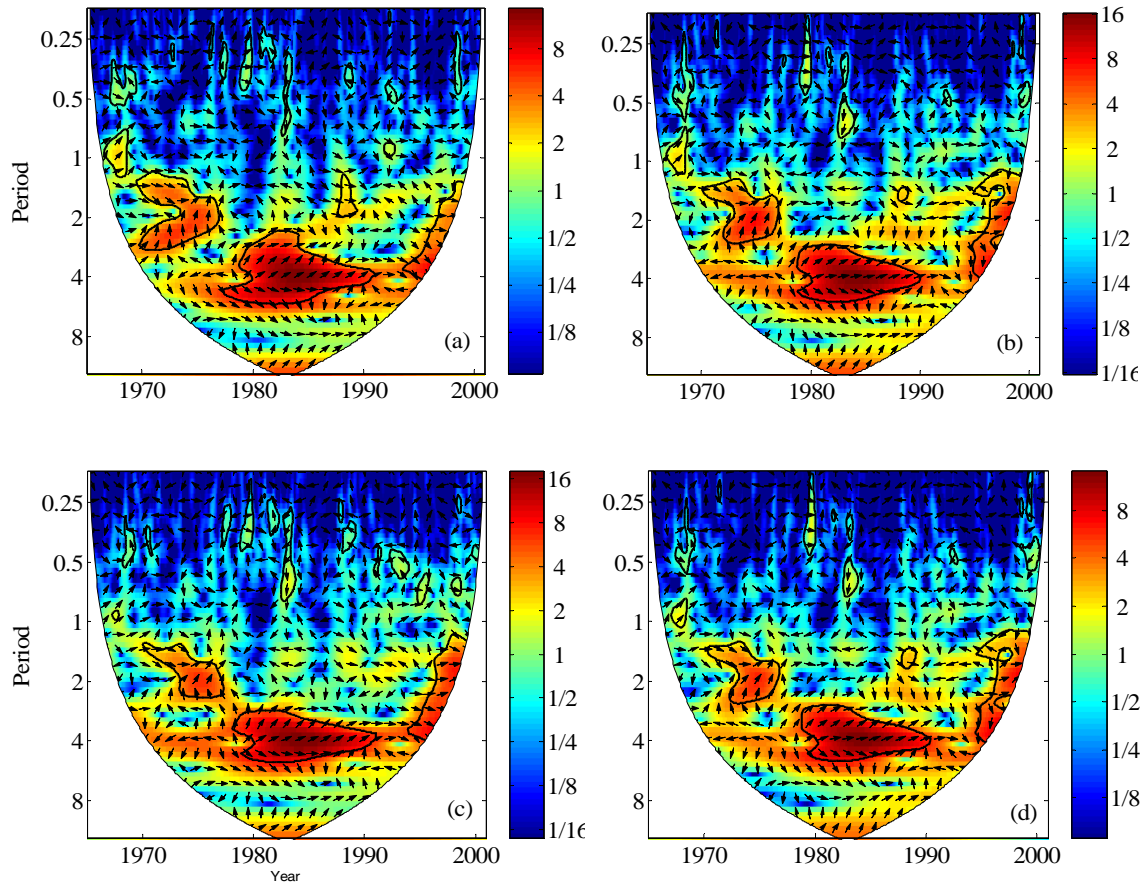


Figure A-2. Cross Wavelet Spectrum between (a) monthly SST and Precipitation (cm), (b) monthly SST and stream flow ( $\text{m}^3/\text{sec}$ ), (c) monthly SST and total P concentration (mg/L), (d) monthly SST and total P Load (kg). Black figure outlines indicate areas significant to 95% confidence, while arrows represent variables' phase relationship.

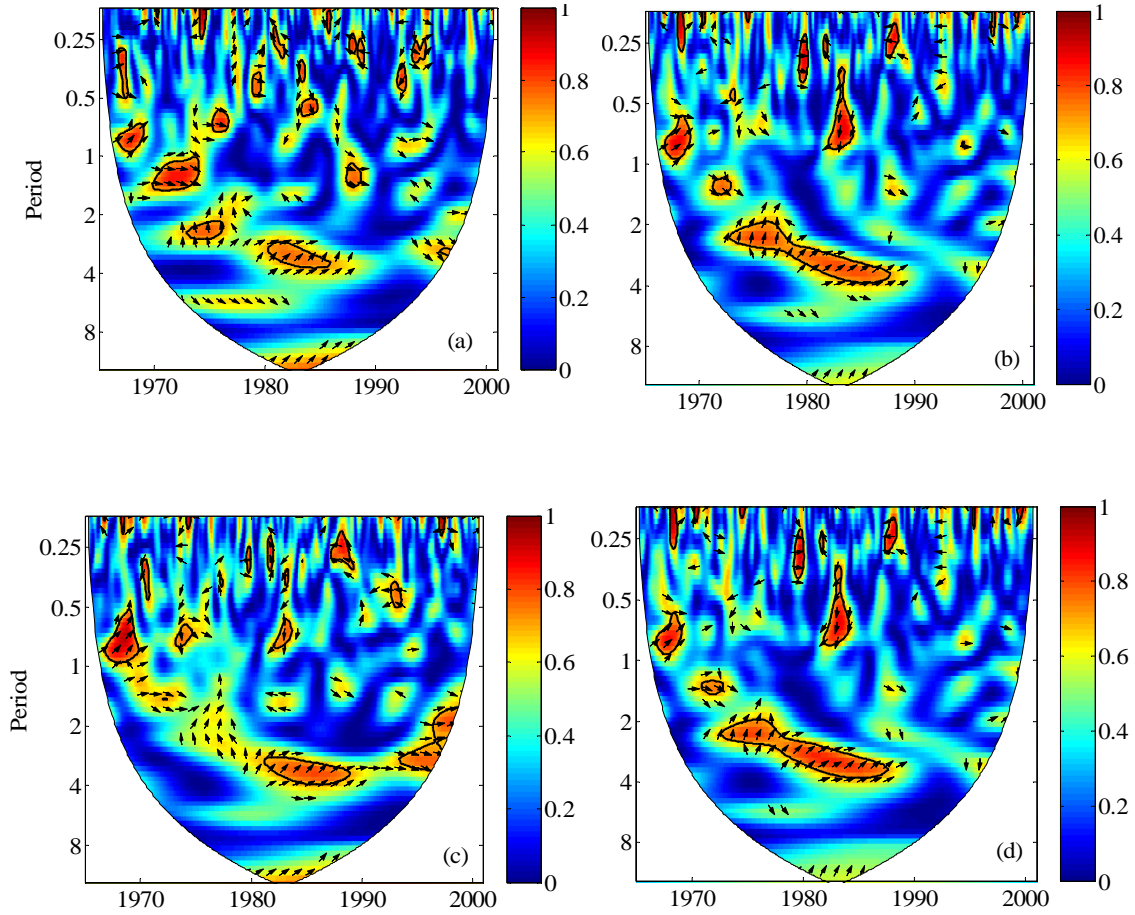


Figure A-3. Wavelet Coherence Analysis between (a) monthly SST and Precipitation (cm), (b) monthly SST and stream flow ( $\text{m}^3/\text{sec}$ ), (c) monthly SST and total P concentration (mg/L), (d) monthly SST and total P load (kg). Black figure outlines indicate areas significant to 95% confidence, while arrows represent variables' phase relationship.

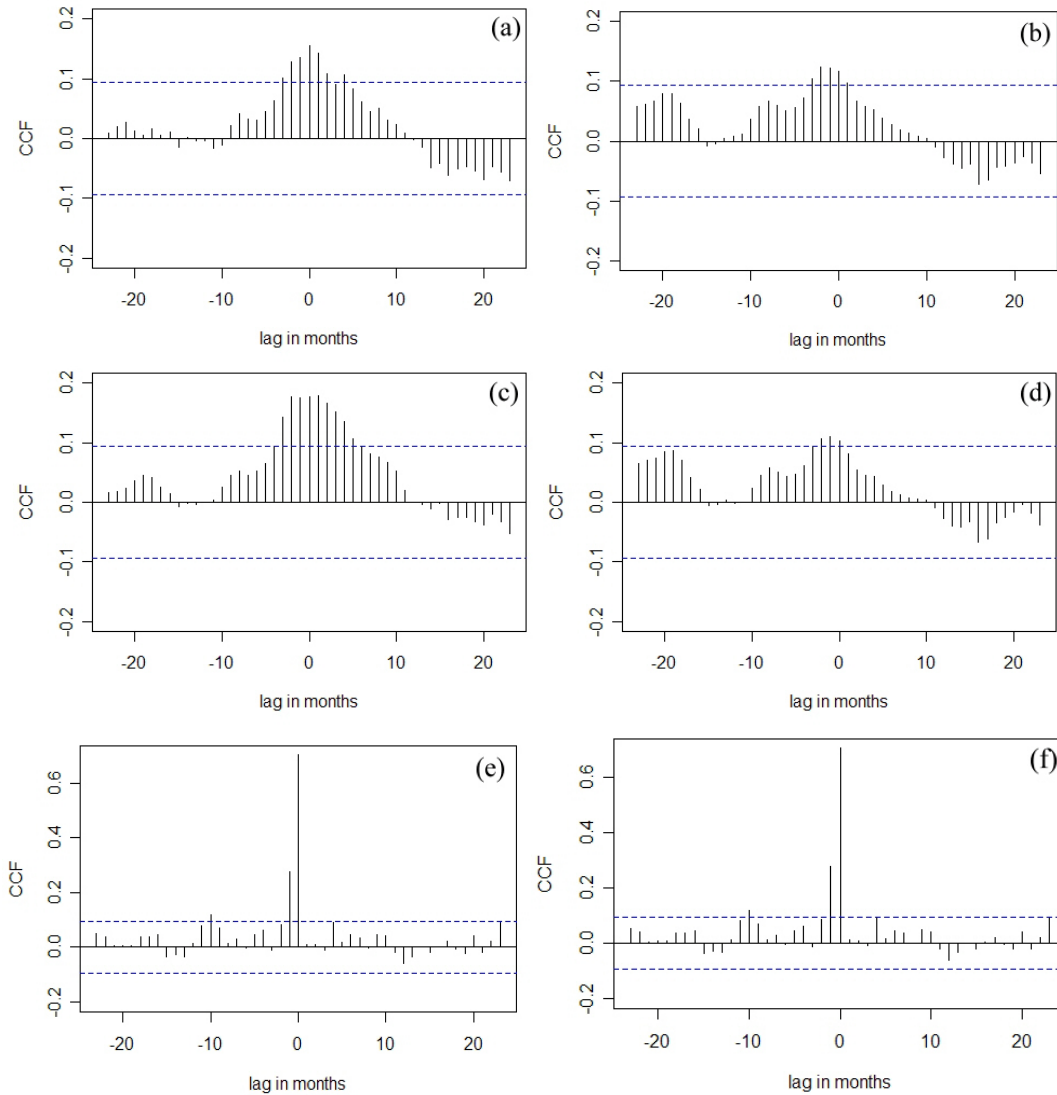


Figure A-4. Cross-correlation analysis between NINO 3.4 ( $^{\circ}\text{C}$ ) and Basin S-191 (a) precipitation (cm) (b) stream flow ( $\text{m}^3$ ) (c) total P (mg/L), (d) total P (kg), and between (e) precipitation (cm) and stream flow ( $\text{m}^3$ ), (f) stream flow and P load. A negative lag indicates months that the NINO 3.4 SST leads the variable in question. The strongest Cross-Correlation Function (CCF) relationship within the NINO 3.4 index is between SST and total P concentration at zero months (no lag), although it is still very weak, while the strongest hydrologic relationship overall is between stream flow and total P load at zero months. Values above or below dashed lines indicate significant correlation above 95% confidence.

## LIST OF REFERENCES

- Aceituno, P. (1988), On the functioning of the Southern Oscillation in the South American sector. Part I: Surface climate, *Mon. Weather Rev.*, 116(3), 505-524.
- AchutaRao, K., and K. Sperber (2002), Simulation of the El Niño Southern Oscillation: Results from the coupled model inter-comparison project, *Clim. Dyn.*, 19(3), 191-209.
- Asefa, T., and A. Adams (2007), Short-term urban water demand forecast models in action: Challenges from model development to implementation to real-time operations, pp. 1-7, Orlando, FL.
- Askar, A., A. E. Cetin, and H. Rabitz (1996), Wavelet transform for analysis of molecular dynamics, *J. Phys. Chem.*, 100(49), 19165-19173.
- Asmussen, L. (1971), Hydrologic effects of Quaternary sediments above the marine terraces in the Georgia coastal plain, *Southeast. Geol.*, 12, 189-201.
- Baigorria, G. A., J. W. Jones, and J. J. O'Brien (2007), Understanding rainfall spatial variability in southeast USA at different timescales, *Int. J. Climatol.*, 27(6), 749-760.
- Baigorria, G. A., J. W. Hansen, N. Ward, J. W. Jones, and J. J. O'Brien (2008), Assessing predictability of cotton yields in the southeastern United States based on regional atmospheric circulation and surface temperatures, *J. App. Meteorol.*, 47(1), 76-91.
- Baldwin, M. P. et al. (2001), The quasi-biennial oscillation, *Rev. Geophys.*, 39(2), 179-229.
- Bates, B. C., Z. W. Kundzewicz, S. Wu, and J. P. Palutikof (2008), *Climate Change and Water. Technical Paper of the Intergovernmental Panel on Climate Change*, IPCC Secretariat, Geneva.
- Baudrillard, J. (1985), *Simulacra and Simulation (The Body, In Theory: Histories of Cultural Materialism)*, University of Michigan Press, Ann Arbor, MI.
- Bingner, R. L., and F. D. Theurer (2007), *AnnAGNPS Technical Processes Documentation, Version 4.0*, U.S. Dept. Agriculture, NRCS, Washington, D.C., USA.
- Bjerknes, J. (1969), Atmospheric teleconnections from the equatorial Pacific, *Mon. Weather Rev.*, 97(3), 163-172.
- Bollerslev, T. (1986), Generalized autoregressive conditional heteroscedasticity, *J. Econometrics*, 31, 307-327.

- Bonham, S. G., A. M. Haywood, D. J. Lunt, M. Collins, and U. Salzmann (2009), El Niño-Southern Oscillation, Pliocene climate and equifinality, *Philos. Transact. A Math. Phys. Eng. Sci.*, 367(1886), 127-156.
- Bosch, D. D., R. Lowrance, J. M. Sheridan, and R. G. Williams (2003), Ground water storage effect on streamflow for a southeastern coastal plain watershed, *Ground Water*, 41(7), 903–912.
- Bosch, D. D., and J. M. Sheridan (2007), Stream Discharge Database: Little River Experimental Watershed, Georgia, United States, *Water Res.*, 43, W09473.
- Bosch, D. D., J. M. Sheridan, H. L. Batten, and J. G. Arnold (2004), Evaluation of the SWAT model on a Coastal Plain agricultural watershed, *Trans. ASABE*, 47(5), 1493-1506.
- Bosch, D. D., J. M. Sheridan, and F. M. Davis (1999), Rainfall characteristics and spatial correlation for the Georgia Coastal Plain, *Trans. ASAE*, 42(6), 1637-1644.
- Bosch, D. D., J. M. Sheridan, R. Lowrance, R. K. Hubbard, T. C. Strickland, G. W. Feyereisen, and D. G. Sullivan (2007), Little River Experimental Watershed database, *WRR*, 43, W09470.
- Bosch, D. D., J. M. Sheridan, and L. K. Marshall (2007), Precipitation, soil moisture, and climate database, Little River Experimental Watershed, Georgia, United States, *Water Resour. Res.*, 43, W09472.
- Bosch, D. D., D. G. Sullivan, and J. M. Sheridan (2006), Hydrologic impacts of land-use changes in Coastal Plain watersheds, *Trans. ASABE*, 49(2), 423-432.
- Bottcher, A. B., N. B. Pickering, and A. B. Cooper (1998), EAAMOD-FIELD: A flow and phosphorus model for high water tables, in *Proceedings of the 7th Annual Drainage Symposium*, pp. 599-606, ASAE, St. Joseph, MI.
- Burkett, V., R. Ritschard, S. McNulty, J. J. O'Brien, R. Abt, J. W. Jones, U. Hatch, B. Murray, S. S. Jagtap, and J. Cruise (2001), *Potential Consequences of Climate Variability and Change for the Southeastern United States in National Assessment Synthesis Team for the US Global Change Research Program*, Cambridge University Press, Cambridge, UK.
- Cai, X., and M. W. Rosegrant (2002), Global water demand and supply projections, Part 1: a modeling approach, *Water Int.*, 27(2), 159-169.
- Calhoun, J. (1983), *Soil Survey of Tift County*, USDA-SCS, Washington, D.C.
- Campbell, K., J. Capece, and T. Tremwel (1995), Surface/ subsurface hydrology and phosphorus transport in the Kissimmee River Basin, Florida, *Ecol. Eng.*, 5(2-3), 301-330.

- Cane, M. A. (1986), El Niño, *Annu. Rev. Earth Planet Sci.*, 14(1), 43-70.
- Cane, M. A. (2005), The evolution of El Niño, past and future, *Earth Planet Sci. Lett.*, 230(3-4), 227-240.
- Cane, M. A., R. J. Patton, S. E. Zebiak, and S. C. Dolan (1986), Experimental forecasts of El Niño, *Nature*, 321(6073), 827–832.
- Carpenter, S. R., N. F. Caraco, D. L. Correll, R. W. Howarth, A. N. Sharpley, and V. H. Smith (1998), Non-point pollution of surface waters with phosphorus and nitrogen, *Ecol. Appl.*, 8(3), 559-568.
- Cayan, D., K. T. Redmond, and L. G. Riddle (1999), ENSO and hydrologic extremes in the western United States, *J. Clim.*, 12(9), 2881–2893.
- Chan, T. F., and J. Shen (2005), *Image Processing and Analysis: variational, PDE, wavelet, and stochastic methods*, Society for Industrial Mathematics.
- Charles, C. D., D. E. Hunter, and R. G. Fairbanks (1997), Interaction between the ENSO and the Asian monsoon in a coral record of tropical climate, *Science*, 277(5328), 925.
- Chavez, F. P., P. G. Strutton, G. E. Friederich, R. A. Feely, G. C. Feldman, D. G. Foley, and M. J. McPhaden (1999), Biological and chemical response of the equatorial Pacific Ocean to the 1997-98 El Niño, *Science*, 286(5447), 2126.
- Chiew, F. H. S., and T. A. McMahon (2003), El Niño/Southern Oscillation and Australian rainfall and streamflow, *Aust. J. Wat. Resour.*, 6(2), 115–129.
- Chiew, F. H. S., T. C. Piechota, J. A. Dracup, and T. A. McMahon (1998), El Niño/Southern Oscillation and Australian rainfall, streamflow, and drought: Links and potential for forecasting, *J. Hydrol.*, 204, 138-149.
- Cho, J., Bosch, D.D., Vellidis, G., Lowrance, R.K., and Strickland, T.C. (2009), Calibrating and validating SWAT for conservation practice assessment at the watershed scale, *Trans. ASABE*, in press.
- Cho, J., Bosch, D.D., Vellidis, G., Lowrance, R.K., and Strickland, T.C. (2010), Evaluation of hydrologic and water quality impacts of crop management in the Little River watershed using SWAT, *J. Am. Water Resour. Assoc.*, accepted.
- Collins, M. (2005), El Niño-or La Niña-like climate change?, *Clim. Dyn.*, 24(1), 89-104.
- Dahl, T. E. (1990), *Wetlands losses in the United States, 1780's to 1980's. Report to the Congress*, National Wetlands Inventory, St. Petersburg, FL (USA).
- d'Arrigo, R., R. Villalba, and G. Wiles (2001), Tree-ring estimates of Pacific decadal climate variability, *Clim. Dyn.*, 18(3), 219–224.

- Daubechies, I. (1990), The wavelet transform, time-frequency localization and signal analysis, *IEEE Trans. Inf. Theory*, 36(5), 961-1005.
- Dean, J., and W. Snyder (1977), Temporally and aerially distributed rainfall, *J. Irrig. Drain. Div. Am. Soc. Civ. Eng.*, (103), 221– 229.
- Dessai, S., M. Hulme, R. Lempert, and R. A. Pielke Jr. (2009), Climate prediction: a limit to adaptation? in *Living with climate change: are there limits to adaptation?*, edited by W. Adger, I. Lorenzoni, and K. O'Brien, Cambridge University Press.
- Dettinger, M., and H. F. Diaz (2000), Global characteristics of stream flow seasonality and variability, *J. Hydrometeorol.*, 1(4), 289-310.
- DHI (2004), *MIKE-SHE, An Integrated Hydrological Modeling System*, Technical Manual, Danish Hydraulic Institute, Hørsholm, Denmark.
- van den Dool, H., and A. Barnston (1995), Forecasts of global sea surface temperature out to a year using the constructed analogue method, in *Proceedings of the 19th Annual Climate Diagnostics Workshop*, pp. 416-419, College Park, Maryland.
- van den Dool, H., J. Huang, and Y. Fan (2003), Performance and analysis of the constructed analogue method applied to US soil moisture over 1981–2001, *J. Geophys. Res.*, 108, 8617.
- Baigorria, G. A., J. W. Hansen, N. Ward, J. W. Jones, and J. J. O'Brien (2008), Assessing predictability of cotton yields in the southeastern United States based on regional atmospheric circulation and surface temperatures, *Journal of Applied Meteorology*, 47(1), 76–91.
- Duda, P., J. Kittke Jr., A. Donigan Jr., and R. Kinerson (2006), *Better Assessment Science Integrating Point and Nonpoint Sources (BASINS)*, Watershed Models, edited by V. Singh and D. Frevert, C.R.C. Press, Taylor & Francis Group, Boca Raton, FL.
- Enfield, D. B., A. M. Mestas-Nunez, and P. J. Trimble (2001), The Atlantic Multi-decadal Oscillation and its relationship to rainfall and river flows in the Continental US, *Geophys. Res. Lett.*, 28, 2077–2080.
- Farge, M. (1992), Wavelet transforms and their applications to turbulence, *Annu. Rev. Fluid Mech.*, 24(1), 395–458.
- Federico, A. C., F. E. Davis, and J. Milleson (1981), Nutrient retention in an unmodified flow-through marsh, *Proceedings of a Symposium on Progress in Wetlands Utilization and Management*, Orlando, FL., p. 432.
- Fedorov, A. V., and S. G. Philander (2001), A stability analysis of tropical ocean–atmosphere interactions: Bridging measurements and theory for El Niño, *J. Clim.*, 14(14), 3086-3101.

- Feyereisen, G. W., R. Lowrance, T. C. Strickland, D. D. Bosch, and J. M. Sheridan (2008), Long-term stream chemistry trends in the southern Georgia Little River Experimental Watershed, *J. Soil Water Conserv.*, 63(6), 475-486.
- Feyereisen, G. W., R. Lowrance, T. C. Strickland, J. M. Sheridan, R. K. Hubbard, and D. D. Bosch (2007), Long-term water chemistry database, Little River Experimental Watershed, southeast Coastal Plain, United States, *Water Resour. Res.*, 43, W09474.
- Feyereisen, G. W., T. C. Strickland, D. D. Bosch, and D. G. Sullivan (2007), Evaluation of SWAT manual calibration and input parameter sensitivity in the Little River Watershed, *Trans. ASABE*, 50(3), 843-855.
- Fisher, R. A. (1935), The logic of inductive inference (with discussion), *J. Royal Stat. Soc.*, 98(1), 39-82.
- Flaig, E. G., and K. R. Reddy (1995), Fate of phosphorus in the Lake Okeechobee watershed, Florida, USA: overview and recommendations, *Ecol. Eng.*, 5(2-3), 127-142.
- Florida DEP (2005), *Florida's Total Maximum Daily Load Program: the First 5 Years. A Report to the Legislature and Governor*, Division of Water Resource Management. Mimi Drew, Director.
- Florida DEP (2001), *Total Maximum Daily Load for Total Phosphorus Lake Okeechobee, Florida*, U.S. EPA, Tallahassee, FL, USA.
- Fox, D. D., S. Gornak, T. D. McCall, D. W. Brown, and C. J. Morris (1993), *Lake Okeechobee fisheries investigations completion report*, Florida Game and Fresh Water Fish Commission, Tallahassee, FL, USA.
- Fraedrich, K., and K. Muller (1992), Climate anomalies in Europe associated with ENSO extremes, *Int. J. Climatol.*, 12(1).
- Fraisse, C. W., and K. Campbell (1997), *FHANTM Version 2.0 User's Manual, Report to South Florida Water Management District*, West Palm Beach, FL.
- Gakstatter, J. H., A. F. Bartsch, and C. A. Callahan (1978), The impact of broadly applied effluent phosphorus standards on eutrophication control, *Water Resour. Res.*, 14, 1155-1158.
- Gérard-Marchant, P. G. F., D. E. Stooksbury, and D. Zierden (2008), Alternative characterization of ENSO episodes and applications to precipitation patterns in the Southeastern US, *submitted to J. Service Climatol.*
- Gioia, G., and F. A. Bombardelli (2002), Scaling and similarity in rough channel flows, *Phys. Rev. Lett.*, 88(1), 6465.

- Goddard, L., S. J. Mason, S. K. Zebiak, C. F. Ropelewski, R. Basher, and M. A. Cane (2001), Current approaches to seasonal-to-interannual climate predictions, *Int. J. Climatol.*, *21*, 1111–1152.
- Graham, A. (1989), Late tertiary paleoaltitudes and vegetational zonation in Mexico and Central America, *Botanica Neerlandica*, *38*, 417-424.
- Grinsted, A., J. C. Moore, and S. Jevrejeva (2004), Application of the cross wavelet transform and wavelet coherence to geophysical time series, *Geophysics*, *11*, 561-566.
- Gu, D., and S. G. H. Philander (1995), Secular changes of annual and interannual variability in the tropics during the last century, *J. Clim.*, *8*, 864.
- Gutierrez, F., and J. A. Dracup (2001), An analysis of the feasibility of long range streamflow forecasting for Colombia using El-Niño/Southern Oscillation indicators, *J. Hydrol.*, *246*, 181-196.
- Haan, C. (2002), *Statistical methods in hydrology*, 2nd ed., Ames: The Iowa State University.
- Halpert, M. S., and C. F. Ropelewski (1992), Surface temperature patterns associated with the Southern Oscillation, *J. Clim.*, *5*(6), 577-593.
- Handler, P. (1990), USA corn yields, the El Niño and agricultural drought: 1867-1988, *Int. J. Clim.*, *10*, 819-28.
- Hansen, J. W., A. Irmak, and J. W. Jones (1997), El Niño-Southern Oscillation influences on Florida crop yields, *Soil Crop Sci. Soc. Florida*, *57*, 12-16.
- Hansen, J. W., J. W. Jones, C. F. Kiker, and A. W. Hodges (1999), El Niño–Southern Oscillation Impacts on Winter Vegetable Production in Florida, *J. Clim.*, *12*(1), 92-102.
- Hanson, K., and G. A. Maul (1991), Florida precipitation and the Pacific El Niño, 1895–1989, *Fla. Sci.*, *54*(3/4), 160–168.
- Harmel, R. D., R. J. Cooper, R. M. Slade, R. L. Haney, and J. G. Arnold (2006), Cumulative uncertainty in measured streamflow and water quality data for small watersheds, *Trans. ASABE*, *49*(3), 689-701.
- Havens, K. E., and D. E. Gawlik (2005), Lake Okeechobee conceptual ecological model, *Wetlands*, *25*(4), 908-925.
- Haywood, A. M., and P. J. Valdes (2004), Modeling Pliocene warmth: contribution of atmosphere, oceans and cryosphere, *Earth Planet. Sci. Lett.*, *218*(3-4), 363-377.

- Hefner, J. M., B.O. Wilen, T. E. Dahl, and W. E. Frayer (1994), *Southeast wetlands; status and trends, mid-1970's to mid-1980's.*, U.S. Dept. Int., Fish and Wildl. Serv., Atlanta, Georgia.
- Hoskins, B. J., and D. J. Karoly (1981), The steady linear response of a spherical atmosphere to thermal and orographic forcing, *J. Atmos. Sci.*, 38(6), 1179-1196.
- Huang, Y., B. Shuman, Y. Wang, T. Webb, E. C. Grimm, and G. Jacobson (2006), Climatic and environmental controls on the variation of C3 and C4 plant abundances in central Florida for the past 62,000 years, *Palaeogeogr. Palaeoclimatol. Palaeoecol.*, 237(2-4), 428-435.
- Huber, M., and R. Caballero (2003), Eocene El Niño: Evidence for robust tropical dynamics in the hothouse, *Science*, 299(5608), 877-881.
- Ice, G. (2004), History of innovative best management practice development and its role in addressing water quality limited water bodies, *J. Environ. Eng.*, 130, 684.
- IPCC (2007), *Climate Change. 2007. Synthesis Report. A Contribution of Working Groups I, II, and III to the Fourth Assessment Report of the Intergovernmental Panel on Climate Change*, IPCC, Geneva, Switzerland.
- IPCC, M. L. Parry, O. F. Canziani, J. P. Palutikof, P. J. van der Linden, and C. E. Hanson (2007), *Climate Change 2007: Impacts, Adaptation and Vulnerability. Contribution of Working Group II to the Fourth Assessment Report of the Intergovernmental Panel on Climate Change*, Cambridge University Press, Cambridge, UK.
- Jacobson, B. (2002), *Hydrologic/water quality characterization of the watershed: Results of Phase 2 analytical approach. Central and Southern Florida project comprehensive Everglades restoration plan (CERP)*, SWET, Inc., Gainesville, Florida.
- Jacobson, B., and A. B. Bottcher (1998), Unique routing algorithm for watershed assessment modeling, *ASAE Conference Paper, Paper #982237*.
- Jagtap, S. S., J. W. Jones, P. Hildebrand, D. Letson, J. J. O'Brien, G. Podesta, D. Zierden, and F. Zazueta (2002), Responding to stakeholder's demands for climate information: from research to applications in Florida, *Agric. Syst.*, 74(3), 415-430.
- Japan Meteorological Agency (1991), *Climate Charts of Sea Surface Temperatures of the Western North Pacific and the Global Ocean*, Marine Department.
- Kaiser, G. (1994), *A Friendly Guide to Wavelets*, Birkhäuser Boston, Cambridge, MA.
- Kaplan, A., M. A. Cane, Y. Kushnir, A. C. Clement, M. B. Blumenthal, and B. Rajagopalan (1998), Analyses of global sea surface temperature 1856-1991, *J. Geophys. Res.*, 103(18), 567-18.

- Keener, V. W., G. W. Feyereisen, U. Lall, J. W. Jones, D. D. Bosch, and R. Lowrance (2010), El Niño/Southern Oscillation (ENSO) influences on monthly NO<sub>3</sub> load and concentration, stream flow, and precipitation in the Little River Watershed, Tifton, Georgia., *J. Hydrol.*, 381(3-4), 352-363.
- Keener, V. W., K. T. Ingram, B. Jacobson, and J. W. Jones (2007), Effects of El-Niño/Southern Oscillation on simulated phosphorus loading, *Trans. ASABE*, 50(6), 2081-89.
- Kiladis, G. N., and H. F. Diaz (1989), Global climate anomalies associated with extremes in the Southern Oscillation, *J. Clim.*, 2, 1069-1090.
- Knisel, W. G., P. Yates, J. M. Sheridan, T. K. Woody III, J. Allen, and L. E. Asmussen (1985), *Hydrology and hydro-geology of Upper Taylor Creek watershed, Okeechobee County, Florida: data and analysis.*, USDA- Agricultural Research Service, Washington, D.C.
- Koutavas, A., P. B. Demenocal, G. C. Olive, and J. Lynch-Stieglitz (2006), Mid-Holocene El Niño-Southern Oscillation (ENSO) attenuation revealed by individual foraminifera in eastern tropical Pacific sediments, *Geology*, 34(12), 993-996.
- Kulkarni, J. R. (2000), Wavelet analysis of the association between the southern oscillation and the Indian summer monsoon, *Int. J. Climatol.*, 20(1).
- Kwon, H. H., U. Lall, and A. Khalil (2007), Stochastic simulation model for nonstationary time series using an autoregressive wavelet decomposition: Applications to rainfall and temperature, *Water Resour. Res.*, 43.
- Kwon, H. H., U. Lall, Y. Moon, A. F. Khalil, and H. Ahn (2006), Episodic interannual climate oscillations and their influence on seasonal rainfall in the everglades national park, *Water Resour. Res.*, 42.
- Labat, D. (2008), Wavelet analysis of the annual discharge records of the world's largest rivers, *Adv. Water Resour.*, 31, 109–117.
- Latif, M., D. Anderson, T. Barnett, M. A. Cane, R. Kleeman, A. Leetmaa, J. O'Brien, A. Rosati, and E. Schneider (1998), A review of the predictability and prediction of ENSO, *J. Geophys. Res.*, 103(14), 375–14.
- Lau, K. M., and P. J. Sheu (1991), Teleconnections in global rainfall anomalies: seasonal to inter-decadal time scales, in *Teleconnections Linking Worldwide Climate Anomalies: Scientific Basis and Societal Impact*, pp. 227–256, Cambridge University Press.
- Leonard, R. A., W. G. Knisel, and D. A. Still (1987), GLEAMS: Groundwater Loading Effects of Agricultural Management Systems, *Trans. ASABE*, 30, 1403-1418.

- Li, X., R. B. Ambrose, and R. Araujo (2004), Modeling mineral nitrogen export from a forest terrestrial ecosystem to streams, *Trans. ASABE*, 47(3), 727-739.
- Lins, H. F., and J. R. Slack (1999), Streamflow trends in the United States, *Geophys. Res. Lett.*, 26(2).
- Livezey, R., and T. Smith (1999), Covariability of aspects of North American climate with global sea surface temperatures on interannual to interdecadal timescales, *J. Clim.*, (12), 289-302.
- Lowrance, R. (1992), Groundwater Nitrate and denitrification in a coastal plain riparian forest, *J. Environ. Qual.*, 21, 401-405.
- Lowrance, R., and R. A. Leonard (1988), Streamflow nutrient dynamics on coastal plain watersheds, *J. Environ. Qual.*, 17(4), 734.
- Lowrance, R., R. A. Leonard, and L. E. Asmussen (1985), Nutrient budgets for agricultural watersheds in the southeastern coastal plain, *Ecology*, 66(1), 287-296.
- Lowrance, R., and J. M. Sheridan (2005), Surface runoff water quality in a managed three zone riparian buffer, *J. Environ. Qual.*, 34(5), 1851.
- Lowrance, R., Sheridan, J.M., Yates, P., and L. E. Asmussen (1983), *Hydrology and Sediment Movement from southeastern Coastal Plain Watersheds*, Nutrient Cycling in Agricultural Ecosystems, Special Publication, University of Georgia, SEWRL.
- Lowrance, R., R. L. Todd, and L. E. Asmussen (1984), Nutrient cycling in an agricultural watershed: Streamflow and artificial drainage, *J. Environ. Qual.*, 13, 27-32.
- Malik, A. S., B. A. Larson, and M. Ribaudo (1994), Economic incentives for agricultural nonpoint source pollution control, *J. Am. Water Resour. Assoc.*, 30(3), 471-480.
- Mason, S. J., and L. Goddard (2001), Probabilistic precipitation anomalies associated with ENSO, *Bull. Am. Met. Soc.*, 82(4), 619-638.
- Maurer, E. P., S. Gibbard, and P. B. Duffy (2006), Amplification of streamflow impacts of El Niño by increased atmospheric greenhouse gases, *Geophys. Res. Lett.*, 33(2), L02707.
- Messina, C. D., J. W. Jones, and J. W. Hansen (2001), Understanding ENSO effects on tomato yields in Florida: a modeling approach, Florence, Italy, pp. 155–156.
- Mo, K., and R. Livezey (1986), Tropical-extratropical geopotential height teleconnections during the Northern Hemisphere winter, *Mon. Weather Rev.*, 114(12), 2488-2515.

- Molnar, P., and M. A. Cane (2007), Early Pliocene (pre-Ice Age) El Niño-like global climate: Which El Niño?, *Geosphere*, 3(5), 337.
- Moorhead, D., and C. Dangerfield (1996), Shifting annual rowcrop production to Conservation Reserve Program tree planting: Impacts on agricultural and personal income, and employment in Georgia, in *Conference Abstracts*, p. 202, The Pennsylvania State University Dept. of Agricultural Economics & Rural Sociology and The School of Forest Resources, University Park, PA.
- Moriyasi, D. N., J. G. Arnold, M. W. Van Liew, R. L. Bingner, R. D. Harmel, and T. L. Veith (2007), Model evaluation guidelines for systematic quantification of accuracy in watershed simulations., *Trans. ASABE*, 50(3), 885-900.
- Mote, P. W., A. F. Hamlet, M. P. Clark, and D. P. Lettenmaier (2005), Declining mountain snowpack in western North America, *Bull. Am. Met. Soc.*, 86(1), 39-49.
- Mouri, H., M. Takaoka, and H. Kubotani (1999), Wavelet identification of vortex tubes in a turbulence velocity field, *Phys. Lett. A*, 261(1-2), 82-88.
- Nash, J. E., and J. V. Sutcliffe (1970), River flow forecasting through conceptual models, Part I: A discussion of principles, *J. Hydrol.*, 10(3), 282-290.
- Neitsch, S. L., J. G. Arnold, J. R. Kiniry, R. Srinivasan, and J. R. Williams (2002), *Soil and water assessment tool: User's manual: Version 2000*, USDA-ARS GSWRL and Blackland Research Center, Temple, TX.
- Neitsch, S. L., J. G. Arnold, J. R. Kiniry, J. R. Williams, and K. W. King (2005), *Soil and Water Assessment Tool: Theoretical documentation, Version 2005.*, Blackland Research Center, USDA-ARS Grassland Soil and Water Research, Temple, TX.
- Nezlin, N. P., and B. Li (2003), Time-series analysis of remote-sensed chlorophyll and environmental factors in the Santa Monica–San Pedro Basin off Southern California, *J. Mar. Syst.*, 39(3-4), 185-202.
- Ouyang, Y. (2003), Simulating dynamic load of naturally occurring TOC from watershed into a river, *Water Res.*, 37, 823–832.
- Park, J., and M. Mann (2000), Interannual Temperature Events and Shifts in Global Temperature: A “Multiwavelet” Correlation Approach, *Earth Interactions*, 4(1), 1-36.
- Pascual, M., X. Rodo, S. P. Ellner, R. Colwell, and M. J. Bouma (2000), Cholera dynamics and El Niño -Southern Oscillation, *Science*, 289, 1766-1769.
- Pathak, T. (2010), Cotton Yield Forecasting for the Southeastern United States, Ph.D. Dissertation, University of Florida.

- Phillips, N. A. (1956), The general circulation of the atmosphere: A numerical experiment, *Q. J. Roy. Meteorol. Soc.*, 82(352).
- Piechota, T. C., and J. A. Dracup (1999), Long-range streamflow forecasting using El Niño-Southern Oscillation indicators, *J. Hydrol. Eng.*, 4(2), 144-151.
- Pielke Jr., R. A. (2009), Collateral damage from the death of stationarity, *GEWEX Newsletter*, (May), 5-7.
- Postgate, J. (1998), *Nitrogen Fixation*, Cambridge University Press, Cambridge, UK.
- Priestley, C., and R. Taylor (1972), On the assessment of surface heat flux and evaporation using large-scale parameters, *Mon. Weather Rev.*, 100(2), 81-92.
- Purdum, E. D. (2002), *Florida Waters: A Water Resources Manual*, Institute of Science and Public Affairs, Florida State University, Tallahassee, Florida.
- Purdum, E. D., L. C. Burney, and T. M. Swihart (1998), *History of Water Management In E.A. Water Resources Atlas of Florida*, Florida State University, Tallahassee, Florida.
- Rabalais, N. N., R. E. Turner, and D. Scavia (2002), Beyond science into policy: Gulf of Mexico hypoxia and the Mississippi River, *Bioscience*, 52(2), 129-142.
- Rajagopalan, B., and U. Lall (1998), Interannual variability in western US precipitation, *J. Hydrol.*, 210, 51-67.
- Rajagopalan, B., U. Lall, and S. E. Zebiak (2002), Categorical climate forecasts through regularization and optimal combination of multiple GCM ensembles, *Mon. Weather Rev.*, 130(7), 1792–1811.
- Rasmusson, E. M., and J. M. Wallace (1983), Meteorological aspects of the El Niño/southern oscillation, *Science*, 222(4629), 1195-1202.
- Rawls, W., P. Yates, and L. Asmussen (1976), *Calibration of selected infiltration equations for the Georgia Coastal Plain*, SEWRL, Tifton, GA.
- Reed, R., W. Campbell, L. Rasmussen, and R. Rogers (1961), Evidence of a downward propagating annual wind reversal in the equatorial stratosphere, *J. Geophys. Res.*, 66, 813–818.
- Rial, J. A. et al. (2004), Nonlinearities, feedbacks and critical thresholds within the Earth's climate system, *Climatic Change*, 65(1), 11–38.
- Ropelewski, C. F., and M. S. Halpert (1987), Global and regional scale precipitation patterns associated with the El Niño/Southern Oscillation (ENSO), *Mon. Weather Rev.*, 115, 1606-1626.

- Ropelewski, C. F., and M. S. Halpert (1986), North American precipitation and temperature patterns associated with the El Niño/Southern Oscillation (ENSO), *Mon. Weather Rev.*, 114, 2352-2362.
- Rosen, B. H., S. Gray, and E. Flaig (1996), *Implementation of Lake Okeechobee Watershed Management Strategies to Control Phosphorus Load*, South Florida Water Management District (SFWMD).
- Rosensweig, C., and D. Hillel (1995), Potential impacts of climate change on agriculture and food supply, *Consequences*, 1(2), 22-23.
- Saha, S., S. Nadiga, C. Thiaw, J. Wang, W. Wang, Q. Zhang, H. M. Van den Dool, H. L. Pan, S. Moorthi, and D. Behringer (2006), The NCEP climate forecast system, *J. Clim.*, 19(15), 3483–3517.
- Schmidt, N., E. K. Lipp, J. B. Rose, and M. Luther (2001), ENSO influences on seasonal rainfall and river discharge in Florida, *J. Clim.*, 14, 615-628.
- Serbruyns, I., and S. Luysaert (2006), Acceptance of sticks, carrots and sermons as policy instruments for directing private forest management, *Forest Policy Econ.*, 9(3), 285-296.
- Serrano, E., R. Compagnucci, and M. Fadio (1992), The use of the wavelet transform for climatic estimates, in *Fifth International Meeting on Statistical Climatology*, vol. Toronto, ON. Canada, pp. 259-262, American Meteorological Society.
- Sheridan, J. M. (1997), Rainfall-streamflow relations for coastal plain watersheds, *Appl. Eng. Agric.*, 13(3), 333-344.
- Sheridan, J. M., and W. G. Knisel (1989), Rainfall trends in the Georgia Coastal Plain, in *Proceedings of the 1989 Georgia Water Resources Conference*, University of Georgia, pp. 9-11, University of Georgia, Athens, GA.
- Sheridan, J. M., W. H. Merkel, and D. D. Bosch (2001), Peak rate factors for flatland watersheds, *Appl. Eng. Agric.*, 18(1), 65-69.
- Sheridan, J. M., P. Yates, and L. E. Asmussen (1983), *Hydrology and nutrient and sediment movement from Southeastern Coastal Plain watersheds*, University of Georgia College of Agricultural Experimental Stations, University of Georgia.
- Shirmohammadi, A., J. M. Sheridan, and L. E. Asmussen (1986), Hydrology of alluvial stream channels in southern coastal plain watersheds, *Trans. ASABE*, 29(1), 135-142.
- Sittel, M. C. (1994), *Marginal probabilities of the extremes of ENSO events for temperature and precipitation in the southeastern United States*, Center for Ocean-Atmospheric Studies, Florida State University, Tallahassee, FL.

- Skaggs, R. W. (1981), *DRAINMOD-Reference report: Methods for design and evaluation of drainage-water management systems for soils with high water tables*, National Resources Conservation Service (NRCS), Wetland Science Institute, Washington, D.C., USA.
- Soil and Water Engineering Technology, Inc. (1996), *EAAMOD, Technical Manual Everglades Agricultural Area MODel - Field (11/96 revision)*, SWET, Inc., Gainesville, Florida.
- Soil and Water Engineering Technology, Inc. (2000), *EAAMOD, User's Manual, Everglades Agricultural Area MODel - Field (11/00 revision). Interface Version 3.0.0, Model version 14.6.0.*, SWET, Inc., Gainesville, FL.
- Soil and Water Engineering Technology, Inc. (2004), *WAM Model Documentation and User Manual*, SWET, Inc., Gainesville, Florida.
- South Florida Water Management District (SFWMD) (2001), *Surface water improvement and management (SWIM) plan-update for Lake Okeechobee.*, South Florida Water Management District (SFWMD), West Palm Beach, FL.
- Stewart, I. T., D. Cayan, and M. Dettinger (2005), Changes toward earlier streamflow timing across western North America, *J. Clim.*, 18(8), 1136-1155.
- Stringfield, V. T. (1966), *Artesian water in Tertiary limestone in the Southeastern States*, Geological Survey Professional Paper, U.S. Government Printing Office, Washington, D.C.
- Sullivan, D. G., and H. L. Batten (2007), Little River Experimental Watershed, Tifton, Georgia, United States: A historical geographic database of conservation practice implementation, *Water Resour. Res.*, 43.
- Tilman, D., J. Fargione, B. Wolff, C. D'Antonio, A. Dobson, R. Howarth, D. Schindler, W. H. Schlesinger, D. Simberloff, and D. Swackhamer (2001), Forecasting agriculturally driven global environmental change, *Science*, 292(5515), 281-284.
- Torrence, C., and G. P. Compo (1998), A practical guide to wavelet analysis, *Bull. Am. Met. Soc.*, 79(1), 61-78.
- Trenberth, K. E. (1997), The Definition of El Niño, *Bull. Am. Met. Soc.*, 78(12), 2771-2777.
- Tsonis, A. A., and K. Swanson (2009), Has the climate recently shifted?, *Geophys. Res. Lett.*, 36, doi:doi:10.1029/2008GL037022.
- Tudhope, A. W., C. P. Chilcott, M. T. McCulloch, E. R. Cook, J. Chappell, R. M. Ellam, D. W. Lea, J. M. Lough, and G. B. Shimmield (2001), Variability in the El Niño-Southern Oscillation Through a Glacial-Interglacial Cycle, *Science*, 291(5508), 1511-1517.

- U.S. EPA (2008), *State adoption of Numeric Nutrient Standards: 1998-2008*, U.S. Environmental Protection Agency, Office of Water, Washington, D.C., USA. [online] Available from: <http://www.epa.gov/waterscience/criteria/nutrient/files/report1998-2008.pdf>
- U.S. EPA (1996), *Environmental indicators of water quality in the United States*, U.S. Government Printing Office, Washington, D.C., USA.
- U.S. EPA (1998), *National Strategy for the Development of Regional Nutrient Criteria*, U.S. Environmental Protection Agency, Office of Water, Washington, D.C., USA.
- UN (2006), *World Water Development Report 2: Water, a Shared Responsibility*, UNESCO, Paris, France.
- USDA (1999), *Census of Agriculture*, National Agricultural Statistics Service, Montgomery, Alabama.
- USDA (1972), *National Engineering Handbook, Hydrology Section*, National Engineering Handbook, Soil Conservation Service.
- USDA-ARS (2005), *Conservation Effects Assessment Project: The Watershed Assessment Study*, USDA Agricultural Research Service, Washington, D.C.
- Van Liew, M. W., T. L. Veith, D. D. Bosch, and J. G. Arnold (2007), Suitability of SWAT for the conservation effects assessment project: Comparison on USDA agricultural research service watersheds, *J. Hydrol. Eng.*, 12, 173.
- Veith, T. L., M. L. Wolfe, and C. D. Heatwole (2003), Optimization procedure for cost effective BMP placement at a watershed scale, *J. Am. Water Resour. Assoc.*, 39(6), 1331-1343.
- Wang, B. (1995), Interdecadal changes in El Niño onset in the last four decades, *J. Clim.*, 8, 267-285.
- Wang, C. (2001), A unified oscillator model for the El Niño–Southern Oscillation, *J. Clim.*, 14(1), 98-115.
- Wang, Y. (1996), Temporal structure of the Southern Oscillation as revealed by waveform and wavelet analysis, *J. Clim.*, (9), 1586-1598.
- Westerling, A. L., H. G. Hidalgo, D. Cayan, and T. W. Swetnam (2006), Warming and earlier spring increase Western U.S. forest wildfire activity, *Science*, 313(5789), 940-943.
- White, K. L., and I. Chaubey (2005), Sensitivity analysis, calibration, and validations for a multisite and multivariable SWAT model, *J. Am. Water Resour. Assoc.*, 41(5), 1077–1089.

- Whiting, J. P., M. F. Lambert, A. V. Metcalfe, P. T. Adamson, S. W. Franks, and G. Kuczera (2004), Relationships between the El-Niño Southern Oscillation and spate flows in southern Africa and Australia, [online] Available from: <http://hal-sde.archives-ouvertes.fr/hal-00304986/> (Accessed 12 January 2010)
- Wilks, D. S. (1995), *Statistical methods in the atmospheric sciences*, Academic Press, San Diego, CA.
- Wolter, K., and M. S. Timlin (1993), Monitoring ENSO in COADS with a seasonally adjusted principal component index, in *Proc. 17th Climate Diagnostics Workshop*, pp. 52–57.
- World Meteorological Organization (1966), *Climatic Change*, Technical Note No. 79, WMO, Geneva, Switzerland.
- Yuan, T. L. (1965), A survey of aluminum status in Florida soils, in *Proc. Soil Crop Sci. Soc. Fla*, vol. 25, pp. 143-152.
- Zebiak, S. E., and M. A. Cane (1987), A model El Niño-Southern Oscillation, *Mon. Weather Rev.*, 115, 2262-2278.
- Zhong, C., and T. Yang (2007), Wavelet analysis algorithm for synthetic pulsar time, *Chin. Astron. Astrophs.*, 31(4), 443-454.
- Zorn, M. R., and P. R. Waylen (1997), Seasonal response of mean monthly streamflow to El Niño/Southern Oscillation in north central Florida, *Prof. Geog.*, 49(1), 51-62.

## BIOGRAPHICAL SKETCH

At the old age of 30, Victoria Keener is finally done with her dissertation. Despite the many stressful nights, mornings, afternoons, and evenings, she made it through mostly intact, minus an Anterior Cruciate Ligament in her left knee, with the help of her feline sidekicks Bun-Bun and Frey, and her superhero husband Keith.

Victoria grew up in Alexandria, Virginia, a suburb of Washington, D.C., and received her B.S. in Bioengineering from Rice University in Houston, Texas, in 2002. After working in a genetics lab for two years, she decided that animal research was not for her, and went back to school to get a Ph.D. in Agricultural and Biological Engineering at the University of Florida. Her current experimental organism is The Earth, which suffers less acutely than a mouse, yet is much more difficult to control for an experiment.

In her spare time, Victoria enjoys numerous non-mathematically centered hobbies, including gardening, cooking, rocking out, and hiking. She is ready to again embrace the seasons after living in the south for the last eleven years.